UNIVERSIDAD COMPLUTENSE DE MADRID

FACULTAD DE CIENCIAS QUÍMICAS

Departamento de Química Orgánica I

TESIS DOCTORAL

Bio-inspired hierarchical organization of electroactive supramolecular architectures based on carbon nanoestructures

Organización bio-inspirada y jerarquizada de arquitecturas supramoleculares electroactivas basadas en nanoestructuras de carbono

MEMORIA PARA OPTAR AL GRADO DE DOCTOR

PRESENTADA POR

Javier López Andarias

Directores

Nazario Martín León

Carmen María Atienza Castellanos

Madrid, 2016

UNIVERSIDAD COMPLUTENSE DE MADRID

FACULTAD DE CIENCIAS QUÍMICAS

Departamento de Química Orgánica I

BIO-INSPIRED HIERARCHICAL ORGANIZATION OF ELECTROACTIVE SUPRAMOLECULAR ARCHITECTURES BASED ON CARBON NANOSTRUCTURES

ORGANIZACIÓN BIO-INSPIRADA Y JERARQUIZADA DE ARQUITECTURAS SUPRAMOLECULARES ELECTROACTIVAS BASADAS EN NANOESTRUCTURAS DE CARBONO

TESIS DOCTORAL

Javier López Andarias

Madrid, 2015

BIO-INSPIRED HIERARCHICAL ORGANIZATION OF ELECTROACTIVE SUPRAMOLECULAR ARCHITECTURES BASED ON CARBON NANOSTRUCTURES

ORGANIZACIÓN BIO-INSPIRADA Y JERARQUIZADA DE ARQUITECTURAS SUPRAMOLECULARES ELECTROACTIVAS BASADAS EN NANOESTRUCTURAS DE CARBONO

Directores:

Prof. Dr. Nazario Martín León
Dra. Carmen María Atienza Castellanos

Memoria que para optar al grado de
DOCTOR EN CIENCIAS QUÍMICAS
presenta

Javier López Andarias

Madrid, 2015

D. Nazario Martín León, Catedrático de Universidad del Departamento de Química Orgánica de la Universidad Complutense de Madrid y **Dña. Carmen María Atienza Castellanos**, Investigadora de Universidad del Departamento de Química Orgánica de la Universidad Complutense de Madrid,

CERTIFICAN

Que la presente Memoria titulada "Bio-inspired hierarchical organization of electroactive supramolecular architectures based on carbon nanostructures" se ha realizado bajo su dirección en el Departamento de Química Orgánica de la Universidad Complutense de Madrid, por el licenciado en Química D. Javier López Andarias y autorizan su presentación para ser calificada como tesis doctoral.

Y para que conste, firmo el presente certificado en Madrid a 5 de Octubre de 2015.

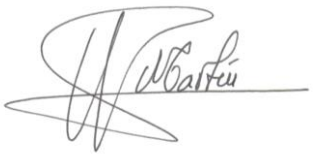

Fdo. Dr. Nazario Martín

Fdo. Dra. Carmen Mª Atienza

The results presented in this thesis have been published and listed below:

1) J. L. López, C. Atienza, A. Insuasty, J. López-Andarias, C. Romero-Nieto, D. M. Guldi and N. Martín, *Angew. Chem., Int. Ed.* **2012**, *51*, 3857-3861.

2) F. G. Brunetti, C. Romero-Nieto, J. López-Andarias, C. Atienza, J. L. López, D. M. Guldi and N. Martín, *Angew. Chem., Int. Ed.* **2013**, *52*, 2180-2184.

3) J. López-Andarias, J.L. López, C. Atienza, F. G. Brunetti, C. Romero-Nieto, D. M. Guldi and N. Martín, *Nat. Commun.* **2014**, *5*, 3763.

4) A. Bolag, J. López-Andarias, S. Lascano, S. Soleimanpour, C. Atienza, N. Sakai, N. Martín and S. Matile, *Angew. Chem., Int. Ed.* **2014**, *53*, 4890-4895.

5) J. López-Andarias, M.J. Rodriguez, C. Atienza, J. L. López, T. Mikie, S. Casado, S. Seki, J. L. Carrascosa and N. Martín, *J. Am. Chem. Soc.* **2015**, *137*, 893-897.

6) J. López-Andarias, A. Bolag, C. Nancoz, E. Vauthey, C. Atienza, N. Sakai, N. Martín and S. Matile, *Chem. Commun.* **2015**, *51*, 7543-7545.

7) S. H. Mejías, J. López-Andarias, T. Sakurai, S. Yoneda, K. P. Erazo, S. Seki, C. Atienza, N. Martín, A. L. Cortajarena, **submitted**.

A mis padres

Acknowledgments

El presente trabajo ha sido realizado en el Departamento de Química Orgánica de la Universidad Complutense de Madrid bajo la dirección del Prof. Nazario Martín y de la Dra. Carmen Atienza.

Querría comenzar dando las gracias a mis dos directores:

Nazario, gracias por darme la oportunidad de trabajar todos estos años en tu grupo. No creo que nunca pueda tener un jefe tan admirable como eres tú. Gracias por transmitirme tus conocimientos y por haber dedicado todo tu tiempo, y más, a sacar adelante este trabajo. Ha sido un honor pertenecer a tu grupo de investigación.

Carmen, gracias por toda tu confianza y todo tu apoyo desde el primer día hasta el último. Tu conocimiento, tu comprensión y tu optimismo son dignos de admirar. Echaré de menos todas nuestras discusiones de química, que tanto nos gustan. No has sido sólo mi directora, también te has convertido en mi amiga. Gracias por todo.

También me gustaría nombrar a otros miembros del grupo que han contribuido en parte del trabajo descrito en esta memoria: Gracias Juan Luis y Fulvio. Ha sido un gran placer trabajar con vosotros y, sobre todo, aprender de vosotros.

En la realización de este trabajo han participado otros grupos de investigación, a los que agradezco enormemente su contribución:

Al grupo de investigación del Prof. Dirk M. Guldi de la Universidad Friedrich-Alexander de Erlangen/Nürnberg (Alemania) y al grupo de investigación del Prof. Shu Seki de la Universidad de Kyoto (Japón) por los diversos estudios fotofísicos que se recogen en la memoria. En este párrafo tengo que destacar a Carlos, tú me enseñaste a querer la química orgánica, luego te convertiste en mi amigo y más tarde tuve la suerte de trabajar contigo, tú desde Erlangen y yo desde Madrid. Gracias por todo.

Al grupo del Prof. José L. Carrascosa del Centro Nacional de Biotecnología (CNB) (España), especialmente a Mª José Rodríguez, por toda su dedicación en la realización de algunos de los estudios de microscopía recogidos en esta memoria.

Al grupo de la Dra. Aitziber L. Cortajarena del Instituto Madrileño de Estudios Avanzados (IMDEA) Nanociencia (Madrid), sin el cual el Capítulo 2 nunca hubiese podido realizarse. Gracias, Aitziber, por todo el tiempo dedicado a estos

proyectos. Es un placer hablar contigo de ciencia. Y gracias, Sara, por todo tu trabajo dentro del laboratorio, por estar siempre disponible y por tu alegría.

To the research group of Prof. Stefan Matile at University of Geneva (Switzerland). Thank you, Stefan, for giving me the opportunity of working in your lab for three months. I would like to mention, as well, to Dr. Naomi Sakai and Dr. Altan Bolag for their immeasurable help and their contribution to the projects. Some lines have to go to my fabulous labmates, François and Jadwiga, thank you a lot for those good moments inside and outside the lab. I hope there will be more in the future.

A continuación me gustaría agradecer a todos los compañeros y amigos del laboratorio y del departamento, tanto los de antes como los de ahora, por todo lo que ha significado tenerlos tan cerca:

Los "mayores", Mª Ángeles, Salvo, Beti, David, Margarita, Emilio y Luis, gracias por vuestra atención y por estar siempre dispuestos a ayudar.

Toda la gente del laboratorio, sois muchos así que espero no dejarme a nadie. Los que aún siguen: los chicos de la pequeña "Turquía", Andrés y Sara, pequeño y a la vez gran labo; Sonia, Silvia, Rosa, María, Laura, "Muchachito", Marina, Valentina, Mikiko, Antonio, Jose, Rafa, Inés, Matteo, Virginia, Ana, Helena; y los que ya se fueron: Andreita, Tony, Juan, André, Helenita, Alberto DJ, Raúl, Enrique, Jaime, Carmen, Vanesa, Hui, David y Pierre. Todos me habéis hecho sentir muy a gusto, tanto dentro como fuera, convirtiendo este trabajo en una pequeña familia.

También a los otros químicos fuera del grupo: Edu, Paula, Julia, Jorge, "las Fátimas", Richard, Constanza y, en especial, Alberto, por su gran amistad y por todos los grandes momentos que hemos pasado estos años, y los que quedan...

Un párrafo aparte lo reservo para Agus, Marta, Noe y LuisMo: Os habéis convertido en personas indispensables para mí. No tengo duda alguna de que la amistad que ha surgido todos estos años será para siempre.

Así mismo, quiero agradecer al CAI de RMN y de Rayos X de la Facultad de Ciencias Químicas y al Centro Nacional de Microscopía Electrónica su gran ayuda y dedicación en la realización de los experimentos, siempre con un trato excepcional.

Pasando ahora al resto de gente fuera de la Universidad: gracias a mi gente de Puertollano, de Bolaños y de Ciudad Real, por hacerme sentir siempre tan querido.

Y para terminar, las personas más importantes de mi vida:

A mis padres, gracias por confiar siempre en mí, por haberos sacrificado tanto para que siempre haya podido realizar mis deseos, y por quererme tanto. Sois mi ejemplo a seguir. Por esto y mucho más esta memoria va dedicada a vosotros.

A mi hermana, gracias por todo tu cariño y tu amistad y por saber que siempre puedo contar contigo. Estoy seguro que te convertirás en una gran química… ¡ya lo estás haciendo! Estoy muy orgulloso de ti.

A Anto, son muchas las cosas que podría decir de ti para agradecerte esta memoria. Siempre has estado a mi lado y me has apoyado en mis decisiones. Siempre has tenido una sonrisa cuando lo he necesitado y me has hecho sentir la persona más querida del mundo. Nunca sentiré tanta admiración por nadie como lo hago por ti. Me siento muy afortunado de haber dado contigo.

Javier López Andarias

Table of contents

References, abbreviations and acronyms 1

Summary 7

Resumen 17

Introduction

I.1. Origins of nanotechnology and nanoscience 27
I.2. Chemistry in nanoscience 28
I.3. Hierarchical architectures in nature 29
I.4. Carbon nanostructures 30

Chapter 1. ***Peptide-based donor/acceptor architectures with hierarchical organization***

1.1. Background

1.1.1. Molecular and supramolecular chemistry for mimicking nature 37
1.1.2. Self-assembled materials based on β-sheets interactions 38
1.1.3. Segregated donor-acceptor assemblies 45
1.1.4. Macroscopically aligned organic materials 50
1.1.5. Supramolecular structures based on single-wall carbon nanotubes 53
1.1.6. exTTF: a butterfly-shaped molecule for supramolecular organizations 60
1.1.7. Molecular assemblies of perylene bisimide 65

1.2. Objectives 71

1.3. Results and Discussion

1.3.1. Self-ordering electron donor-acceptor nanohybrid based on single-walled carbon nanotubes across different scales 75

1.3.1.1. Design and synthesis of dendritic exTTF **1** 76
1.3.1.2. Spectroscopic and photophysical characterization of **1**/SWCNT nanohybrid 79
1.3.1.3. Microscopy and X-ray diffraction studies of **1**/SWCNT nanohybrid 85

1.3.2. Controlling the crystalline three-dimensional order in bulk materials by single-wall carbon nanotubes 91

1.3.2.1. Synthesis of exTTF-tripeptide **12** and exTTF-pentapeptide **13** 91
1.3.2.2. Study of the supramolecular organization of **12** and **13** in well-ordered *p*-nanofibers 93
1.3.2.3. Interfacing between *p*-nanostructures and SWCNTs 99
1.3.2.4. Formation of *n*/*p*-nanocomposite hydrogels 110

1.3.3. Highly Ordered *n*/*p*-Co-assembled Materials with Remarkable Charge Mobilities 115

1.3.3.1. Synthesis of perilenebisimide-based derivatives **20** and **21** 116
1.3.3.2. Self-organization of PBI compounds in water 117
1.3.3.3. Spectroscopic characterization of the *n*/*p*-material 119
1.3.3.4. Microscopy and X-Ray Diffraction studies 124
1.3.3.5. Charge mobility measurements 130

1.4. Conclusions 137

1.5. Experimental section

1.5.1. Synthesis 141

1.5.1.1. Synthesis of exTTF derivative **1** 141
1.5.1.2. Synthesis of peptide-based exTTF derivatives **12** and **13** 145
1.5.1.3. Synthesis of cationic PBI derivatives **20** and **21** 148

1.5.2. Characterization of nanohybrids, hydrogels and solid materials 151

Chapter 2. ***TPR proteins as a new tool for the organization of organic materials.***

2.1. Background

2.1.1. DNA-based nanostructures 159
2.1.2. Protein-based nanostructures 160

2.1.2.1. Amyloid-like assemblies 161
2.1.2.2. α-Helix-based assemblies 162

2.1.2.3. TPR proteins: the versatile helix 163

2.1.3. DNA and protein as scaffolds for chromophore arrays 165
2.1.4. Non-covalent interactions between proteins and CNTs 170

2.2. Objectives 175

2.3. Results and Discussion

2.3.1. TPR protein scaffolds as templates for ordering porphyrin arrays in solution and solid state 179

2.3.1.1. Design and synthesis of porphyrin derivatives **25** and **26** 179
2.3.1.2. Design and synthesis of mutated CTPR protein 182
2.3.1.3. Synthesis of **CTPR4-25** and **CTPR4-26** conjugates 183
2.3.1.4. Characterization of conjugates in solution 185
2.3.1.5. Characterization of conjugates in the solid state 187
2.3.1.6. Characterization of the anisotropic photoconductivity of the thin films 190

2.3.2. Donor/acceptor nanohybrids based on superhelical protein-porphyrin conjugates and SWCNTs 193

2.3.2.1. Compatibility of morphology and composition of CTPR proteins and SWCNTs 193
2.3.2.2. Design, synthesis and characterization of CTPR proteins and conjugates 197
2.3.2.3. Wrapping SWCNTs by CTPR proteins and conjugates 201

2.4. Conclusions 213

2.5. Experimental section

2.5.1. Synthesis

2.5.1.1. Synthesis of porphyrin derivatives **25** and **26** 217
2.5.1.2. Synthesis of conjugates 221

2.5.2. Characterization of conjugates 222

Chapter 3. ***Evaluation of a collection of fullerenes in triple-channel photosystems.***

3.1. Background

3.1.1. Self-Organizing Surface-Initiated Polymerization 229
3.1.2. Self-Organizing Surface-Initiated Polymerization Templated Stack Exchange 232
3.1.3. Non-NDI-based photosystems obtained from SOSIP-TSE strategy. Access to non-planar systems: fullerenes 233
3.1.4. Triple-channel Oriented Photosystem 235
3.1.5. Tuning the LUMO levels of fullerene derivatives by chemical modifications 237

3.2. Objectives 245

3.3. Results and Discussion

3.3.1. 1,4-Diaryl[60]fullerene and 1,2-dihydromethano[60]fullerene derivatives for synthetic access towards oriented charge-transfer cascades in triple-channel photosystems 249

3.3.1.1. Synthesis of fullerenes **32**-**37** and dyads **T4-32** and **T4-33** 250
3.3.1.2. Electrochemical characterization of fullerene derivatives 254
3.3.1.3. Stack Exchange of dyads **T4-32** to **T4-37** 256
3.3.1.4. Functional characterization of dyads **T4-32** to **T4-37** 258

3.3.2. Electron-deficient fullerenes in triple-channel photosystems 263

3.3.2.1. Synthesis of fullerenes **60**-**64** 263
3.3.2.2. Electrochemical characterization of fullerene derivatives **60** to **64** 267
3.3.2.3. Stack Exchange of dyads **T4-60** to **T4-64** 268
3.3.2.4. Functional characterization of dyads **T4-60** to **T4-64** 269

3.4. Conclusions 273

3.5. Experimental section

3.5.1. Synthesis 277

3.5.1.1. Synthesis of 1,4-fullerene addends **32** and **33** and their oligothiophene-based dyads **T4-32** and **T4-33** 277
3.5.1.2. Synthesis of Bingel fullerenes **54**, **57** and **59** 286
3.5.1.3. Synthesis of electron-deficient fullerenes **60** to **64** 289

3.5.2. Template Stack-Exchange and Electrode Characterization 297

References 301

References, abbreviations and acronyms

Bibliographic citations have been placed as footnotes in the pages where they were first cited in the section and at the end of this manuscript.

The following terms have been used in this manuscript:

1D	One dimensional
2D	Two dimensional
3D	Three dimensional
A	Ampere
a. u.	Arbitrary units
AFM	Atomic force microscopy
Alloc	Allyloxycarbonyl-
Ar	Argon
Boc	*tert*-Butyloxycarbonyl
c_{SOSIP}	Critical SOSIP concentration
ca.	Approximately
CD	Circular dichroism
CNT	Carbon nanotube
CT	Charge transfer
CTPR	Consensus tetratricopeptide repeat
CV	Cyclic voltammetry
ΔE_g	Optical bandgap
DBU	1,8-Diazabicyclo[5.4.0]undec-7-ene
DCTB	*trans*-2-[3-(4-*tert*-Butylphenyl)-2-methyl-2-propenylidene]malononitrile
DFT	Density functional theory
DIPEA	*N*,*N*-Diisopropylethylamine
DMF	*N*,*N*-Dimethylformamide
DMSO	Dimethylsulfoxyde
DPM	Diphenylmethano[60]fullerene
DTT	DL-Dithiotreitol
ε	Molar absorption coefficient
E	Energy
e^-	Electron
$E_{1/2}$	Half-wave potential
E_a	Activation energy
EDC	*N*-(3-Dimethylaminopropyl)-*N′*-ethylcarbodiimide hydrochloride
E_{HOMO}	HOMO energy
E_{LUMO}	LUMO energy
E_{ox}	Oxidation potential
E_{red}	Reduction potential
ESI	Electrospray ionization
eV	Electron-Volt
exTTF	π-Extended tetrathiafulvalene
Fc	Ferrocene

FF	Fill factor
FFT	Fast Fourier transform
Fmoc	Fluorenylmethyloxycarbonyl-
FP-TRMC	Flash-photolysis time-resolved microwave conductivity
FPLC	Fast protein liquid chromatography
FRET	Förster resonant energy transfer
h^+	Hole
HBTU	*o*-(Benzotriazole-1-yl)-*N,N,N',N'*-tetramethyluronium hexafluorophosphate
HOBt	Hydroxybenzotriazole
HOMO	Highest occupied molecular orbital
HOPG	Highly ordered pyrolytic graphite
HR	High resolution
λ	Wavelength
I	Current
ITO	Indium tin oxide
J	Current density
l	Optical path
LUMO	Lowest unoccupied molecular orbital
μ_e	Electron mobility
μ_h	Hole mobility
m-	*meta*-
MALDI	Matrix-assisted laser desorption/ionization
MS	Mass spectrometry
Mp.	Melting point
MW	Molecular weight
η	Power conversion efficiency
η_{BR}	Bimolecular charge recombination efficiency
NDI	Naphtalenediimide
NMR	Nuclear magnetic resonance
o-	*ortho*-
OC	Open circuit
OMARG	Oriented multicomponent antiparallel redox gradients
ϕ	Quantum yield of charge-carrier generation
$\phi\Sigma\mu$	Photoconductivity transients
$(\phi\Sigma\mu)_{max}$	Maximum photoconductivity transients
p-	*para*-
PDB	Protein data bank
PCBM	1-(3-Methoxycarbonylpropyl)-1-phenyl[6,6]methanofullerene
PBI	Perylenebisimide
PTLC	Preparative thin-layer chromatography
RET	Resonant energy transfer
r.p.m.	Revolution per minute
rt	Room temperature
$\Sigma\mu$	Sum of charge-carrier mobilities
SEM	Scanning electron microscopy
SAM	Self-assembled monolayer

SAXS	Small angle X-ray scattering
SC	Short circuit
SDBS	Sodium dodecylbenzenesulfonate
SHJ	Supramolecular heterojunction
SOSIP	Self-organizing surface-initiated polymerization
STM	Scanning tunneling microscope
SWCNT	Single wall carbon nanotube
T	Temperature
t-Bu	*tert*-Butyl-
TEA	Triethylamine
TEM	Transmission electron microscopy
TEOA	Triethanolamine
TFA	Trifluoroacetic acid
TLC	Thin-layer chromatography
TMS	Trimethylsilyl
TPR	Tetratricopeptide repeat
TSE	Templated stack-exchange
UV	Ultraviolet
V	Voltage
V	Volt
vis	Visible
XPS	X-ray photoelectron spectroscopy
XRD	X-ray diffraction

Summary

"Bio-inspired Hierarchical Organization of Electroactive Supramolecular Architectures based on Carbon Nanostructures"

Introduction

Nanotechnology, referring as the manipulation of matter at the molecular and supramolecular scale, is an emerging area with promising benefits for humanity.[1] In particular, carbon nanostructures have received a great attention due to their exciting electronic and mechanical properties. Mimicking nature, that is, developing bioinspired procedures, could be one of the most intelligent strategies to organize matter, in particular carbon-rich nanostructures, with the aim of maximizing their fabulous optoelectronic properties.

Objectives

Chapter 1: Development of new strategies based on small peptide assemblies for the generation of ordered donor/acceptor materials.

Chapter 2: Using TPR proteins as robust scaffolds for ordering porphyrins in solution and solid state and as wrapping agents for SWCNTs.

Chapter 3: Testing a series of fullerene derivatives with different chemical functionalization and different LUMO energy levels in oriented triple-channel photosystems.

Results and Discussion

Chapter 1. *Peptide-based donor/acceptor architectures with hierarchical organization.*

i) Self-ordering electron donor-acceptor nanohybrids based on single-walled carbon nanotubes across different scales.[40]

We have designed and synthesized derivative **1** based on an exTTF moiety acting as electron donating unit and as recognition component of SWCNT surface, a dipeptide sequence to promote organization and a dendritic termini to ensure solubility in water (Figure S1a).

Spectroscopic and photophysical characterization of **1** in the presence of SWCNTs revealed the formation of the donor/acceptor nanohybrid with a lifetime of the charge-separated state considerably longer than that of previously reported related systems.[23]

Interestingly, a close inspection of this nanohybrid in the solid state through different microscopic techniques revealed the presence of self-aligned structures, mainly in 2D (Figure S1b,c).

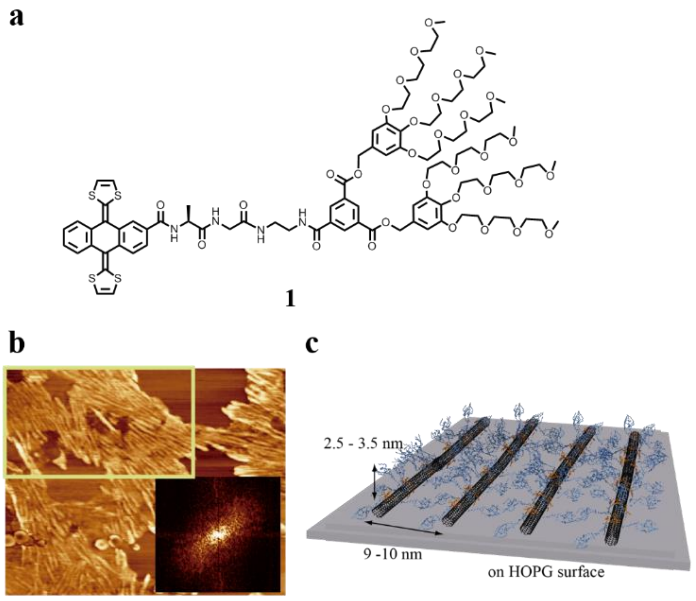

Figure S1. Self-ordering nanohybrids based on exTTF and SWCNT. (a) Molecular structure of compound **1**. (b) AFM image of the 2D architecture. (c) Schematic drawing of the nanostructures in (b).

ii) Controlling the crystalline three-dimensional order in bulk materials by single-wall carbon nanotubes.[49]

Encourage by the previous results, we redesigned the exTTF derivative extending the peptide sequence and replacing the dendritic termini by a carboxylic group for controlling the self-assembly process by pH adjustment and charge-screening. In this sense, derivatives **12** and **13** were synthesized (Figure S2a).

Firstly, a deep study of the supramolecular organization of these derivatives was carried out. Curve rope-like nanofibers were obtained in aqueous media, stabilized by the presence of $NaHCO_3$. Absorption spectroscopy indicated π-π stacking between exTTF units and CD assays revealed a major ordering of π-π interacting exTTFs in the form of chiral arrays and a *β*-sheet secondary structure of the peptides.

Secondly, the aforementioned supramolecular polymers have been used as wrapping agents of SWCNTs. Titration experiments indicated that derivative **13**, with a larger peptide sequence, presented more stability in the presence of SWCNTs. Photoexcitation of these nanohybrids showed lifetimes of the electron transfer product between 125-210 ps.

The most interesting aspect of this approach is the generation of ordered hydrogels by charge-screening with Ca^{2+}. The presence of SWCNTs clearly influence the crystallinity of the material, acting as a template and producing long-range ordering in the architecture (Figure S2b-d).

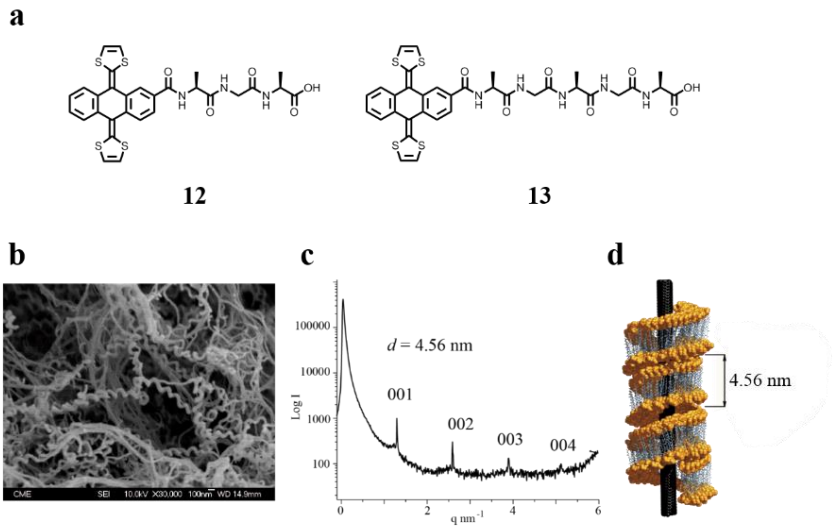

Figure S2. Approach for the generation of long-range ordered materials. (a) Molecular structures of compounds **12** and **13**. (b) SEM image of the xerogel obtained from **13**/SWCNT/$CaCl_2$. (c) SAXS diffractogram of the same hydrogel. (d) Schematic drawing of the ordered nanostructure.

iii) Highly ordered *n*/*p*-co-assembled materials with remarkable charge mobilities.[56]

Considering the efficiency of compound **13** to generate stable materials, we decided to extend the approach replacing SWCNTs and Ca^{2+} by positively charged *n*-type nanofibers based on PBI. Two different building blocks were designed and synthesized differing in the charged group, that is, a guanidinium salt in **20** and a quaternary ammonium salt in **21** (Figure S3a).

The ability of these molecules to generate nanofibers in water was tested and successfully achieved. Then, both donor and acceptor water-soluble

nanofibers were mixed, instantaneously obtaining a solid precipitate which maintained the electronic properties of individually aggregated chromophores (exTTF and PBI). The molecular composition of the materials was confirmed by XPS and UV-*vis* spectroscopy with a stoichiometry of **$13_2$20** and **$13_2$21**.

The most interesting features of these *n*/*p*-materials were found by microscopic and X-ray diffraction studies, where aligned fibers ranging from the nano to the macroscopic scale composed of segregated donor and acceptor domains were found (Figure S3b,c).

The effectiveness of this methodology was proven by their excellent photoconductivity properties, with charge mobility values between 0.5 - 0.8 $cm^2V^{-1}s^{-1}$.

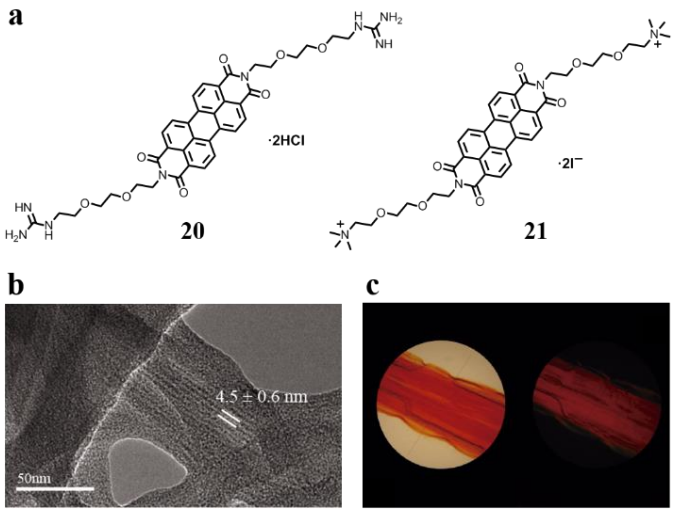

Figure S3. Attainment of *n*/*p*-co-assembled materials from exTTF and PBI small molecules. (a)Molecular structures of PBI derivatives **20** and **21**. (b) TEM image of the material showing the segregated donor/acceptor domains. (c) Optical micrographs of the bulk material displaying birefringence features.

Chapter 2. ***TPR proteins as a new tool for the organization of organic materials.***

i) TPR protein scaffolds as templates for ordering porphyrin arrays in solution and solid state.

A free-base and a zinc-metalloporphyrin derivatives, **25** and **26**, were designed and synthesized, provided of water-soluble chains and a maleimide reactive group as efficient cross-linker for the conjugation reaction with the eight cysteine residues contained in a mutated **CTPR4** protein.

The conjugation reaction was nearly optimal, as confirmed by electrophoresis gel and mass spectrometry. Moreover, the characterization of the conjugates confirmed the formation of *J*-type porphyrin arrays and their chiral arrangement induced by the geometry of the protein. As expected, the structural integrity of this biological framework was fully conserved (Figure S4).

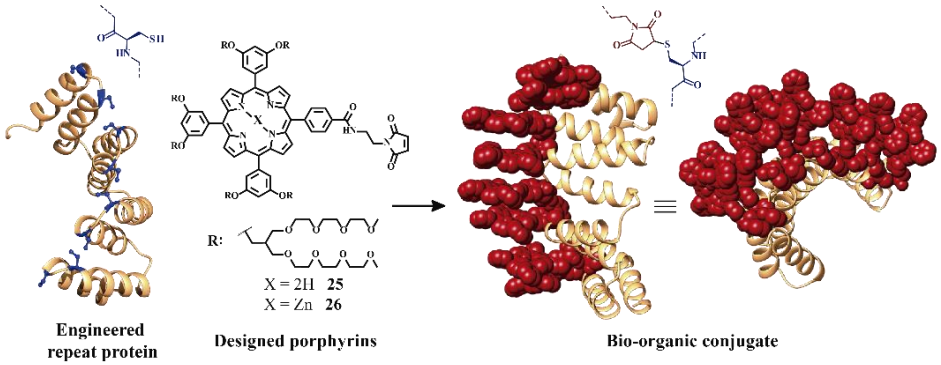

Figure S4. Scheme showing the approach to generate porphyrin/protein conjugates with precise positioning of the chromophores.

Thin films with both conjugates were successfully generated, retaining the protein structure and featuring anisotropic alignment and crystalline organization. Due to the potential interest of this organized porphyrin arrays in thin films, their photoconductivity was examined revealing anisotropic electrical conductivity with values of hole mobility ranging from 1.3 – 1.5 x 10^{-3} $cm^2V^{-1}s^{-1}$.

ii) Donor/Acceptor nanohybrids based on superhelical protein-porphyrin conjugates and SWCNTs.

Taking advantage of the superhelical structure of CTPR proteins, different lengths of these proteins, **CTPR4**, **CTPR8** and **CTPR16**, and their corresponding conjugates with porphyrin **26** were assessed as wrapping agents of SWCNTs (Figure S5).

Firstly, some theoretical assessments were made regarding morphology and composition of these proteins to accommodate one SWCNT in their inner cavity.

Then, after synthetizing and characterizing all the proteins and conjugates, their interaction with SWCNTs was proven by different techniques such as UV-*vis*, CD and Raman spectroscopies and TEM.

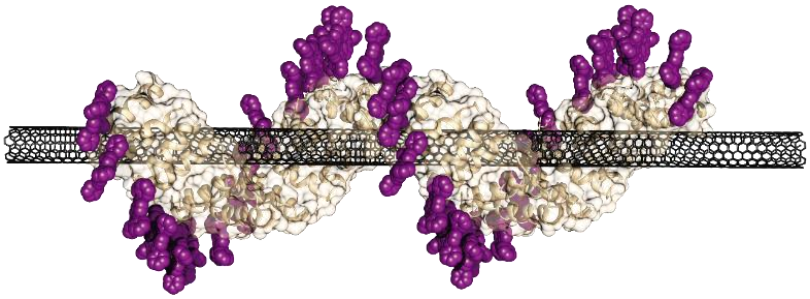

Figure S5. Schematic drawing of the nanohybrid obtained from a porphyrin/protein conjugate and a SWCNT.

Chapter 3. ***Evaluation of a collection of fullerenes in triple-channel photosystems.***

i) 1,4-Diaryl[60]fullerene and 1,2-dihydromethano[60]fullerene derivatives for synthetic access towards oriented charge-transfer cascades in triple-channel photosystems.[111]

Two diarylfullerene, **32** and **33**, and four methanofullerene, **34**-**37**, derivatives were synthetized having in common an aldehyde functional group and good solubility in polar aprotic solvents. The reduction potentials of all derivatives were determined by DPV measurements.

Derivatives **32**-**37** were attached to an oligothiophene derivative through an oxime bridge. Their corresponding donor/acceptor dyads were implemented in a solid supported architecture prefunctionalized with NDI columns, through hydrazone exchange (Figure S6).

All the ITO-supported triple-channel photosystems were characterized by means of photocurrent generation and recombination efficiency. This study provided us some information regarding the influence in the organization, nature of fullerene substitution and LUMO levels of fullerene derivatives in the photocurrent generation.

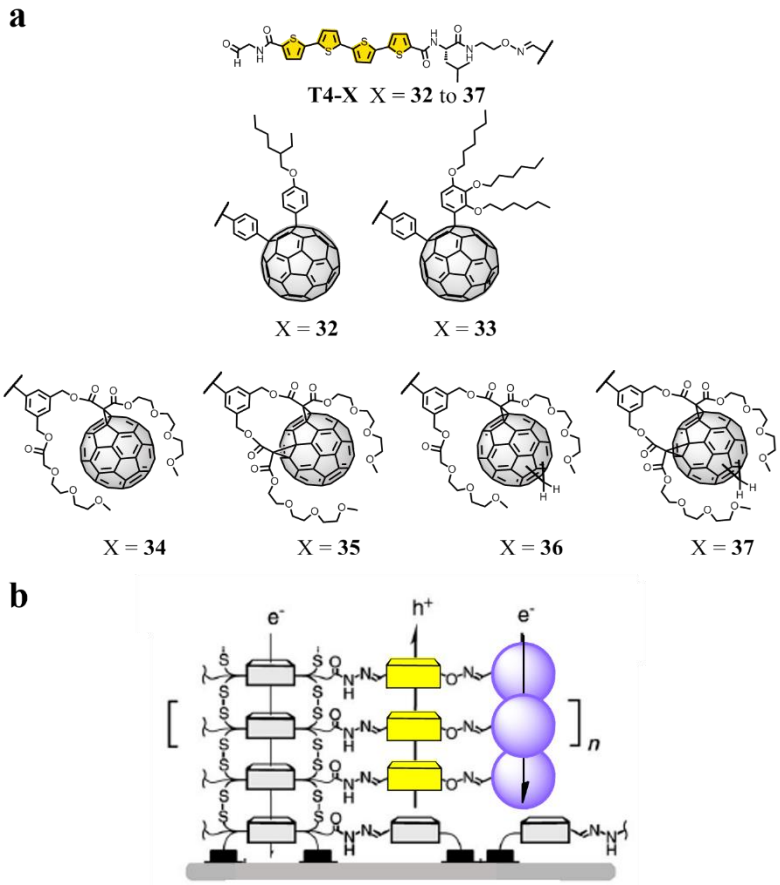

Figure S6. Collection of fullerene derivatives for triple-channel photosystems. (a) Molecular structures of oligothiophene-fullerene dyads **T4-32** to **T4-37**. (b) Approach to triple-channel architectures.

ii) Electron-deficient fullerenes in triple-channel photosystems.[116]

Five new fullerene derivatives, **60**-**64**, with decreasing LUMO level were synthetized and attached to the oligothiophene derivative and, lately, to the solid-supported photosystem. For reducing the LUMO level, one, two or three electron-withdrawing cyano groups were introduced in its structure (Figure S7).

Also, the influence of the increasing π-acidity and the structural homogeneity of the fullerenes in the photocurrent generation values were tested.

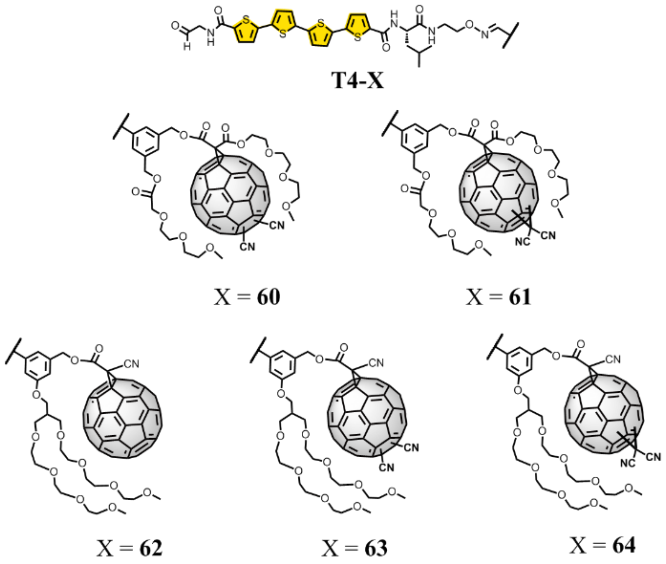

Figure S7. Molecular structures of dyads T4-60 to T4-64.

Conclusions

Chapter 1: A versatile and facile supramolecular approach based on short peptide-based photoactive molecules has permitted the formation of highly ordered donor/acceptor functional materials. These materials included exTTF/SWCNT and exTTF/PBI composites having hierarchical organization across different scales.

Chapter 2: An innovative bio-inspired approach has been developed in which a designed protein has evidenced its potential to precisely organize porphyrins in solution and solid state. Moreover, a series of proteins and conjugates have demonstrated their effective employment as wrapping agents of SWCNTs.

Chapter 3: This collection of fullerene derivatives has permitted a deep evaluation in triple-channel photosystems. Best activities were found for fullerenes with best preserved π-system and with the least rigid substituent for better fitting in the free spaces of the architecture.

Resumen

"Organización Bio-inspirada y Jerarquizada de Arquitecturas Supramoleculares Electroactivas basadas en Nanoestructuras de Carbono"

Introducción

La nanotecnología, referida a la manipulación de la materia a nivel molecular y supramolecular, es un área emergente con prometedores beneficios para la humanidad.[1] En particular, las nanoestructuras de carbono han captado gran atención debido a sus atractivas propiedades electrónicas y mecánicas. Imitar la naturaleza mediante el desarrollo de procedimientos bioinspirados puede ser una interesante estrategia para organizar nanomateriales ricos en carbono con el fin de maximizar sus propiedades optoelectrónicas.

Objetivos

Capítulo 1: Desarrollar nuevas estrategias basadas en agregados peptídicos para la generación de materiales organizados dador/aceptor.

Capítulo 2: Utilizar proteínas de repetición como plataformas para la organización de porfirinas en disolución y en el estado sólido y para funcionalizar supramolecularmente nanotubos de carbono.

Capítulo 3: Probar una serie de derivados de fullereno con distinta funcionalización y diferentes niveles de energía LUMO en fotosistemas de triple-canal orientados.

Resultados y Discusión

Capítulo 1. *Arquitecturas jerarquizadas dador/aceptor basadas en péptidos.*

i) Nanohíbridos dador/aceptor auto-organizados basados en nanotubos de carbono de pared simple.[40]

Se diseñó y sintetizó el derivado **1**, basado en el elemento de exTTF como unidad dadora y componente de reconocimiento de la superficie de los SWCNTs, una secuencia dipeptídica para fomentar la organización y una terminación de tipo dendrítica para garantizar la solubilidad en agua (Figura R1a).

La caracterización espectroscópica y fotofísica de **1** en presencia de los SWCNTs reveló la formación del nanohíbrido dador/aceptor con un tiempo de vida del estado con separación de cargas considerablemente mayor que el correspondiente a otros derivados similares descritos en bibliografía.[23]

La inspección de dicho nanohíbrido en el estado sólido a través de una serie de técnicas microscópicas indicó la presencia de estructuras alineadas y organizadas, principalmente en 2D (Figura R1b,c).

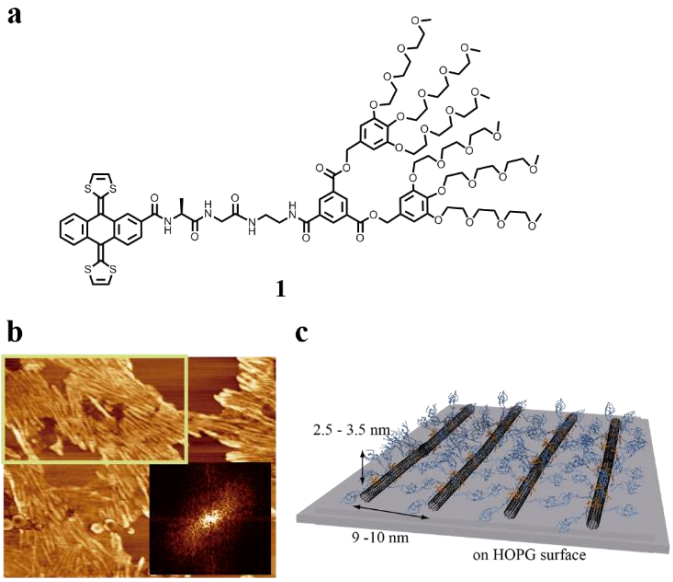

Figura R1. Nanohíbridos auto-organizados basados en exTTF y SWCNT. (a) Estructura del compuesto **1**. (b) Imagen de AFM de la arquitectura 2D. (c) Dibujo esquemático de las arquitecturas en (b).

ii) Control de la cristalinidad en materiales mediante la adición de nanotubos de carbono de pared simple.[49]

Tras los buenos resultados previamente obtenidos, se rediseñó el derivado de exTTF amplificando la secuencia peptídica y reemplazando la terminación dendrítica por un ácido carboxílico. Esta última modificación nos permite controlar el proceso de auto-ensamblaje mediante cambios de pH o adición de metales. De esta forma, los derivados **12** y **13** fueron sintetizados (Figura R2a).

Inicialmente se estudió la capacidad de estos derivados de autoensamblarse. Ambos derivados formaron nanofibras en agua, estabilizadas mediante la adición de $NaHCO_3$. Estudios espectroscópicos de UV-*vis* y CD indicaron interacciones de tipo π-π entre unidades de exTTF, formando agregados quirales y estructuras de lámina-β de la zona peptídica.

Tras ello, dichos polímeros supramoleculares preformados fueron utilizados para 'envolver' SWCNTs en agua. Estudios espectroscópicos revelaron una mayor estabilidad en el caso del derivado **13**, posiblemente debido a la mayor longitud de la cadena peptídica. Los datos fotofísicos de estos nanohíbridos mostraron tiempos de vida de los productos de transferencia electrónica entre 125-210 ps.

El aspecto más interesante de nuestra aproximación fue la generación de hidrogeles a partir de los nanohíbridos, mediante adición de Ca^{2+}. La presencia de SWCNTs en dichos materiales influyó enormemente en su cristalinidad y su orden interno, actuando como 'plantillas' de los polímeros supramoleculares (Figura R2b-d).

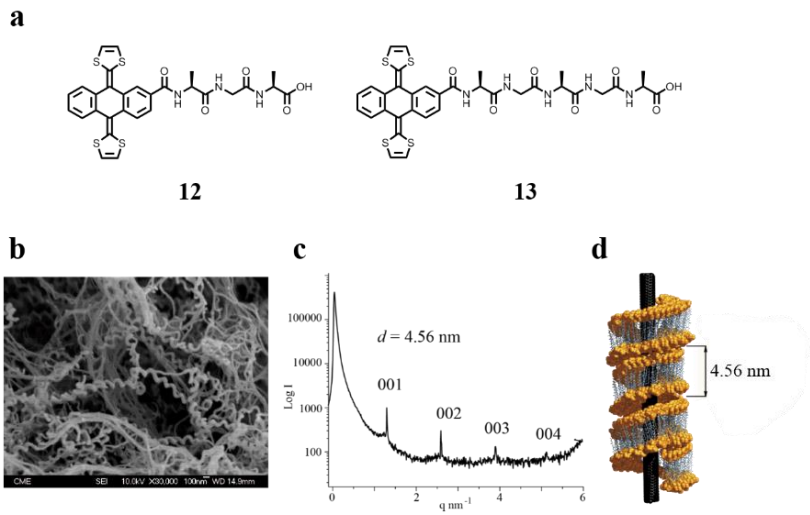

Figura R2. Aproximación para la generación de materiales organizados. (a) Estructura de los compuestos **12** y **13**. (b) Imagen de SEM del xerogel obtenido a partir de **13**/SWCNT/$CaCl_2$. (c) Difractograma de SAXS de dicho hidrogel. (d) Dibujo esquemático de la nanoestructura organizada.

iii) Materiales co-ensamblados de tipo *n*/*p* con alto orden y notables valores de movilidad de carga.[56]

Considerando la eficacia del compuesto **13** para generar materiales estables y ordenados, decidimos ampliar nuestra aproximación a otros sistemas electrón-aceptores como las perilenbisimidas. En este contexto, se sintetizaron dos derivados de este cromóforo, diferenciándose en sus funcionalizaciones

terminales: sal de guanidinio en **20** y sal de amonio cuaternaria en **21** (Figura R3a).

Se ha estudiado la capacidad de ambas moléculas para auto-asociarse en agua. Tras ello, ambas nanofibras solubles en agua, dadoras (exTTF) y aceptoras (PBI), se mezclaron, formándose de forma instantánea un precipitado del producto de co-ensamblaje. Este material mantenía las propiedades electrónicas de sus agregados iniciales y una composición estequiométrica de **13$_2$20** y **13$_2$21**, como fue confirmado por espectroscopía UV-*vis* y XPS.

Las propiedades más interesantes de dichos materiales se hallaron mediante estudios de microscopía de rayos-X, mostrando estructuras fibrilares organizadas desde la nano hasta la macroescala compuestas por dominios segregados de dadores y aceptores (Figura R3b,c).

Además, la efectividad de nuestra metodología fue confirmada por los excelentes valores de movilidad de carga que mostraron los materiales, en torno a 0.5 - 0.8 $cm^2V^{-1}s^{-1}$.

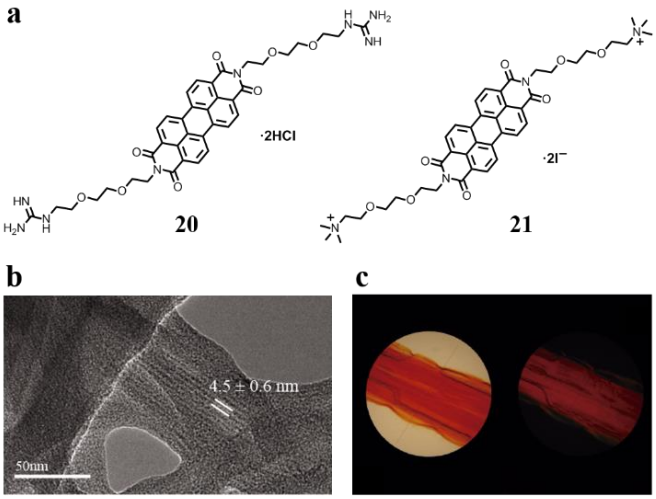

Figura R3. Materiales co-ensamblados de tipo n/p a partir de derivados de exTTF y PBI. (a) Estructura de los derivados de PBI **20** y **21**. (b) Imagen de TEM del material, mostrando dominios dador/aceptor segregados. (c) Micrografías del material manifestando propiedades birrefringentes.

<u>Capítulo 2.</u> ***Proteínas TPR como nueva herramienta para la organización de materiales orgánicos***

i) Proteínas TPR como molde para la organización de porfirinas en disolución y en el estado sólido

En primer lugar se llevó a cabo el diseño y síntesis de un derivado de porfirina sin metalar y otro derivado de porfirina de zinc, **25** y **26** respectivamente, provistos de cadenas solubilizantes en agua y un grupo maleimida para su posterior conjugación con una proteína mutada **CTPR4**, a través de las ocho cisteínas introducidas en su secuencia.

La eficiencia de la reacción de conjugación fue confirmada mediante gel de electroforesis y espectrometría de masas. Además, la caracterización de los conjugados mostró la formación de agregados de tipo *J* y la organización quiral de las porfirinas, inducidas por la geometría de la proteína, manteniéndose intacta la integridad estructural de dicho molde biológico (Figura S4).

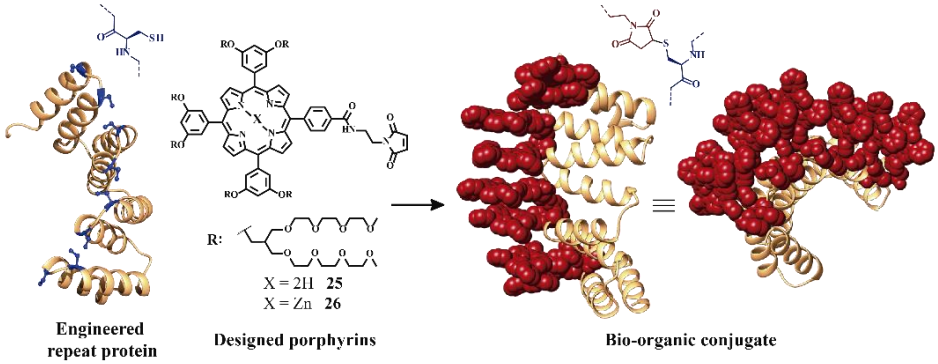

Figura R4. Esquema monstrando nuestra aproximación de generar conjugados de portifina/proteína con un posicionamiento preciso de los cromóforos.

Se formaron películas delgadas con dichos conjugados que, de nuevo, retuvieron la estructura de la proteína y mostraron, además, organización cristalina y anisotrópica. La fotoconductividad de estas películas mostró valores entre 1.3 – 1.5 x 10^{-3} $cm^2V^{-1}s^{-1}$además de conductividad eléctrica anisotrópica.

ii) Nanohíbridos dador/aceptor basados en conjugados proteína/porfirina con morfología de superhélice y SWCNTs.

Conociendo la estructura de superhélice de las proteínas CTPR, diferentes tamaños de proteínas, **CTPR4**, **CTPR8** y **CTPR16**, y sus repectivos

conjugados con la porfirina 26 han sido utilizados para funcionalizar supramolecularmente SWCNTs. (Figura S5).

Inicialmente, se evaluaron teóricamente tanto la morfología como la composición de dichas proteínas para acomodar SWCNTs en su cavidad.

Tras ello, se sintetizaron las proteínas de diseño y sus respectivos conjugados y se comprobó la validez de nuestra aproximación para 'envolver' SWCNTs mediante diferentes técnicas espectroscópicas y microscópicas.

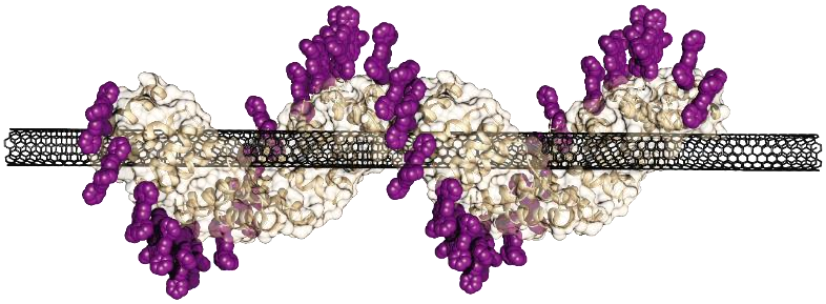

Figura S5. Dibujo del nanohíbrido obtenido de uno de los conjugados y un SWCNT.

Capítulo 3. ***Evaluación de una colección de fullerenos en fotosistemas de triple-canal.***

i) Derivados tipo 1,4-diaril[60]fullereno y 1,2-dihidrometano[60]fullereno como acceso a cascadas orientadas de transferencia de carga en fotosistemas de triple-canal.[111]

Dos derivados de diarilfullereno, **32** y **33**, y cuatro de metanofullereno, **34**-**37**, han sido sintetizados teniendo en común un grupo aldehído y buena solubilidad en disolventes polares apróticos. El potencial de reducción de todos ellos se calculó mediante medidas de DPV.

Dichos derivados se enlazaron a un derivado de oligotiofeno mediante un grupo oxima. Las correspondientes díadas formadas se implementaron en una arquitectura soportada sobre ITO y prefuncionalizada con columnas de NDI, mediante formación de un enlace hidrazona (Figura R6).

Se han calculado tanto la generación de fotocorriente como la eficiencia de recombinación de cargas en todos los fotosistemas, proporcionando dichos

datos valiosa información sobre la influencia de la organización, naturaleza de los sustituyentes y niveles de LUMO de los derivados de fullereno.

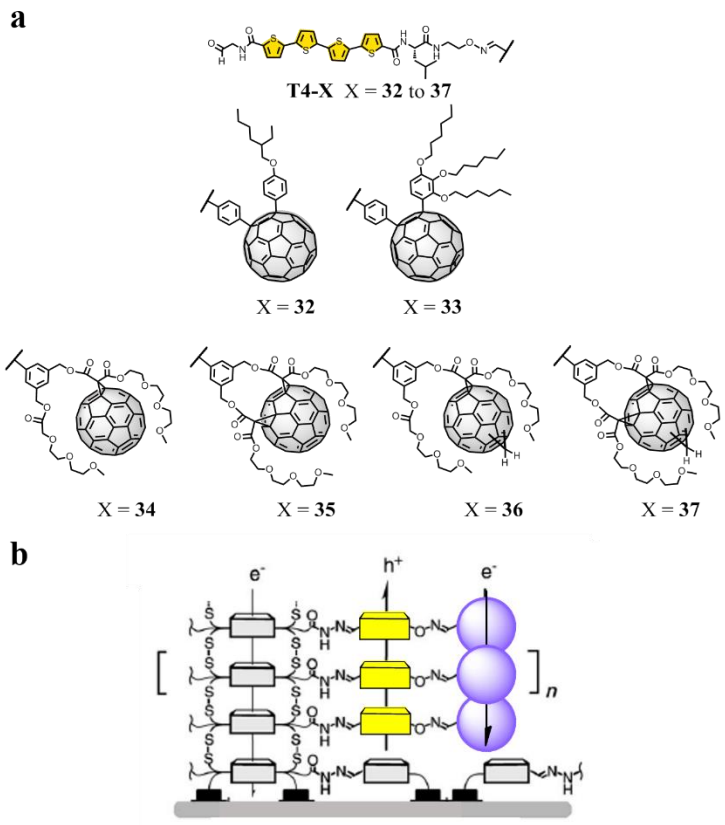

Figura R6. Derivados de fullereno para fotosistemas de triple-canal. (a) Estructuras de las díadas de oligotiofeno-fullereno **T4-32** a **T4-37**. (b) Dibujo esquemático de las arquitecturas de triple-canal.

ii) Fullerenos electrón-deficientes en fotosistemas de triple-canal.[116]

Cinco nuevos derivados de fullereno, **60**-**64**, con nivel de LUMO decreciente han sido sintetizados y enlazados a un derivado de oligotiofeno para, después, ser incluidos en fotosistemas soportados sobre superficie. Los niveles de LUMO de estos derivados se disminuyeron mediante la adición de uno, dos o tres grupos ciano sobre la superficie del fullereno. (Figura R7).

Además, se ha evaluado la influencia de estas modificaciones en los niveles energéticos del fullereno y de su homogeneidad estructural en la generación de fotocorriente.

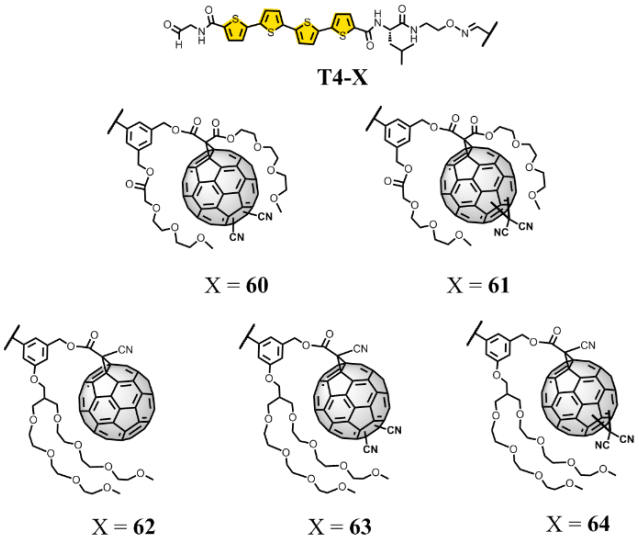

Figura R7. Estructura de las díadas T4-60 a T4-64.

Conclusiones

Capítulo 1: Se ha desarrollado una propuesta de organización supramolecular que ha permitido el diseño de moléculas fotoactivas unidas a péptidos pequeños y la formación de materiales funcionales dador/aceptor altamente ordenados. Estos materiales incluyen heterouniones de exTTF/SWCNT y exTTF/PBI organizados jerarquicamente a través de diferentes escalas.

Capítulo 2: Se ha desarrollado una innovadora aproximación bio-inspirada en la cual una proteína de diseño ha demostrado su potencial para organizar porfirinas tanto en disolución como en el estado sólido. Además, una serie de proteínas y sus correspondientes conjugados con porfirinas han demostrado su uso para funcionalizar SWCNTs supramolecularmente.

Capítulo 3: El trabajo desarrollado ha permitido la evaluación de once derivados distintos de fullereno en fotosistemas de triple-canal. Las mejores actividades las mostraron aquellos derivados con el sistema π-electrónico más preservado y con los sustituyentes menos rígidos.

Introduction

I.1. Origins of nanotechnology and nanoscience

Human being has always been attracted for those things which exceed the limits of the world revealed by the senses. Nowadays, telescopes can show us the unmeasurable immensity of the universe, even surpassing our ability to fully understand it. On the opposite side, the invisible and tiny world of cells, molecules and atoms is presented to us so intriguing and fascinating as the universe. In this way, one current challenge for the scientific community is not only the discovery of the nature of these small elements that shape the macroscopic sphere but, more importantly, be able to control and manipulate them for real applications in fields such as medicine, electronics, energy production and consumer products. With this goal is how nanoscience and nanotechnology is engendered.[1]

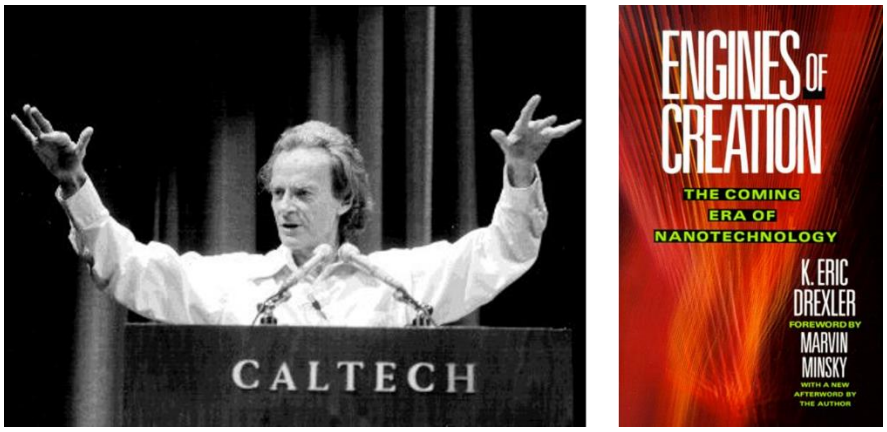

Figure I1. Origins of nanotechnology. Richard P. Feynman at Caltech giving his famous lecture he entitled "There's Plenty of Room at the Bottom" (left) and cover of the book “Engines of Creation: The Coming Era of Nanotechnology” of K. Eric Drexler (right).

The visionary lecture of the physicist Richard P. Feynman in 1959 “There is plenty of room at the bottom” is traditionally considered the seed to the nanoscale science and nanotechnology, in which he contemplated the possibility of synthesis through direct manipulation of atoms (Figure I1). However, the term “nano-technology” was not introduced until 1974 by Norio Taniguchi referring to materials smaller than one micron. K. Eric Drexler was who promoted this concept in his 1986 book “Engines of Creation: The Coming

1 G. M. Whitesides, *Small* **2005**, *1*, 172-179.

Era of Nanotechnology", with some statements related more to science fiction than real world, for example, the idea of small machines, called "assemblers", able to replicate themselves and escape from the laboratory. Thus, the authentic development of nanotechnology as a practical field took place in the 1980s, with the invention of the scanning tunneling microscope (STM) by Binnig and Rohrer and the discovery of the first discrete, graphite-like nanostructure, the Buckminsterfullerene C_{60}, by Robert F. Curl Jr., Harold W. Kroto y Richard E. Smalley.[2]

I.2. Chemistry in nanoscience

Several fields are involved in the development of nanotechnology, being chemistry one of them. Actually, chemistry plays a leading role in this emerging area. No other branch in science is able to manipulate matter by connecting atoms as impeccable as chemistry does. In particular, chemistry is not only important in nanoscience because of its capacity to covalently bond atoms in more complex molecules. Its ability to program molecules by design to generate ordered nanostructures with diverse shapes and dimensionalities make chemistry a powerful tool in this emerging area.

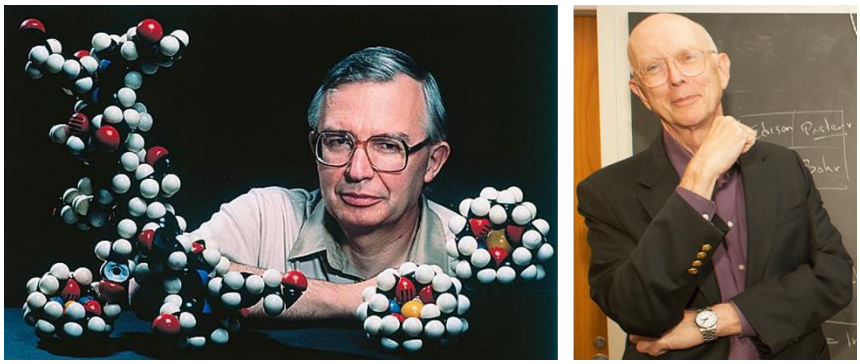

Figure I2. Pioneers of supramolecular chemistry and self-assembly. Jean Marie Lehn (left) and George Whitesides (right).

This concept of assembled molecular subunits establishing ordered nanostructures, referring as supramolecular chemistry, was firstly introduced by Jean Marie Lehn, for which he was recognized with the Nobel Prize in 1987

2 H. W. Kroto, J. R. Heath, S. C. O'Brien, R. F. Curl and R. E. Smalley, *Nature* **1985**, *318*, 162-163.

(Figure I2). During the 1990s, this idea was employed by George Whitesides to generate functional bulk materials from the self-assembly of small molecules acting as building blocks. Up to date, supramolecular chemistry has enabled the development of fascinating materials including metal organic frameworks, organogels and biomolecular materials.

Thus, some of the opportunities for chemistry to contribute in nanoscience, highlighted by G. Whitesides, are described below:

1. *Synthesis of nanostructures*: invention of novel nanostructures could be only achieved by synthetizing new forms of matter, employing the knowledge of current organic, inorganic and organometallic chemistry.

2. *Materials*: The development and economically efficient production of materials will be part of the job of chemistry.

3. *Molecular mechanism in nanobiology*: Understanding the mechanism of life matter at the molecular level would enormously contributed to the development of nanoscience, related to the production of bioinspired materials. No other scientific area could understand these molecular mechanism as good as chemistry does.

4. *Tools and Analytical Methods*: New techniques will be necessary to characterize and deeply define these original forms of matter. In this sense, physical and analytical chemistry play a crucial role.

5. *Risk Assessment and Evaluation of Safety*: Nanotechnology is new and the effects of its outputs on health are still unknown. Cooperation across disciplines ranging from chemistry to physiology is highly required.

I.3. Hierarchical architectures in nature

The most sophisticated functional materials created by self-assembly of simple building blocks are those found in nature. All the complex task in cells are performed by nanostructures: ribosome, histones and chromatin, the Golgi apparatus, the interior structure of the mitochondrion, the flagellar micromotor and the photosynthetic reaction center are some of them.[3]

3 a) D. S. Goodsell, *Bionanotechnology: Lessons from Nature*, Wiley, **2004**; b) J. Deisenhofer and H. Michel, *Science* **1989**, *245*, 1463-1473.

In addition to these functions in cells, in living organisms we can also find materials with hierarchical architectures from which function arises. Great examples include the color of the wings in *morpho* butterflies and in the bird feathers. This color is produce by microscopically structured surfaces which selectively reflect some wavelengths, depending on the exact structure and interspatial distance between diffracting layers (Figure I3). Other meaningful example is the structure of muscles in which bundles of fibers are aligned over long macroscopic distances.[4] Therefore, nature has much to teach nanoscience and nanotechnology and it is not surprising that much effort in this research area is directed to mimick these natural materials or living matter, regarding structure, properties or function.

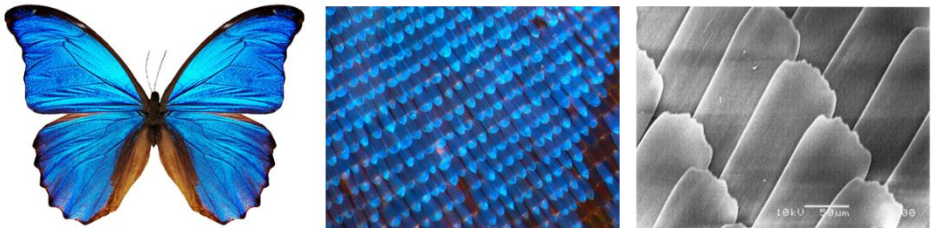

Figure I3. *Morpho* butterfly wings at different magnifications.

I.4. Carbon nanostructures

Some of the structures that have captured much attention in the nanotechnology community are the newly discovered carbon allotrope forms, in particular, fullerenes, carbon nanotubes and graphene. Until the last two decades of 20th century, graphite and diamond were the only known carbon allotropes. As mentioning before, the C_{60} molecule was the first one of this new family to be discovered.[2] This molecule focused enormous attention due to its truncated icosahedral structure, the ability of accepting 6 electrons in solution and its size in the nanometer scale. The importance of this discovery led to the recognition of Kroto, Smalley and Curl with the Nobel Prize in 1996.

A few years later, in 1991, another carbon allotrope, known as carbon nanotubes, was discovered by S. Iijima in Japan.[5] Although the attribution of this discovery has aroused some controversy and discussion due to the considerable amount of work between 1950-1970 decades on these filamentous carbon

4 L. Tskhovrebova and J. Trinick, *Nat. Rev. Mol. Cell Biol.* **2003**, *4*, 679-689.
5 S. Iijima, *Nature* **1991**, *354*, 56-58.

structures, Iijima was who really set the focus of the whole scientific community on carbon nanotubes. These structures have a range of remarkable properties, including metallic electrical conductivity, semiconductivity with very high carrier mobility, and extraordinary mechanical strength.

Finally, in the early 21st century, Geim and Novoselov described the mechanical exfoliation of isolated sheets from graphite to yield a new material named as graphene, which exhibit even higher values of electron mobility and less resistivity than carbon nanotubes (Figure I4).[6]

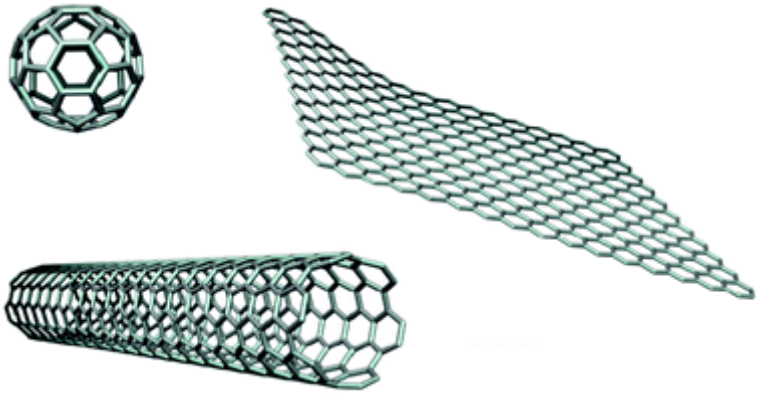

Figure I4. Newly discovered carbon allotropes. Fullerene (top, left), carbon nanotube (bottom) and graphene (right).

Finally, before going into detail in the overall discussion performed in this thesis, we would like to underline the aim of this project: Enclosed in the field of nanoscience and nanotechnology, and centered in the use of some of these fabulous structures that are the carbon nanoforms and their excellent properties, we attempt to mimic some aspects of nature such as structure and even function for the development of artificial hierarchical architectures with, at a final stage, could have a potential repercussion in the development of suitable nanomaterials for electronics and energy production from renewable energy.

6 K. S. Novoselov, A. K. Geim, S. V. Morozov, D. Jiang, Y. Zhang, S. V. Dubonos, I. V. Grigorieva and A. A. Firsov, *Science* **2004**, *306*, 666-669.

Chapter 1.

Peptide-based donor/acceptor architectures with hierarchical organization.

1.1. Background

1.1. Background

1.1.1. Molecular and supramolecular chemistry for mimicking nature.

Photosynthesis, as the principal producer of both oxygen and organic matter on earth, is a process used by plants to convert light into chemical energy. The process begins when energy from the sunlight is absorbed by proteins called reaction centers that contain green chlorophyll pigments. Then, the electron of the excited chlorophyll is transferred from one to another molecule creating a chain of redox reactions, resulting in an electron transport chain. These hole and electron flows are used, ultimately, to generate the products ATP and NADPH.

These two fundamental aspects in natural photosynthesis in proteins, that is, light-harvesting and charge separation processes, have inspired the construction of artificial photosynthetic systems. These are based in the development of complex, covalent molecular structures comprised of both electron donor and electron acceptor chromophores. These systems have allowed to determine electron transfer rate constant dependencies on donor-acceptor distance and orientation, electronic interaction and the free energy of the process.[7] However, these findings at the molecular level have not provided the functionality required in an applied material for real applications.

Supramolecular chemistry, in general, and self-assembly principles, in particular, offer a facile means for organizing large numbers of molecules into supramolecular structures that can bridge length scales from nanometers to macroscopic dimensions. This approach represents an extraordinary source of innovation with strong impact in material science.[8]

In this regard, the development of supramolecular chemistry, defined by Lehn as the chemistry beyond the molecule, offers a framework to design a wide variety of exciting structures ranging from simple guest-host systems based on

7 D. M. Guldi, B. M. Illescas, C. M. Atienza, M. Wielopolski and N. Martín, *Chem. Soc. Rev.* **2009**, *38*, 1587-1597.

8 a) T. F. A. De Greef, M. M. J. Smulders, M. Wolffs, A. P. H. J. Schenning, R. P. Sijbesma and E. W. Meijer, *Chem. Rev.* **2009**, *109*, 5687-5754; b) T. Aida, E. W. Meijer and S. I. Stupp, *Science* **2012**, *335*, 813-817; c) J. D. Tovar, *Acc. Chem. Res.* **2013**, *46*, 1527-1537; d) M. R. Wasielewski, *Acc. Chem. Res.* **2009**, *42*, 1910-1921; e) S. I. Stupp and L. C. Palmer, *Chem. Mater.* **2014**, *26*, 507-518.

molecular recognition to complex supramolecular objects and crystalline networks.[9]

Self-assembly in this context of material science implies that the components are programmed to create ordered functional structures, at any scale. The most promising research in soft matter has been focused on the design and creation of relatively simple small molecules, acting as building blocks, which are provided of functional groups able to interact by using weak interactions, such as hydrogen bonding, π-π stacking, metal-ligand interactions, electrostatic forces, strong dipole-dipole association, hydrophobic forces and steric repulsion, along with others of minor relevance.

1.1.2. Self-assembled materials based on *β*-sheets interactions.

One of the most extended biomimetic architectures that have been used in the development of ordered organic materials at the nanometric scale is the *β*-sheets scaffold, one of the secondary structures of proteins.

β-Sheets are comprised of oligopeptide *β*-strands which are a pleated linear array of amino acids whose side chains alternate above and below the peptide backbone (Figure 1). The *β*-strands can run in either the same or opposite directions, forming either parallel or antiparallel *β*-sheets. The *β*-strands are spaced approximately 4.7-4.8 Å apart and are approximately 3.3-3.5 Å per residue in length.[10]

9 J.-M. Lehn, *Angew. Chem., Int. Ed.* **1990**, *29*, 1304-1319.
10 a) P.-N. Cheng, J. D. Pham and J. S. Nowick, *J. Am. Chem. Soc.* **2013**, *135*, 5477-5492; b) J. D. Pham, R. K. Spencer, K. H. Chen and J. S. Nowick, *J. Am. Chem. Soc.* **2014**, *136*, 12682-12690.

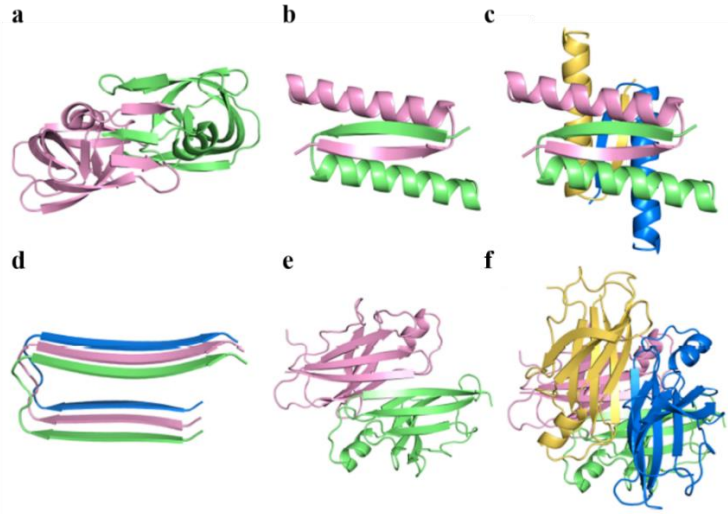

Figure 1. Representative structures and interactions of *β*-sheets. (a) Homodimer of HIV protease. (b) Homodimer of the p53 tetramerization domain. (c) Homotetramer of the p53 tetramerization domain. (d) Aβ_{1-42} fibril. (e) Homodimer of transthyretin. (f) Homotetramer of transthyretin.

Interactions among *β*-sheets occur widely in protein quaternary structure, protein−protein interaction, and protein aggregation[11] and are central in Alzheimer's and other amyloid-related diseases. *β*-Sheets interact through edge-to-edge hydrogen bonding to form extended layers and through face-to-face hydrophobic or van der Waals interactions to form layered sandwich-like structures. Side chains from adjacent layers can fit together through simple hydrophobic contacts or can participate in complementary interdigitation or knob−hole interactions.

These aforementioned features of *β*-sheets interactions make these structures a powerful platform to create functional nanoscale materials with optoelectronic properties. For this purpose, a careful balancing of all the possible supramolecular interactions should be consider, because the suitable geometries for stabilizing peptide assemblies may not necessary correspond to those suitable for maximizing intermolecular π-electron interactions.[8c] Nonetheless, this powerful approach seems to be fairly robust, as widely demonstrated in the literature.

11 A. Greenberg, C. M. Breneman and J. F. Liebman, *The Amide Linkage: Structural Significance in Chemistry, Biochemistry, and Materials Science*, Wiley, **2002**.

Tovar and col. have described, in the last years, a series of molecules able to self-assemble in aqueous media forming enthalpically stabilizing *β*-sheet arrays between intermolecular peptide sequences, which forced the π-units into cofacial intermolecular interactions.[12] Some of these designed molecules are exemplified in Figure 2. These molecules were composed of a central core based of a π-conjugated system, including arylene ethynylenes, phenylene oligomers or oligothiophenes, symmetrically functionalized with two oligopeptide units able to form parallel *β*-sheets.

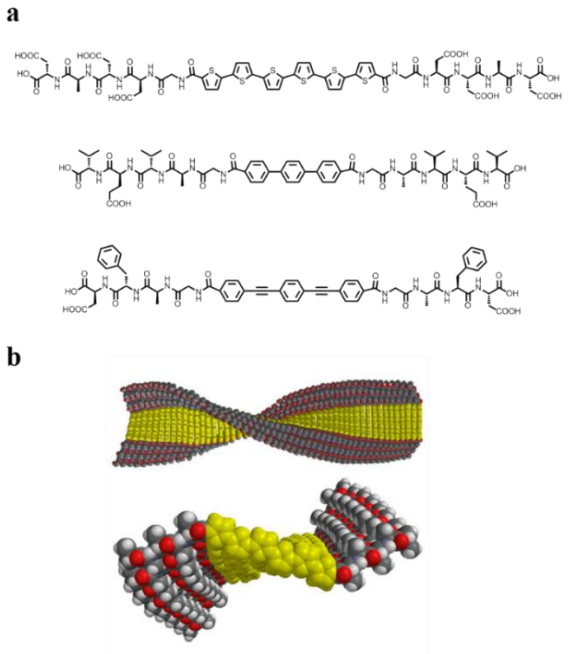

Figure 2. Peptide-π-peptide triblock molecules and a possible aggregate nanostructure. (a) Some molecular designs, including oligothiophene, phenylene and phenylene ethynylene derivatives. (b) Possible aggregate obtained upon *β*-sheet-type hydrogen bonding interactions.

12 a) G. S. Vadehra, B. D. Wall, S. R. Diegelmann and J. D. Tovar, *Chem. Commun.* **2010**, *46*, 3947-3949; b) H. A. M. Ardona, K. Besar, M. Togninalli, H. E. Katz and J. D. Tovar, *J. Phys. Chem. C.* **2015**; c) S. R. Diegelmann, N. Hartman, N. Markovic and J. D. Tovar, *J. Am. Chem. Soc.* **2012**, *134*, 2028-2031; d) H. A. M. Ardona and J. D. Tovar, *Chem. Sci.* **2015**, *6*, 1474-1484; e) S. R. Diegelmann, J. M. Gorham and J. D. Tovar, *J. Am. Chem. Soc.* **2008**, *130*, 13840-13841.

It is important to remark two important aspects in these materials: i) peptides can enforce intermolecular π-electron orientations that, otherwise, may not be energetically favorable and ii) the novel properties that these ensembles exhibit, comparing with the unstructured building blocks, due to the exciton coupling among the transition dipoles of the π-conjugated systems.

The 1D peptidic nanostructures generated by this approach can be extensively characterized by spectroscopic and microscopic techniques. Following with some examples from Tovar and col., these authors were able to tune the aggregated/disaggregated state of the peptide-based molecules by means of pH values.[12a] In particular, oligophenylene vinylene (OPV) derivative illustrated in Figure 3a remained dispersed at basic pH (specifically, at pH levels above aspartic acid's pK_a) due to the electrostatic repulsion among the deprotonated carboxylic acids. Lowering the solution pH, carboxylates were protonated and, thereby, directed the formation of self-supporting hydrogels from solutions with very low peptide weight percents (0.1–0.5 wt%).

Steady-state absorption data showed a blue-shift and photoluminescence data showed a quenching and red-shift expected upon the formation of H-type aggregates of the OPV peptides in acidic aqueous conditions, demonstrating the electronic delocalization existing within the peptidic nanostructures. Similarly, circular dichroism (CD) turned from no absorbance in the OPV absorption region at basic pH values, to a very strong and characteristic bisignate Cotton effect indicative of chromophore interactions within chiral environments (Figure 3b).

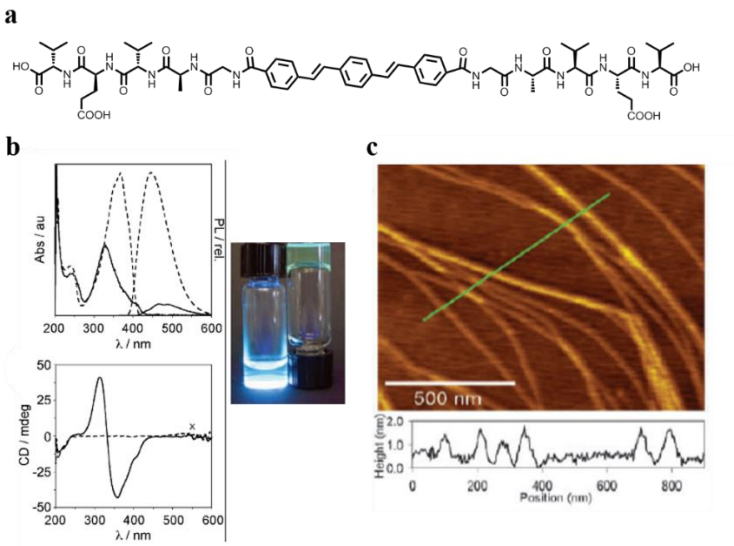

Figure 3. Characterization of the peptide-based aggregates. (a) Peptide-oligophenylene vinylene-peptide molecule. (b) Representative spectroscopic data for building blocks in their molecularly dissolved (basic pH, dashed line) and self-assembled (acidic pH, solid line) states in water: UV-vis and fluorescence (top) and circular dichroism (bottom). (c) AFM image obtained from assembled samples.

The internal structure of these hydrogels in their dried states could be visualized by atomic force (AFM), transmission electron (TEM) and scanning electron (SEM) microscopies, obtaining different information in each one of the aforementioned techniques. Atomic force micrograph in Figure 3c revealed that the internal structure of the formed hydrogels consisted of flat tape 1D nanostructures ca. 2 nm in height.

Recently, the same authors described a new architecture using these peptide-π-peptide triblock molecules but, in this case, incorporating two different semiconducting units co-assembled within the peptide nanostructure.[12d] Particularly, using OPV-moiety as donor unit and quaterthiophene as acceptor (Figure 4). This system showed an energy transfer process that involves exciton migration and resonance energy transfer, of high interest for mechanistic studies. Nevertheless, these systems would not be useful for the development of high-performance solution-processable photovoltaic cells, since segregation of donor an acceptor domains is a compulsory requirement and this type of charge-transfer (CT) complexes very often hampers photovoltaic outputs.

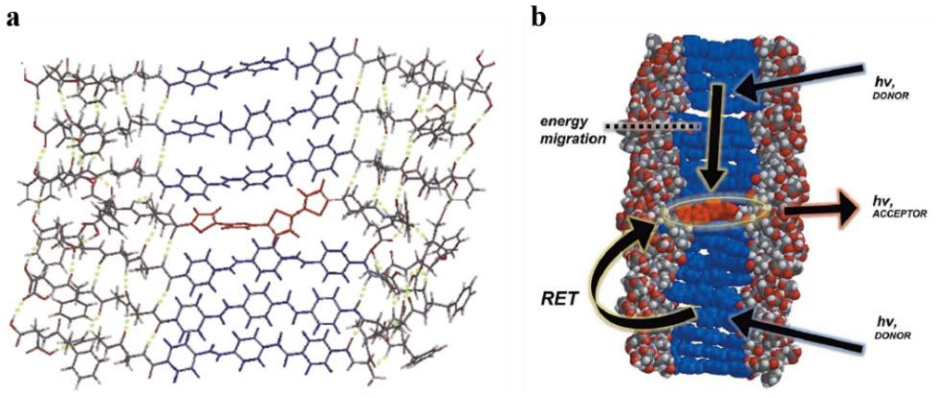

Figure 4. π-Conjugated co-assembled peptide based nanostructures. (a) Energy-minimized assembly model for a hypothetical portion of the heterostructure. (b) Possible energy processes (resonance energy transfer (RET) and carrier migration).

Another approach for organizing chromophores by using peptide-based structures in aqueous solution has been described by Stupp and col.[13] In this case, long fibers assembled from *β*-sheet-promoted peptide amphiphiles are capable of binding and encapsulating zinc metalloporphyrins in supramolecular architectures in the mesoscale. The amphiphilic motif shown in Figure 5a consists in a polar head, with three lysine residues, and a nonpolar aliphatic tail, that is, palmitic acid. Three leucine residues in the central core of the oligopeptide were employed to enhance structural organization using well-documented *β*-sheet conformers. A single histidine as the metalloporphyrin binding site was chosen. Finally, to provide additional space for the chromophore to bind, a single alanine was introduced as a spacer between the functional binding group and the aliphatic tail.

CD spectroscopy indicated that a sample of the amphiphile (500 μM) in water yielded no observable structure, even when the sample was aged for days (Figure 5b). Addition of NH_4OH yielded a twisted or aggregated *β*-sheet conformation, as indicated by the red-shift in the signature band of a typical *β*-sheet. After adding zinc metalloporphyrin (50 μM) to a solution of the peptide amphiphile (500 μM in 125 mM NH_4OH) that had been aged for 1 h, UV-*vis* spectroscopy indicated histidyl axial binding of the chromophore, as the B-band and Q-bands were red-shifted from the unbound porphyrin in 125 mM NH_4OH

13 H. C. Fry, J. M. Garcia, M. J. Medina, U. M. Ricoy, D. J. Gosztola, M. P. Nikiforov, L. C. Palmer and S. I. Stupp, *J. Am. Chem. Soc.* **2012**, *134*, 14646-14649.

(Figure 5c). Interestingly, circular dichroism showed a strong bisignate signal in the visible region indicating exciton coupling between well-ordered neighboring chromophores (Figure 5d).

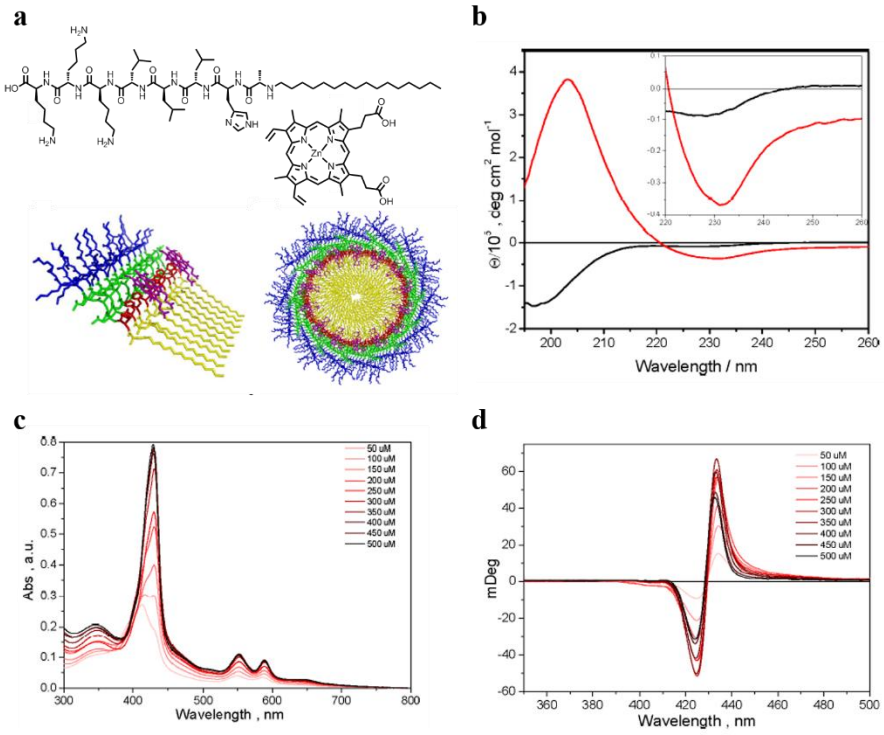

Figure 5. Self-assembly of peptide amphiphile metalloporphyrin arrays. (a) From left to right and top to bottom: Peptide amphiphile design, zinc metalloporphyrin, *β*-sheet organization with the porphyrin and cross section of the self-assembled fiber. (b) CD spectra of peptide amphiphile in water (black) and 125 mM NH_4OH (red). Inset: expanded view of the minima representing the *β*-sheet signal. (c) Absorption of 50 μM metalloporphyrin in 125 mM NH_4OH with 50−500 μM peptide amphiphile. (d) CD spectra of 50 μM metalloporphyrin in 125 mM NH_4OH with 50−500 μM peptide amphiphile.

1.1.3. Segregated donor-acceptor assemblies.

As briefly mentioned in the previous section, for applications in photovoltaics, the presence of bicontinuous donor and acceptor arrays is essential for facilitating photocurrent generation whereas formation of CT complexes inhibit photocurrent through recombination processes.[14]

Possible interactions between a *p*-type donor and a *n*-type acceptor are depicted in Figure 6, together with the different possible hierarchical structures that these building blocks can lead: 'Path a' shows the nanofibers obtained by formation of mixed-stacked complexes. Meanwhile, self-sorting of the donor and the acceptor may result in entangled fibers with localized heterojunctions ('path b') or aligned fibers with interfacial heterojunctions ('path c').[15] For better charge separation, 'path c' is preferred.

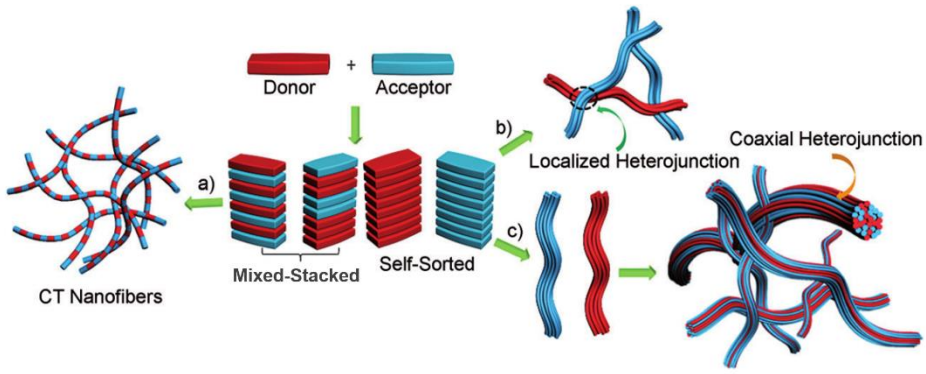

Figure 6. Conceptual representation showing the possible interactions between a *p*-type donor and an *n*-type acceptor and their possible hierarchical structures. (a) Mixed-stacked nanofiber; (b) self-sorted nanofibers with localized heterojunction; (c) self-shorted nanofibers with interfacial heterojunction.

With this purpose, different approaches have been undertaken both by using restricted conditions during the formation of the supramolecular

14 a) S. S. Babu, S. Prasanthkumar and A. Ajayaghosh, *Angew. Chem., Int. Ed.* **2012**, *51*, 1766-1776; b) A. Das and S. Ghosh, *Angew. Chem., Int. Ed.* **2014**, *53*, 2038-2054.
15 a) S. Prasanthkumar, S. Ghosh, V. C. Nair, A. Saeki, S. Seki and A. Ajayaghosh, *Angew. Chem., Int. Ed.* **2015**, *54*, 946-950; b) S. K. M. Nalluri, N. Shivarova, A. L. Kanibolotsky, M. Zelzer, S. Gupta, P. W. J. M. Frederix, P. J. Skabara, H. Gleskova and R. V. Ulijn, *Langmuir* **2014**, *30*, 12429-12437; c) S. K. M. Nalluri and R. V. Ulijn, *Chem. Sci.* **2013**, *4*, 3699-3705.

architectures or by using an appropriate design of the molecules.[16,15a] Some of these approaches are summarized thereafter:

Aida and col. have used amphiphilic dyads carrying both the donor and the acceptor moieties.[16h,16i] The driving force for the spontaneous formation of bicontinuous *p*-type and *n*-type arrays was the amphiphilic molecular design, suppressing the intermolecular CT complexation. In particular, these authors used a hexabenzocoronene-fullerene (HBC-fullerene) dyad as first approach, and a hexabenzocoronene-trinitrofluorenone (HBC-TNF) as second one, both with a similar design consisting on two dodecyl alkyl chains in one side of the core and two oligoethyleneglycol chains in the other (Figure 7a).

In both examples, nanotubes with segregated domains were obtained, with an electron-donating graphitic layer of π-stacked HBC and a molecular layer of electron-accepting TNF laminates or fullerene clusters (Figure 7b,c). In the case of HBC-TNF, nanotube formation took place upon diffusion of methanol vapor into a THF solution of the dyad. In the case of the molecule with fullerene as acceptor, the self-assembly was achieved by first heating and then slowly cooling a toluene solution of the sample.

In the first example, the coaxial *p*/*n*-heterojunction structure enables photocurrent generation with a large on/off ratio greater than 10^4. In the case of the fullerene-containing structure, the nanotube showed, upon light illumination, an ambipolar charge-carrier transport profile, where the intratubular mobility was as large as the intersheet mobility in graphite.

16 a) R. Charvet, S. Acharya, J. P. Hill, M. Akada, M. Liao, S. Seki, Y. Honsho, A. Saeki and K. Ariga, *J. Am. Chem. Soc.* **2009**, *131*, 18030-18031; b) R. Charvet, Y. Yamamoto, T. Sasaki, J. Kim, K. Kato, M. Takata, A. Saeki, S. Seki and T. Aida, *J. Am. Chem. Soc.* **2012**, *134*, 2524-2527; c) Y. Che, H. Huang, M. Xu, C. Zhang, B. R. Bunes, X. Yang and L. Zang, *J. Am. Chem. Soc.* **2011**, *133*, 1087-1091; d) H. Hayashi, W. Nihashi, T. Umeyama, Y. Matano, S. Seki, Y. Shimizu and H. Imahori, *J. Am. Chem. Soc.* **2011**, *133*, 10736-10739; e) Y. Hizume, K. Tashiro, R. Charvet, Y. Yamamoto, A. Saeki, S. Seki and T. Aida, *J. Am. Chem. Soc.* **2010**, *132*, 6628-6629; f) A. Kira, T. Umeyama, Y. Matano, K. Yoshida, S. Isoda, J. K. Park, D. Kim and H. Imahori, *J. Am. Chem. Soc.* **2009**, *131*, 3198-3200; g) W.-S. Li, Y. Yamamoto, T. Fukushima, A. Saeki, S. Seki, S. Tagawa, H. Masunaga, S. Sasaki, M. Takata and T. Aida, *J. Am. Chem. Soc.* **2008**, *130*, 8886-8887; h) Y. Yamamoto, T. Fukushima, Y. Suna, N. Ishii, A. Saeki, S. Seki, S. Tagawa, M. Taniguchi, T. Kawai and T. Aida, *Science* **2006**, *314*, 1761-1764; i) Y. Yamamoto, G. Zhang, W. Jin, T. Fukushima, N. Ishii, A. Saeki, S. Seki, S. Tagawa, T. Minari, K. Tsukagoshi and T. Aida, *Proc. Natl. Acad. Sci. U.S.A.* **2009**, *106*, 21051-21056.

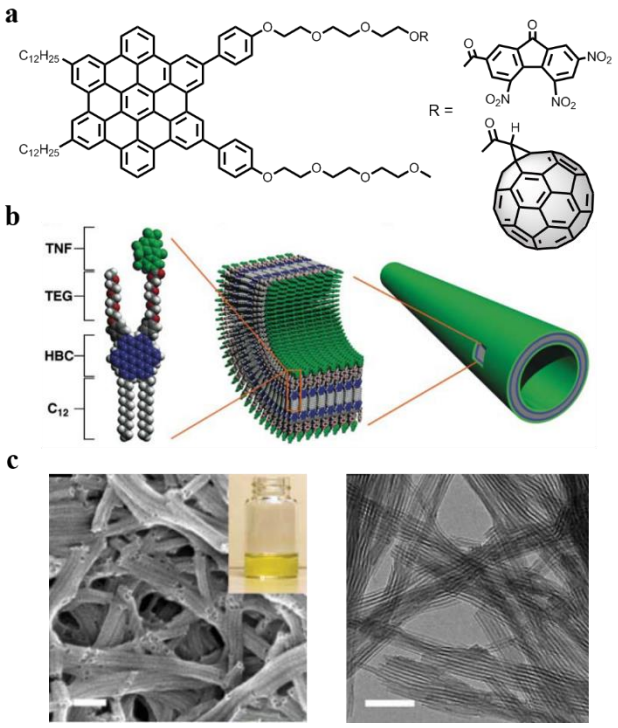

Figure 7. Coaxial *p*/*n*-heterojunction approach based on HBC core. (a) Molecular design of the amphiphile building blocks with HBC as donor moiety and TNF or fullerene as acceptor. (b) Schematic representation of the self-assembled HBC-TNF molecule into a nanotube aggregate. (c) SEM (left and TEM (right) images of the HBC-TNF architectures.

Another methodology was used by Ajayaghosh and col. who recently described the construction of coaxially aligned supramolecular heterojunction fibers of a *p*-type gelator based on a trithienylenevynilene derivative (TTV) with an *n*-type perilenebisimide (PBI) semiconductor (Figure 8a).[15a]

Mixing TTV and PBI in a 1:1 molar ratio in *n*-decane or in chloroform gave rise to, firstly, the creation of self-sorted 1D supramolecular nanostructures and, secondly, the generation of the interfacial heterojunction. The reason to discourage the direct CT interaction between the two molecules is, presumably, their structural features. In the case of TTV, the propensity to self-assemble through hydrogen-bonding interaction is very strong. Meanwhile, large π-surface-induced stacking could be the major force in the self-assembly of PBI molecules.

This hypothesis was proved by UV-*vis* absorption spectroscopy where the spectrum of the mixed solution retained the individual absorption spectral features of the two components (Figure 8b). Moreover, by powder X-ray diffraction (XRD) analysis, the authors could observe that the mixture of TTV/PBI showed a diffraction pattern which was a combination of those of the individual TTV and PBI patterns (Figure 8c).

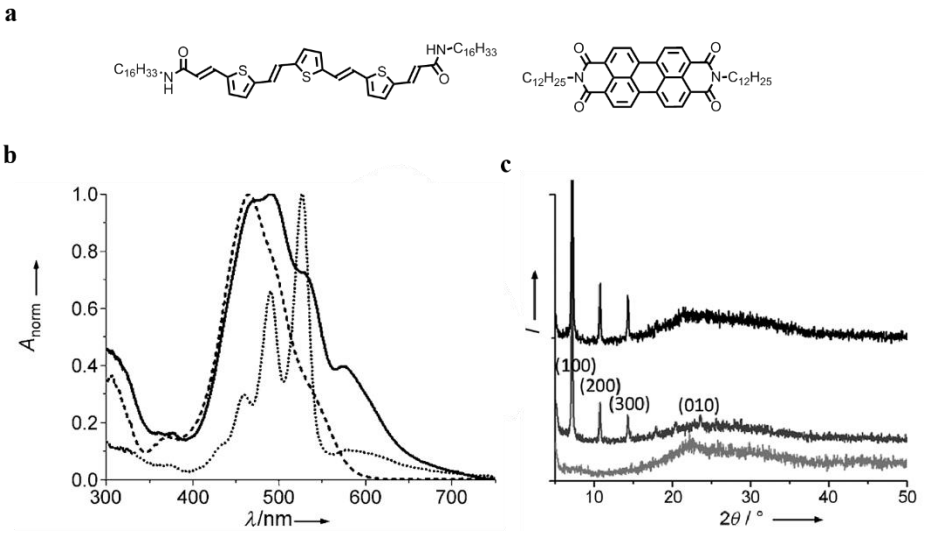

Figure 8. Organic donor–acceptor assemblies from coaxial *p*/*n*-heterojunctions. (a) Chemical structure of TTV (left) and PBI (right). b) UV-*Vis* absorption spectra of TTV (dashed line), PBI (dotted line), and a mixture of TTV/PBI in a 1:1 molar ratio (solid line) in *n*-decane. (c) Powder XRD pattern of TTV (light gray), PBI (dark gray), and TTV/PBI (black) in the self-assembled film state.

Furthermore, the photoconductivity properties of the mixed assembly was studied by flash-photolysis time-resolved microwave conductivity (FP-TRMC) measurements, showing up to 12-fold enhancement in $\phi\Sigma\mu$ values of the mixed assembly compared with that of TTV and PBI. Moreover, anisotropic photoconductivity measurements performed for TTV/PBI films revealed a very efficient unidirectional alignment of donors and acceptors, underpinning the interpretation of the authors of the mesoscopic co-assembly of the self-sorted structures.

Meanwhile, another strategy for obtaining nanosized domain segregation of *p*/*n* arrays employing a block copolymer bearing both photoactive donor porphyrin and acceptor fullerene units was developed by Ariga and col. (Figure 9a).[16a] Nanowire-like 1D nanostructures were formed by drop-casting a solution of this copolymer in chloroform onto mica, silicon, glass or highly oriented pyrolitic graphite (HOPG) surfaces. TEM inspections revealed that these nanowires contained regularly alternating domains oriented perpendicular to their long-axis. (Figure 9b).

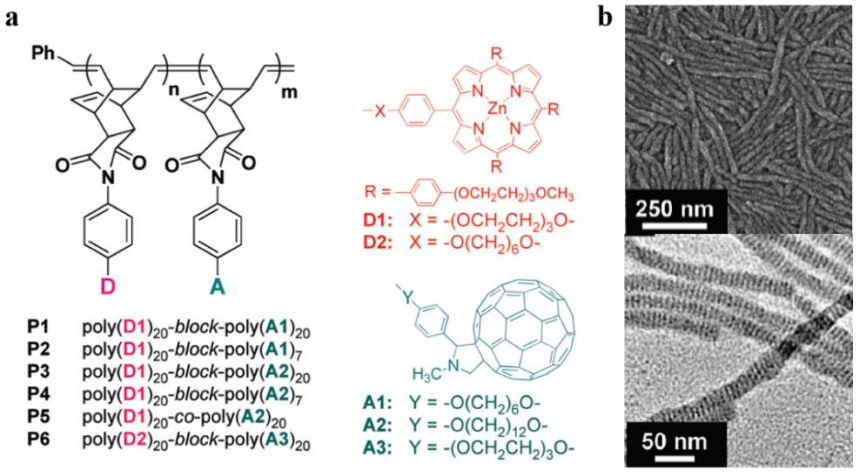

Figure 9. Block copolymer arrays with stacked *p*/*n*-heterojunction arrays. (a) Structures of the donor-acceptor copolymers. (b) SEM (top) and TEM (bottom) images of the nanowires drop-cast from $CHCl_3$ solution.

Interestingly, the overall conductivity of these materials ($\phi\Sigma\mu$) calculated in terms of FP-TRMC was clearly dependent of the side chains attached to both the porphyrin and the fullerene. For example, polymer **P1** showed a conductivity as high as 6.4×10^{-4} cm^2 V^{-1} s^{-1} while that in **P5** was one order of magnitude weaker. These experimental findings suggested the close relationship between charge carrier mobility and packing state.

1.1.4. Macroscopically aligned organic materials

Materials where the order parameters exist at different length scales are typically found in living organisms. For example, muscles in animals are formed of well-aligned bundles of fibers over long macroscopic distances. This structural continuum across different length scales makes possible the emergency of properties and function in these materials.[4]

For this reason, the development of strategies to promote these structural features in artificial organic materials is a compulsory requirement in order to transfer the potential of supramolecular materials to the real world.[17,8e]

Stupp and col. were pioneers in the creation of hierarchically ordered materials.[18] Recently, they have discovered the formation of macroscopically ordered membranes at the interface between droplets of aqueous solution of a high molecular weight polyelectrolyte, that is hyaluronic acid, and an oppositely charge peptide amphiphile. When mixing both solutions at appropriate values of charge density, a closed sac with a solid membrane was formed at the liquid-liquid interface on millisecond time scales (Figure 10a). At longer time scales, the initially formed membrane served to prevent the chaotic mixing of the two solutions, and perpendicular and ordered fibers were grown, driven by a synergy of, firstly, the dynamic osmotic pressure difference between the solution and, secondly, the self-assembly principles (Figure 10b,c).

17 B. Vigolo, A. Pénicaud, C. Coulon, C. Sauder, R. Pailler, C. Journet, P. Bernier and P. Poulin, *Science* **2000**, *290*, 1331-1334.
18 R. M. Capito, H. S. Azevedo, Y. S. Velichko, A. Mata and S. I. Stupp, *Science* **2008**, *319*, 1812-1816.

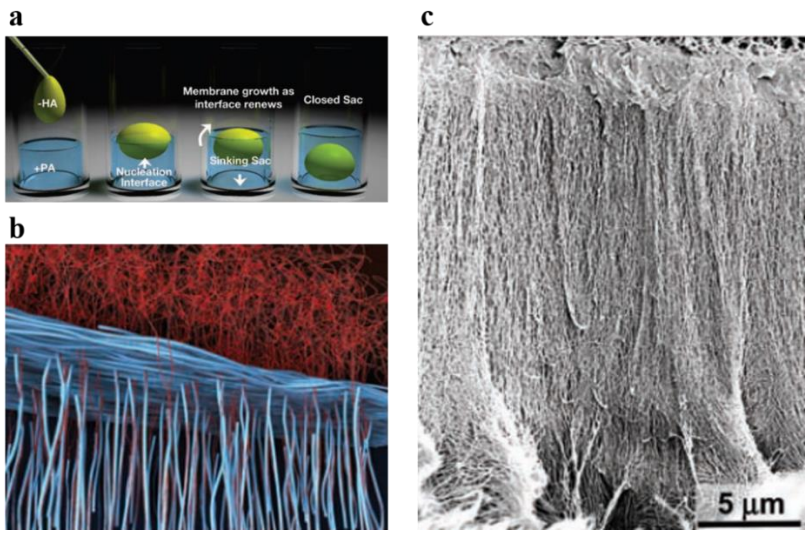

Figure 10. Self-assembly of large and small molecules into hierarchical ordered sacs and membranes. (a) Schematic representation of one method to form a self-sealing closed sac. A sample of the denser negatively charged biopolymer solution is dropped onto a positively charged peptide amphiphile solution. (b) Schematic representation of the growth of the nanofibers perpendicular to the interface over time. (c) SEM image of the sac membrane after 4 days.

Another discovery of Stupp and col. was the alignment of small molecules in supramolecular and macroscopic bundled filaments, as depicted in Figure 11.[19] Peptide amphiphiles that were able to form liquid crystals after heating-cooling treatment were synthetized, obtaining strongly birefringent materials consisting of bundled supramolecular filaments. By manually dragging this liquid crystal from a pipette onto salty media to screen charges, in particular onto a $CaCl_2$ saturated solution or a phosphate-buffered saline, the alignment of the fibers was extended over centimeters in noodle-shaped viscoelastic strings. Furthermore, the strings of aligned peptide amphiphiles nanofibers were used to direct the orientation of cells in 3D environments, highlighting their biocompatibility and their use in biological applications.

19 S. Zhang, M. A. Greenfield, A. Mata, L. C. Palmer, R. Bitton, J. R. Mantei, C. Aparicio, M. O. de la Cruz and S. I. Stupp, *Nat. Mater.* **2010**, *9*, 594-601.

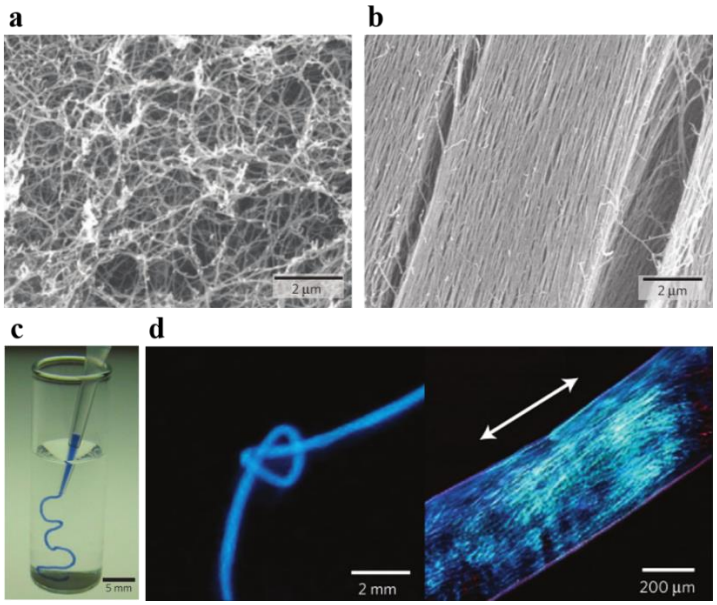

Figure 11. Aligned monodomain gels based on peptide amphiphiles. (a) Isotropic *versus* (b) aligned nanofiber bundles observed by SEM. (c) A peptide amphiphile solution coloured with trypan blue injected into phosphate-buffered saline after heat treatment. (d) Birefrigence of a single string, at different magnifications, observed under a polarized optic microscope.

The versatility of the Stupp technique has been used lately by other authors.[20] For instance, Tovar and col. applied this simple technique to their π-conjugated peptide nanostructures, in particular, to the oligothiophene-based peptide, for ultimately obtaining noodle-like objects. The alignment was observed locally by SEM analysis of critical-point dried samples (Figure 12a) and globally by polarized optical microscopy and one-photon fluorescence microscopy (Figure 12b), suggesting large-scale alignment. In contrast to the Stupp methodology, the formation of well-ordered hydrogels not only was possible to achieve by dispensing the solution into a salty solution but into a HCl solution, as well. These authors also observed that anisotropic alignment, induced by the applied shear force, markedly influence the photophysical and electrical properties of the π-conjugated nanostructure. Hole mobility calculated for the parallel and perpendicular direction respecting to the long axis of the

20 B. D. Wall, S. R. Diegelmann, S. Zhang, T. J. Dawidczyk, W. L. Wilson, H. E. Katz, H.-Q. Mao and J. D. Tovar, *Adv. Mater.* **2011**, *23*, 5009-5014; c) S. R. Diegelmann, N. Hartman, N. Markovic and J. D. Tovar, *J. Am. Chem. Soc.* **2012**, *134*, 2028-2031.

noodle revealed values of μ = 0.03 ± 0.005 and 0.0014 ± 0.0001 $cm^2\ V^{-1}\ s^{-1}$, respectively, bringing out the anisotropic alignment of the photoactive units.

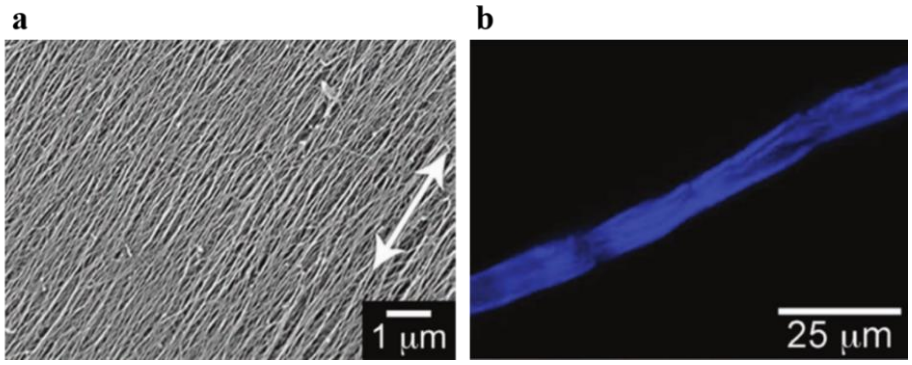

Figure 12. Macroscopic alignment of oligothiophene-based hydrogels. (a) SEM and (b) one-photon fluorescence images of the aligned structures at different scales

1.1.5. Supramolecular structures based on single-wall carbon nanotubes

Single-Wall Carbon Nanotubes (SWCNTs) are single sheets of graphite rolled forming cylindrical nanostructures with diameters ranging from 0.5 to 5.0 nm an lengths than can exceed 1 μm.[21] SWCNTs can be either semiconductors or metallic, depending on their diameter and the spiral alignment of the hexagonal rings of graphite along the tube axis. Regarding their features, they show remarkable electrical, thermal and mechanical properties which provide a wide range of potential applications in the field of materials, such as electronic devices, sensors and energy storage materials.[22]

The main difficulty to exploit these novel properties of SWCNTs for real applications is their extreme hydrophobicity, forming insoluble aggregates that are difficult to assemble into useful structures. In this sense, self-assembly or guide assembly of these materials into highly ordered superstructures is one of the most promising strategies to reach this goal, preserving at the same time their unique physical and optoelectronic properties.[17]

21 S. Dresselhaus, G. Dresselhaus and P. Avouris, *Carbon Nanotubes: Synthesis, Structure, Properties, and Applications*, Springer, **2001**.
22 R. Saito, G. Dresselhaus and S. Dresselhaus, *Physical Properties of Carbon Nanotubes*, Imperial College Press, **1998**.

In this regard, some of the most representative examples found in the literature are presented, to elucidate the possibilities that non-covalent interactions, in general, and self-assembly principles, in particular, can provide when working with SWCNTs.

Firstly, an example of non-covalent interactions between an electron-donor 9,10-di(1,3-dithiol-2-ylidene)-9,10-dihydroanthracene, most commonly known as π-extended tetrathiafulvalene, (exTTF) derivative and SWCNTs, described recently by Martín and col., is presented.[23] The recognition of SWCNTs by the aromatic anthracene-type core in exTTF through π-π interactions and the amphiphilic nature of the organic molecule are the driving forces to generate these donor/acceptor nanohybrids in aqueous media, as Figure 13 represents. Moreover, these systems presented electronic communication between the exTTF moiety and the SWCNTs both in the ground state and in the excited state, deeply demonstrated by spectroscopic and photophysical studies. Nonetheless, this molecular design and, in turn, this approach, did not produce any ordered structure neither at the nano or the mesoscale, reducing dramatically their possibilities for a functional application.

23 C. Romero-Nieto, R. García, M. Á. Herranz, C. Ehli, M. Ruppert, A. Hirsch, D. M. Guldi and N. Martín, *J. Am. Chem. Soc.* **2012**, *134*, 9183-9192.

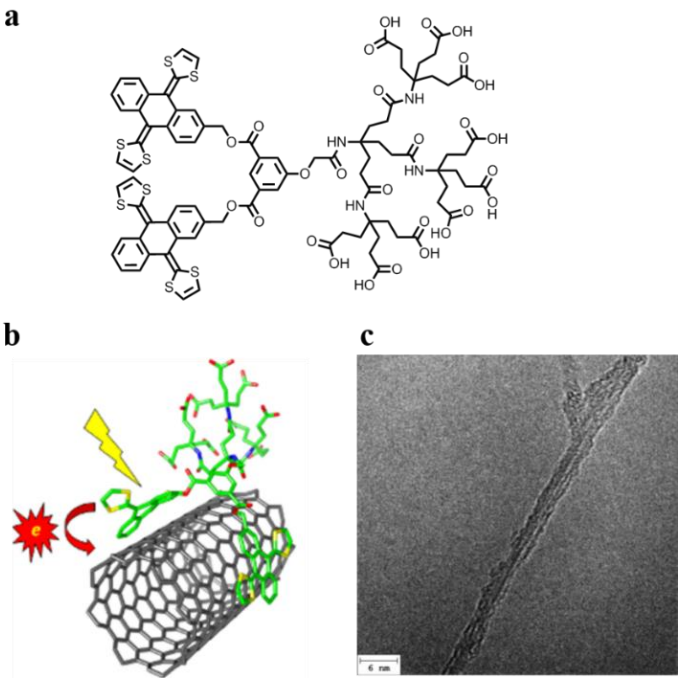

Figure 13. Noncovalent binding of SWCNTs by exTTF-based nanotweezers. (a) Molecular design of exTTF nanotweezer. (b) Schematic representation of noncovalent interaction and electronic communication between the exTTF derivative and SWCNT. (c) Representative HRTEM image of exTTF/SWCNT nanohybrid.

Turning into more sophisticated superstructures in which well-defined morphologies have been achieved, three examples are highlighted:

The first one came from Therien and col., who described some years ago the capability of a water-soluble and conformationally restricted conjugated polymer, i.e. poly(*p*-(2,5-bis(3-propoxysulfonicacid-sodiumsalt))phenylene)ethynylene (PPES, Figure 14a), to debundle and wrap SWCNTs in water.[24] Molecular dynamics simulation (Figure 14b), in one hand, and microscopic characterization of the nanohydrid (Figure 14c), in the other, clearly probed that PPES adopted a helical conformation in the presence of

24 a) Y. K. Kang, O.-S. Lee, P. Deria, S. H. Kim, T.-H. Park, D. A. Bonnell, J. G. Saven and M. J. Therien, *Nano Lett.* **2009**, *9*, 1414-1418; b) J.-H. Olivier, P. Deria, J. Park, A. Kumbhar, M. Andrian-Albescu and M. J. Therien, *Angew. Chem., Int. Ed.* **2013**, *52*, 13080-13085.

SWCNTs, increasing the helical wrapping and providing suspensions where ~80% of the solubilized tubes are individualized.

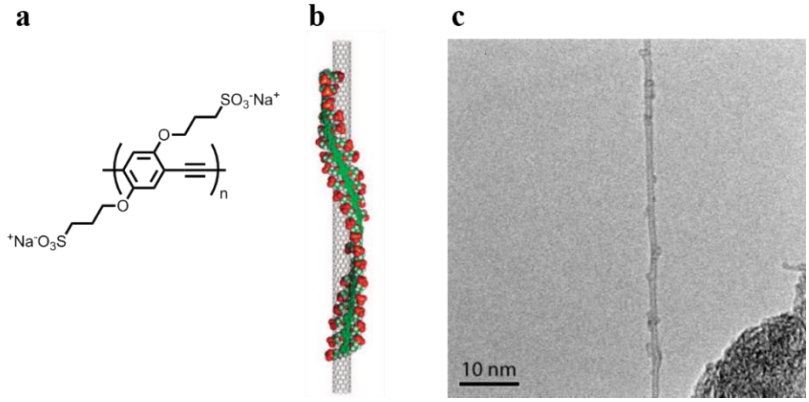

Figure 14. Wrapping of SWCNTs by a water-soluble polymer. (a) Chemical structure of the anionic polymer PPES. (b) Molecular dynamics simulation showing the helical wrapping of a SWCNT with a fragment of the polymer. (b) HRTEM of a PPES/SWCNT.

In view of these results, the same authors used the aforementioned wrapping strategy to produce dense arrays of individualized and aligned SWCNTs.[24b] In particular, the negative charges of the sulfonate groups in the [arylene]ethynylene polymer were used to create new nanostructures and functional materials by coupling them with oppositely charged building blocks through electrostatic attractions (Figure 15a). This powerful tool has been previously applied, being known as ionic self-assembly (ISA).

A bulky and paraffinic countercation was used for this purpose, enabling the solubility of these functionalized SWCNTs in fully organic solvents, and inducing the assembly into complex hierarchical structures that features aligned nanotubes. Furthermore, under restricted conditions, the appearance of SWCNT-based organogels was possible, as illustrated in Figure 15b,c, featuring individualized nanotubes densities as high as 2.5×10^{10} cm^{-2}.

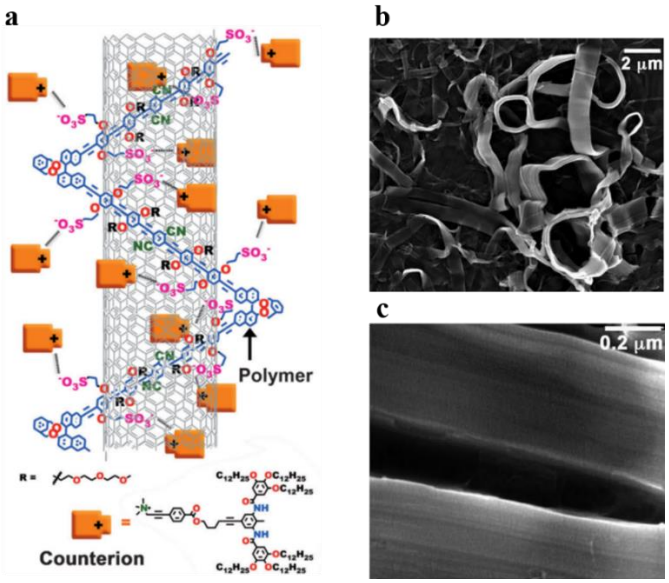

Figure 15. Ionic self-assembly approach applied on SWCNTs. (a) Representation of the ionic coupling between the anionic wrapped-SWCNT and the cationic building block. (b,c) SEM images of ribbon-like superstructures at different magnifications.

Second example of controlled assembly involving SWCNTs came from Dieckmann and col.,[25] who used an amphiphilic oligopeptide as wrapping and order-promoted agent. The designed peptide was composed of 29 amino acids able to arrange into a superhelix based on seven α-helical structures in which the apolar and aromatic residues occupied the internal face of the helix and more polar residues the external one (Figure 16a).

In solution, this peptide successfully dispersed SWCNTs in aqueous media, not only maintaining but stabilizing its α-helical conformation in the presence of nanotubes through hydrophobic interactions between the peptide and the nanotube surface, corroborated by CD assays and shown in Figure 16b. Moreover, the polar residues of the peptide promoted, after the addition of increasing amounts of NaCl or DMF to the dispersion, the assembly of peptide-coated nanotubes into larger and higher order structures (i.e., cylindrical

25 G. R. Dieckmann, A. B. Dalton, P. A. Johnson, J. Razal, J. Chen, G. M. Giordano, E. Muñoz, I. H. Musselman, R. H. Baughman and R. K. Draper, *J. Am. Chem. Soc.* **2003**, *125*, 1770-1777.

microfiber or flat ribbon) (Figure 16c), implying extensive alignment of the SWCNTs within the superstructures, as Figure 16d represents.

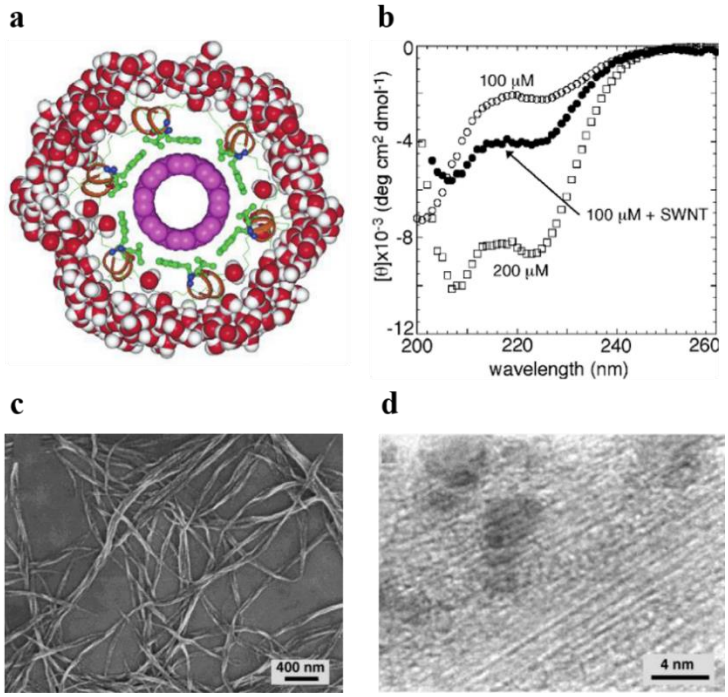

Figure 16. Assembly of SWCNTs by designed amphiphilic peptide helices. (a) Cross-section view of a model illustrating potential interactions between the amphiphilic peptide and a SWCNT. (b) CD spectra of the peptide and peptide/SWCNT at different concentrations, showing the α-helical conformation. (c) SEM image of fibers from addition of small amounts of DMF to a peptide/SWCNT dispersion. (d) HRTEM image of the same fibers showing alignment of the nanotubes.

Finally, the last example of SWCNT-based supramolecular structures comes from Choi and col.[26] The procedure that these authors applied is described below:

Firstly, a clean dispersion of SWCNTs in water was achieved by using a water soluble and polymerizable surfactant, that is, cetyltrimethylammonium 4-vinylbezoate (CTVB).[27] Figure 17a shows how a surfactant monolayer was permanently fixed on the nanotube surface by *in situ* polymerization of the counterions, obtaining individually isolated and non-covalently functionalized SWCNTs (*p*-SWCNTs).

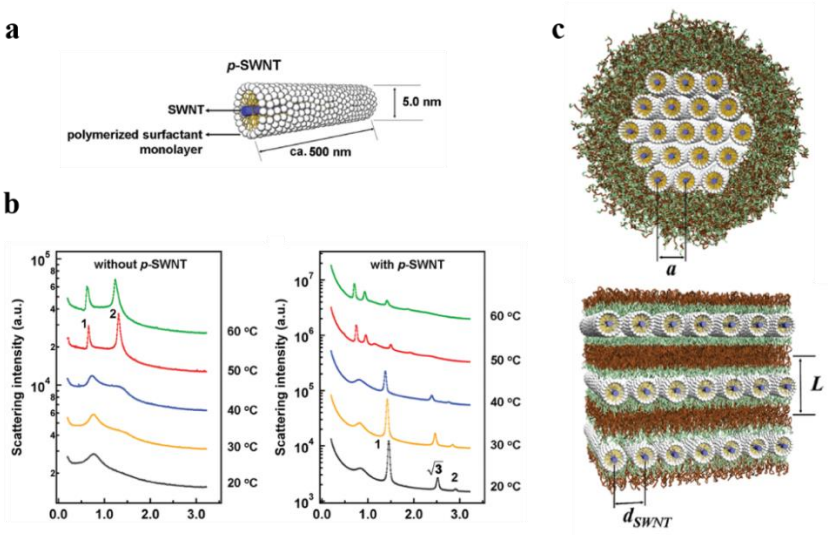

Figure 17. SWCNT arrays embedded in a polymeric system. (a) Schematic representation of isolated SWCNTs surrounded by a monolayer of polymerized surfactant (CTVB). (b) SAXS intensities of PE6200/water (left) and *p*-SWNT/PE6200/water (right) at various temperatures during heating. (c) Schematic representation of hexagonal arrays of SWCNTs (top) and one-dimensional lattices of SWCNTs (bottom).

26 C. Doe, H.-S. Jang, T.-H. Kim, S. R. Kline and S.-M. Choi, *J. Am. Chem. Soc.* **2009**, *131*, 16568-16572.
27 T. H. Kim, C. Doe, S. R. Kline and S. M. Choi, *Adv. Mater.* **2007**, *19*, 929-933.

Secondly, the block copolymer PE6200 was selected as order-induced material to organize *p*-SWCNTs in multidimensional arrays.[28] This polymer system, when is mixed with water (50/50 by weight), can exhibit both an isotropic phase and a highly ordered phase depending on temperature. In this sense, a mixture of *p*-SWCNT/PE6200/water (10/50/50 by weight) was prepared and their behavior depending on the temperature was studied by SAXS (Figure 17b).

Importantly, the authors found that when PE6200/water is in an isotropic phase, two-dimensional hexagonal arrays of *p*-SWCNTs were formed due to depletion attraction (Figure 17c, top). When PE6200/water was in a lamellar phase, one-dimensional lattices of *p*-SWCNTs intercalated in the polar region of the polymeric lamellar structure due to entropically driven segregation and two-dimensional depletion attraction (Figure 17c, bottom). In conclusion, this approach represents an interesting methodology to prepare temperature-dependent self-assembled materials based on SWCNTs, playing an important role in developing thermosensitive hybrid materials.

1.1.6. π-Extended TTF (exTTF): a butterfly-shaped molecule for supramolecular organizations

Tetrathiafulvalene (TTF) is a well-known non-aromatic heterocyclic molecule recognized because of its interesting conducting properties when mixed with valence species or strong acceptor molecules, leading to the formation of charge-transfer complexes.[29]

Due to these interesting properties, a wide range of chemical modifications on pristine TTF have been carried out along decades to enhance these features. One of these alterations is the separation of the 1,3-dithiole rings through a *p*-quinoid π-conjugated system conferring a strong donor character, namely π-extended TTF or exTTF.[30]

28 G. Wanka, H. Hoffmann and W. Ulbricht, *Macromolecules* **1994**, *27*, 4145-4159.
29 a) D. O. Cowan, C. LeVanda, J. Park and F. Kaufman, *Acc. Chem. Res.* **1973**, *6*, 1-7; b) J. Ferraris, D. O. Cowan, V. Walatka and J. H. Perlstein, *J. Am. Chem. Soc.* **1973**, *95*, 948-949; c) M. Bendikov, F. Wudl and D. F. Perepichka, *Chem. Rev.* **2004**, *104*, 4891-4946.
30 a) F. G. Brunetti, J. L. Lopez, C. Atienza and N. Martín, *J. Mater. Chem.* **2012**, *22*, 4188-4205; b) J. Yamada and T. Sugimoto, *TTF Chemistry: Fundamentals and Applications of Tetrathiafulvalene ; with 47 Tables*, Kodansha, **2004**.

Contrary to the TTF analogues, that show two well-separated one-electron oxidation processes at relatively low oxidation potential values (E_{ox}^1 = 0.37 V and E_{ox}^2 = 0.67 V), exTTF exhibits a two-electron oxidation process to form the dication species (E_{ox}^1 = 0.44).[31] Interestingly, this oxidation process is accompanied by a dramatic geometrical change from a butterfly-shaped neutral state to a planar di-cationic structure (Figure 18). Moreover, this remarkable gain of aromaticity and planarity upon oxidation involves a noteworthy stabilization of the dication, compared to other aromatic donors such as porphyrin, ferrocene, etc.

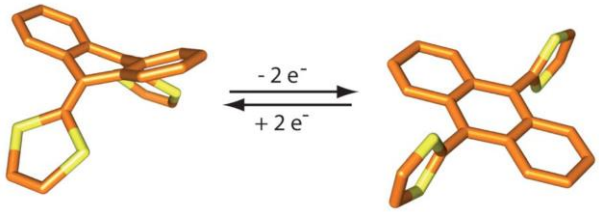

Figure 18. Geometrical change of exTTF molecule upon oxidation process.

As repeatedly aforementioned, the supramolecular organization of photo and elecroactive units dramatically influences the properties and behavior of the bulk material. Due to the non-planar geometry of exTTF unit, this molecule has been traditionally considered an inappropriate candidate for the construction of highly ordered nanostructures. However, new opportunities are emerging in the last years related to the organization of this electron-donor moiety, which will be described below:

The first stage in the growth of a self-assembled lateral superlattice of donor exTTF and acceptor phenyl-C_{61}-butyric acid methyl ester (PCBM) was achieved some years ago by Miranda and col., using variable-temperature scanning tunneling microscopy (STM) on Au (111).[32] Both units were found to grow in segregated lateral superlattices of about 10-20 nm. Moreover, a close examination of the exTTF islands at submolecular resolution showed a particular molecular organization, consisting of an ordered array of 1D molecular rows, without reflecting the geometry of the Au surface.

The next logical step was to promote the formation of well-ordered nanostructures in solution through noncovalent interactions using rational

31 D. M. Guldi, L. Sánchez and N. Martín, *J. Phys. Chem. B* **2001**, *105*, 7139-7144.
32 R. Otero, D. Écija, G. Fernández, J. M. Gallego, L. Sánchez, N. Martín and R. Miranda, *Nano Lett.* **2007**, *7*, 2602-2607.

molecular design of the building blocks. In this sense, Martín and col. was pioneer in demonstrating the use of exTTF moiety as essential frame for the construction of twist-shaped superstructures involving efficient π-π interactions between the curved exTTF scaffolds.[33]

exTTF derivative in Figure 19a consisted of a diamino-*s*-triazine, a π-conjugated *p*-phenylenevinylene spacer and the exTTF appendant. Meanwhile, the cyanurate derivative was chosen as a well-known and versatile hydrogen-bonding building-block. Without going into details about the complete procedure to produce the microscaled twisted fibers, the key aspects, illustrated in Figure 19b, implied the following steps: Hydrogen bonding between both complementary building blocks to produce a 1:1 complex (primary structure); formation of extended supramolecular ensembles (secondary structure); lateral interdigitation of these ensembles to form nanoribbons (tertiary structure); and intertwining of the nanoribbons affording the twisted fibers (quaternary structure, Figure 19c). In this complete process, the authors believed that the interactions between the exTTFs played a decisive role in terms of energetic imbalances.

33 J. L. López, C. Atienza, W. Seitz, D. M. Guldi and N. Martín, *Angew. Chem., Int. Ed.* **2010**, *49*, 9876-9880.

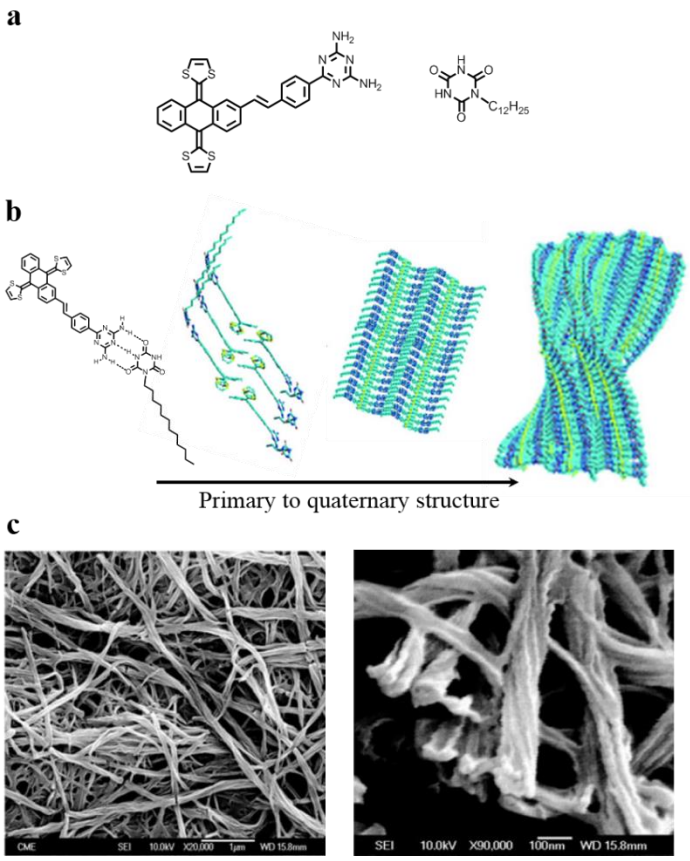

Figure 19. Hierarchical organization of exTTF-based building blocks. (a) Complementary triazine and cyanurate-type building blocks. (b) Primary to quaternary structures propoused. (c) SEM images of several fibers at different magnifications.

Furthermore, photophysical measurements confirmed that this quaternary structure enabled remarkable stabilization of the photogenerated radical ion pair, with two orders of magnitude longer than that of the simple complex.

Following with the same assessment on the capability of non-planar exTTF moiety to create hierarchically ordered supramolecular structures, a deep study was performed by Martín and col. about the influence of the geometry at molecular level in the creation of helical mesostructures.[34]

In this work, three different amphiphile derivatives were evaluated, with a central L-pentapeptide sequence, an amide functional group in one side and the aromatic appendant in the other side. The concave-shape exTTF derivative was compared with related but more planar fluorene and anthracene-type molecules (Figure 20a).

Under the same conditions, that is, allowing to form *β*-sheet secondary structures in 1,1,2,2-tetrachloroethane and solvophobic collapsing of the nanostructures in methylcyclohexane, a completely different scenario was envisioned when comparing the different building blocks. While the chirality of the peptide is not expressed in the mesostructures obtained from the planar systems, it is effectively exhibited in the exTTF-based mesoarchitecture. The different supramolecular objects of these systems are shown in Figure 20b, in the two stages of the process, using different microscopic techniques such as AFM and SEM, depending of the size of the ensembles.

34 J. L. López, C. Atienza, A. Insuasty, J. López-Andarias, C. Romero-Nieto, D. M. Guldi and N. Martín, *Angew. Chem., Int. Ed.* **2012**, *51*, 3857-3861.

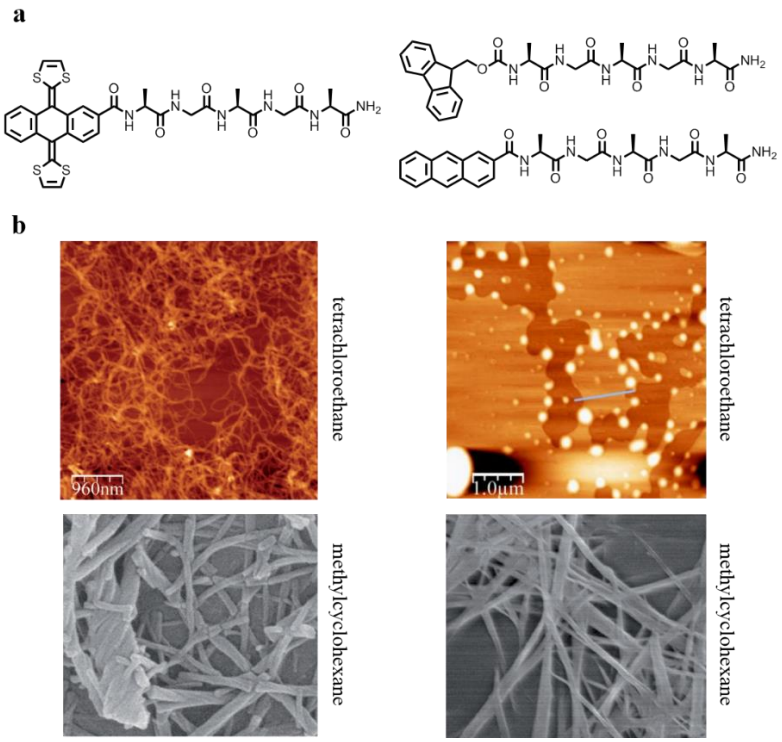

Figure 20. Effect of concave-shape exTTF in the self-assembled nanostructures. (a) Chemical structures of pentapeptide-based compounds. (b) AFM (top) and SEM (bottom) images of their corresponding nanostructures.

1.1.7. Molecular assemblies of perylene bisimide

Perylene bisimide (PBI) is an organic molecule well recognized as a versatile chromophore with strong absorption, near unity fluorescence quantum yield and high photostability.[35] PBIs were initially applied for industrial purposes as red vat dyes but, during the last decades, new applications have emerged in the field of electronic materials, provided that PBIs are one of the

35 a) W. Herbst and K. Hunger, *Industrial organic pigments: production, properties, applications*, VCH, **1993**; b) C. W. Struijk, A. B. Sieval, J. E. J. Dakhorst, M. van Dijk, P. Kimkes, R. B. M. Koehorst, H. Donker, T. J. Schaafsma, S. J. Picken, A. M. van de Craats, J. M. Warman, H. Zuilhof and E. J. R. Sudhölter, *J. Am. Chem. Soc.* **2000**, *122*, 11057-11066; c) C. D. Dimitrakopoulos and P. R. L. Malenfant, *Adv. Mater.* **2002**, *14*, 99-117.

best *n*-type semiconductors available to date.[36] This semiconducting behavior is related to the high electron affinity of rylene-type bisimide dyes.[37]

The packing of PBIs has been studied in great detail both in the solid state, as crystals, and in solution when forming supramolecular assemblies. Comprehensive studies have been carried out in this sense to elucidate the relationship of the color upon the longitudinal and transverse offset of the dyes, connecting the bathochromic shift and the band broadening to the extent of the π-π contact area between the stacked PBIs.[38]

After this brief introduction about the main features of PBIs, a couple of examples will be illustrated, related to self-assembled supramolecular structures based on PBIs in water, of great interest for our research.

Würthner and col. has widely studied these supramolecular ensembles and their fascinating photophysical properties that emerged.[39] These authors demonstrated that PBIs could be easily derivatized for the self-assembly of supramolecular aggregates in water by simple incorporation of hydrophilic side groups in the imide substituents.[39a] In Figure 21a, a PBI with six ethyleneglycol chains in the imide position is illustrated. The propensity of this molecule to undergo π-π stacking in water is extremely pronounced, with binding constant of $K > 10^8$ M^{-1}. The aggregation process could be followed by the spectral changes while changing the solvent from acetonitrile to water or by increasing the concentration (Figure 21b). In the first solvent, a clear vibronic fine structure of the electronic transition from the S_0 to S_1 state was observed, while this information disappeared during the aggregation process in water because of strong excitonic interactions between the PBI chromophores (Figure 21c).

36 P. E. Hartnett, A. Timalsina, H. S. S. R. Matte, N. Zhou, X. Guo, W. Zhao, A. Facchetti, R. P. H. Chang, M. C. Hersam, M. R. Wasielewski and T. J. Marks, *J. Am. Chem. Soc.* **2014**, *136*, 16345-16356.
37 S. K. Lee, Y. Zu, A. Herrmann, Y. Geerts, K. Müllen and A. J. Bard, *J. Am. Chem. Soc.* **1999**, *121*, 3513-3520.
38 P. M. Kazmaier and R. Hoffmann, *J. Am. Chem. Soc.* **1994**, *116*, 9684-9691.
39 a) Z. Chen, B. Fimmel and F. Wurthner, *Org. Biomol. Chem.* **2012**, *10*, 5845-5855; b) D. Görl, X. Zhang and F. Würthner, *Angew. Chem., Int. Ed.* **2012**, *51*, 6328-6348; c) S. Rehm, V. Stepanenko, X. Zhang, T. H. Rehm and F. Würthner, *Chem. Eur. J.* **2010**, *16*, 3372-3382; d) F. Wurthner, *Chem. Commun.* **2004**, 1564-1579; e) S. Yagai, T. Seki, T. Karatsu, A. Kitamura and F. Würthner, *Angew. Chem., Int. Ed.* **2008**, *47*, 3367-3371; f) X. Zhang, Z. Chen and F. Würthner, *J. Am. Chem. Soc.* **2007**, *129*, 4886-4887.

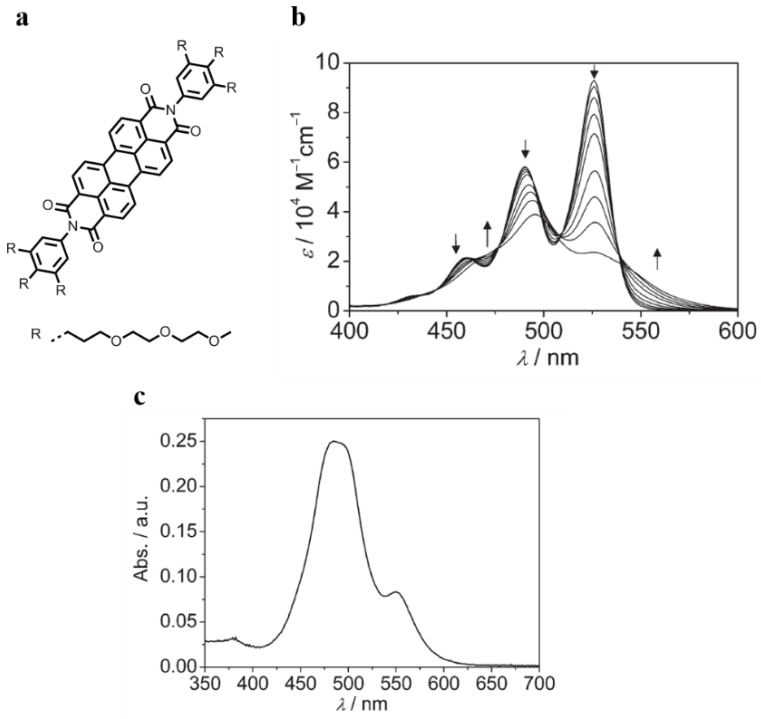

Figure 21. Water-soluble PBI derivative endowed with ethyleneglicol chains. (a) Molecular structure of the PBI derivative. (b) Concentration-dependent UV-*vis* spectra. (c) UV-*vis* spectrum in aqueous solution (9.1 x 10^{-6} M).

Another approach developed by the same authors to obtain aggregated PBIs in water was by introducing multicharged ionic side chains.[39c] In particular, spermine-functionalized PBIs were obtained (Figure 22a). Upon increasing the distance between the protonated amine groups by the introduction of an aliphatic spacer, the aggregation of the PBIs was increased, stabilizing, in turn, the π-π stacking of the aromatic core. AFM and TEM studies showed that the PBI molecules were arranged into large rod-type structures, whose length and diameter enlarged as the spacer length increased (Figure 22b).

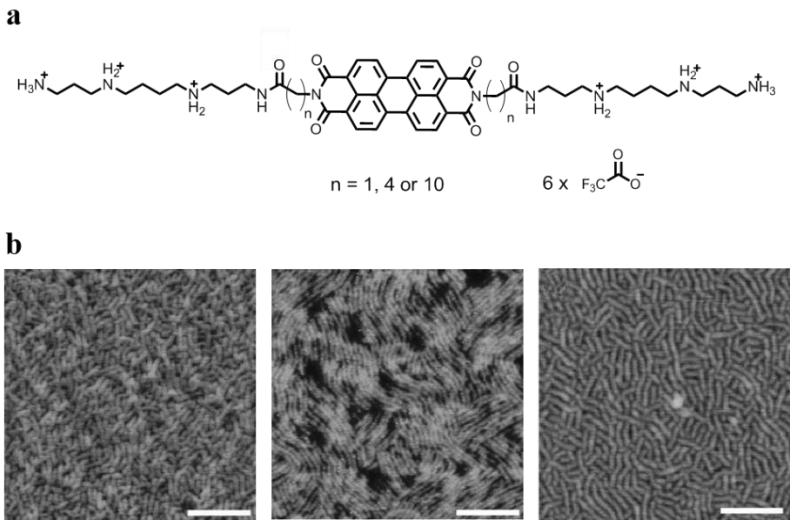

Figure 22. Spermine-funtionalized PBIs. (a) Molecular structure of the different cationic PBI derivatives. (b) AFM images of the supramolecular architectures obtained from PBI derivatives with n=1, 4 and 10 (from left to right). Scale bare: 50 nm.

1.2. Objectives

1.2. Objectives

The main objective of this chapter is the development of new strategies for the achievement of ordered organic *p*/*n*-materials with undeniable high impact in photovoltaics and optoelectronics. Thus we propose combining the advantages of peptide assemblies for organizing chromophores at the nanometric scale with the powerful of generating segregated donor/acceptor domains in bulk materials.

In particular, this chapter is based on the design and synthesis of small building blocks, endowed with donor and acceptor electroactive units, which are able to self-assemble in complex supramolecular architectures mainly through hydrogen-bonding and π-π stacking together with other non-covalent interactions.

The next section is divided in three different consecutive projects. These projects are presented in chronological order and the results obtained in each case are employed for the design and development of the next one, in order to improve or amplify the strategy.

Firstly, we want to demonstrate the ability of an exTTF-based amphiphile to debundle and solubilize SWCNTs in aqueous media and impose their organization on surface. This exTTF derivative is provided of a dipeptide sequence and a water-soluble dendritic termini. The aim of this strategy is to evaluate the aforementioned design for producing ordered exTTF/SWCNTs nanohybrids and the impact in the lifetime of their charge-separated state.

In a second stage, inspired by the results obtained in the first project, we propose to redesign the exTTF building block, lengthening the peptide sequence to improve the assembly and substituting the dendritic termini by a carboxylic group. The ambition of this idea is preorganizing the donor molecules in supramolecular nanofibers which should act as wrapping agents of the SWCNTs, in the same way that a covalent polymer but preserving the synthetic advantages of small molecules. Moreover, the carboxylic group can allow us to externally modulate the hierarchical organization by pH regulation and charge screening.

Finally, we want to consolidate the previously developed strategy to control the organization of donor and acceptor domains through charge screening. In this sense, we plan to expand this methodology to another acceptor units based on small molecules and not only to SWCNTs. To overcome this issue, we prepare PBI derivatives symmetrically functionalized with water-

soluble chains and different cationic groups in the periphery. This innovative design allow us to introduce the acceptor species and the external charge screening additive in one single process. With this methodology, we will be able to study the organization of the donor and the acceptor domains in the bulk material, the possible control on the macroscopic ordering in terms of external inputs and the impact of the morphology on the charge mobilities.

1.3. Results and Discussion

1.3. Results and Discussion

1.3.1. Self-ordering electron donor-acceptor nanohybrid based on single-walled carbon nanotubes across different scales.[40]

Controlling the self-assembly of nanostructures containing donor and acceptor moieties is one of the major challenges in materials science, in general, and in carbon nanotubes research, in particular.

In this first approach towards the creation of donor/acceptor ordered materials, we describe the design, synthesis and application of a photo-active small molecule containing an exTTF unit covalently linked to an alanyl-glycine dipeptide sequence and an oligoethyleneglycol-based dendron, that is, compound **1**.

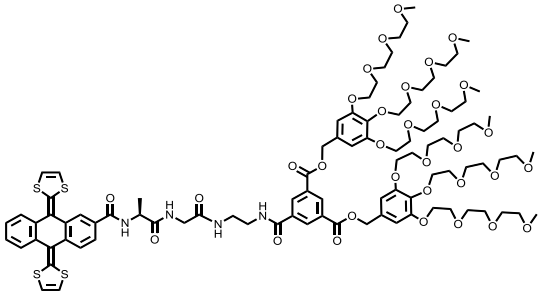

1

Scheme 1. Molecular structure of target compound 1.

This electron-donor molecule **1** is tested as wrapping agent of electron-acceptor SWCNTs, promoting their supramolecular organization across different scales, that is, from the nano- to the macroscale. The formation of this nanohybrid is demonstrated by different spectroscopic and microscopic techniques. Moreover, the photophysical properties of the resulting electron donor–acceptor nanohybrid are evaluated.

40 F. G. Brunetti, C. Romero-Nieto, J. López-Andarias, C. Atienza, J. L. López, D. M. Guldi and N. Martín, *Angew. Chem., Int. Ed.* **2013**, *52*, 2180-2184.

1.3.1.1. Design and synthesis of dendritic exTTF ***1***

Three different elements could be distinguished in the designed molecule **1**, playing each of them an important role to fulfill the final objective: 1) exTTF moiety serves not only as electron donating element, but also as recognition component of the curved surface of SWCNTs due to its butterfly-type shape; 2) dipeptide sequence can promote organization in the supramolecular structure through intermolecular hydrogen-bonding; 3) dendritic termini ensures water-solubility and enables the formation of higher ordered structures through the interdigitation of the oligoethyleneglycol chains.

The synthetic procedure of compound **1** is described below:

Firstly, exTTF derivative **3** with a carboxylic acid group in position 2 was prepared in five synthetic steps (Scheme 2). Initially, dimethyl 1,3-dithiol-2-ylphosphonate precursor **2** was achieved by a well stablished procedure involving *S*-methylation, reduction, treatment with HBF_4 and phosphonylation with trimethylphosphite, starting from commercially available vinylene trithiocarbonate.[41] Double carbonyl olefination of anthraquinone-2-carboxylic acid with phosphonate **2** produced **3** in moderate yield, without requiring the use of any protecting group for the carboxylic acid appendant.[34]

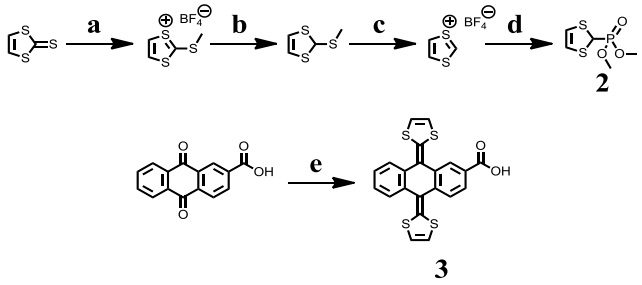

Scheme 2. Synthesis of exTTF derivative 2. (a) 1. Me_2SO_4, 100 ºC; 2. AcOH, 0 ºC, 3. $HBF_4{\cdot}Et_2O$, 0 ºC, 95 %, (3 steps); (b) $NaBH_4$, EtOH, rt, 95%; (c) $HBF_4{\cdot}Et_2O$, Ac_2O, 0 ºC, 90%; (d) $P(OMe)_3$, NaI, MeCN, rt, 95%; (e) **2**, *n*BuLi, THF, - 78 ºC, 55%.

41 A. J. Moore and M. R. Bryce, *J. Chem. Soc., Perkin Trans. 1* **1991**, 157-168.

Compound **5** was prepared in two steps by amidation reaction between **3** and alanylglycine methyl ester hydrochloride using HBTU as activating agent, followed by hydrolysis of the corresponding ester **4** (Scheme 3).

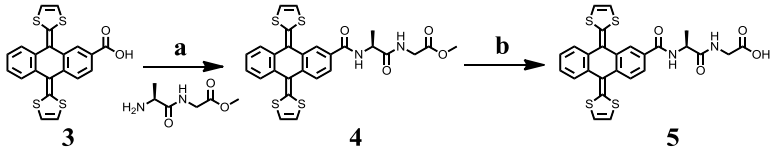

Scheme 3. Synthesis of exTTF-dipeptide 5. (a) HBTU, DIPEA, THF, rt, 62%; (b) KOH, EtOH/H_2O, reflux, 98%.

The synthesis of dendron **10**, with six oligoethylene glycol tails, was carried out as follows (Scheme 4): Alcohol **7** was obtained by triple O-alkylation of methyl 3,4,5-trihydroxybenzoate with 3,6,9-trioxadecyl 4-toluenesulfonate and subsequent reduction of **6** to the bencyl alcohol, following a procedure previously described in the literature.[42] Meanwhile, 3,5-bis(ethoxycarbonyl)benzoic acid was converted into compound **8** by amidation with tert-butyl (2-aminoethyl)carbamate in excellent yield. Quantitative hydrolysis of both methyl ester groups (**9**) and double esterification with the previously prepared alcohol **7** yielded building block **10**.

42 S. Zhang, H.-J. Sun, A. D. Hughes, B. Draghici, J. Lejnieks, P. Leowanawat, A. Bertin, L. Otero De Leon, O. V. Kulikov, Y. Chen, D. J. Pochan, P. A. Heiney and V. Percec, *ACS Nano* **2014**, *8*, 1554-1565.

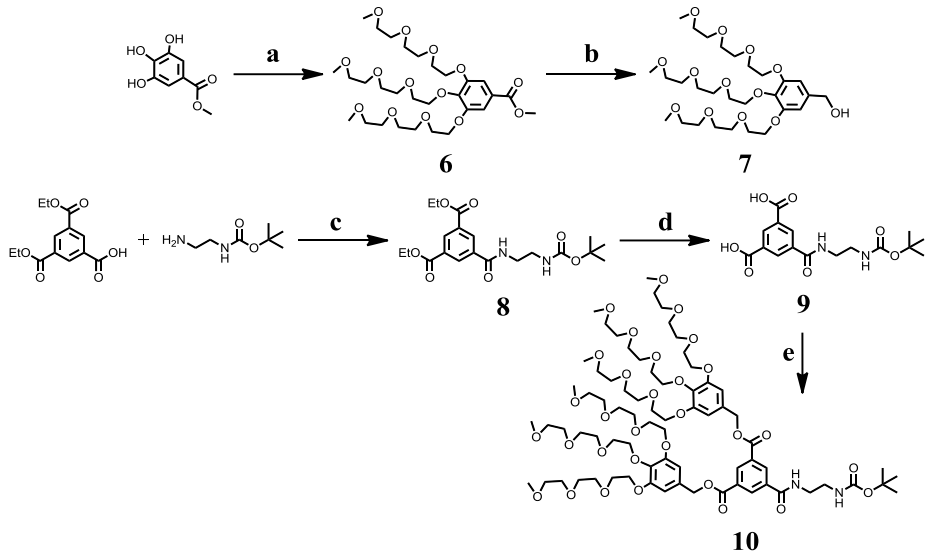

Scheme 4. Synthesis of dendron 10. (a) 3,6,9-Trioxadecyl 4-toluenesulfonate, K_2CO_3, KI, DMF, 80 ºC, 95%; (b) $LiAlH_4$, THF, 0 °C to rt, 99%; (c) HBTU, TEA, DMF, rt, 95%; (d) KOH, EtOH/H_2O, reflux, 98%; (e) EDC, DMAP, CH_2Cl_2, rt, 51%.

Finally, target compound **1** was achieved as depicted in Scheme 5 by the coupling of the carboxylic acid in **5** and free primary amine in **11**, which was previously deprotected under acidic conditions from **10**, just before the coupling reaction.

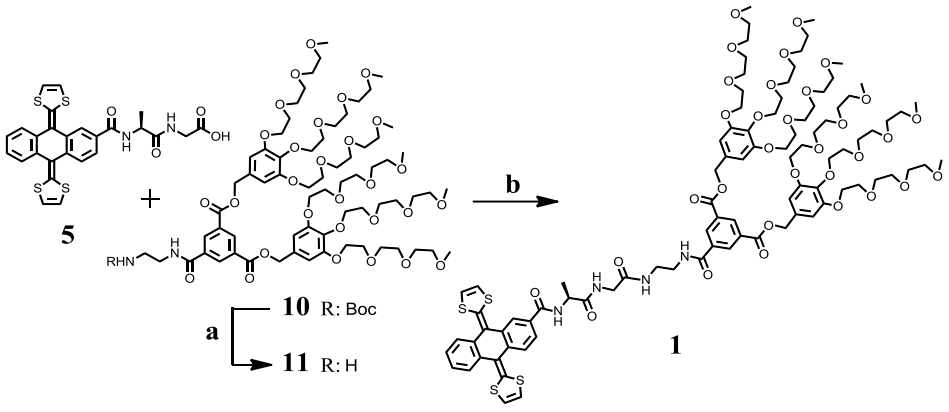

Scheme 5. Synthesis of target compound 1. (a) HCl, CH_2Cl_2, rt; (b) HBTU, DIPEA, DMF, rt, 76% (2 steps).

*1.3.1.2. Spectroscopic and photophysical characterization of **1**/SWCNT nanohybrid.*

Owing to the electron-donating and chromophoric features of the exTTFs, spectroscopic measurements were performed. To this end, we monitored the absorption of **1** in water and in the presence of increasing amounts of SWCNTs (Figure 23a). Interestingly, the addition of SWCNTs resulted in an intensity decrease of the exTTFs centered features in the visible at 453 and 382 nm, the simultaneous increase of SWCNT absorptions in the near-infrared, and the formation of pseudo-isosbestic and isosbestic points at 363 and 489 nm, respectively. These experimental findings are in agreement with the solubilization of SWCNTs in water through their supramolecular functionalization by compound **1**. Further insights into the formation of **1**/SWCNTs came from variable temperature absorption analyses (Figure 23b). Here, the absorption intensity of **1** increased as the temperature was raised up from room temperature to 90 ºC without the formation of SWCNT precipitates. More importantly, the initial spectrum was recovered when the temperature was adjusted to the initial value. The aforementioned is in sound agreement with SWCNT debundling in water, especially at higher temperatures.[43]

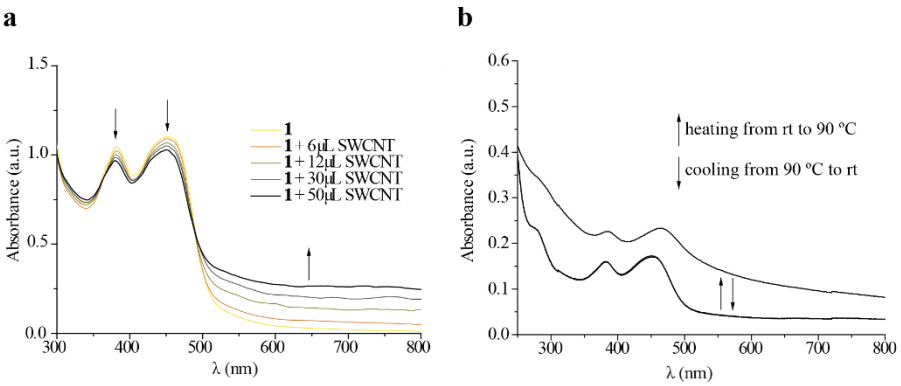

Figure 23. UV-*vis* titration of 1 with SWCNTs. (a) Titration of **1** (2.0 x 10^{-4} M in H_2O) with increasing amount of SWCNTs (suspension of 1-2mg in 0.5 ml of THF). (b) Temperature dependent absorption spectra of **1**/SWCNT in H_2O.

43 C. Backes, C. D. Schmidt, F. Hauke, C. Böttcher and A. Hirsch, *J. Am. Chem. Soc.* **2009**, *131*, 2172-2184.

The results of our non-covalent functionalization strategy were further investigated by Raman spectroscopy, that is, the radial breathing mode (RBM) and D, G, and G' modes of SWCNTs. D band intensities in the Raman spectra of pristine SWCNTs and of **1**/SWCNTs revealed no difference. Such a similarity corroborated the absence of oxidative/damaging processes during the workup procedure. As a matter of fact, we hypothesize that the original SWCNT properties must be preserved in **1**/SWCNTs. In sharp, RBMs changed in intensity and frequency with an overall decrease and a 3.5 cm^{-1} shift to higher frequencies (Figure 24) in **1**/SWCNTs compared with pristine SWCNTs. RBMs are strictly related to SWCNT diameters, chiralities, and the presence of bundles.[21] Thus, modified RBMs are in agreement with data reported for wrapped SWCNTs.[44] Only in cases of high molecular weight macromolecules, which thoroughly wrap around SWCNTs, Raman shifts are as high as 3–5 cm^{-1}.[45] Commonly, no appreciable changes in the RBMs are detected for non-covalent interactions based on π–π interacting building blocks.[46] Thus, our coating of SWCNT walls with such a small molecule, that is **1**, should be highly extensive, in the order of polymers and macromolecules.

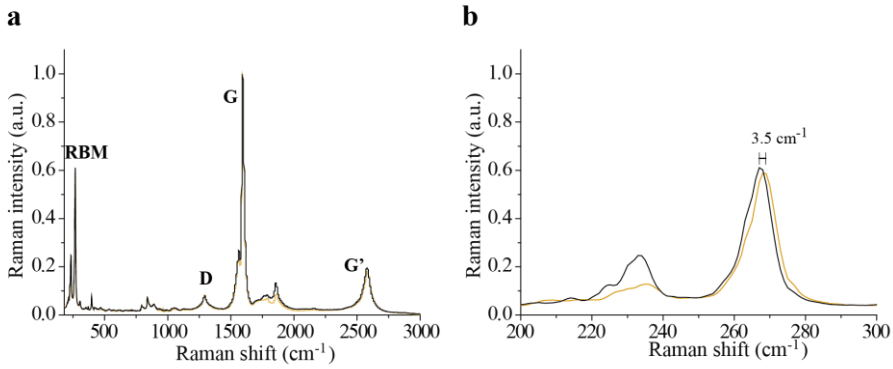

Figure 24. Raman characterization of 1/SWCNTs. (a) Raman spectra of SWCNT (black spectra) and **1**/SWCNT (orange spectra). (b) Amplification on the RBM region.

44 M. Zheng, A. Jagota, M. S. Strano, A. P. Santos, P. Barone, S. G. Chou, B. A. Diner, M. S. Dresselhaus, R. S. Mclean, G. B. Onoa, G. G. Samsonidze, E. D. Semke, M. Usrey and D. J. Walls, *Science* **2003**, *302*, 1545-1548.
45 H. Cathcart, V. Nicolosi, J. M. Hughes, W. J. Blau, J. M. Kelly, S. J. Quinn and J. N. Coleman, *J. Am. Chem. Soc.* **2008**, *130*, 12734-12744.
46 M. Á. Herranz, C. Ehli, S. Campidelli, M. Gutiérrez, G. L. Hug, K. Ohkubo, S. Fukuzumi, M. Prato, N. Martín and D. M. Guldi, *J. Am. Chem. Soc.* **2008**, *130*, 66-73.

In addition, we monitored the absorption features of SWCNTs in the absence and presence of **1**. The addition of **1** to aqueous suspensions of SWCNTs evoked an appreciable red-shift of the absorption maxima from 570, 590, 653, 727, 985, 1023, and 1123 nm for sodium dodecylbenzene sulfonate (SDBS)/SWCNT to 576, 601, 661, 737, 1011, 1052, and 1157 nm for **1**/SWCNT (Figure 25a). But it is not only the absorption features that were impacted by **1**, also the SWCNT fluorescence maxima bathochromically shifted from 965, 1032, 1127, and 1256 nm for SDBS/SWCNT to 995, 1059, 1158, and 1296 nm for **1**/SWCNT. Interestingly, an overall fluorescence quenching of 91% goes hand in hand with the formation of **1**/SWCNTs and, as such, prompts to a fast deactivation of photoexcited SWCNTs in the presence of **1** (Figures 25b-d).

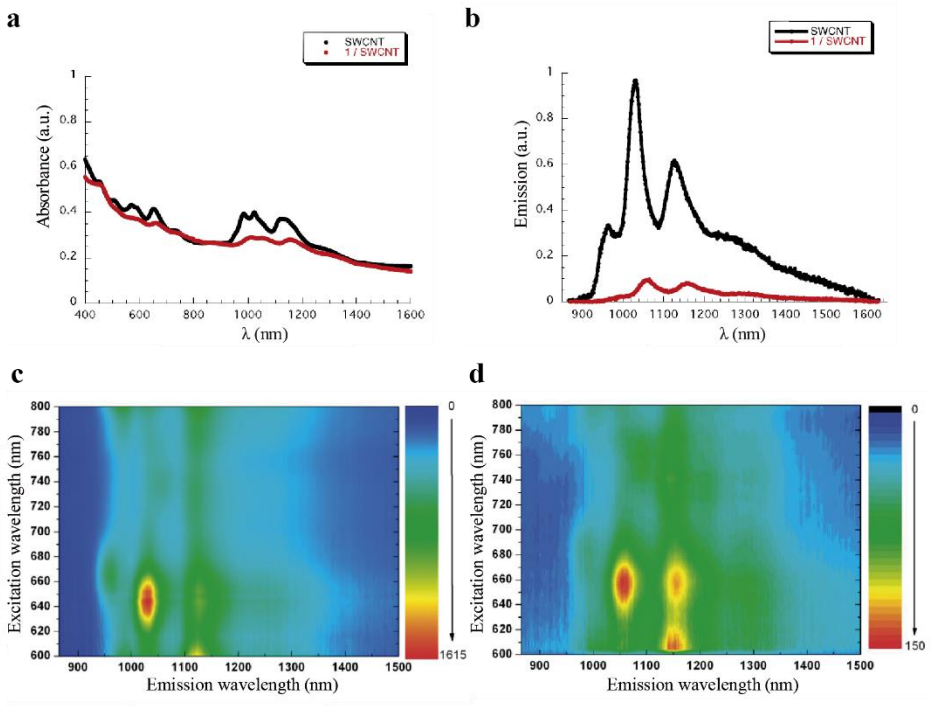

Figure 25. NIR absorption and fluorescence of SWCNTs. (a) Absorption spectra of SWCNT/SDBS (black spectrum) and **1**/SWCNT (red spectrum) in D_2O. (b) Comparison of the NIR fluorescence spectra of SDBS/SWCNT (black spectrum) and **1**/SWCNT (red spectrum) in D_2O (652 nm excitation). (c) 3D steady-state fluorescence spectra of SDBS/SWCNT in D_2O. d) 3D steady-state fluorescence spectra of **1**/SWCNT in D_2O.

To shed light onto the fast excited-state deactivation in **1**/SWCNT, transient absorption measurements were performed. By laser excitation at 387 nm, SDBS/SWCNT gave rise to the instantaneous formation of a transient spectrum that featured minima at 512, 597, 647, 1022, and 1131 nm, as well as maxima at 485 and 1430 nm. The SWCNT centered transient was metastable and its decay was dominated by two major processes. In fact, lifetimes of 2.8 and 67 ps resulted from a multiexponential decay of the aforementioned features. Owing to the shifts seen in the absorption spectra, photoexcitation of **1**/SWCNT at 387 nm led to transient features that were red-shifted with respect to SDBS/SWCNT. For **1**/SWCNT, minima emerged at 462, 515, 601, 651, 1062, and 1155 nm, together with maxima at 485, 853 and 1492 nm. Figure 26 shows that these features transformed with a lifetime of 6 ps into a new transient. Importantly, the newly developing transient was composed in the visible range of a broad maximum at 685 nm. The latter resembled the one-electron oxidized radical cation of **1**. In the near-infrared, minima at 1014 and 1131 nm as well as maxima at 485, 535, 616, 883, and 1415 nm implied new conduction band electrons in SWCNTs. Summarizing, upon photoexcitation of **1**/SWCNT, the singlet excited state gave rise to an electron transfer product, in which **1** was oxidized and SWCNT was reduced. From multiwavelength analyses of the charge-separated state, we deduced a lifetime of 280 ± 20 ps, which is considerably longer than that for a pyrene derivative functionalized with exTTF/SWCNT.[46]

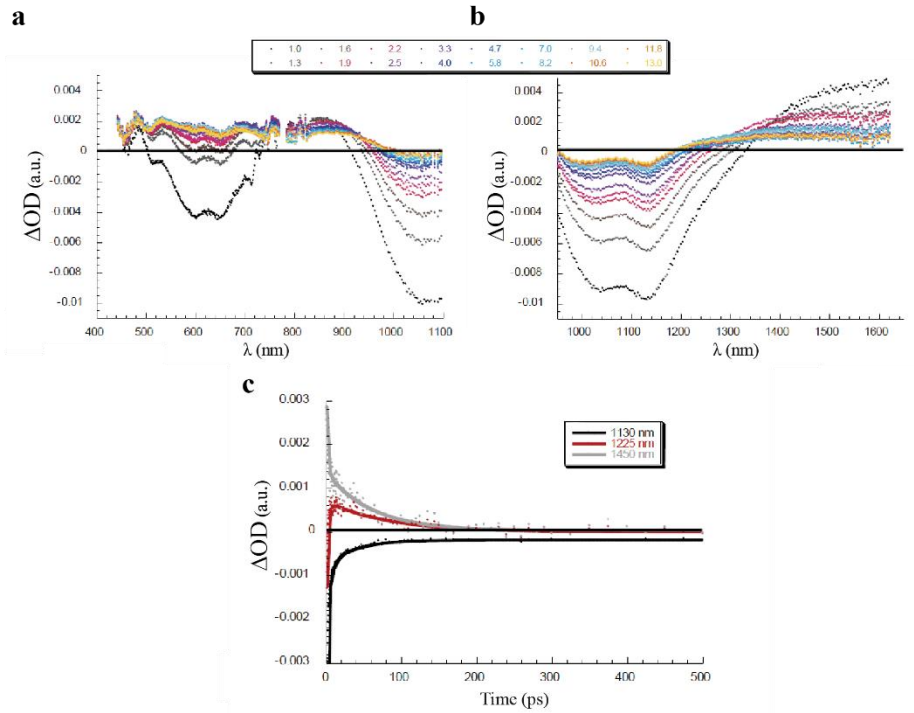

Figure 26. Transient absorption measurements on 1/SWCNTs. (a,b) Differential absorption spectra obtained upon femtosecond pump probe experiments (387 nm) of **1**/SWCNT in D_2O with several time delays between 1.0 and 13.0 ps at room temperature and in the visible / near-infrared and extended near-infrared, respectively. (c) Time absorption profiles at 1130, 1225, and 1450 nm monitoring the electron transfer.

To probe the electron-transfer impact of **1** on different SWCNTs, we turned to (6,5) and (7,6)-enriched SWCNTs (Figures 27a,b and 27c,d, respectively). Because of the SWCNT enrichment, fewer minima, that is at 475, 515, 665, 1055, and 1150 nm, evolved for **1**/(7,6) than for the mixture of **1**/SWCNT. In line with the size quantization, the corresponding minima for **1**/(6,5) were blue-shifted to 475, 595, and 675 nm in the visible and to 1020 nm in the near-infrared when compared to **1**/(7,6). In both cases, charge separation led within 5.0 ps to the oxidation of **1** with its prominent feature at 685 nm. Evidence for the SWCNT reduction, on the other hand, differed between **1**/(7,6) and **1**/(6,5) with minima at 1025/1140 and 1000 nm, respectively. Quite interesting was the trend seen in the charge recombination dynamics with 260 ± 10 ps for **1**/(6,5) and 105 ± 20 ps for **1**/(7,6). In other words, the lower charge-

separated state energy in (6,5)-enriched SWCNTs was beneficial to stabilize the charge-separated state. From a comparison of the spectral changes, we concluded that **1**/SWCNTs nanohybrid contain predominantly **1**/(7,6). On the contrary, comparing the charge recombination dynamics it appeared that the dynamics in **1**/SWCNTs are governed predominantly by **1**/(6,5).

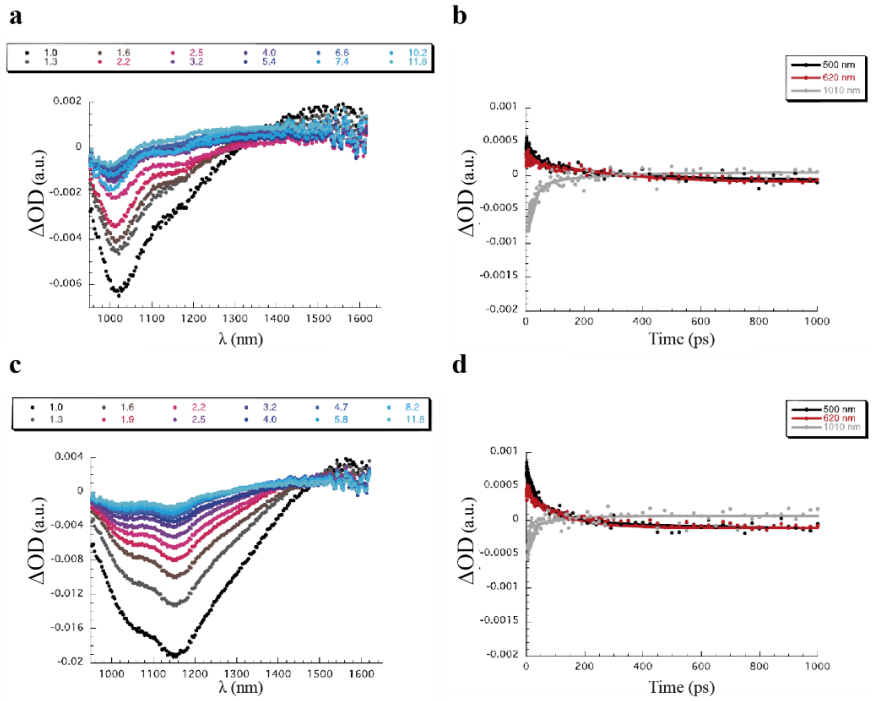

Figure 27. Comparison between (6,5) and (7,6)-enriched SWCNTs. (a) Differential absorption spectra (extended near-infrared) obtained upon femtosecond pump probe experiments (387 nm) of **1**/(6,5)-enriched SWCNT in D_2O with several time delays between 1.0 and 13.0 ps at room temperature. (b) Time absorption profiles at 500, 620, and 1010 nm monitoring the electron transfer in **1**/(6,5)-enriched SWCNT. (c) Differential absorption spectra (extended near-infrared) obtained upon femtosecond pump probe experiments (387 nm) of **1**/(7,6)-enriched SWCNT in D_2O with several time delays between 1.0 and 13.0 ps at room temperature. d) Time absorption profiles at 500, 620, and 1010 nm monitoring the electron transfer in **1**/(7,6)-enriched SWCNT.

*1.3.1.3. Microscopy and X-ray diffraction studies of **1**/SWCNT nanohybrid.*

For the preparation of the supramolecular *p*/*n*-nanohybrid, a simple procedure was carried out, without the need of employing any surfactant. In a typical experiment, a small amount of the corresponding SWCNTs (ca. 1 mg) were added to an aqueous solution of **1** (3 mL, 4 x 10^{-4} M) and sonicated in an ultrasound bath until a dark solution was obtained. This process usually took from 5 to 15 minutes. It should be noted that, in general, SWCNTs possess a limited solubility in common organic solvents[47] while they are completely insoluble in water. Due to their high hydrophobicity they float on the surface due to the water's superficial tension or they precipitate out. Low-power ultrasound bath ensures their non-covalent functionalization process, avoiding any significant oxidation issues that can be generated by the use of strong and invasive ultrasound equipment. The solution containing the coated **1**/SWCNT was then centrifuged at low rpm rate (1500 rpm for 3 min) in a microcentrifuge tube to remove the excess of unfunctionalized SWCNTs that precipitated out. The upper 75% of the supernatant was recovered from the centrifugation tubes, avoiding sediment at the bottom, transferred to a clean tube and recentrifugated for 30 min at 12000 rpm. The supernatant was removed and the precipitated **1**/SWCNTs nanohybrid was washed with deionized water until the solution was colorless, removing the unreacted **1** (Figure 28).

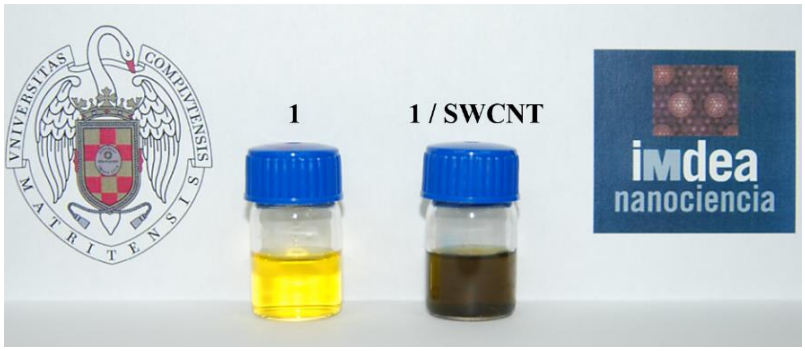

Figure 28. Photograph of aqueous suspensions of 1 and 1/SWCNT.

47 J. L. Bahr, E. T. Mickelson, M. J. Bronikowski, R. E. Smalley and J. M. Tour, *Chem. Commun.* **2001**, 193-194.

Upon their formation, **1**/SWCNT nanohybrid was fully characterized by means of TEM, SEM, AFM and small angle X-ray scattering (SAXS):

For **1**/SWCNTs, representative TEM images are displayed in Figure 29a,b. At first glance, a high degree of nanohybrid organization is discernable. A closer look reveals the formation of fairly well-aligned SWCNT structures (Figure 29c). Similar figures have been obtained by Dieckman and col., described in the background section.[25] In contrast to their case, our strategy has focused on aligning SWCNTs with a small molecule bearing only a dipeptide sequence, the dendrimeric tails and, more importantly, an electron donating termini, that is, exTTF group. When compared to pristine SWCNTs, **1**/SWCNTs lacked any randomly aggregated bundles. SWCNTs revealed, for instance, bundles with diameters that range from 12 to 50 nm (Figure 29e). In control experiments, dichloromethane, which was used instead of water, gave an organization that is best described as the coexistence of pristine SWCNTs, and **1**/SWCNTs (Figure 29d). The different organization was presumably related to the strong change in solvent polarity, that is, water *versus* dichloromethane.

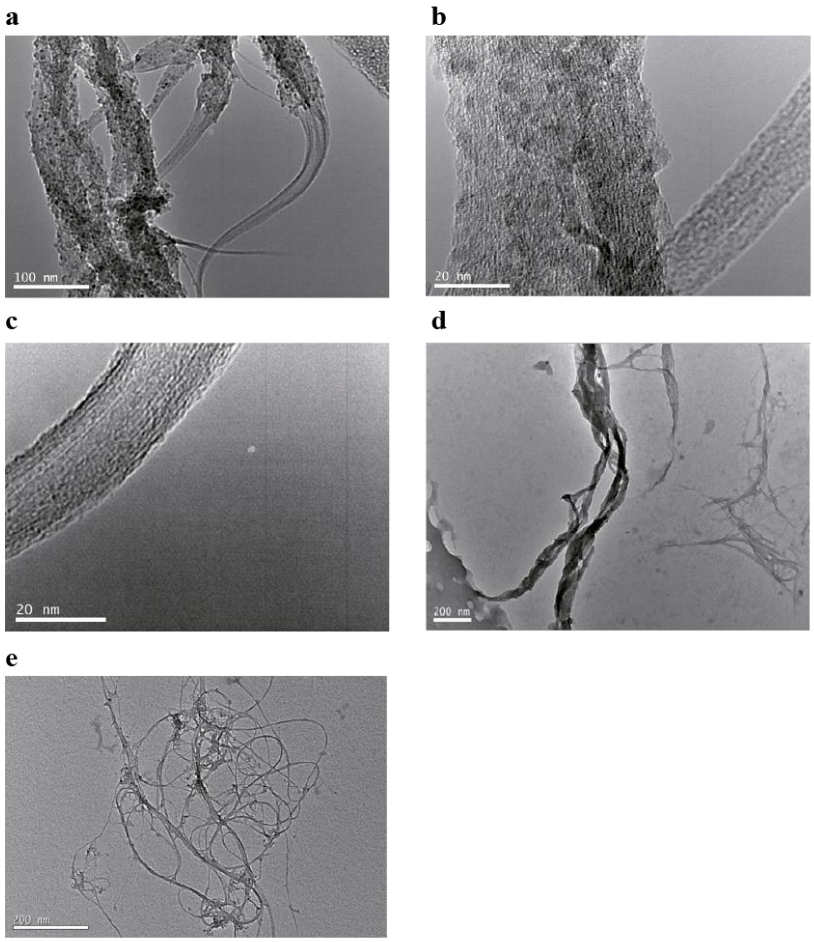

Figure 29. TEM studies of 1/SWCNTs. (a–c) TEM images of **1**/SWCNTs drop-coated from water at different magnifications (scale bars: 100, 20, and 20 nm, respectively. (d) TEM image of **1**/SWCNTs drop-coated from CH_2Cl_2 (scale bar: 200 nm. (e) TEM image of pristine SWCNT in a "spaghetti"-like conformation (scale bar: 200 nm).

SEM analysis further confirmed self-aligning **1**/SWCNTs and, in certain specific cases, a clear higher organization of these nanocomposites is discerned in Figure 30. Particularly, Figure 30b shows a magnification of the self-oriented SWCNTs and their ordered structure. Although the formation of these three-dimensional nano-objects are quite interesting, our approach seems to more effectively align the carbon nanotubes in 2D rather than in 3D.

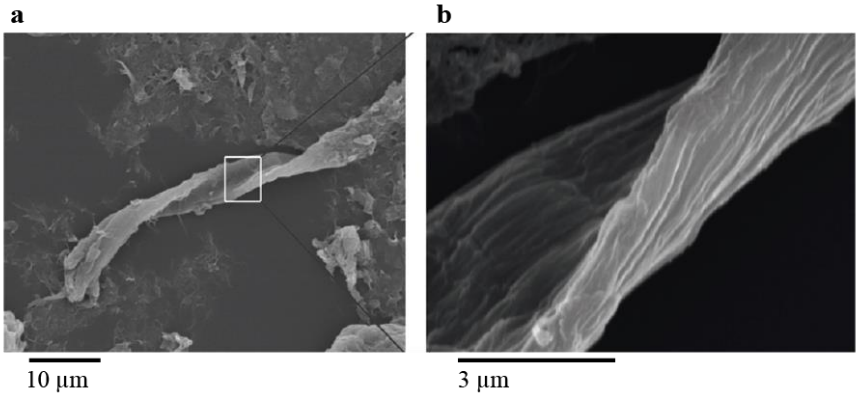

Figure 30. **SEM studies of 1/SWCNTs.** (a) SEM images of coated **1**/SWCNTs. (b) Amplification of SEM image in (a), representing the self-organization of **1**/SWCNTs nanohybrids.

AFM assays, where 2D organized domains that were exclusively composed of **1**/ SWCNTs were found, confirmed our hypothesis (Figure 31). On highly ordered pyrolytic graphite (HOPG) wafers, AFM images reveal upon correcting for the tip broadening, a lateral *d*-spacing for the 2D nanocomposite of around 10 nm. This measurement was calculated after correcting the tip broadening according with following equation:

$$e= 2\ [r^2-(r-h)^2)]^{1/\ 2}$$

where e is the error in horizontal dimension, r is the average radius of the tip, and h is the height of the feature. In cases where $h \geq r$ then the equation is no longer valid and, instead, the correction $e = 2\ r$ was applied. Radius of the tip (BUKER, Model: TESPSS) is 2 nm.[48]

Fast Fourier Transform (FFT) analyses of the AFM images point unmistakably towards the preferred SWCNT alignment in the resulting 2D order (Figure 31a,b). Height profiles underscore that **1**/SWCNTs possessed heights in excess of 2.5 nm (Figure 31c). Histograms, in which the AFM diameter distributions of **1**/SWCNTs were gathered, are displayed in Figure 31d. These implied the homogeneous immobilization of **1** onto individualized SWCNTs.

48 a) S. Yagai, S. Kubota, H. Saito, K. Unoike, T. Karatsu, A. Kitamura, A. Ajayaghosh, M. Kanesato and Y. Kikkawa, *J. Am. Chem. Soc.* **2009**, *131*, 5408-5410; b) B. Ohler, I. Revenko and C. Husted, *J. Struct. Biol.* **2001**, *133*, 1-9.

Accordingly, we derive from AFM that more than 80% of the nanostructures were formed by individual **1**/ SWCNTs laterally assembled into two dimensions.

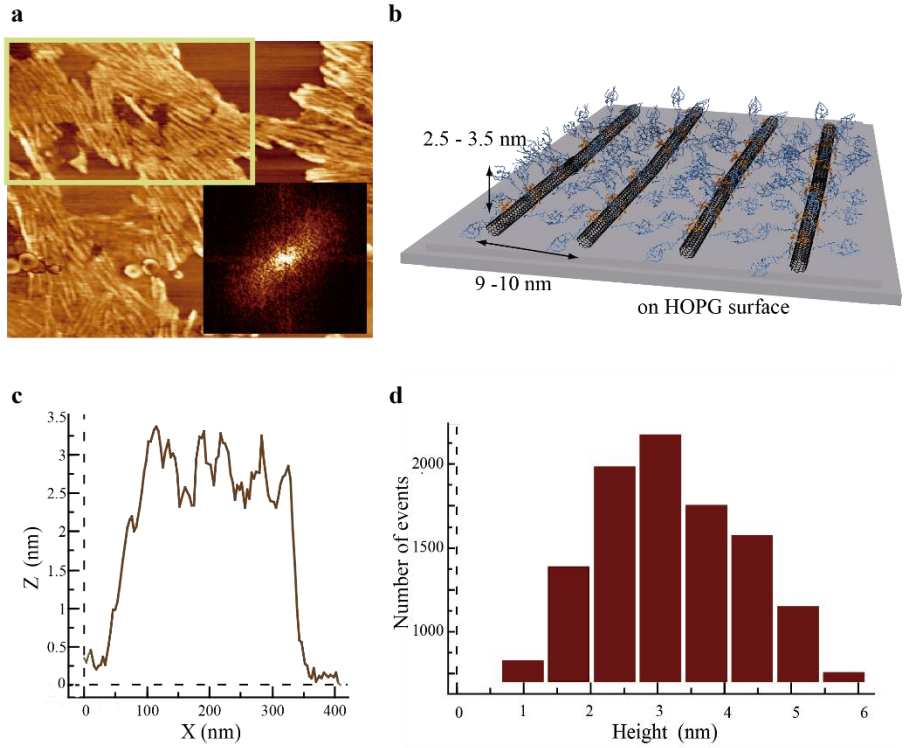

Figure 31. AFM assays of 1/SWCNTs. (a) AFM image of **1**/SWCNTs on a HOPG surface (1 mm x 1 mm). Inset: FFT analysis of the highlighted area in the square. (b) Schematic drawing of **1**/SWCNTs on a HOPG surface. (c) Height profile of the section highlighted in (a). (d) Histogram of the height distribution.

In solution, the presence of well-ordered **1**/SWCNTs was confirmed by means of SAXS measurements. X-ray scattering of **1**/SWCNTs in aqueous media at 25 ºC gave rise to a q^{-4} dependence within the low "*q*" range, which is indicative for the presence of large aggregates. In addition, a scattering peak in the intermediate "*q*" range with a spacing of approximately 8.97 nm was discernible (Figure 32a). This spacing is in excellent agreement with the lateral *d*-spacing observed after the tip-broadening correction in AFM and in the range of **1**/SWCNT diameters. On the other hand, such spacing suggests that an effective shielding/coating of **1** led to the individualization of SWCNTs and resulted in a uniform and homogeneous SWCNT functionalization. Important

are also the hydrophilic dendrimer termini, which favored engagement with the surrounding water. SAXS measurements with just **1** as control lack any ordered supramolecular ensemble in this media (Figure 32b).

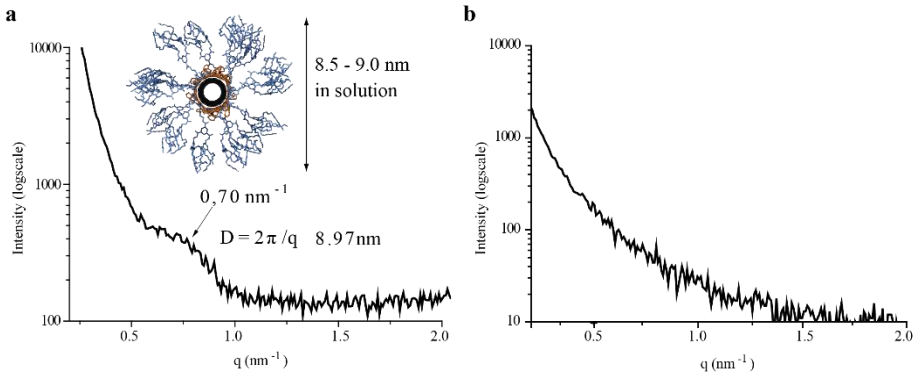

Figure 32. SAXS experiments in solution. (a) SAXS scattering of **1**/SWCNTs in aqueous solution at 25 ºC and the schematic drawing of **1**/SWCNTs in solution. (b) SAXS scattering of **1** in aqueous solution at 25 ºC.

1.3.2. Controlling the crystalline three-dimensional order in bulk materials by single-wall carbon nanotubes[49]

Encourage of the the good results afforded with compound **1** relating to the organization of SWCNT-based *p*/*n*-systems, we proposed to modify the structural features of the exTTF-peptide molecules. In this way, a more preorganized electron-donor architecture would lead to a higher degree of order in the final material when introducing the SWCNTs.

In this work, we describe the design and synthesis of the two novel exTTF building blocks, **12** and **13**, and the characterization of the supramolecular polymers generated by their self-assembly. Furthermore, these assemblies are used as wrapping agents of SWCNTs, generating their corresponding nanohybrids, fully characterized by spectroscopic and microscopic assays. In the last section, we demonstrate the possibility to create very organized 3D bulk materials by external additives, in which the presence of the SWCNTs play a crucial role regarding to the crystallinity of the heterojunctions.

*1.3.2.1. Synthesis of exTTF-tripeptide **12** and exTTF-pentapeptide **13***

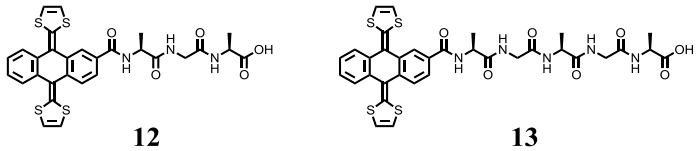

12 **13**

Scheme 6. Molecular structures of the target exTTF-based molecules 12 and 13.

We have designed and synthesized two new exTTF derivatives, where the alanyl- and glycyl- sequence is lengthened comparing with the previously described compound **1**. Moreover, the dendrimeric polar appendant is substituted by a terminal carboxylic group, enabling the control in the formation of supramolecular ensembles through pH adjustment and charge-screening with metal cations (Scheme 6). In particular, compound **12** is decorated by an alanyl-glycyl-alanyl-tripeptide sequence covalently connected to the exTTF electroactive unit in one side, and the carboxylic acid functional group in the

49 J. López-Andarias, J. L. López, C. Atienza, F. G. Brunetti, C. Romero-Nieto, D. M. Guldi and N. Martín, *Nat. Commun.* **2014**, *5*, 3763.

other side. Meanwhile, compound **13** possesses an analogous structure but the peptide sequence is increased by an extra alanyl-glycyl-dipeptide, finally constituting a pentapeptide sequence.

These peptide sequences are comprised of two of the most commonly available and cheapest amino acids (alanine and glycine) able to form antiparallel *β*-sheets through intermolecular hydrogen bonding. In nature, the repeating pattern Gly-Ala can be found in the crystalline *β*-sheet domain in *Bombyx mori* silk, which is responsible of the mechanical properties of silk fibers. In artificial systems, this motif has also been used to promote ordering in molecular assemblies.[34,50]

The synthesis of L-alanyl-glycyl-L-alanine ethyl ester hydrochloride **15** was achieved by amidation reaction between *N*-(*tert*-butoxycarbonyl)-L-alanyl-glycine and L-alanine ethyl ester hydrochloride yielding **14**, which was deprotected in acidic conditions leaving free primary amine in **15** ready for the next coupling. Pentapeptide **16** was obtained using Fmoc-amino acids and standard solid phase hydroxymethyl-based resin preloaded with Fmoc-L-alanine, minimizing epimerization.[51] After cleavage, the carboxylic acid group was methylated using trimethylsilyldiazomethane as reagent under mild conditions, affording **17** (Scheme 7).

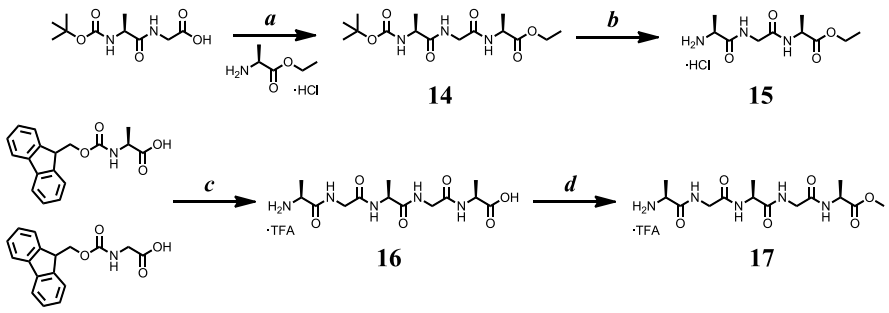

Scheme 7. Synthetic scheme for peptide-based ester 15 and 17. (a) HBTU, DIPEA, DMF, rt, 96%; (b) HCl, CH_2Cl_2, rt, 86%; (c) 1. Standard solid phase hydroxymethyl-based resin preloaded with Fmoc-L-alanine, HBTU, DIPEA, DMF. 2. Cleavage with TFA/H_2O; (d) TMS-diazomethane, CH_3OH, rt, 87%.

50 a) A. Jatsch, E. K. Schillinger, S. Schmid and P. Bauerle, *J. Mater. Chem.* **2010**, *20*, 3563-3578; b) Q. Wang, Y. Chen, P. Ma, J. Lu, X. Zhang and J. Jiang, *J. Mater. Chem.* **2011**, *21*, 8057-8065; c) G. W. M. Vandermeulen, K. T. Kim, Z. Wang and I. Manners, *Biomacromolecules* **2006**, *7*, 1005-1010.

51 J. Howl, *Peptide Synthesis and Applications*, Humana Press, **2005**.

Once the corresponding peptide derivatives were synthesized, they were coupled through an amide group to exTTF carboxylic acid **3**, obtaining esters **18** and **19**, which were hydrolyzed under basic conditions affording the desired derivatives **12** and **13** in an overall good yield in both cases (Scheme 8).

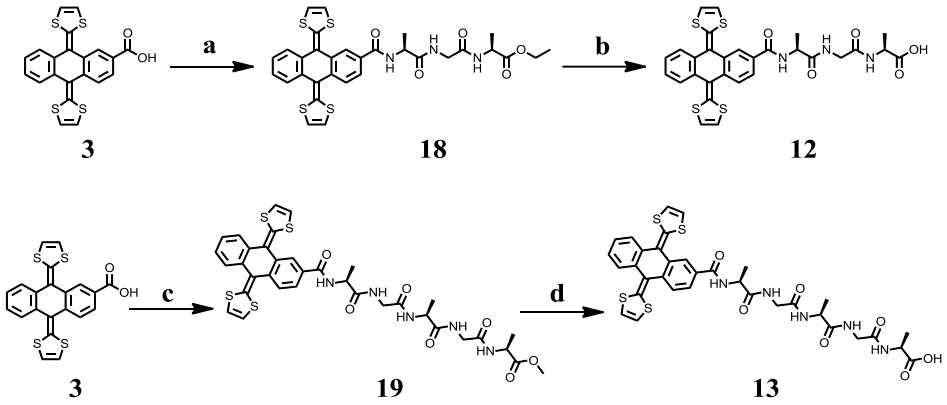

Scheme 8. Synthetic scheme for target derivatives 12 and 13. (a) **15**, HBTU, DIPEA, DMF, rt, 76% (b) KOH, ethanol/H_2O, rt, 98%; (c) **17**, EDC, DMAP, CH_2Cl_2, -15 ºC to rt, 76%; (d) KOH, ethanol/H_2O, rt, 95%.

*1.3.2.2. Study of the supramolecular organization of **12** and **13** in well-ordered p-nanofibers.*

Initially, a deep study of the supramolecular organization of the exTTF-based molecular building blocks (**12** and **13**) in aqueous solution was performed through a variety of complementary spectroscopic and microscopic techniques.

In absorption spectroscopy, tripeptide **12** gave rise under soft basic conditions in aqueous solution (pH = 8.5 - 9 using $NaHCO_3$ as base), to the diagnostic absorption band of $\pi-\pi$ interacting exTTFs at around 490nm.[33-34] The original absorption bands of pristine exTTFs were, however, recovered after either applying heat or the addition of an organic protic solvent such as methanol, which attested the reversibility of the process (Figure 33a,b). In the case of pentapeptide **13**, the 490 nm diagnostic band was observed at both soft basic conditions and in distilled water. Similarly to **12**, this process was found to be reversible either applying heat or adding methanol (Figure 33c,d).

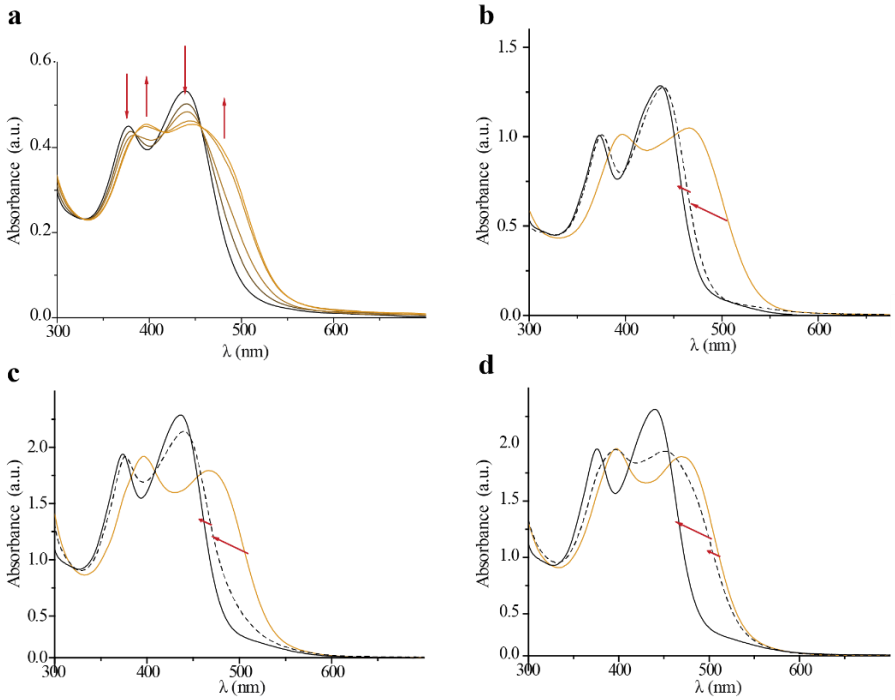

Figure 33. UV-*vis* spectra in the exTTF absorption region of 12 and 13. (a) Absorption spectra of **12** (3.2 x 10^{-5} M) after increasing progressively the pH with $NaHCO_3$ (red arrows). (b) Room temperature absorption spectra of **12** (8 x 10^{-5} M) under soft basic conditions (orange), after addition of 25% of CH_3OH (black dashed), and 50% of CH_3OH (black solid). (c) Room temperature absorption spectra of **13** (1.3 x 10^{-4} M) maturated during 1 hour in distilled water (orange), after addition of 25% of CH_3OH (black dashed), and after addition of 50% of CH_3OH (black solid). (d) Room temperature absorption spectra of **13** (1.3 x 10^{-4} M) under soft basic conditions (orange), after addition of 25% of CH_3OH (black dashed), and after addition of 50% of CH_3OH (black solid).

Circular dichroism (CD) assays carried out with **12**, under soft basic conditions, led to a strong bisignate signal with a positive Cotton effect at 480 nm, a negative Cotton effect at 431 nm and a zero cross point at 456 nm (Figure 34a). The strong ellipticity observed under these experimental conditions suggests a major ordering of π-π interacting exTTFs in the form of chiral arrays. In addition, the dichroic spectrum in the range of peptide absorbance showed the typical fingerprint for *β*-sheet secondary structure when $NaHCO_3$ salt was added to the aqueous solution (Figure 34b). XRD experiments supported the existence

of these well-defined *β*-sheets in the aforementioned supramolecular architecture (Figure 34c). However, random coil profile was observed in the peptide region in the dichroic spectrum when **12** was dissolved in distilled water, without any other additive (Figure 34d).

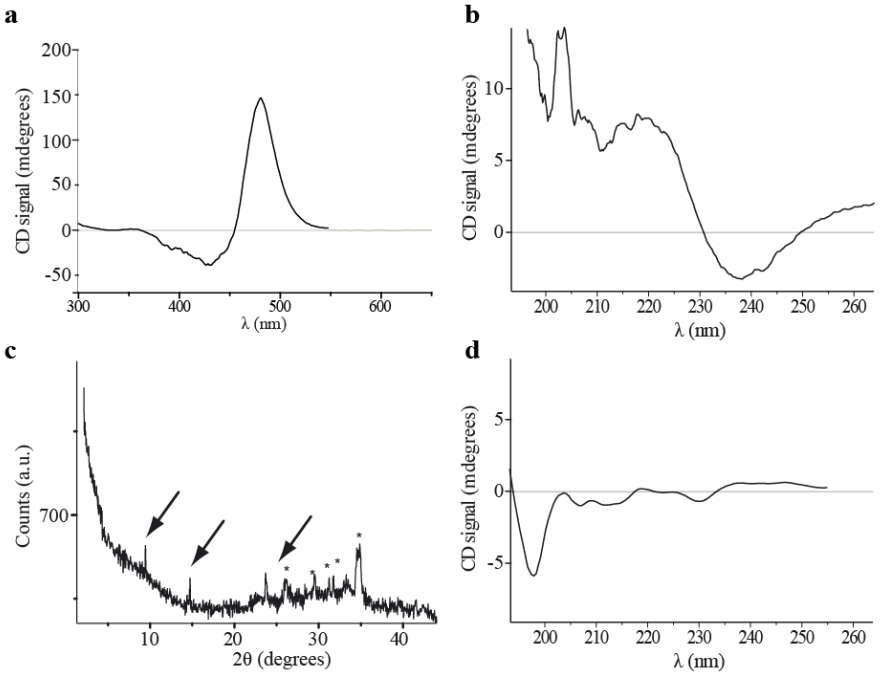

Figure 34. CD and XRD studies of compound 12. (a) CD spectrum of **12** in the exTTF absorption range at 2 x 10^{-3} M in water under soft basic conditions (pH 8–9). (b) CD spectra of **12** in the peptide absorption range at 5 x 10^{-5} M recorded in water under soft basic conditions. (c) XRD powder diffractogram of **10** in aqueous solution under soft basic conditions (arrows indicate diffraction peaks of compound **12** while asterisks designate those of $NaHCO_3$). (d) The same than (b) but recorded in distilled water.

Similar to **12**, CD experiments with **13** indicated the presence of a strong bisignated signal (Figure 35a). In accordance with the results stemming from absorption spectroscopy, this trend was presented under both distilled water and soft basic conditions, as well as the typical fingerprint for *β*-sheet secondary structure in the peptide absorption range (Figure 35b,c). Comparable to **12**, XRD experiments for **13** confirmed the exclusive presence of *β*-sheet type structures (Figure 35d).

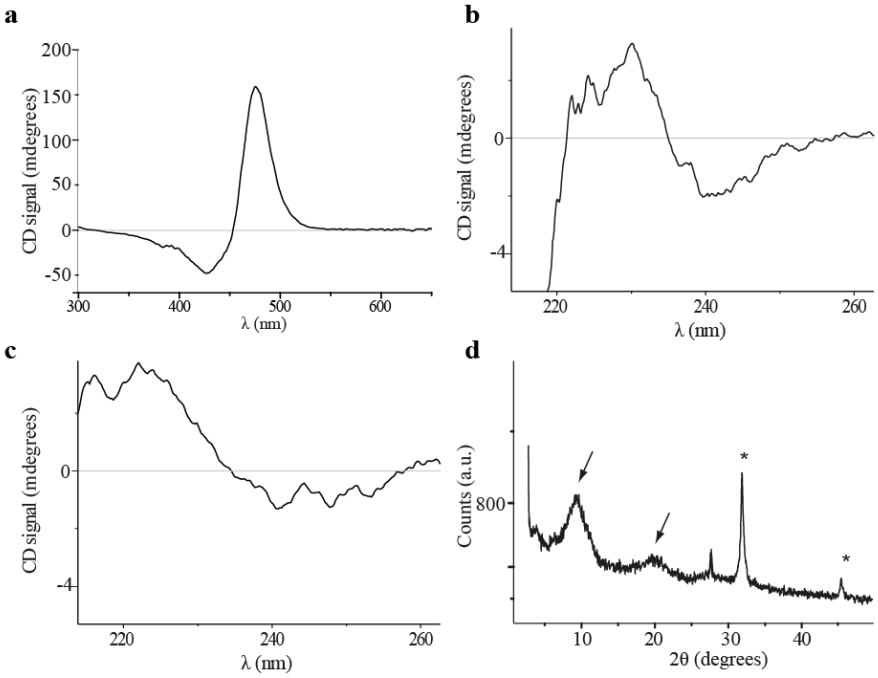

Figure 35. CD and XRD studies of compound 13. (a) CD spectrum of **13** in the exTTF absorption range at 2 x 10^{-3} M in water under soft basic conditions (pH 8–9). (b) CD spectra of **13** in the peptide absorption range at 5 x 10^{-5} M recorded in water under soft basic conditions. (c) The same than (b) but recorded in distilled water. (d) XRD powder diffractogram of **13** in aqueous solution under soft basic conditions (arrows indicate diffraction peaks of compound **13** while asterisks designate those of $NaHCO_3$).

AFM inspections carried out with **12** and **13** supported the existence of curved rope-like nanofibres with average diameters of 1.5 ± 0.5 nm and 3.0 ± 0.5 nm, respectively, and twisted shapes when aqueous solutions of these building-blocks were deposited onto mica (Figure 36). Again, compound **13** demonstrated its ability to self-organize in peptide-based supramolecular architectures without needing any additive or basic media.

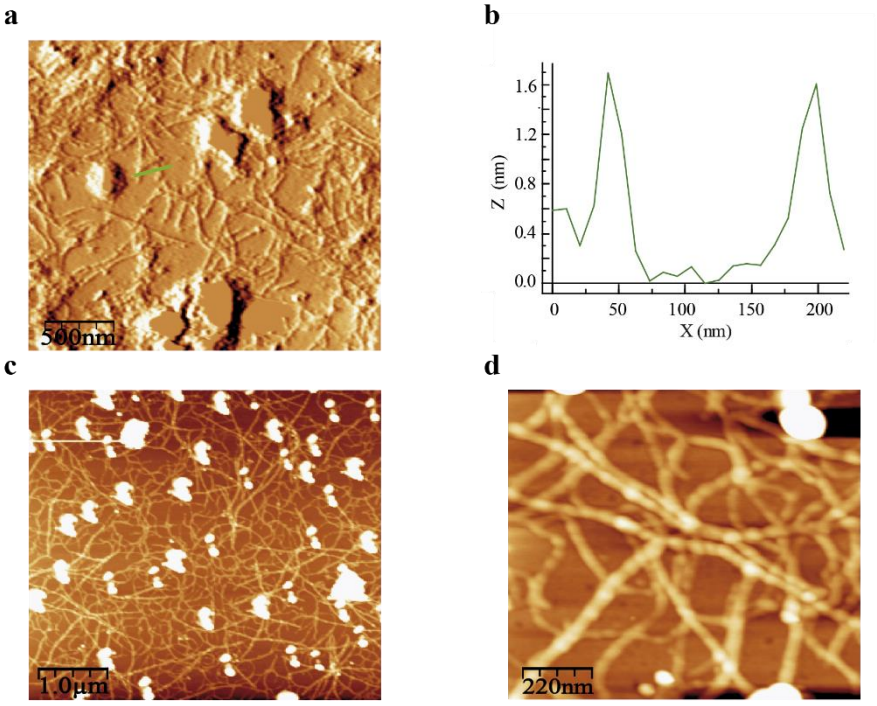

Figure 36. Atomic force micrographs of the *p*-type nanofibers. (a) AFM image of **12** deposited under soft basic conditions (pH 8–9) onto mica; scale bar: 500 nm. (b) Height profile across the green line in (a). (c) AFM image of **13** deposited from a distilled water solution onto mica; scale bar: 1000 nm. (d) Magnification of image (c); scale bar: 220 nm.

In Figure 37, a possible structure of the nanofiber produced from **13** is depicted. In this model, the long axis of the nanofiber is generated through the π-π stacking between exTTF aromatic units (Figure 37a). The concave shape of the exTTF is probably the responsible of the twisted shape of these architectures. Meanwhile, the antiparallel *β*-sheet, responsible of the short-range order found in XRD experiments would be found in the short axis of the nanofibers (Figure 37b).

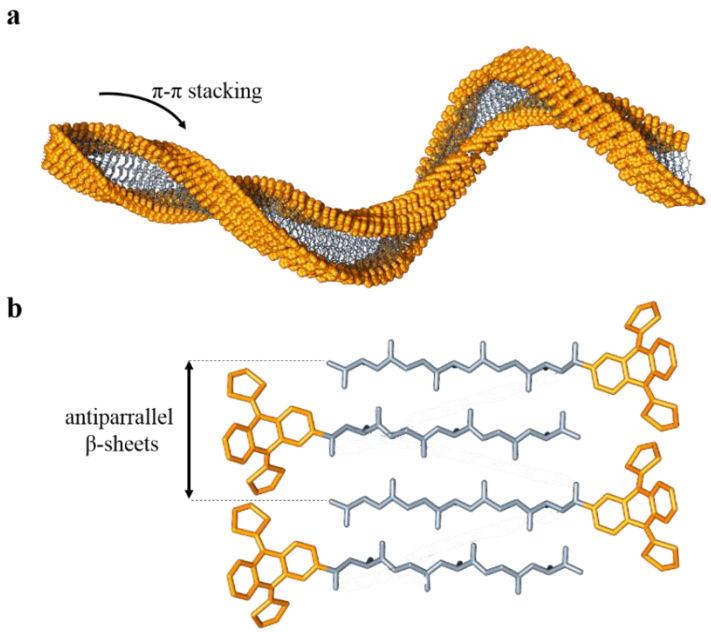

Figure 37. Possible model of the nanofiber generated from exTTF derivative 13. (a) Long-axis of the nanofiber, stabilized by π-π stacking between exTTF moieties. (b) Short-axis of the nanofiber, stabilized by the hydrogen-bonding between antiparallel *β*-sheets.

In summary, exTTF derivatives of tripeptide **12** and pentapeptide **13** self-aggregated at the nanoscale to yield twisted *p*-type nanofibres similar to those mentioned in the background of this chapter related to exTTF moiety.[33-34] Moreover, the requirements for each compound for obtaining well-ordered structures were evaluated indicating that in the case of derivative **12**, with a shorter peptide chain, the addition of a weak base was an essential requirement to promote deprotonation of the carboxylic acid and, consequently, to enlarge the amphiphilic nature of the building block. Another explanation for the role of the $NaHCO_3$ in the polymerization process of **12** could be the dependence of the supramolecular polymerization on the ionic strength of the aqueous solution. This fact has previously been evaluated by Besenius and col. who demonstrated by both experimental and theoretical approaches that counterions that are effectively bound to the highly charged surfaces of self-assembled nanostructures enhances the cooperativity of the equilibrium polymerization.[52]

52 C. Schaefer, I. K. Voets, A. R. A. Palmans, E. W. Meijer, P. van der Schoot and P. Besenius, *ACS Macro Letters* **2012**, *1*, 830-833.

Derivative **13**, in turn, with a longer peptide chain, was able to self-aggregate without needing any external contribution, as was depicted in all spectroscopic and microscopic characterizations performed over this building block. Notwithstanding, the possibility to modify the net electrical charge of the nanofibers by means of pH adjustment is an interesting feature that will be exploited in the following section.

1.3.2.3. Interfacing between p-nanostructures and SWCNTs.

After finding the conditions for obtaining well-defined *p*-architectures, these nanofibers were evaluated as wrapping agents for SWCNTs. The general method for the *p*/*n*-nanohybrid formation is described below:

In a typical experiment, to an aqueous solution of **12** or **13** (1 mL of 5 x 10^{-3} M) in the presence of 7.5 eq of $NaHCO_3$, around 2 mg of SWCNTs were added. The suspension was sonicated in an ultrasound bath until a dark red solution was obtained. This process usually took from 30 to 60 min. Low-power ultrasound bath ensures their non-covalent functionalization process, avoiding any significant oxidation stemming from the use of strong and invasive ultrasound equipment. The solution containing the coated **12**/SWCNT or **13**/SWCNT was then centrifuged at low r.p.m. rate (1500 r.p.m. for 3 min) in a microcentrifuge tube to remove the excess of unfunctionalized SWCNTs that precipitated out. The 75% of the supernatant was recovered from the centrifugation tubes, avoiding sediment at the bottom, and was transferred to a clean tube.

First insights into mutually interacting components came from absorption spectroscopy with focus on the exTTF absorption features. Interestingly, **12** and **13** dispersed SWCNTs reasonably well in aqueous solutions. In both cases, the 490 nm absorption band decreased in intensity and red shifted by nearly 10 nm in the presence of SWCNTs while the SWCNT absorptions increased (Figure 38). Implicit in this bathochromic shift is the successful wrapping of the nanofibers around SWCNTs.

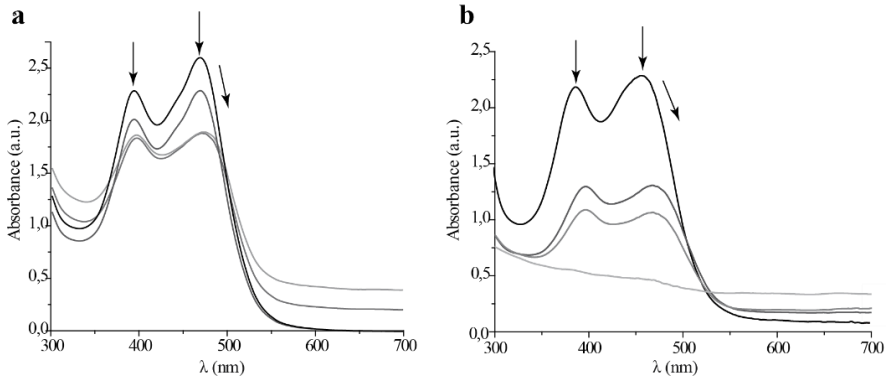

Figure 38. UV-*vis* experiments for *p*-nanostructures/SWCNTs. (a) Absorption assay of **12** (1.3 x 10^{-4} M) under soft basic conditions (pH 8–9) with SWCNTs (black arrows shown the progression). (b) Same than (a) but with **13**.

Complementary CD titrations showed that when titrating **12** with SWCNTs (Figure 39a) the bisignate signals of the exTTF nanostructures progressively decrease with the concomitant formation of a new, red-shifted bisignate signal. Importantly, the latter signal revealed an opposite helical handedness relative to the initial signal. It is worth mentioning that similar inversions have previously been observed for supramolecular[53] and covalent helical polymers[54] under certain external stimuli. Another observation in CD experiments with **12** was that, in the presence of SWCNTs, the typical *β*-sheet signatures in the CD spectrum disappeared (Figure 39b). This experimental finding suggested some kinetic instability stemming from the presence of SWCNTs in the case of **12**. This is also confirmed by the strong decreasing ellipticity and the inversion of the handedness observed for the bisignate signal.

On the other hand, CD titrations carried out with **13** and SWCNTs gave rise to a partial depletion of the bisignate signals of the exTTF nanostructures and the formation of a red-shifted bisignate signal, but in this case without helical inversion. These experimental observations support the notion of an efficient wrapping of the exTTF nanostructures around SWCNTs, without losing their helical ordering (Figure 39c). Moreover, the typical *β*-sheet signatures are still present in **13**/SWCNT and transform into a more complex CD spectrum after a short period of 15 min (Figure 39d).

53 P. A. Korevaar, S. J. George, A. J. Markvoort, M. M. J. Smulders, P. A. J. Hilbers, A. P. H. J. Schenning, T. F. A. De Greef and E. W. Meijer, *Nature* **2012**, *481*, 492-496.
54 F. Freire, J. M. Seco, E. Quiñoá and R. Riguera, *Angew. Chem., Int. Ed.* **2011**, *50*, 11692-11696.

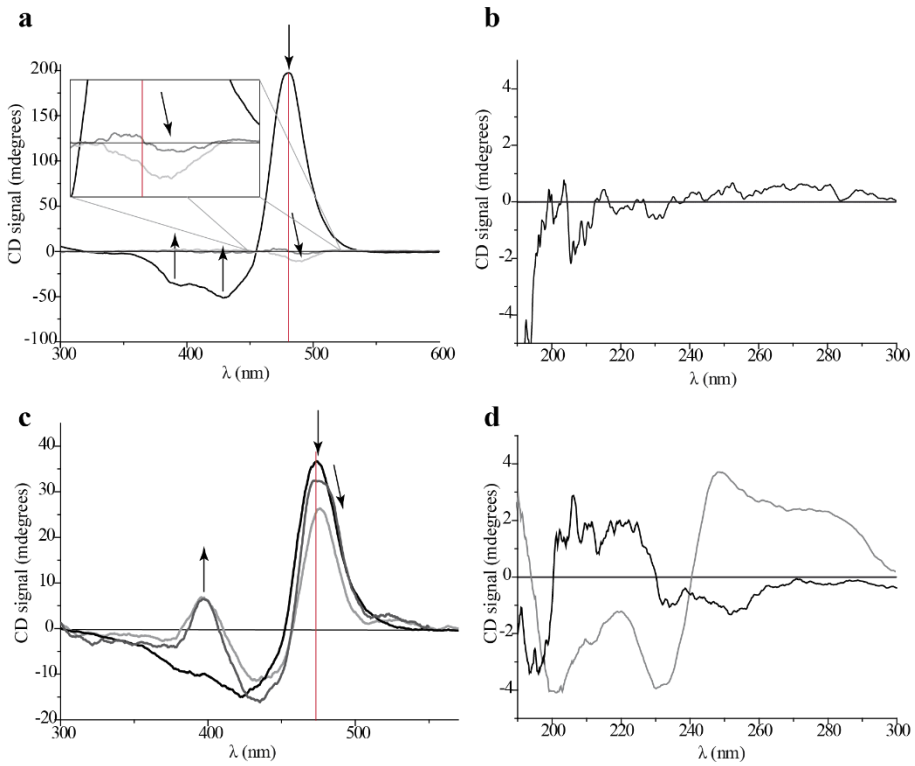

Figure 39. CD experiments for *p*-nanostructures/SWCNTs. (a) CD assay of *p*-nanofibres of **12** under soft basic conditions (pH 8–9) with SWCNTs; black arrows shown the progression. (b) Same than (a) but with **13**. (c) Peptide zone of CD spectrum of **12** under soft basic conditions (pH 8–9) with SWCNTs. (d) Peptide zone of CD of **13** under soft basic conditions (pH 8–9) immediately on addition of SWCNTs (black line) and 15 min later (grey line).

Similar results emerged when focusing on the absorption of SWCNTs in the NIR region. Here the features of the E_{11} absorption peaks of SWCNTs red shifted from 980, 1025, 1155 and 1265 nm in the case of SDBS/SWCNT to 1006, 1052, 1156 and 1292 nm in the case of **12**/SWCNT (Figure 40a). On the other hand, the E_{22} absorption peaks in SDBS/SWCNT at 450, 500, 570, 590, 650 and 725 nm were only marginally affected by the presence of **12** with red shifts that were on the order of a few nanometres. For **13**/SWCNT, maxima evolved at 1006, 1054, 1150 and 1290 nm (Figure 40b).

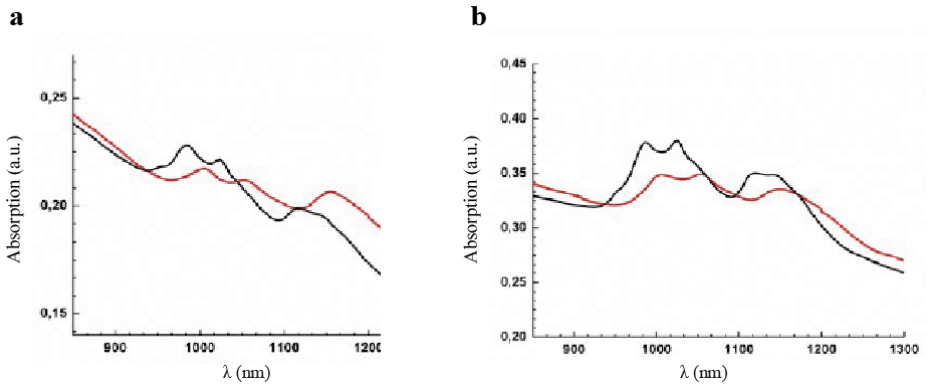

Figure 40. NIR spectra of SWCNTs. (a) Absorption spectra of SDBS/SWCNT (black spectrum) and **12**/SWCNT (red spectrum) under soft basic conditions in D_2O. (b) Absorption spectra of SDBS/SWCNT (black spectrum) and **13**/SWCNT (red spectrum) under soft basic conditions in D_2O.

Insights into exTTF/SWCNT ground-state electronic interactions came from Raman experiments. Here the three most important signatures, that is, RBM-, D- and G-modes, reveal upshifts in D_2O suspensions of SDBS/SWCNT with respect to **12**/SWCNT as well as in the solid without evidencing losses in resonance. For example, the G mode shifted from 1590 ± 2 to 1592 ± 2 and 1591 ± 2 cm^{-1} in the presence of **12** and **13**, respectively (Figure 41). This fact strongly indicated that π-π interactions are operative between **12** or **13** and SWCNTs.

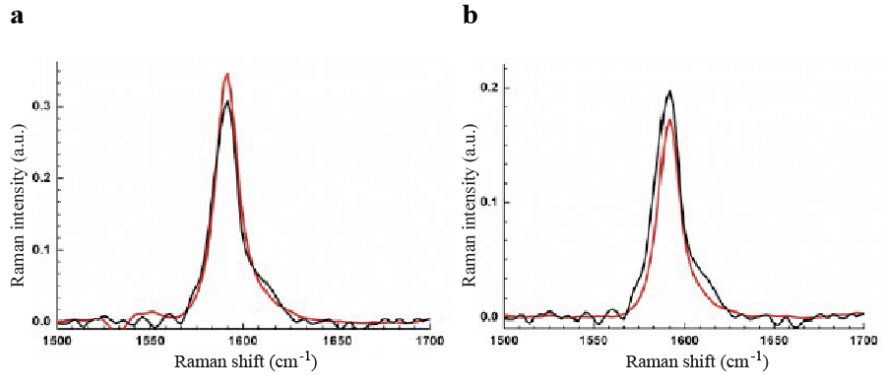

Figure 41. Raman spectra of SWCNTs. (a) Raman spectra of SDBS/SWCNT (black spectrum) and **12**/SWCNT (red spectrum) under soft basic conditions in D_2O (excitation: 1064 nm). (b) Raman spectra of SDBS/SWCNT (black spectrum) and **13**/SWCNT (red spectum) under soft basic conditions in D_2O (excitation: 1064 nm).

The fluorescence of **12**/SWCNT under soft basic conditions (pH 8–9) were in the same way red shifted as seen for the absorption features. For example, the corresponding maxima appeared for SDBS/SWCNT at 958, 1028, 1125 and 1250 nm, which were attributed to (6,5), (7,5), (7,6) and (8,7) SWCNTs, evolved at 1003, 1069, 1172 and 1311 nm for **12**/SWCNT nanohybrid (Figure 42a,b). When comparing the fluorescence intensity of **12**/SWCNT with that of SDBS/SWCNT exhibiting both equal absorbances at the excitation wavelength, a significant quenching was noted. In **12**/SWCNT, the quenching was as strong as 99% (Figure 42e). When inspecting the fluorescence of **13**/SWCNT nanohybrid, the same behavior was observed related to the red shifting but with an overall quenching as high as 95% (Figure 42c,d,f).

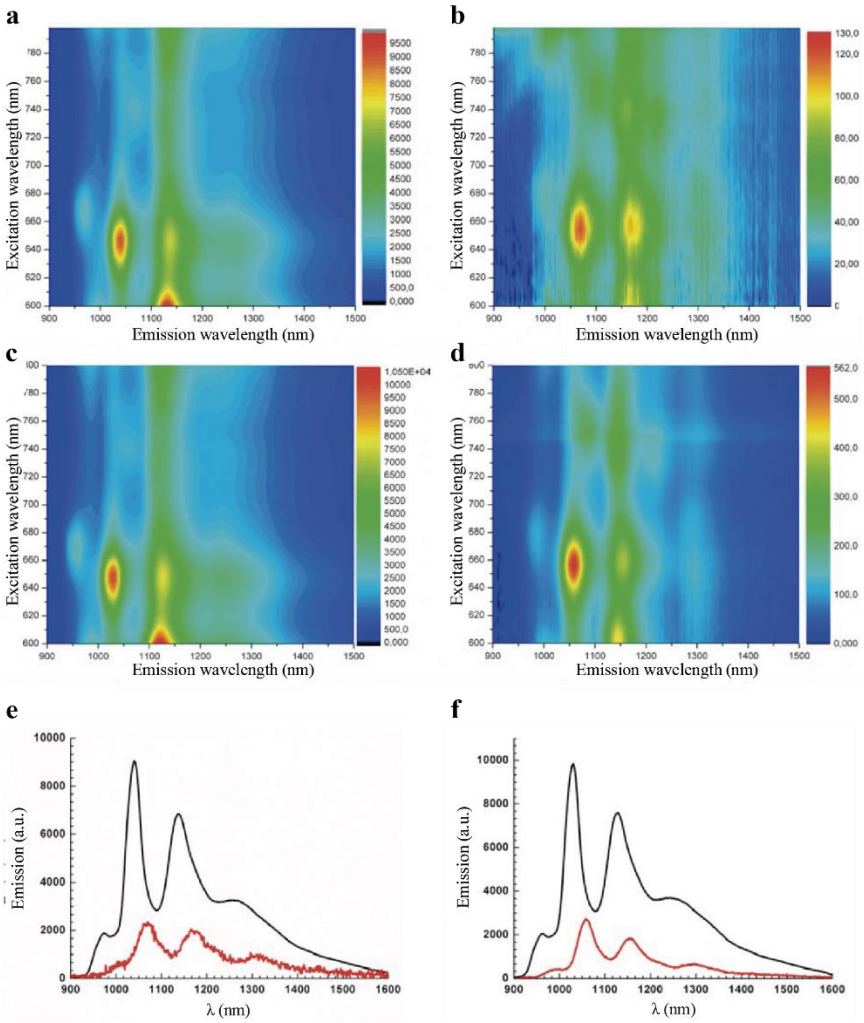

Figure 42. Fluorescence spectra for 12/SWCNT and 13/SWCNT. (a) 3D steady-state fluorescence spectra of SDBS/SWCNT in D_2O. (b) 3D steady-state fluorescence spectra of **12**/SWCNT under soft basic conditions in D_2O. Both recorded with equal absorbances at the excitation wavelengths. (c) 3D steady-state fluorescence spectra of SDBS/SWCNT in D_2O. (d) 3D steady-state fluorescence spectra of **13**/SWCNT under soft basic conditions in D_2O. Both recorded with equal absorbances at the excitation wavelengths. (e) Comparison of the NIR fluorescence spectra of SDBS/SWCNT in D_2O (black spectrum) and **12**/SWCNT under soft basic conditions in D_2O (red spectrum) amplified by a factor of 20 (650 nm excitation). (f) Comparison of the NIR fluorescence spectra of SDBS/SWCNT in D_2O (black spectrum) and **13**/SWCNT under soft basic conditions in D_2O (red spectrum) amplified by a factor of 5 (650 nm excitation).

The fluorescence assays were complemented by transient absorption spectroscopy to determine the dynamics of the ultrafast singlet excited-state deactivation in **12**/SWCNT as well as **13**/SWCNT and to characterize the products evolving from interacting of **12** and **13** *p*-nanofibres with SWCNTs. We started our investigations with SDBS/SWCNT reference experiments. The baseline was, in the case of SDBS/SWCNT, replaced with a strong bleaching that dominated the differential absorption spectra throughout the visible and near-infrared (NIR) regions. The major minima were seen at 570, 590, 650, 725, 985 and 1130 nm in addition to shoulders at 1025 and 1270 nm and a maximum at 1465 nm. Multiwavelength analyses of the bleaching characteristics resulted in complex dynamics with two dominant lifetimes, namely, 0.6 and 68 ps.[23] In control experiments, **12** and **13** were probed by photoexcitation at 387 nm (Figure 43a,b). In particular, exTTF-centred excited states evolved featuring spectral characteristics that include transient maxima around 470, 600 and 920 nm for **12**, and 574, 615 and 820 nm as well as a transient bleaching at 465nm for **13**. The lifetimes were, however, less than 2 ± 1 ps in both cases, correlating with a strong second-order vibronic spin orbit coupling.

Following photoexcitation of **12**/SWCNT at 387 nm, we observed in line with the absorption spectra the rapid formation of transient maxima at 465, 545 and 680 nm as well as transient bleaching at 1040 and 1145 nm that substantiates the excitation of **12** and SWCNTs, respectively (Figure 43c-e). The red shifting of the differential absorption changes when compared with SDBS/SWCNT was also notable.[23] Such a trend mirror imaged the differences in the absorption spectra of **12**/SWCNT and SDBS/SWCNT. In general, the photoexcited exTTF and SWCNT states were in **12**/SWCNT shorter lived and transform with a lifetime of 1.4 ± 0.3 ps into a new transient. In the visible, the newly formed transient was characterized by a broad maximum at 680 nm. The latter resembled the radiolytically and photolytically generated fingerprint of the one electron-oxidized radical cation of exTTF.[55] In the NIR, appreciable blue shifts of the transient bleaching were detected, with minima that shift from 1040 and 1145 nm to 1010 and 1135 nm, respectively, followed by a broad transient between 1150 and 1600 nm. Implicit were new conduction band electrons, injected from the exTTF, shifting the transitions to lower energies. As a matter of fact, we concluded that the selective excitation of **12**/SWCNT, in which sizeable shifts

55 A. E. Jones, C. A. Christensen, D. F. Perepichka, A. S. Batsanov, A. Beeby, P. J. Low, M. R. Bryce and A. W. Parker, *Chem. Eur. J.* **2001**, *7*, 973-978; 31 D. M. Guldi, L. Sánchez and N. Martín, *J. Phys. Chem. B* **2001**, *105*, 7139-7144.

of electron density prevail even in the ground state, was followed by a full separation of charges.

The latter inferred oxidation of exTTF and reduction of SWCNTs. By following the characteristics of the oxidized exTTF and the reduced SWCNTs, we deduced a lifetime of the electron transfer product of 125 ± 20 ps. Fairly similar were the differential absorption changes in the NIR on photoexcitation of **13**/SWCNT at 387 nm. A marked difference was seen, however, in the visible. In particular, transient bleaching in the range of absorptive transitions of semiconducting SWCNTs at 590 and 650 nm dominated the exTTF features. Nevertheless, also in **13**/SWCNT the photoexcited exTTF and SWCNT states were short lived with lifetimes of 15 ± 0.3 ps (Figure 43f-h). The product of the excited-state decay was attributed to oxidized exTTF and reduced SWCNTs. When turning to the lifetime of the electron transfer product in **13**/SWCNT, it was longer lived than in **12**/SWCNT with a lifetime of 210 ± 10 ps.

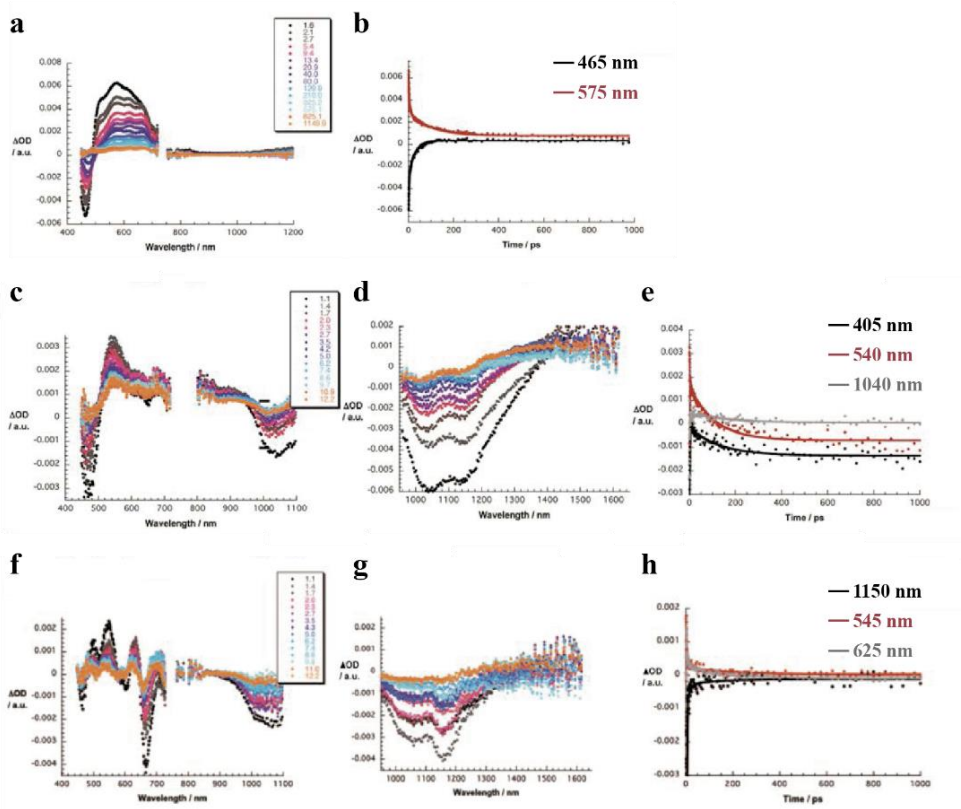

Figure 43. Differential absorption spectra and kinetic profiles. (a) Differential absorption spectra (visible and near-infrared) obtained upon femtosecond pump probe experiments (387 nm) of **12** in D_2O at room temperature with several time delays between 1.6 and 1149.9 ps. (b) Time absorption profiles at 465 and 575 nm monitoring the excited state decay. (c) Same than (a) for **12**/SWCNT with several time delays between 1.1 and 12.2 ps. (d) Differential absorption spectra (extended near-infrared) obtained upon femtosecond pump probe experiments (387 nm) of **12**/SWCNT in D_2O at room temperature with several time delays between 1.1 and 12.2 ps. (e) Time absorption profiles at 475, 540, and 1040 nm monitoring the electron transfer. (f) Same than (a) for **13**/SWCNT with several time delays between 1.1 and 12.2 ps. (g) Same than (d) for **13**/SWCNT with several time delays between 1.1 and 12.2 ps. with several time delays between 1.1 and 12.2 ps. (h) Time absorption profiles at 545, 625 and 1150 nm monitoring the electron transfer.

Turning to AFM assays, the images could be described as homogenous distributions of nanofiber/SWCNT nanohybrids in both **12**/SWCNT and **13**/SWCNT. A closer inspection revealed that SWCNTs were uniformly covered with nanofibers of **12** and **13** (Figure 44). Analyses of individual nanohybrids by means of AFM confirmed heights of around 2.5 ± 1.0 nm for **12**/SWCNT and 4.0 ± 1.0 nm for **13**/SWCNT. Taking the average diameter of the rope-like nanofibers into account, these increments in the diameters of the nanohybrids are in accordance with the presence of individual SWCNTs, which were wrapped by nanofibers. In the same line, the height histogram, which features maxima at 2.5 nm and onsets at around 6.0 nm, confirmed the coexistence of mostly individualized **12**/SWCNT and/or **13**/SWCNT with small clusters.

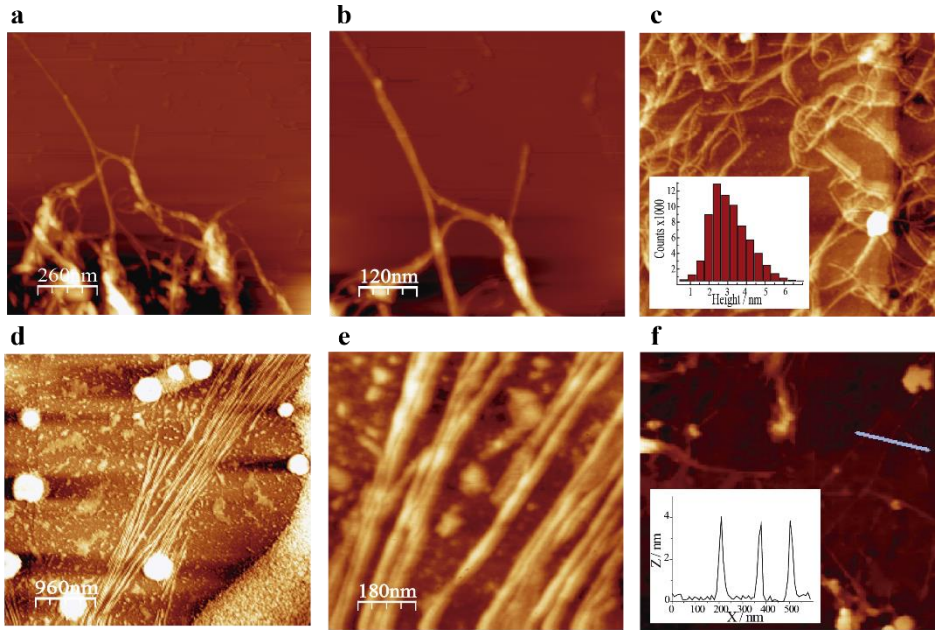

Figure 44. AFM images of 12/SWCNT and 13/SWCNT nanohybrids. (a,b,c) AFM images of **12**/SWCNTs deposited onto highly ordered pyrolytic graphite (HOPG) and height histogram (c, inset). (d,e,f) AFM images of **13**/SWCNT deposited onto HOPG and height distribution (f, inset).

With the use of TEM, the coexistence of individualized SWCNTs and of loosened bundles was further attested (Figure 45a,b). Clearly, the nanohybrids possessed a different organization when compared with random bundles of pristine SWCNTs. In agreement with the AFM images, HRTEM images attested the homogenous coverage of SWCNTs (Figure 45c,d).

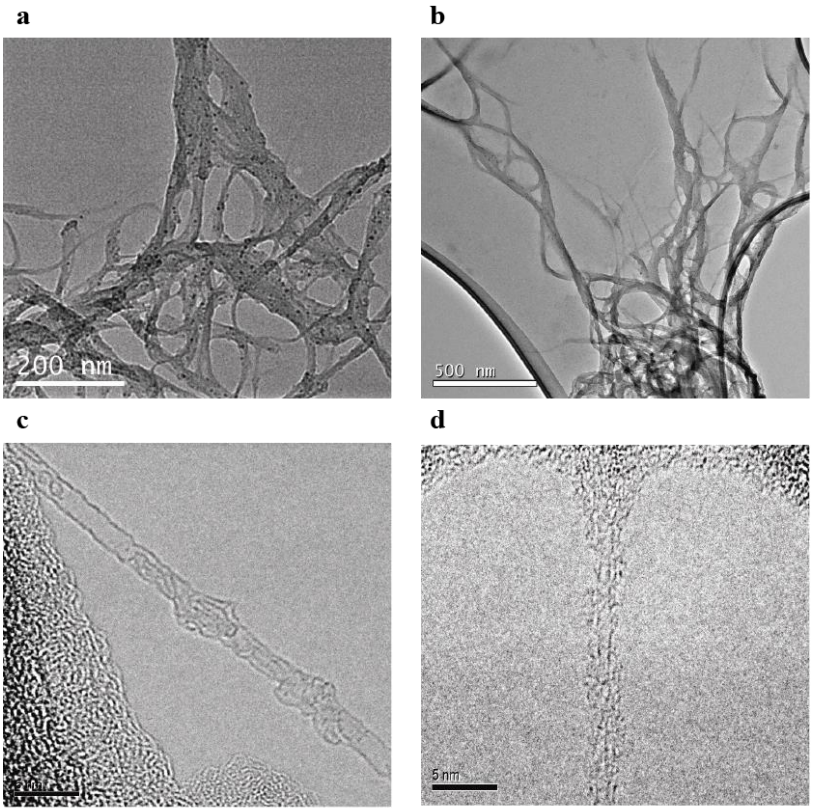

Figure 45. TEM images of 12/SWCNT and 13/SWCNT nanohybrids. (a,b) TEM images of **12**/SWCNT and **13**/SWCNT, respectively (1 x 10^{-4} M) – drop-casted on a LC200-Cu TEM grid. Scale bar 200 and 500 nm, respectively. (c,d) HRTEM images of **12**/SWCNT and **13**/SWCNT, respectively. Scale bar 5 nm in both cases.

1.3.2.4. *Formation of n/p-nanocomposite hydrogels*

In the search for 3D bulk long-range-ordered *n*/*p*-materials prepared by simple experimental procedures, an imperative requisite was to transfer these well-stablished water-soluble nanohybrids to the solid state, avoiding any damage of the architectures during the solvent casting.

In this sense, addition of few drops of a saturated aqueous solution of $CaCl_2$ into the soft basic solution of anionic nanofibers of **12** or **13** (> 5 x 10^{-3} M, 7.5 eq $NaHCO_3$) was seen to induce gel formation by charge screening of anionic carboxylates with calcium dications. SEM inspections of the xerogels, previously treated under supercritical conditions to remove the water, revealed a highly-porous material composed by a network of soft curve fibers (Figure 46).

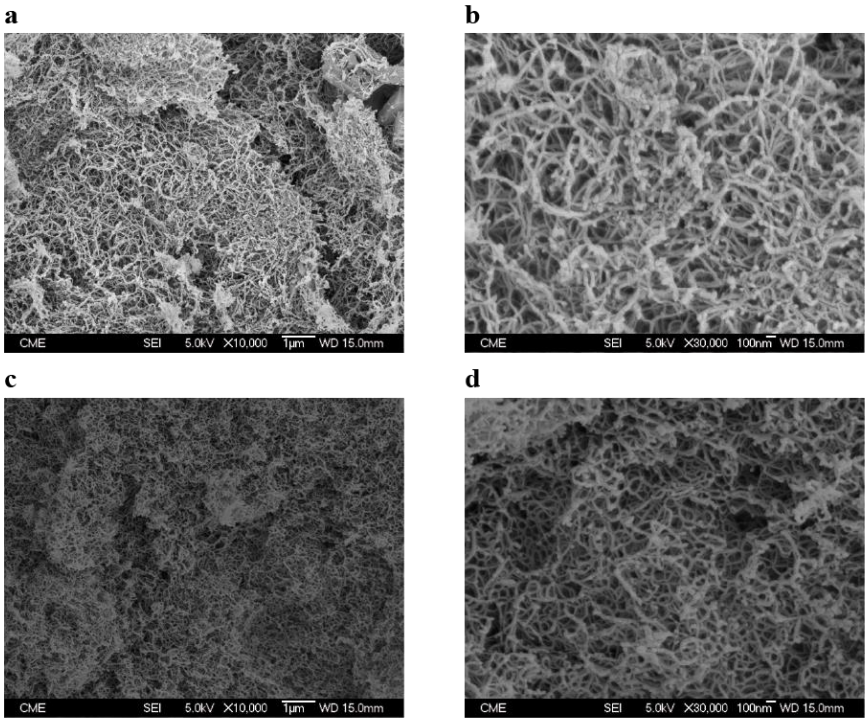

Figure 46. Scanning electron micrographs for the xerogels formed from 12 (a,b) and 13 (c,d), at different magnifications.

Interestingly, when applying this simple protocol on solutions based on exTTF anionic fibers together with SWCNTs, a slightly different scenario was emerged. Stable hydrogels were formed just after the addition of $CaCl_2$, and SEM images revealed the presence of larger and straighter fibers comparing with the corresponding without SWCNTs, with diameters ranging from 30 to 50 nm. In addition, in the particular case of **13**/SWCNTs/$CaCl_2$ the presence of left-handed superhelixes with similar diameters was also clearly observed (Figure 47).

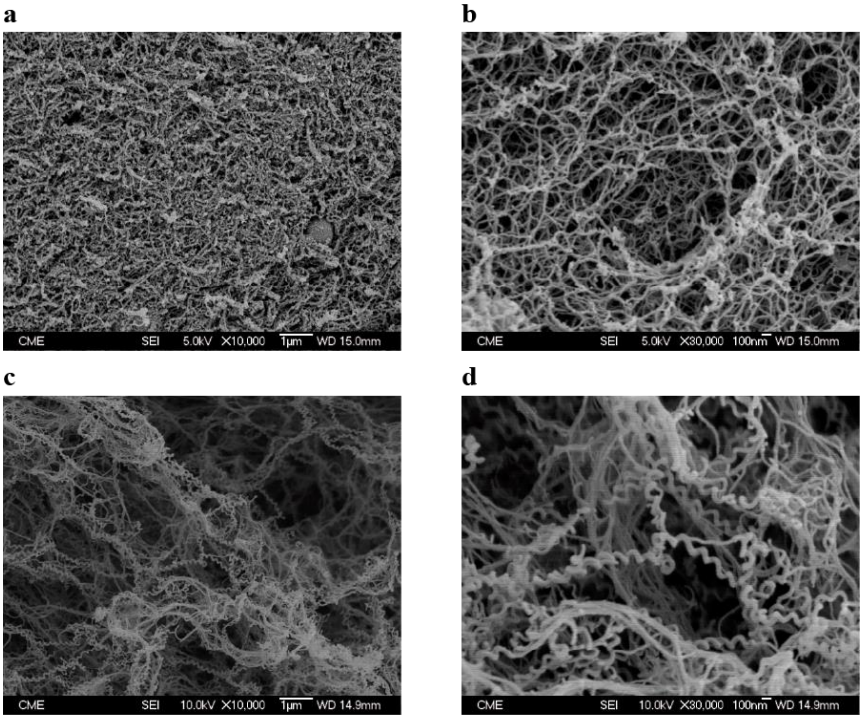

Figure 47. Scanning electron micrographs for the xerogels formed from 12/SWCNTs (a,b) and 13/SWCNTs (c,d), at different magnifications.

In complementary TEM investigations, the presence of SWCNTs and $CaCl_2$ revealed the existence of homogeneous domains with large straight fibres in both cases and the presence of superhelixes in the case of **13**/SWCNT/$CaCl_2$ (Figure 48a,b), a finding that is in agreement with the SEM investigations. Moreover, energy-dispersive X-ray (EDX) analyses confirmed the presence of carbon, sulphur, calcium and chloride (Figure 48c). HRTEM images of such bundles prompted to the fact that they are formed by few SWCNTs, which were surrounded by organic materials (Figure 48d,e). It is worth mentioning that SWCNTs were placed here parallel to the axial axis of the fiber bundles, which

supports the templating role of SWCNTs in the overall construction of such fibers. These observations support the notion that SWCNTs, placed within the organic matrix, induced morphology in the bulk material that was substantially different from that of its individual components. In addition, it was corroborated by this technique the absence of randomly SWCNT bundles sticking out of the organic matrix. We consider this fact a strong evidence for an efficient interfacing between exTTFs and SWCNTs.

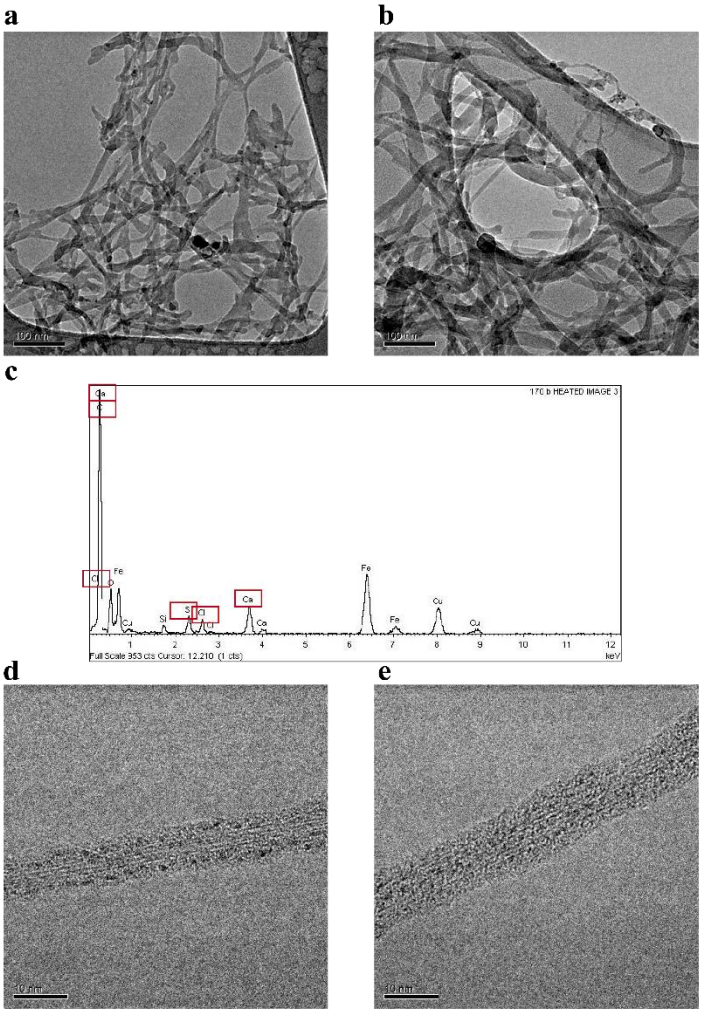

Figure 48. TEM images and EDX analysis of exTTF/SWCNTs xerogels. (a,b) TEM images of **12**/SWCNTs/$CaCl_2$ and **13**/SWCNTs/$CaCl_2$ xerogels, respectively.Scale bars: 100 nm (c) EDX analysis of **12**/SWCNTs/$CaCl_2$ sample. (d,e) HRTEM images of **12**/SWCNTs/$CaCl_2$ and **13**/SWCNTs/$CaCl_2$ xerogels, respectively. Scale bars: 10 nm.

To determine whether the changes of the bulk material morphology observed in the presence of SWCNTs involved a sudden change of its internal structure, we carried out complementary SAXS and XRD experiments. SAXS experiments with both hydrogels obtained without using SWCNTs as additive did not give rise to any intense peak in the diffractograms, inferring the low long-range order in the bulk material (Figure 49a,b).

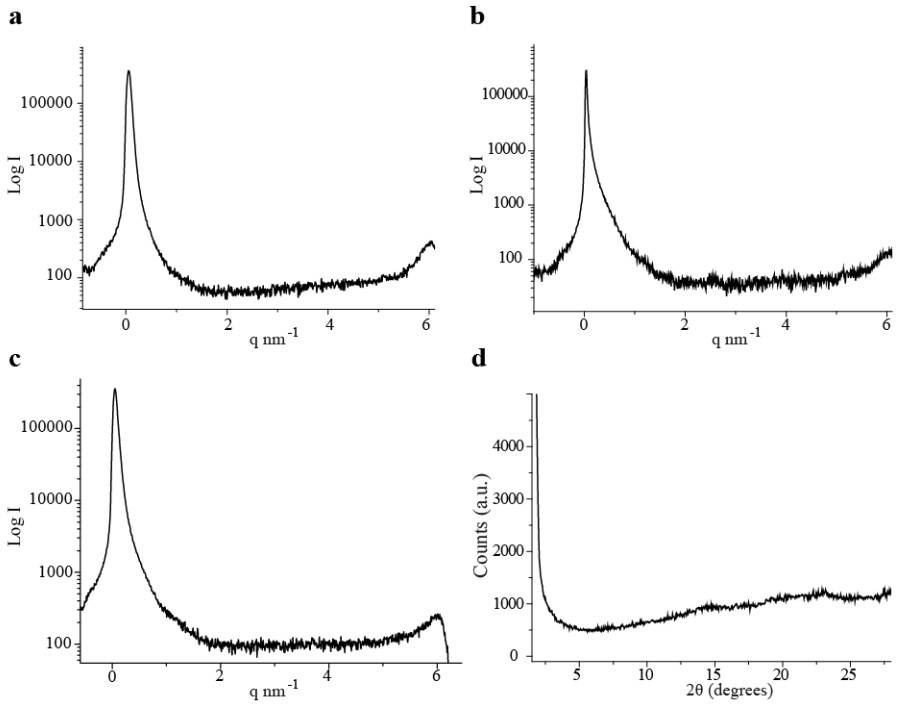

Figure 49. SAXS and powder X-Ray diffractograms. SAXS diffractogram for (a) **12**/$CaCl_2$ hydrogel, (b) **13**/$CaCl_2$ hydrogel and (c) **12**/SWCNT/$CaCl_2$ hydrogel. (d) Powder X-Ray diffractogram for **12**/SWCNT/$CaCl_2$ hydrogel.

Turning to **12**/SWCNT/$CaCl_2$ hydrogel, a similar SAXS diffractogram without any discernable peak or broad shoulder was found (Figure 49c). These experimental findings correlated with the shorter peptide chain, which resulted in a lower stability of the exTTF supramolecular structures when wrapping around the surface of SWCNTs, and, which prevents the induced order in the bulk material. As it was previously shown, this behavior was in agreement with the inversion and loss of ellipticity observed for **12** in the presence of SWCNTs by means of CD assays. Moreover, the reflection peaks corresponding to the β-sheet secondary structure were also lost in this nanocomposite (Figure 49d).

In sharp contrast, in SAXS experiments with **13**/SWCNT/$CaCl_2$ hydrogel, up to four peaks corresponding to lamellar packing with a periodical *d*-spacing of 4.56 nm were discernable (Figure 50a). The latter indicates the presence of long-range order in the bulk material. Such a long-range order is new and inherent for the formed bulk material and it was not observed in any of the individual components. The HRTEM images previously exposed relating to the bulk material from **13** in the presence of SWCNTs did not show any clear evidence of such crystalline packing between adjacent SWCNTs. Therefore, the origin of the lamellar packing observed in SAXS experiments with **13**/SWCNT/$CaCl_2$ must stem from other types of supramolecular order. As a matter of fact, we postulate that the lamellar packing relates to the organization of **13**-based fibers around SWCNTs (Figure 50b,d). Furthermore, the typical *β*-sheet reflections in XRD experiments with the bulk material in the presence of SWCNTs demonstrated that the internal exTTF order is not disrupted by the presence of CNTs (Figure 50c).

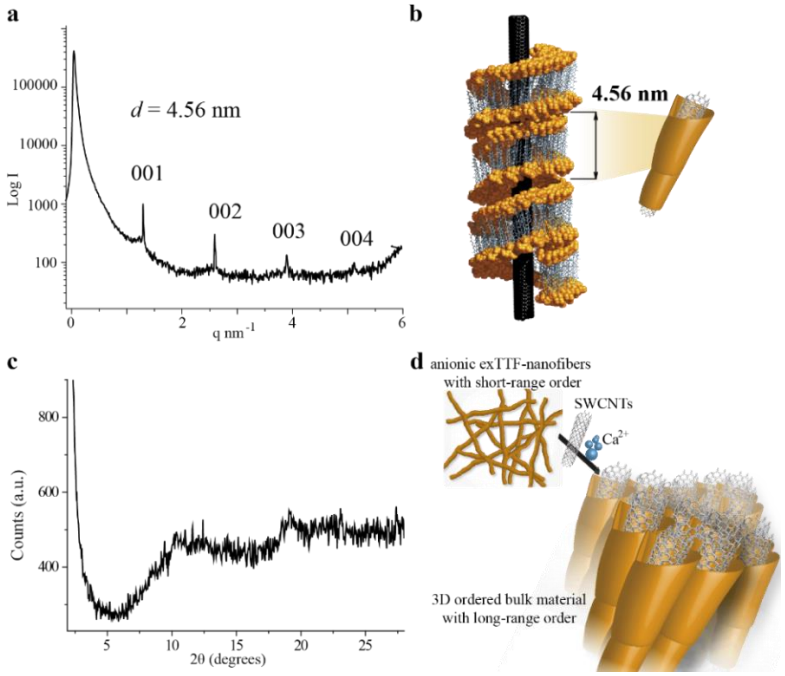

Figure 50. X-ray characterization and schematic illustration of 13/SWCNT/$CaCl_2$ *p*/*n*-nanocomposite hydrogel. (a) SAXS pattern of the hydrogel. (b) Schematic illustration depicting the lamellar packing of **13** around a SWCNT. (c) Powder X-Ray diffractogram of the hydrogel. (d) Cartoon showing CNTs as additives for controlling the crystalline ordering in the bulk *p*/*n*-material.

1.3.3. Highly Ordered *n*/*p*-co-assembled materials with remarkable charge mobilities[56]

In the previous section, exTTF derivative **13**, with the pentapeptide sequence and the carboxylic acid in the termini position, has been validated as a good candidate to produce ordered and stable *p*-type nanofibers through π-π stacking and *β*-sheet-type hydrogen bonding. Carboxylic acid not only guaranteed water solubility of the aggregates, but also provided negative charges on the surface of fibers, which further enabled an external control by charge screening.

Considering the above points, we propose to control the formation of long-range ordered materials with positively charged organic molecules instead of the formerly used inorganic salt $CaCl_2$, without forgetting the initial goal to generate donor/acceptor systems.

Thus, two electron-accepting perilenebisimide (PBI) building blocks with cationic groups are initially designed and synthetized (compounds **20** and **21** in Scheme 9). Then, their ability to self-assemble in water-soluble *n*-type nanofibers are tested. Finally, the aforementioned *p*-type exTTF nanofibers and these new *n*-type PBI architectures are mixed, studying the structural, morphological and spectroscopic features of the produced *n*/*p*-co-assembled material.

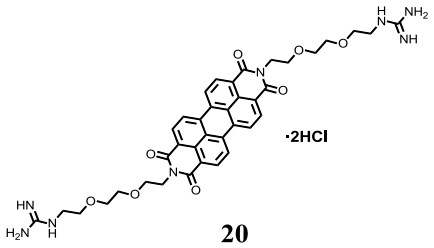

20

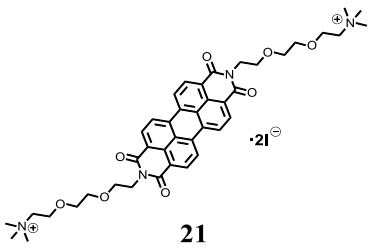

21

Scheme 9. Molecular structures of the target PBI-based molecules 20 and 21.

56 J. López-Andarias, M. J. Rodriguez, C. Atienza, J. L. López, T. Mikie, S. Casado, S. Seki, J. L. Carrascosa and N. Martín, *J. Am. Chem. Soc.* **2015**, *137*, 893-897.

1.3.3.1. Synthesis of perilenebisimide-based derivatives **20** and **21**

We have designed two different complementary acceptor moieties of perilenebisimide which are symmetrically functionalized with polar tails to ensure the solubility in aqueous medium. Furthermore, guanidinium or quaternary ammonium groups (**20** and **21**, respectively) present in the terminal positions of PBI were acting as counterions for the carboxylic acids in the complementary exTTF´s arrays of **13**.

A simple and efficient synthetic route was followed for the achievement of the electron acceptor building blocks **20** and **21**. The synthesis started with molecule **22**, which was prepared from commercially available perylene-3,4,9,10-tetracarboxylic dianhydride and *tert*-butyl 2-[2-(2-aminoethoxy)ethoxy]ethylcarbamate in good yield. Further deprotection of the two *tert*-butyl groups in acidic conditions produced diamine **23** (Scheme 10) which was used as intermediate of both target compounds.

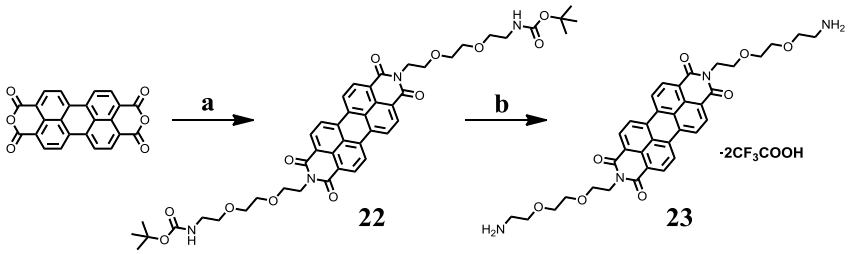

Scheme 10. Synthetic route for intermediate 23. (a) $Zn(OAc)_2$, imidazole, 150 ºC, 80%; b) TFA, $CHCl_3$, rt, 95%.

For the synthesis of derivative **20**, it was necessary to transform primary amines in **23** into guanidine functional groups. In this regard, coupling reaction in basic conditions using 1,3-bis(*tert*-butoxycarbonyl)-2-methyl-2-thiopseudourea as reagent and $HgCl_2$ as catalyst yielded **24**. This molecule was found to be highly soluble in chloroform but, after deprotection of the four *tert*-butyl groups attached in this molecule, the solubility in common organic solvents turned to be null while successfully high in water, empowering the possibility to probe this electron acceptor derivative **20** in our approach. Meanwhile, tetraalkylammonium derivative **21** was obtained from **23** in one step by treatment with the strong electrophile iodomethane, resulting in a compound equally soluble in aqueous solution (Scheme 11).

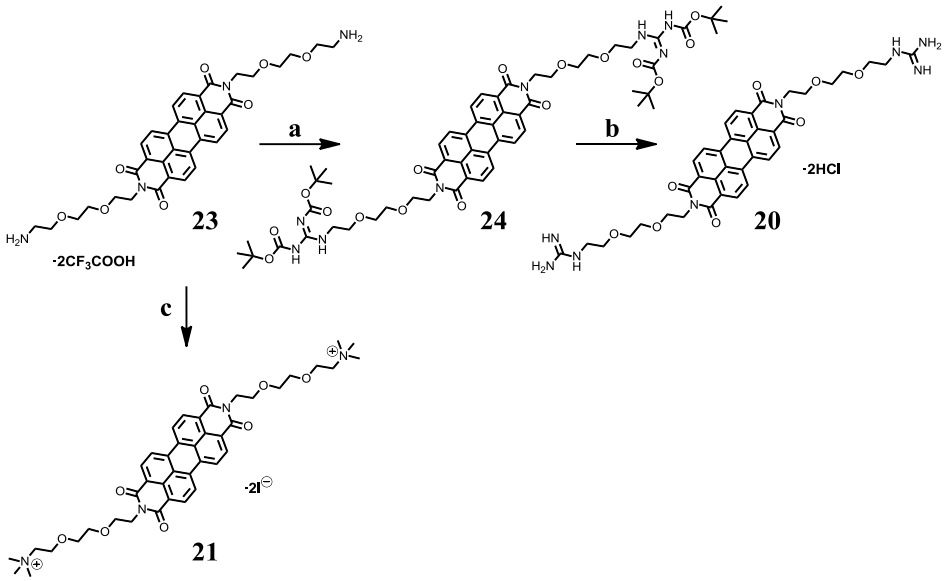

Scheme 11. Synthetic route for final compounds 20 and 21. (a) 1,3-Bis(*tert*-butoxycarbonyl)-2-methyl-2-thiopseudourea, TEA, $HgCl_2$, DMF, rt, 37%; (b) HCl (aq), CH_3OH, rt, quant; (c) CH_3I, K_2CO_3, CH_2Cl_2/CH_3OH, rt, 62%.

1.3.3.2. Self-organization of PBI compounds in water

Initially, the ability of the PBI derivatives (**20** and **21**) to form self-assembled architectures was examined by UV-*vis* spectroscopy and microscopic techniques. The absorption spectra of **20** and **21** in methanol showed a well-resolved vibronic structure ranging from 400 to 500 nm which is characteristic for the S_0-S_1 transition of isolated PBI chromophore (Figure 51, orange lines). However, the absorption spectra of **20** and **21** in distilled water at different concentrations (10^{-5} – 10^{-3} M) showed a broad spectrum with decrease in the peak intensity and significant blue-shift in the absorption maximum (from 520 to 500 nm) with appearance of a shoulder peak at 542 nm (Figure 51, purple lines). These features suggested the formation of face-to-face π-stacks (H-aggregate) of PBI chromophores.[36,39b]

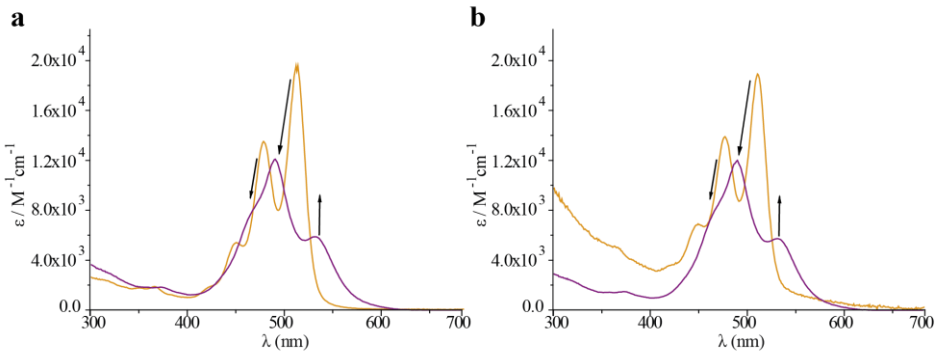

Figure 51. Absorption spectra of 20 (a) and 21 (b) in methanol (orange) and water (purple). Arrows show changes in the absorption maxima.

The morphology of these PBI aggregates (**20** and **21**) dried from aqueous solution was also studied using atomic force microscopy (AFM) and the images obtained are shown in Figure 52. The formation of fiber-like supramolecular structures were observed for **20** and **21** with a height around 3.0 nm in both cases.

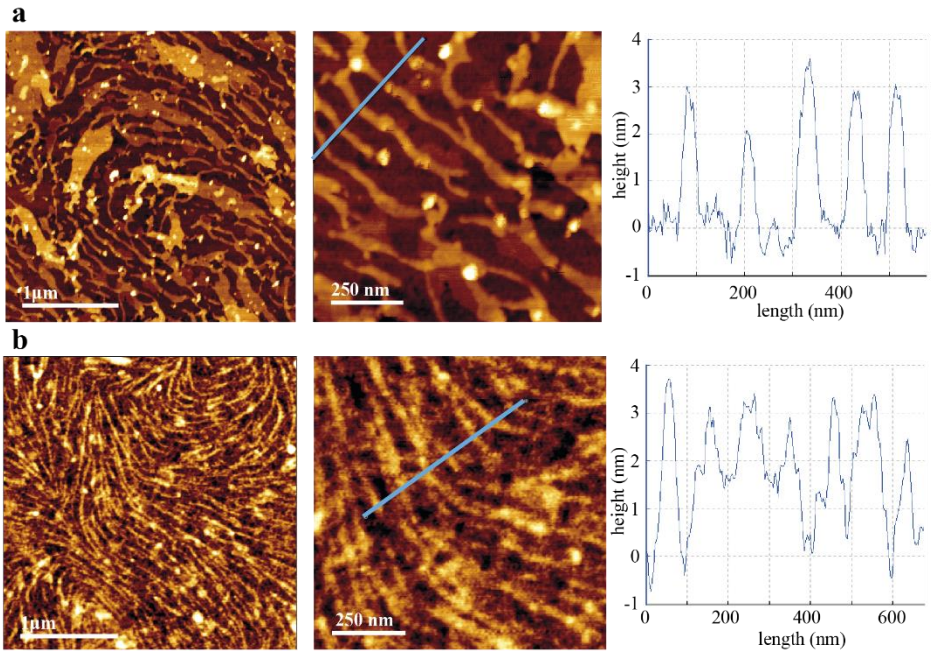

Figure 52. AFM images and height profiles of 20 (a) and 21 (b) deposited onto a cover slide, from aqueous solution (MilliQ water, 5 x 10^{-5} M).

1.3.3.3. Spectroscopic characterization of the n/p-material.

After studying the self-assembly properties of these three small molecules separately, we prepared the hybrid materials by combining *p*-type exTTF fibers (**13**) and *n*-type PBI fibers (**20** and **21**) by utilizing the electrostatic interaction between negative carboxylate groups in **13** and positive guanidinium or quaternary ammonium groups in **20** or **21**, respectively, in aqueous solution.

When equal volumes of dilute aqueous solutions of **13** (1×10^{-4} M, 10 eq of $NaHCO_3$) and **20**/**21** (1×10^{-4} M) were mixed, we observed an immediate formation of red precipitate in solution. The precipitates based on **13** and **20** or **13** and **21** were separated from the starting materials by repeated centrifugation and redispersion in distilled water. The purified homogeneous dispersions of **13** and **20** and **13** and **21** in water were characterized by UV-*vis* absorption spectroscopy (Figure 53a,b).

The UV-*vis* spectra obtained for the dispersions were essentially a combination of those acquired for **13** and **20**/**21** individually in aqueous solution, indicating that the electronic properties of individually aggregated chromophores (exTTF and PBI) were not perturbed in the co-assembled state. Moreover, the intensity in the observed absorption spectra of both co-assembled materials resembled the simulated spectra for the combination of 2:1 equivalents of **13** and **20**/**21**, respectively, which indicates the quantitative electrostatic interactions and formations of co-assembled $\mathbf{13_2}$**20** and $\mathbf{13_2}$**21**. Moreover, only by addition of polar protic organic solvents such as methanol, the original absorption bands for isolated molecules of **13** and **20**/**21** were recovered, disrupting every possible non-covalent interactions in the *n*/*p*-nanostructure. This fact, in turn, attests the reversibility of the process (Figure 53c,d).

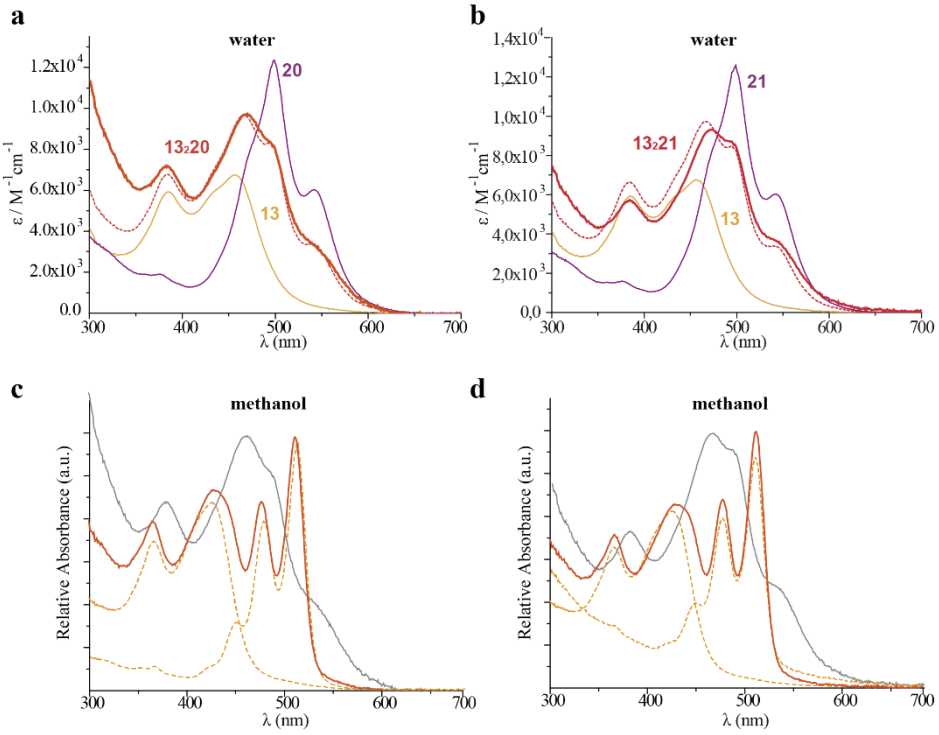

Figure 53. UV-*vis* studies. (a,b) Absorption spectra for aqueous solutions of **13** (yellow), **20** (a) or **21** (b) (purple) and for the dispersion obtained by mixing both solutions (solid orange). Dashed orange line represents the simulated spectra for mixture with a stoichiometry of **13**$_2$**20** (a) or **13**$_2$**21** (b). (c,d) Absorption spectra of co-assembled **13**$_2$**20** (c) and **13**$_2$**21** (d) before addition of a protic polar solvent (grey line), and after the addition (orange line) to probe the reversibility of the supramolecular interactions. Dash orange lines correspond to molecules **13**, **20** (c) and **21** (d) in methanol.

The *n*/*p*-co-assembly of **13** with **20** or **21** through electrostatic interactions were also monitored by circular dichroism (CD) spectroscopy. The evolution of the dichroic signal from **13** to **13**$_2$**20** and **13**$_2$**21** is shown in Figure 54a. Initially, as it has been described in the previous work,[49] a soft basic aqueous solution of compound **13**, where the *p*-type exTTF nanofiber were formed, exhibited a strong bisignate signal with a positive Cotton effect at 480 nm, a negative Cotton effect at 431 nm, and a zero crossing point at 456 nm due to the chiral organization of exTTF units. When the dichroic spectra of a clean dispersion of **13**$_2$**20** and **13**$_2$**21** is monitored, it is remarkable that the negative Cotton effect of exTTF at 431 nm is maintained, and two new negative Cotton

signals were appeared at 542 and 500 nm, which are matching with the absorption bands of **20** and **21**, being more evident in the case of **13**$_2$**21**. These observations indicate the existence of chiral PBIs aggregates in the *n*/*p*-co-assembly which is induced by the exTTF´s arrays. The positive peak at 480 nm was significantly reduced since it has been presumably neutralized by the intensity of new negative dichroic signals. It is worth to mention that intensity before and after addition of **20** and **21** was not comparable due to the scattering in the dispersion of the *n*/*p*-co-assembly. Moreover, the characteristic *β*-sheet finger-print for *p*-type nanofibers of **13** (between 220-260 nm) was preserved in the *n*/*p*-nanostructure (Figure 54b). All these experimental findings demonstrated the maintenance of the chirality and the order in the co-assembled systems.

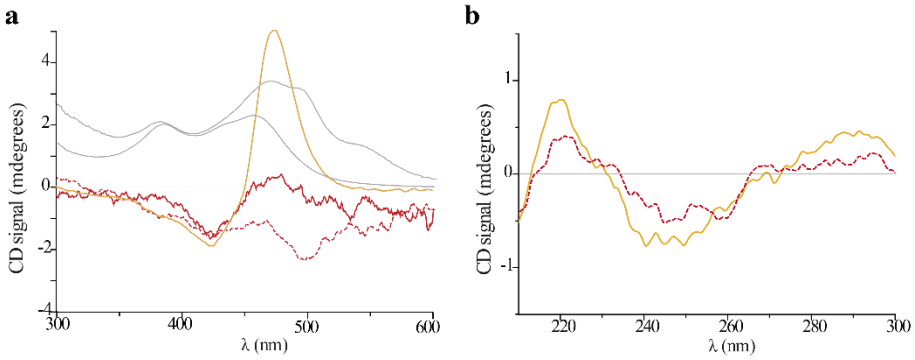

Figure 54. CD experiments. Circular dichroic spectra of **13** (yellow), **13**$_2$**20** (solid red), and **13**$_2$**21** (dashed red) in the exTTF and PBI absorption region (a) and the peptide absorption region (b).

The efficient electrostatic interactions between the carboxylate and guanidinium or quaternized amine were confirmed by X-ray photoelectron spectroscopy (XPS). In XPS measurement, no detectable signals of Na-1s as counter cation of **13**-based nanofibers and Cl-2p and I-3d as counter anions of **20**- and **21**-based nanofibers were observed in the 1072 eV, 198 eV and 620 eV regions, respectively, which indicates that interactions occur between carboxylate and guanidinium or quaternized amine (Figure 55).

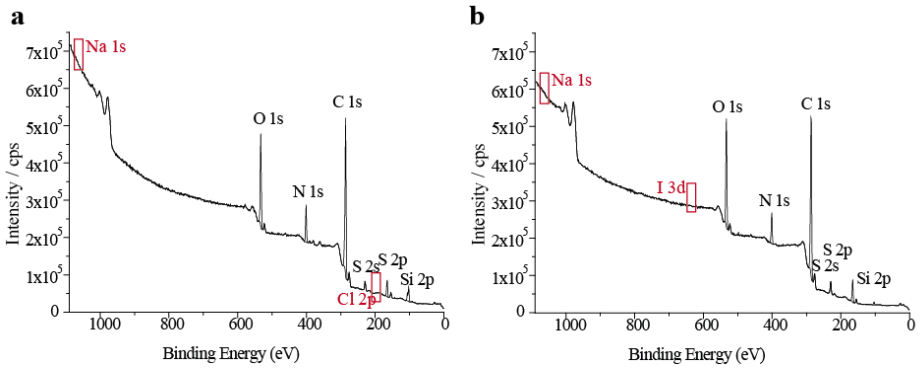

Figure 55. XPS survey spectra of a solid sample of $13_2$20 (a) and $13_2$21 (b).

In order to confirm the molecular composition of the materials in **$13_2$20** and **$13_2$21**, the corresponding thin films were investigated by XPS (Figure 56), which ascertained the quantitative coupling between oppositely charged building blocks at the molecular level. As it has already been reported in other cases, through a Gaussian deconvolution of the N-1s signal obtained by XPS, it is possible to determine the populations of electronically distinct N atoms.[24b] For example, in the case of the solid obtained by mixing **13** and **21**, deconvolution of the total N-1s signal intensity revealed the presence of 15% of the oscillator strength derives from the quaternized amine at 403 eV and 85 % from the tertiary amines at 400 eV, which were attributed to a 2:1 stoichiometry for the *n*/*p*-co-assembled nanostructure (**$13_2$21**).

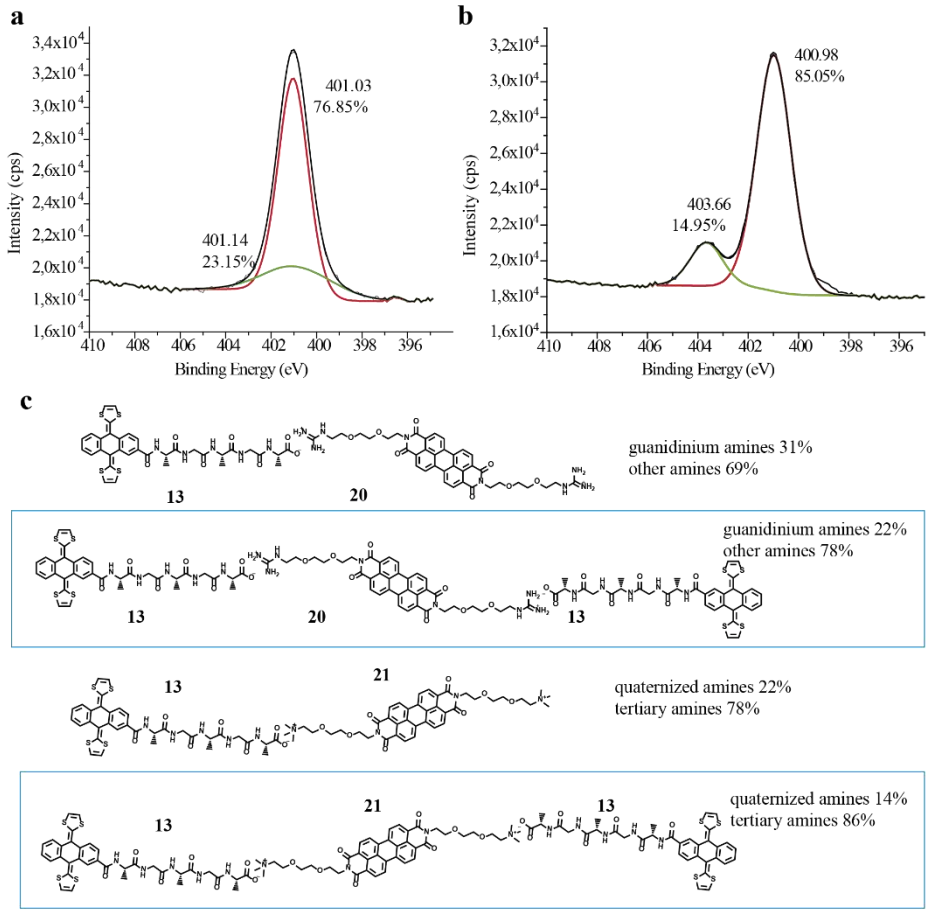

Figure 56. Gaussian deconvolution of the N-1s signal in XPS survey spectra. (a) High-resolution XPS survey spectra of the N-1s region of a solid sample of **13$_2$20**. (b) The same for **13$_2$21**. (c) Gaussian deconvolution of the N-1s signal determines the populations of electronically distinct N atoms. This deconvolution demonstrates the quantitative ionic interactions between exTTFs and PBIs at the molecular level, that is, two molecules of exTTF (one carboxylate group each) per one molecule of PBI (two guanidinium or ammonium groups each). This experimental data is more obvious in the case of **13$_2$21**, where the difference between the binding energy of the cationic amines and the rest of amines is bigger, resulting in a more accurate deconvolution of the N-1s signal.

1.3.3.4. Microscopy and X-Ray Diffraction studies

The most interesting features of these *n*/*p*-materials were obtained from scanning and transmission electron microscopies (SEM, TEM), and also by small angle X-ray scattering (SAXS) measurements. Stupp and coworkers thoroughly investigated the co-assembly of small molecules and polymers such as peptide amphiphiles and polysaccharide hyaluronic acids. They reported the formation of ordered sacs and membranes by co-assembly of these molecules.[18]

In line with those studies, using the same methodology, we propose the formation of electroactive closed sacs by co-assembly of two self-assembled small molecules (**13** and **20**/**21**). These supramolecular ensembles can be easily prepared by injecting small amount of concentrated aqueous solution (5×10^{-3} M) of one chromophore into equally concentrated bulk solution of other (Figure 57a). Although these sacs are formed instantaneously, they were allowed to grow further within the solution for several days before investigating the morphology and achieve the maximum organization.

SEM of dried sacs revealed the presence of regions with seemingly perfect parallel alignment of fibers, together with randomly distributed fiber areas. In both cases, homogeneous fibers with diameters ranging from 10 to 20 nm were observed. The length of the fibers was found to be several tens of micrometers (Figure 57b,c). Moreover, it was possible to observe a dense packing of the fibers longitudinal to its long axis, with a thickness of around 30 μm. To the best of our knowledge, this is the first example where the ionic co-assembly of two oppositely charged self-assembled molecular aggregates leads to the formation of *n*/*p*-type functional material with this level of organization. Moreover, it is important to remark that our approach leads to fibers alignment through the long-axis, which should impact on the charge transport properties of the *n*/*p*-materials, as it has recently been reported by Ajayaghosh and col.[57]

57 K. Sakakibara, P. Chithra, B. Das, T. Mori, M. Akada, J. Labuta, T. Tsuruoka, S. Maji, S. Furumi, L. K. Shrestha, J. P. Hill, S. Acharya, K. Ariga and A. Ajayaghosh, *J. Am. Chem. Soc.* **2014**, *136*, 8548-8551.

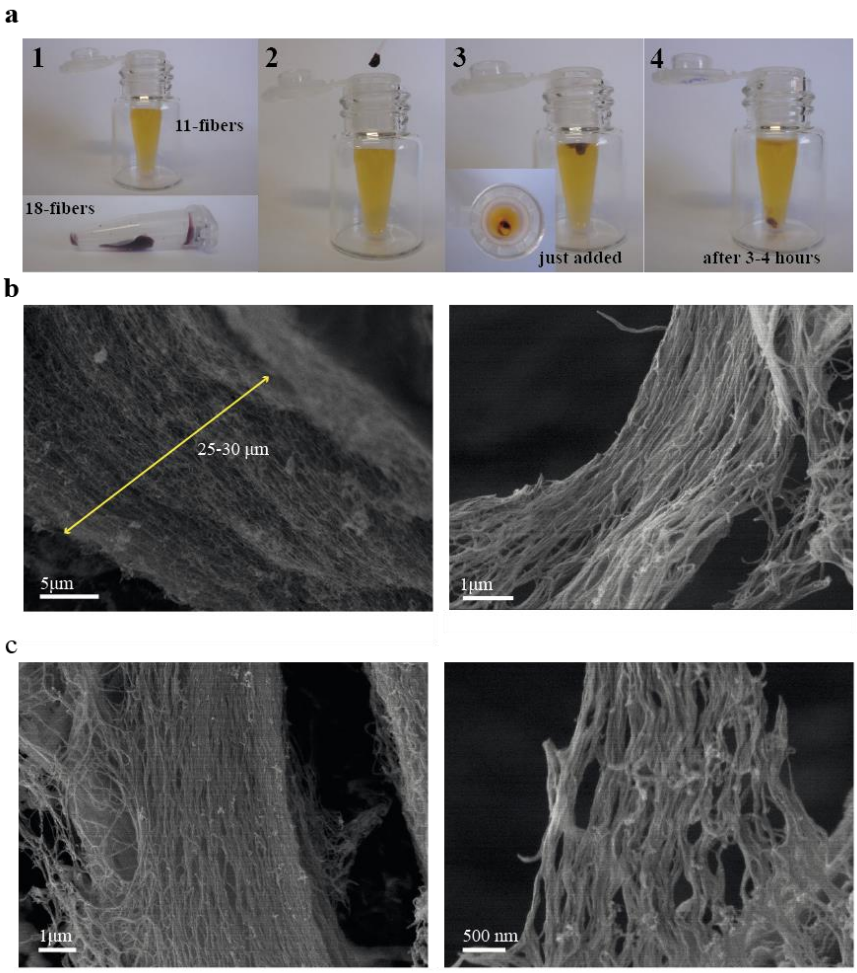

Figure 57. Preparation and SEM characterization of *n*/*p*-co-assembled materials. (a) Procedure for the preparation of closed sacs for SEM imaging of aligned fibers in the liquid-liquid interface between both self-assembled molecules. In this example, one drop of **20** is added into the bulk of a solution of **13**. This methodology can also be carried out for **21**, and in the opposite sense as well. (b,c) SEM micrographs of the fiber-composed membrane at different magnifications for $\mathbf{13_2 20}$ (b) and $\mathbf{13_2 21}$ (c).

We further investigated the surface morphology of the *n*/*p*-co-assembled materials by AFM. The AFM images revealed the presence of fibers with a height in the range of 8 to 14 nm, measured on the most individualized ones (Figure 58), which are in accordance with the diameter observed in SEM images.

These results confirm the dramatic increase in overall width of the *n*/*p*-co-assembled materials when compared with the individually self-assembled *p*-type exTTF or *n*-type PBI fibers.

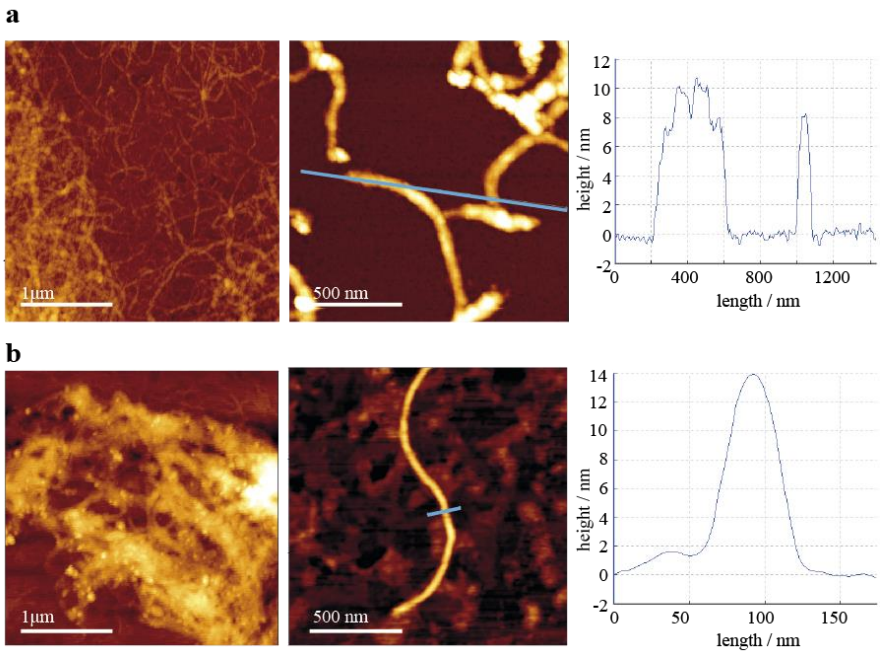

Figure 58. AFM studies of the n/p-co-assembled materials. (Left and center) AFM images at different length scales of randomly distributed fibers of **13$_2$20** (a) and **13$_2$21** (b) *n*/*p*-co-assembled nanostructures. (Right) Height profile across the blue line.

The internal structure of these self-assembled materials was elucidated by TEM by drop-casting a clear dispersion of **13$_2$20** or **13$_2$21**. Regularly alternating domains arranged longitudinal to the long axes of the fibers were found, as shown in Figure 59 (dark regions in the micrograph indicate positive staining of carboxylates by uranyl acetate), with a domain width of around 4.5 ± 0.6 nm (Figure 59e).

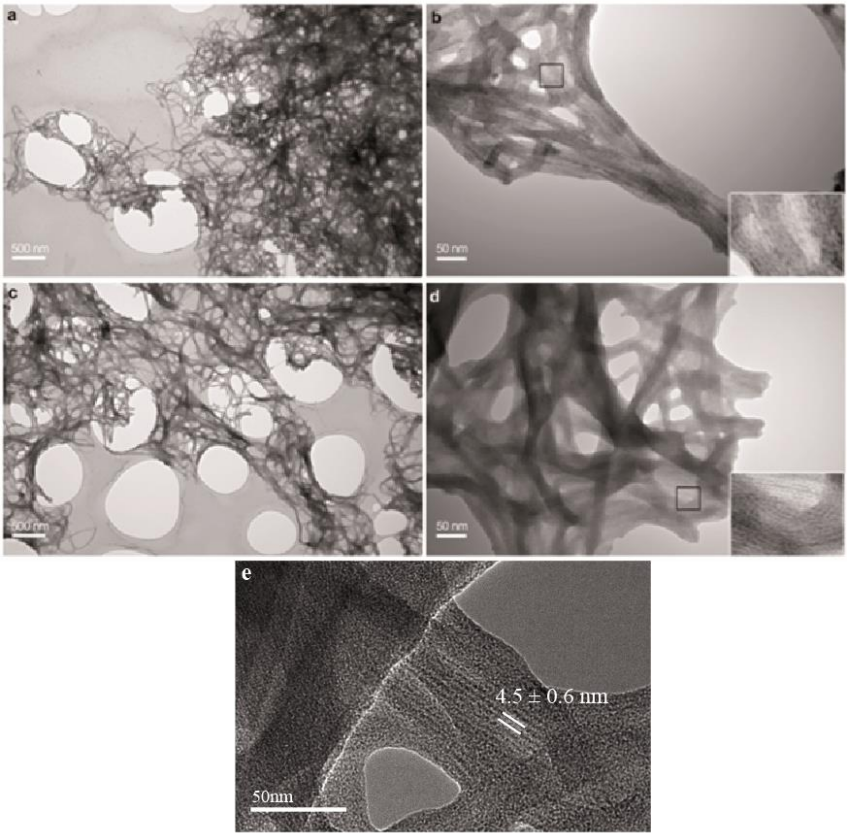

Figure 59. TEM images at different length scales of the fiber-like structures. (a,b) Fibers of **$13_2$20** at different length scales. (c,d) Fibers of **$13_2$21** at different length scales. (e) Amplification of the fibers obtained from **$13_2$20**, showing the domain width.

Interestingly, we found that not only sacs with ordered membranes but also macroscopically aligned bundled filaments can be prepared by manual drawing of one solution into the other using a pipette (Figure 60i). When these filaments are taken out of the solution and deposited on a surface, birefringence was observed along the length of the strand using a polarized optical microscope (Figure 60a-f). This observation also proved the control in the macroscopic alignment of these hybrid materials extending over centimeters. Furthermore, this fact was confirmed by fluorescence confocal microscopy where fluorescence coming from PBI moieties presents an unambiguous orientation along the string axis (Figure 60g,h).

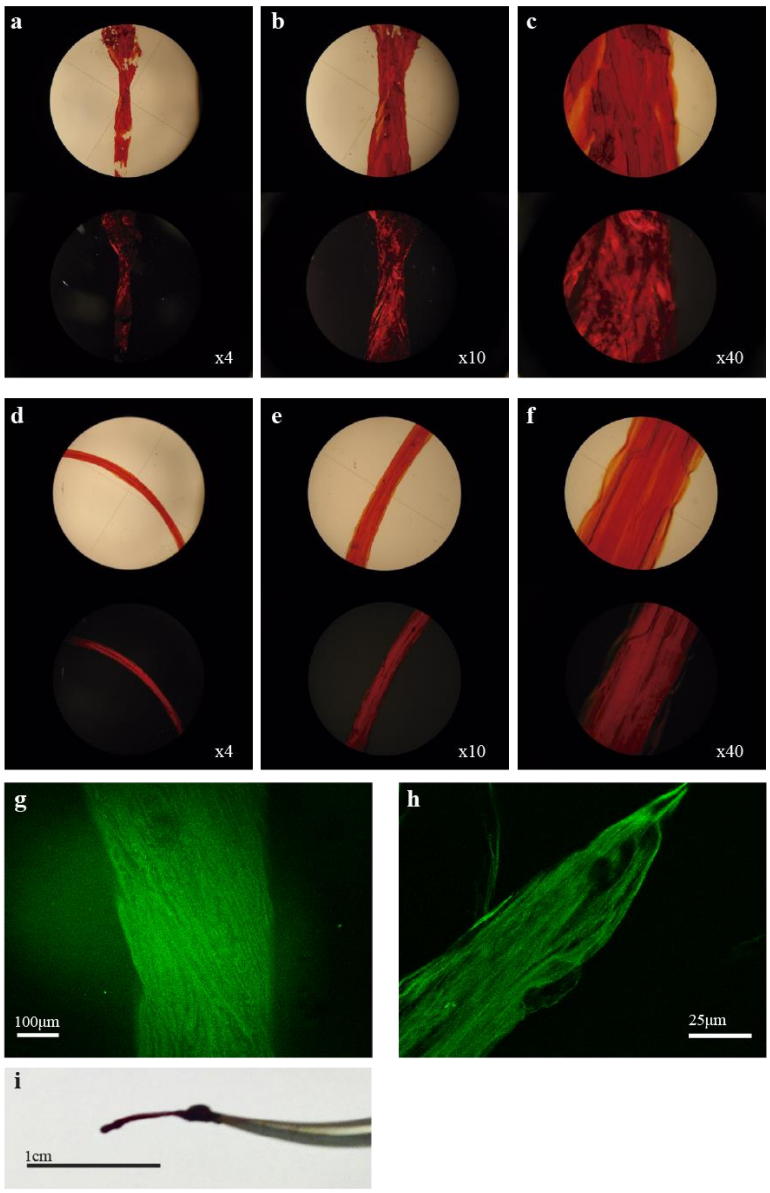

Figure 60. Images of the macroscopically aligned materials, acquired by different techniques. (a-f) Photographs from an optical microscope of macroscopically aligned bundled filaments of **$13_2$20** (a-c) and **$13_2$21** (d-f), at different amplifications, using non-polarized (top) and polarized light (bottom). (g-h) Fluorescence confocal micrograph of the filament obtained from **$13_2$20** (g) and **$13_2$21** (h). (i) Photograph of the just-formed filament.

To verify the extent of supramolecular order in the *n*/*p*-co-assembled material, we carried out the SAXS studies of aligned bundled filaments. The SAXS analysis for **$13_2$20** and **$13_2$21** showed two peaks with *d*-spacing of 9.3 and 5.8 nm, which were attributed to the (10) and (01) reflections of a rectangular packing, corroborating the presence of long-range order in the hybrid materials (Figure 61a). Moreover, X-ray powder diffraction (XRD) experiments supported the existence of well-defined *β*-sheets showing a set of two broad peaks with 2θ = 9.7º and 19.3º (*d*-spacing= 9.1 and 4.6 Å, respectively) (Figure 61b). The molecular model supports the periodicity in the internal organization which was observed in TEM images with a width of around 3.9 - 5.1 nm (Figure 59e). A schematic representation the co-assembly is depicted in Figure 61c.

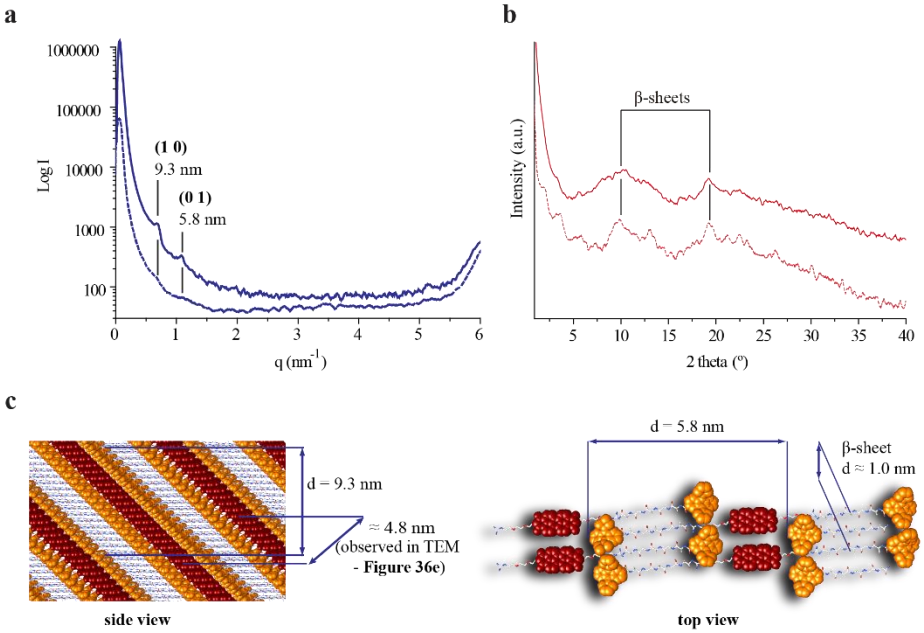

Figure 61. X-ray studies and proposed model. (a) SAXS pattern for the co-assembled filament of **$13_2$20** (solid blue) and **$13_2$21** (dashed blue). (b) XRD patterns of *n*/*p*-co-assembled **$13_2$20** (solid red) and **$13_2$21** (dashed red). (c) Schematic representation of the organization punctuating the repetition distance. Yellow- and red-colored parts represent the exTTF and PBI units, respectively.

1.3.3.5. Charge mobility measurements

Based on the confined stacking structure of PBI and exTTF motifs with interplanar distances of ~3.5 Å,[34,58] presumed value of electron and hole mobilities along the stacking axes were examined by Flash-Photolysis time-resolved microwave conductivity measurements.[59] Upon photoexcitation with a 355 nm laser pulse at room temperature, films of these composites on quartz substrates displayed fairly clear photo-conductivity transients ($\phi\Sigma\mu$), where ϕ and $\Sigma\mu$ denotes the quantum yield of charge-carrier generation and the sum of the charge-carrier mobilities, respectively. In contrast to the pristine solid films of **13**, **20** and **21** (Figure 62a), the co-assembled materials **13$_2$20** and **13$_2$21** showed an effective photocharge carrier generation with long lifetimes (> 3 μs), which suggest that the exciton formed at the *p*/*n*-heterojunction were charge separated and freely transferred along the π-stack of **13** and **20**/ **21** (Figure 62b,c).

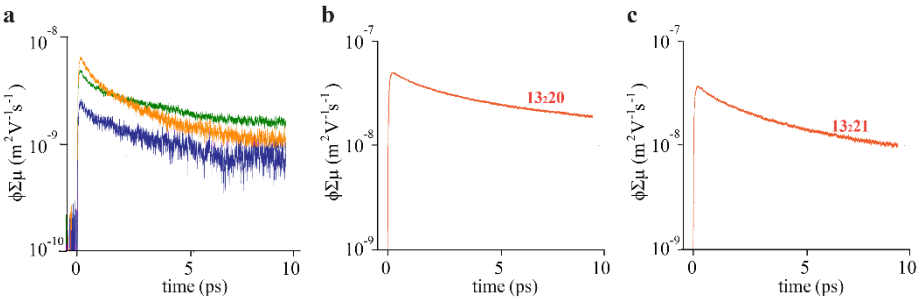

Figure 62. Photoconductivity transients. (a) Photo-conductivity transients observed for **13** (orange), **20** (green) and **21** (blue), respectively. (b) Conductivity transients observed for **13$_2$20**. (c) Conductivity transients observed for **13$_2$21.** The excitations were carried out at 355 nm, 9.1 x 10^{15} photons/cm^2.

58 a) V. Percec, H.-J. Sun, P. Leowanawat, M. Peterca, R. Graf, H. W. Spiess, X. Zeng, G. Ungar and P. A. Heiney, *J. Am. Chem. Soc.* **2013**, *135*, 4129-4148; b) Z. Chen, U. Baumeister, C. Tschierske and F. Würthner, *Chem. Eur. J.* **2007**, *13*, 450-465.
59 A. Saeki, S. Seki, Y. Koizumi and S. Tagawa, *J. Photochem. Photobiol. A* **2007**, *186*, 158-165.

The maximum values of the transients $(\phi\Sigma\mu)_{max}$ for **$13_2$20** and **$13_2$21** were recorded as 5.1 x 10^{-4} $cm^2V^{-1}s^{-1}$ and 1.2 x 10^{-4} $cm^2V^{-1}s^{-1}$ respectively, which were one order of magnitude higher than the values recorded for the individual self-assembly of **13** (cations on exTTF units) and **20** or **21** (anions on PBI moieties). The observed $(\phi\Sigma\mu)_{max}$ values for **13**, **20** and **21** are 4.9 x 10^{-5}, 2.6 x 10^{-5} and 6.5 x 10^{-5} $cm^2V^{-1}s^{-1}$, respectively. This implies the existence of highly conducting pathways for holes or electrons in the co-assembly of exTTF and PBI systems. No significant changes in the lifetime of **$13_2$20** and **$13_2$21** was observed, which indicates that the contribution from terminal groups and counter ions are negligible in the charge recombination processes.

Linearity in the reciprocal conductivity transients (Figure 63a,b) suggests that the recombination processes in **$13_2$20** and **$13_2$21** can be interpreted by the 2^{nd} order protocols. The contribution of negative charge (electron) conductivity in the transient was also confirmed by the selective scavenging of photo-generated electrons in the media (Figure 63c,d), where the decrease of end-of-pulse conductivity (< 100 ns range) was observed, associated with a significant elongation of the lifetime of the charge carriers with the long-lived tail (>μs range). Suppressed charge recombination reaction is responsible for the stable positive charge carrier species in the present system.

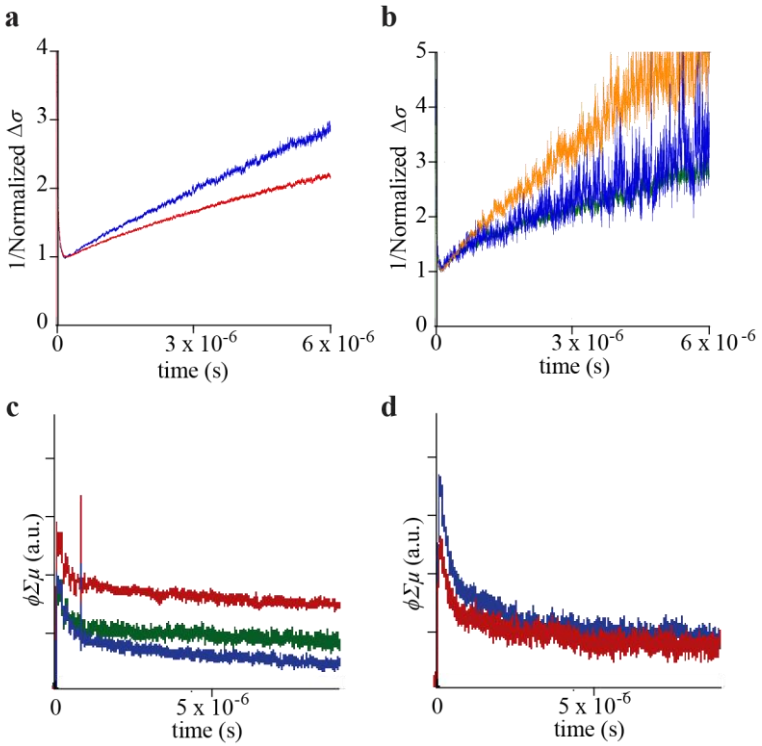

Figure 63. Reciprocal normalized and anisotropic conductivity transients. (a) Reciprocal normalized photo-conductivity transients for **13$_2$20** (red) and **13$_2$21** (blue). (b) The same than (a) for **13** (orange), **20** (green) and **21** (blue). (c) Anisotropic conductivity transients observed for **13$_2$20** deposited on a quartz substrate under controlled orientation by rubbing. Blue and red transients were observed along the directions rectangular and parallel to the rubbing direction. The kinetic trace was also observed for an identical oriented sample of **13$_2$20** material under Ar (blue) and SF_6 (green) atmospheres. (d) Same than (d) for **13$_2$21**. All transients were observed upon excitation to 355 nm, 9.1 x 10^{15} photons/cm^2.

The yield of photo-carrier generation was also discussed quantitatively by tracing radical anions of PBI motifs as an indicator (Figure 64a,b). Figure 64c and Figure 64d show the transient absorption spectra for **13$_2$20** and **13$_2$21**, respectively in solid films which were identical to the FP-TRMC results, this providing a clear signature of $PBI^{\bullet-}$ at 780 nm. Based on the molar extinction

coefficient of $PBI^{\bullet-}$ (7.4 x 10^4 $mol^{-1}dm^3cm^{-1}$),[60] the yield of the photo-carrier generation (ϕ) was estimated immediately after the pulse exposure and are found to be 2.2 x 10^{-4} and 1.2 x 10^{-4} for **$13_2$20** and **$13_2$21**, respectively. On the assumption of balanced number of charges between exTTF cations and PDI anions, the quantitative analysis of ϕ was performed, giving $\Sigma\mu$ in hydrogels of **$13_2$20** and **$13_2$21** as 0.5 and 0.8 $cm^2V^{-1}s^{-1}$, and this is the case giving a high value of $(\phi\Sigma\mu)_{max}$, hence provided the effective heterojunction structures in **$13_2$20** and **$13_2$21**.

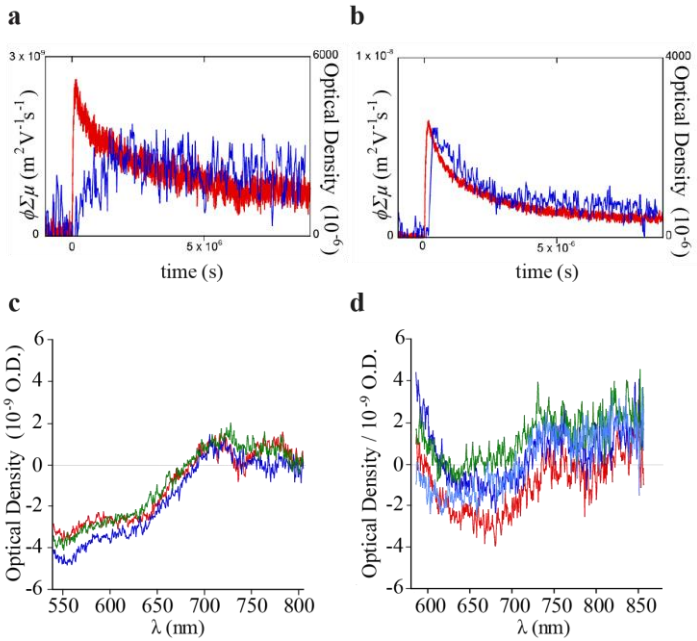

Figure 64. Conductivity transients and TAS upon excitation at 355 nm, 5.5 x 10^{16} photons cm^{-2}. (a) TRMC (red) and TAS (blue) kinetic traces at 740 -750 nm recorded for **$13_2$20**. (b) The same than (a) for **$13_2$21**. (c) Transient absorption spectra recorded for **$13_2$20** in solid films. Red, green, and blue spectra were recorded immediately after the pulse exposure of 1 (red), 2 (green), and 8 (blue) μs, respectively. (d) The same than (c) for **$13_2$21** solid films.

60 S. Seki, A. Saeki, T. Sakurai and D. Sakamaki, *Phys. Chem. Chem. Phys.* **2014**, *16*, 11093-11113.

1.4. Conclusions

1.4. Conclusions

Part 1. *Self-ordering electron donor–acceptor nanohybrids based on single-walled carbon nanotubes across different scales.*

We have described a versatile non-covalent functionalization of SWCNTs in water. Our protocol enables the spontaneous self-assembly of SWCNTs into well-ordered structures at different scales. As such **1**/SWCNT nanohybrid represents a unique example of short- and long-range organization, mainly in 2D, induced by a short peptide sequence linked to electron-donating exTTF. Importantly, photoexcitation of **1**/SWCNTs affords SWCNT-centered excited states that transform into long-lived charge-separated states in water. Their stability is enhanced by the long-range ordering in the nanohybrid.

Part 2. *Controlling the crystalline three-dimensional order in bulk materials by single-wall carbon nanotubes.*

Short-ordered *p*-type nanofibers based on exTTF derivatives **12** and **13**, together with their ability to act as wrapping agents of SWCNTs are demonstrated. The electronic communication in the excited state between the donor and the acceptor units in the nanohybrids are highlighted, with relatively long lifetimes of the electron transfer products. Finally, the presence of SWCNTs together with the charge-screening with $CaCl_2$ in form of external additives induce a new crystalline long-range ordered exTTF/SWCNT 3D bulk material, which is completely different in terms of internal structure and morphology from that observed in the absence of SWCNTs.

Part 3. *Highly ordered n/p-co-assembled materials with remarkable charge mobilities.*

We have demonstrated the formation of highly ordered functional materials from small molecules such as electron-donor exTTF derivative **13** endowed with carboxylate groups and electron-acceptor PBI derivatives **20** and **21** as electron-acceptors provided of guanidinium and quaternary ammonium salts, respectively. The electrostatic co-assembly of both complementary self-assembled nanofibers gave rise to a controlled alignment of the *n*/*p*-material with remarkably high values of photoconductivity. This ease and readily available methodology paves the way to new highly ordered materials with a defined D/A stoichiometry and excellent photoconductivity properties.

1.5. Experimental Section

1.5. Experimental Section

2.5.1. Synthesis

Reagents for synthesis were mostly purchased from Sigma-Aldrich and Acros. HiPCO and CoMoCAT SWCNTs were purchase from Carbon Nanotechnologies and Southwest Nanotechnologies, respectively, and used without any further purification treatment. Column chromatography was carried out on silica gel 60 (Fluka, 40-63 μm). IR spectra were recorded on a Bruker Tensor 27 spectrometer equipped with ATR and reported as wavenumbers in cm^{-1} with band intensities indicated as s (strong), m (medium), w (weak), br (broad). ^{1}H and ^{13}C NMR spectra were recorded either on a Bruker DPV 300MHz, a Bruker AV 500MHz or a Bruker AVIII 700MHz and reported as chemical shifts (δ) in ppm relative to tetramethylsilane (δ = 0) at room temperature. Spin multiplicities are reported as a singlet (s), broad singlet (br s), doublet (d), triplet (t) and quartet (q) with proton-proton coupling constants (*J*) given in Hz, or multiplet (m). Matrix-assisted laser desorption ionization (MALDI) mass spectrometry (MS) was performed on a Bruker Ultraflex spectrometer using dithranol or DCTB as matrix.

*1.5.1.1. Synthesis of exTTF derivative **1***

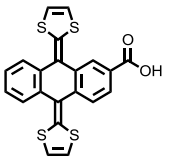

Compound 3. 9,10-Di(1,3-dithiol-2-ylidene)-9,10-dihydroanthracene-2-carboxylic acid. This product was synthesized according to reported procedures.[34]

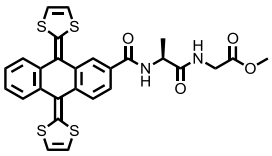

Compound 4. *N*-[9,10-Di(1,3-dithiol-2-ylidene)-9,10-dihydroanthracene-2-carbonyl]-L-alanylglycine methyl ester. To a solution of **2** (70 mg, 0.17 mmol), alanylglycine methyl ester hydrochloride (46 mg, 0.23 mmol) and DIPEA (0.1 mL, 0.50 mmol) in dry THF (10 mL) at room temperature, was added HBTU (94 mg, 0.25 mmol) under Argon flow. The resultant mixture was stirred for 2 hours. The solvent was removed under reduced pressure and the residue was purified by silica gel flash chromatography (eluent: CH_2Cl_2/CH_3OH, 30:1). The product was obtained as a bright yellow powder (58 mg, 62 %). ^{1}H NMR ($CDCl_3$, 500 MHz): 8.15 (s, 1H), 7.75-7.66 (m, 4H), 7.32-7.27 (m, 2H), 6.99-6.82 (m, 2H), 6.31 (s, 2H), 6.30 (s,

2H), 4.81 (m, 1H), 4.07 (d, 2H, ^3J = 4 Hz), 3.74 (s, 3H), 1.55 (d, 3H, ^3J = 7 Hz); ^{13}C NMR ($CDCl_3$, 125 MHz): 170.9, 170.4, 167.2, 139.1, 138.4, 137.6, 136.2, 135.5, 135.4, 131.1, 126.6 (2), 125.5, 125.3, 125.0, 124.2, 121.7, 121.6, 117.8, 117.7, 117.6, 52.8, 49.5, 41.7, 18.6; MS (ESI, CH_2Cl_2): 566 (100, $[M]^+$), calculated: 566.1.

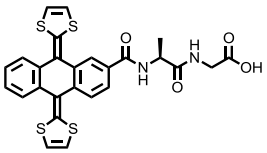

Compound 5. *N*-[9,10-Di(1,3-dithiol-2-ylidene)-9,10-dihydroanthracene-2-carbonyl]-L-alanylglycine. To a solution of KOH 0.2 M in EtOH/H_2O (9:1, 8 mL), compound **4** (50 mg, 0.09 mmol) was added. The mixture reaction was stirred at room temperature for 120 min. After addition of hydrochloric acid until aqueous solution became neutral, the product was extracted with CH_2Cl_2 (3 x 20 mL). The combined organic layers was dried over Na_2SO_4 before the solvent were removed under reduced pressure to afford **5** as a yellow powder in excellent yield (48 mg, 98%). ^{1}H NMR (DMSO, 700 MHz): 8.67-8.58 (m, 1H), 8.25-8.15 (m, 2H), 7.93-7.85 (m, 1H), 7.76-7.66 (m, 2H), 7.40-7.36 (m, 1H), 6.90-6.63 (m, 4H), 4.57 (q, 1H, ^3J = 7.2 Hz), 3.84-3.69 (m, 2H), 1.37 (d, 3H, ^3J = 7 Hz); ^{13}C NMR (DMSO, 175 MHz): 173.2, 171.6, 165.8, 151.9, 139.7, 138.8, 137.8, 137.6 (2), 135.1 (2), 134.9, 132.0, 131.9, 126.9 (2), 125.8, 125.7, 125.4, 125.2 (2), 124.8, 124.6, 120.5 (2), 118.8, 49.3, 40.5, 18.4; MS (ESI, CH_3OH): 553 (100, $[M+H]^+$), calculated: 553.0.

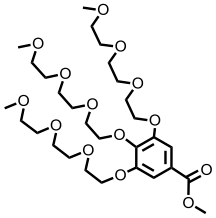

Compound 6. Methyl 3,4,5-tris{2-[2-(2-methoxyethoxy) ethoxy]ethoxy}benzoate. This product was synthesized according to reported procedures.[42]

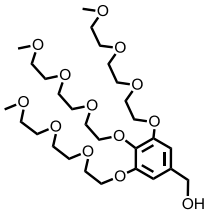

Compound 7. {3,4,5-Tris[2-(2-(2-methoxyethoxy)ethoxy) ethoxy]phenyl}methanol. This product was synthesized according to reported procedures.[42]

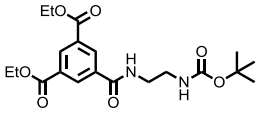

Compound 8. Diethyl 5-{[2-((*tert*-butoxycarbonyl) amino)ethyl]carbamoyl} isophthalate. To a solution of 3,5-bis(ethoxycarbonyl)benzoic acid (1 g, 3.76 mmol) in dry DMF (40 mL), HBTU (2.51 g, 5.63 mmol) and TEA (1.6 mL, 11.3 mmol) were added. The reaction mixture was stirred under Argon at room temperature for 5 min. *tert*-Butyl (2-aminoethyl)carbamate (602 mg, 3.76 mmol) was added and the reaction mixture was stirred for 3 hours. The solvent was removed under reduced pressure and the residue was redissolved in CH_2Cl_2 (50 mL), washed with a Na_2CO_3 aqueous solution (3 x 50 mL) and a saturated NH_4Cl aqueous solution (3 x 50 mL), and finally dried over Na_2SO_4. The solvent was removed under reduced pressure to obtain **8** as a pale yellow powder without further purification (1.45 g, 95%). IR (neat): 3345, 2982, 1723, 1537, 1244; ^{1}H NMR ($CDCl_3$, 300 MHz): 8.80 (t, 1H, ^4J = 1.5 Hz), 8.66 (d, 2H, ^4J = 1.5 Hz), 7.47 (br s, 1H), 5.00 (t, 1H, ^3J = 5 Hz), 4.43 (c, 4H, ^3J = 7 Hz),) 3.60 (dt, 2H, ^3J = 6.3 Hz, ^3J = 4.9 Hz), 3.43 (m, 2H), 1.43 (s, 9H), 1.42 (t, 6H, ^3J = 7 Hz); ^{13}C NMR ($CDCl_3$, 75 MHz): 165.9 165.2, 157.6, 135.0, 133.2, 132.0, 131.5, 77.2, 61.7, 42.3, 40.1, 28.3, 14.3; MS (ESI, CH_2Cl_2): 431 (100, $[M+Na]^+$), calculated: 431.2.

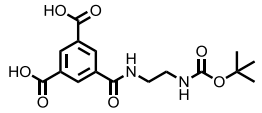

Compound 9. 5-((2-((*tert*-Butoxycarbonyl)amino) ethyl)carbamoyl)isophthalic acid. To a solution of KOH 2 M in EtOH/H_2O 9:1 (15 mL), compound **5** (750 mg, 1.84 mmol) was added. The reaction mixture was stirred at reflux for 30 min. After addition of hydrochloric acid until aqueous solution became neutral, the product was extracted with AcOEt (3 x 25 mL). The combined organic layers were dried over Na_2SO_4 before the solvent was removed under reduced pressure to afford **9** as a white solid in excellent yield (635 mg, 98%). IR (neat): 3357, 3310, 2984, 2940, 1692, 1645, 1538, 1283; ^{1}H NMR (CD_3OD, 300 MHz): 8.79 (t, 1H, ^4J = 1.5), 8.72 (d, 2H, ^4J = 1.5 Hz), 3.52 (dt, 2H, ^3J = 3.4 Hz, ^3J = 3.5 Hz), 3.33 (m, 2H), 1.44 (s, 9H); ^{13}C NMR (CD_3OD, 75 MHz): 168.6, 168.1, 158.9, 136.7, 134.4, 133.5, 133.2, 80.4, 41.6, 40.8, 28.8; MS (ESI, CH_3OH): 375 (100, $[M+Na]^+$), calculated: 375.1.

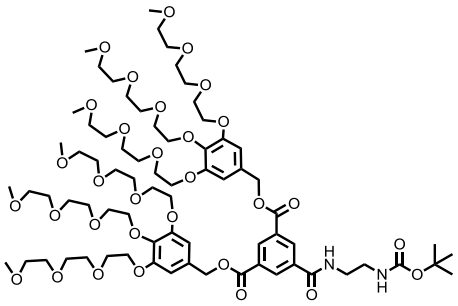

Compound 10. **Bis{3,4,5-tris[2-(2-(2-methoxyethoxy)ethoxy)ethoxy] benzyl} 5-{[2-((*tert*-butoxycarbonyl) amino)ethyl] carbamoyl} isophthalate.** Compound **9** (192 mg, 0.546 mmol) was dissolved in dry CH_2Cl_2 (30 mL) at -15 ºC under argon flow and EDC (314 mg, 1.64 mmol) and DMAP (267 mg, 2.184 mmol)

were added. Then **7** (650 mg, 1.09 mmol) was added and the reaction mixture was stirred at room temperature overnight. The solvent was removed under reduced pressure and the residue was dissolved in CH_2Cl_2 (25 mL) and washed with NH_4Cl 0.5 M aqueous solution (3x25 mL). The organic phase was dried over Na_2SO_4 and the solvent was evaporated. The residue was purified by silica gel flash chromatography (eluent: CH_2Cl_2/CH_3OH, 15:1), providing **10** as a brown oil (420 mg, 51%). ^{1}H NMR ($CDCl_3$, 300 MHz): 8.73 (t, 1H, ^4J = 1.5 Hz), 8.63 (d, 2H, ^4J = 1.5 Hz), 7.77 (br s, 1H), 6.63 (s, 4H), 5.41 (br s, 1H), 5.20 (s, 4H), 4.15-4.01 (m, 12H), 3.81-3.74 (m, 8H), 3.74 - 3.68 (m, 4H), 3.68-3.61 (m, 12H), 3.61 - 3.51 (m, 26H), 3.51 - 3.42 (m, 14H), 3.30 - 3.26 (m, 18H), 1.34 (s, 9H); ^{13}C NMR ($CDCl_3$, 75 MHz): 165.7, 165.5, 164.8, 152.7, 138.6, 136.9, 135.3, 133.4, 133.1, 132.4, 131.0, 130.8, 108.4, 79.6, 77.4, 72.2, 71.8, 70.7, 70.6, 70.5, 69.7, 68.9, 67.3, 64.9, 58.9, 52.4, 41.8, 40.0, 28.3; MS (MALDI, dithranol): 1527.7 (100, $[M+Na]^+$), calculated: 1527.7.

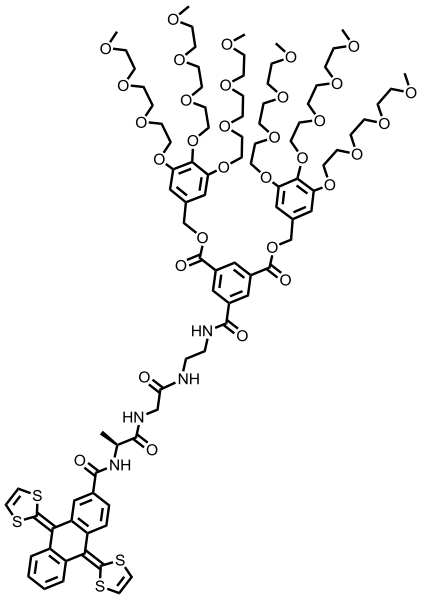

Compound 1. To a solution of **10** (83 mg, 0.054 mmol) in dry CH_2Cl_2 (4 mL), a solution of HCl 2M in diethyl ether (0.05 mL) was added and the reaction mixture was stirred under Argon for 24 hours. DIPEA was added (0.02 mL, 0.13 mmol) to the reaction mixture and the solvent was removed under reduced pressure to obtain compound **11**, which was used without characterization. **11** was redissolved in dry DMF (10 mL) and **5** (23 mg, 0.042 mmol), DIPEA (0.02 mL, 0.13 mmol) and HBTU (24 mg, 0.06 mmol) were added. The reaction mixture was stirred under Argon flow at room temperature for 4 hours. The solvent was removed under reduced pressure and the residue was purified by silica gel flash chromatography (eluent: CH_2Cl_2/CH_3OH, 10:1). The product was further purified by precipitation and centrifugation in hexane and washed with diethyl ether. Final product **1** was obtained as a bright yellow oil (62mg, 76 %). ^{1}H NMR ($CDCl_3$, 500 MHz): 8.78 (s, 2H), 8.74 (s, 1H), 8.48-8.31 (m, 1H), 8.20-7.94 (m, 1H), 7.79 (br s, 1H), 7.71-7.58 (m, 4H), 7.52 (br s, 1H), 7.42 (br s, 1H), 7.28 (m, 2H), 6.68 (s, 4H), 6.37-6.06 (m, 4H), 5.31-5.11 (m, 4H), 4.38 (m, 1H), 4.15 (t, 8H, ^3J = 4.8 Hz), 4.14 (t, 4H, ^3J = 4.8 Hz), 3.95-3.83 (m, 2H), 3.83 (t, 8H, ^3J = 4.7 Hz), 3.78 (t, 4H, ^3J = 5.1 Hz), 3.73 (t, 4H, ^3J = 5 Hz), 3.72 (t, 8H, ^3J

= 6 Hz), 3.66 (t, 8H, ^3J = 5.3 Hz), 3.64 (t, 16H, ^3J = 5.3 Hz), 3.59-3.44 (m, 16H), 3.37 (s, 6H), 3.32 (s, 12H), 1.51 (d, 3H, ^3J = 6 Hz); ^{13}C NMR ($CDCl_3$, 125 MHz): 170.4, 166.1, 165.5, 153.0, 139.2, 138.4, 137.7, 136.1, 135.4, 135.2, 133.7, 133.2, 131.4, 131.3, 126.6, 126.5, 125.3, 125.2, 125.1, 124.9, 121.7, 121.0, 117.9, 117.7, 117.5, 117.4, 109.3, 72.8, 72.3, 71.2, 71.0, 70.9, 70.2, 69.4, 67.7, 51.9, 43.9, 40.8, 40.2, 17.3; HRMS (MALDI, DCTB): 1961.7165 (100, $[M+Na]^+$), calculated for $C_{93}H_{126}N_4O_{32}S_4Na$: 1961.7130.

*1.5.1.2. Synthesis of peptide-based exTTF derivatives **12** and **13***

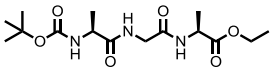

Compound 14. *N*-(*tert*-Butoxycarbonyl)-L-alanyl-glycyl-L-alanine ethyl ester. To a solution of *N*-(*tert*-butoxycarbonyl)-L-alanyl-glycine (500 mg, 2.03 mmol) in dry DMF (20 ml), HBTU (1.16 g, 3.05mmol) and DIPEA (1.1 ml, 6.09 mmol) were added under argon flow at room temperature. After 5 min of activation, L-alanine ethyl ester hydrochloride (406 mg, 2.64 mmol) was added and the reaction mixture was stirred for 3 h. The solvent was removed under reduced pressure and the residue was redissolved in CH_2Cl_2 (30 ml) and washed with a saturated Na_2CO_3 aqueous solution (3 x 10 ml) and a saturated NH_4Cl aqueous solution (3 x 10 ml) and the organic layer was dried over Na_2SO_4. The solvent was removed under reduced pressure to obtain **14** as a brown oil with enough purity to be used in the next reaction (745 mg, 96%); ^{1}H NMR (300 MHz, $CDCl_3$): 7.37 (br s, 1H), 7.24 (br s, 1H), 5.41 (br s, 1H), 4.48 (m, 1H), 4.19–4.08 (m, 3H), 4.08–3.79 (m, 2H), 1.38 (d, ^3J = 7Hz, 2H), 1.38 (s, 9H), 1.33 (d, ^3J = 7Hz, 2H), 1.22 (t, ^3J = 7Hz, 3H); ^{13}C NMR (75 MHz, $CDCl_3$): 172.9, 172.1, 170.1, 158.1, 80.7, 61.8, 49.6, 48.4, 43.1, 28.4, 18.3, 17.4, 14.7; HRMS (ESI; +ve): 346.1986 (100, $[M+H]^+$), calculated for $C_{15}H_{28}N_3O_6$: 346.1972.

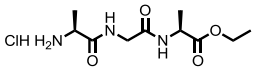

Compound 15. L-Alanyl-glycyl-L-alanine ethyl ester hydrochloride. To a solution of **14** (550 mg, 1.44 mmol) in dry CH_2Cl_2 (4 ml), a solution of HCl 2M in diethyl ether (1 ml) was added and the reaction mixture was stirred under argon flow for 24 h. Reaction was monitored by TLC using ninhydrin as a revealing agent. The solvent was evaporated at reduced pressure and the residue was redissolved in the minimum volume of methanol for being precipitated by adding cold diethyl ether. Product **14** was obtained as a colourless oil after centrifugation (350 mg, 86%). ^{1}H NMR (300 MHz, CD_3OD): 4.40 (q, ^3J = 7Hz, 1H), 4.17 (q, 2H), 4.03–3.92 (m, 3H), 1.53 (d, ^3J = 7Hz, 3H), 1.39 (d, ^3J = 7.3 Hz, 3H), 1.26 (t, ^3J = 7Hz, 3H); ^{13}C NMR (75 MHz, CD_3OD): 174.2, 171.6, 170.8, 62.5, 50.4, 49.5, 43.2, 17.8, 17.6,

14.5; HRMS (ESI; +ve): 246.1454 (100, $[M+H]^+$), calculated for $C_{10}H_{20}N_3O_4$: 246.1448.

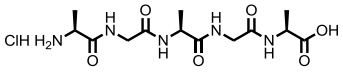

Compound 16. L-Alanyl-glycyl-L-alanyl-glycyl-L-alanine hydrochloride. Standard solid phase hydroxymethyl-based resin procedure was used to synthesize the desired pentapeptide sequence with a free amine and carboxylic acid groups at the N-terminus and C-terminus positions, respectively.[51] A Wang resin preloaded with Fmoc-L-alanine (Fmoc-L-alanine-*p*-alkoxybenzyl alcohol resin) was used as followed: Fmoc-deprotection was achieved by a solution of piperidine (20%) in DMF yielding the free amine group. This deprotection step was tested by a Kaiser test, consisting on submerging and heating few beads of resin on a solution of ninhydrin in ethanol and checking the color. Second Fmoc-protected amino acid was introduced in the presence of HBTU as activating agent and DIPEA as base, in DMF at room temperature. From this point, repetitive step reactions were performed, that is, deprotection of the Fmoc group of the lately attached peptide and subsequent coupling of the corresponding Fmoc-protected amino acid. Final cleavage of peptide **16** from the resin was performed by treatment with TFA:H_2O (95:5). Compound **16** was obtained as a white solid after precipitation in cold diethyl ether, with enough purity for the next step. $[\alpha]_D$ = -24.8 (0.029M in methanol); ^{1}H NMR (300 MHz, CD_3OD): 4.49–4.30 (m, 2H), 4.04–3.86 (m, 5H), 3.72 (s, 3H), 1.54 (d, ^3J = 7.1 Hz, 3H), 1.40 (d, ^3J = 7.3 Hz, 6H); ^{13}C NMR (75 MHz, CD_3OD): 175.9, 175.4, 171.7, 171.2, 171.1, 50.9, 50.3, 49.4, 43.4, 43.3, 17.7, 17.4; HRMS (ESI; +ve): 346.1727 (100, $[M+H]^+$), calculated for $C_{13}H_{24}N_5O_6$: 346.1721.

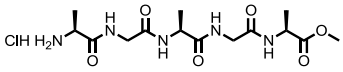

Compound 17. L-Alanyl-glycyl-L-alanyl-glycyl-L-alanine methyl ester hydrochloride. To a solution of **16** (140 mg, 0.37 mmol) in methanol (5 ml), 1.8 ml of a solution of trimethylsilyldiazomethane (3.6 mmol) in hexane (2.0 M) was added dropwise. The mixture was allowed to react over 30 min at room temperature. The solvent was evaporated at reduced pressure and the residue was redissolved in the minimum volume of methanol. Precipitation of the product was carried out by adding cold diethyl ether. After centrifugation, product **17** was obtained as a white solid (127 mg, 87%). $[\alpha]_D$ = -34.5 (0.028M in methanol); ^{1}H NMR (300MHz, CD_3OD): 4.46–4.27 (m, 2H), 4.06–3.82 (m, 5H), 1.53 (d, ^3J = 7.1 Hz, 3H), 1.40 (d, ^3J = 7.2 Hz, 3H), 1.39 (d, ^3J = 6.9 Hz, 3H); ^{13}C NMR (75 MHz, CD_3OD): 173.7, 173.4, 171.7, 171.2, 171.1, 50.9, 50.3, 49.4, 48.1, 43.4, 43.3,

17.7, 17.1; HRMS (ESI; +ve): 360.1888 (100, $[M+H]^+$), calculated for $C_{14}H_{26}N_5O_6$, 360.1877.

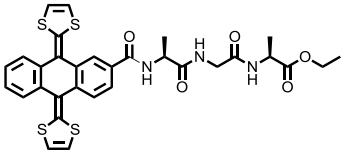

Compound 18. *N*-[9,10-Di(1,3-dithiol-2-ylidene)-9,10-dihydroanthracene-2-carbonyl] -L-alanylglycyl-L-alanine ethyl ester. To a solution of **3** (30 mg, 71 mmol), **15** (26 mg, 92 mmol) and DIPEA (40 ml, 213 mmol) in dry DMF (7 ml), HBTU (42 mg, 107 mmol) was added at room temperature under argon flow. The resultant mixture was stirred under argon for 1 h. The solvent was evaporated at reduced pressure and the residue was subjected to column chromatography (eluent: CH_2Cl_2:CH_3OH, 25:1). Product **18** was precipitated in hexane and it was obtained as a bright orange powder (35 mg, 76%). ^{1}H NMR (700 MHz, $CDCl_3$): 8.18 (s, 1H), 7.79 – 7.68 (m, 4H), 7.38 – 7.31 (m, 2H), 7.14 – 7.05 (br s, 1H), 7.05 – 6.94 (m, 1H), 6.87 (d, ^3J = 6.5 Hz, 1H), 6.37 – 6.32 (m, 4H), 4.75–4.63 (m, 1H,), 4.62 - 4.51 (m, 1H), 4.25 – 4.12 (m, 3H), 3.92 (m, 1H), 1.58 (d, ^3J = 7Hz, 3H), 1.50 – 1.43 (m, 3H), 1.25 (t, ^3J = 7Hz, 3H); ^{13}C NMR (175 MHz, $CDCl_3$): 172.9, 172.8, 168.3, 167.2, 138.7, 138.2, 135.8, 135.1, 135.0, 126.2, 125.1, 124.9, 124.6, 123.8, 117.4, 117.3, 117.1, 61.6, 49.9, 48.3, 43.1, 18.1, 17.9, 14.1; HRMS (MALDI, dithranol): 651.0984 (100, $[M]^+$), calcd. for $C_{31}H_{29}N_3O_5S_4$: 651.0985.

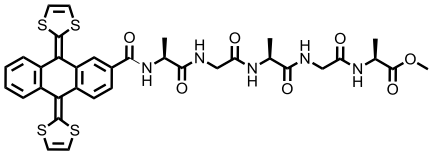

Compound 19. *N*-[9,10-Di(1,3-dithiol-2-ylidene)-9,10-dihydroanthracene-2-carbonyl]-L-alanylglycyl-L-alanyl-glycyl-L-alanine methyl ester. To a solution of **3** (45 mg, 0.106 mmol) in dry CH_2Cl_2 (15 ml), EDC (61 mg, 0.318 mmol) and 4-dimethylaminopyridine (2 mg, 16 mmol) were added at -15 ºC under argon flow. After 5 min of activation, **17** (50 mg, 0.106 mmol) was added dissolved in dry DMF (3 ml). The reaction mixture was allowed to stir at room temperature for 2 h. The mixture was washed with a saturated NH_4Cl aqueous solution (3 x 10 ml) and the organic layer was dried over Na_2SO_4. The residue was subjected to neutral aluminum oxide column chromatography (eluent: CH_2Cl_2/ethanol, 20:1). The solvent was removed under reduced pressure to yield **19** as a bright orange powder (62 mg, 76%). ^{1}H NMR (500 MHz, CD_3OD): 8.25 (s, 1H), 7.83 (dd, ^3J = 8Hz, ^3J = 1.6 Hz, 1H), 7.79–7.74 (m, 1H), 7.72–7.67 (m, 2H), 7.32–7.27 (m, 2H), 6.53–6.44 (m, 4H), 4.55–4.47 (m, 1H), 4.46–4.30 (m, 2H), 4.05–3.94 (m, 2H), 3.89–3.80 (m, 2H), 3.69 (s, 3H), 1.54 (d, ^3J = 7Hz, 3H),

1.52–1.46 (m, 3H), 1.35 (d, ^3J = 7Hz, 3H); ^{13}C NMR (125 MHz, CD^{3}OD): 174.5, 173.5, 170.9, 170.3, 139.1, 136.1, 135.6, 135.5, 130.7, 126.2 (2), 125.1, 125.0, 124.6, 120.9, 117.7, 117.5, 51.8, 51.2, 50.0, 48.6, 42.9, 42.4, 16.5 (2), 16.4; HRMS (MALDI; dithranol): 765.1397 (100, $[M]^+$), calculated for $C_{35}H_{35}N_5O_7S_4$: 765.1414.

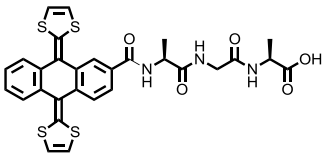

Compound 12. *N*-[9,10-Di(1,3-dithiol-2-ylidene)-9,10-dihydroanthracene-2-carbonyl]-L-alanylglycyl-L-alanine. To a solution of KOH 0.2M in ethanol/H_2O (9:1, 8 mL), compound **16** (50 mg, 0.09 mmol) was added. The mixture reaction was stirred for 120 min at room temperature. After addition of hydrochloric acid until aqueous solution became neutral, the product was extracted with CH_2Cl_2 (3 x 20 ml). The combined organic layers were dried over Na_2SO_4 before the solvent was removed in vacuum to yield final product **12** as an orange powder (48 mg, 98%). ^{1}H NMR (500 MHz, CD_3OD): 8.25 (s, 1H), 7.85–7.75 (m, 2H), 7.74–7.68 (m, 2H), 7.32–7.28 (m, 2H), 6.50 (s, 1H), 6.48 (s, 1H), 4.54 (q, ^3J = 7Hz, 1H), 4.48–4.39 (m, 1H), 4.05–3.83 (m, 2H), 1.57–1.50 (m, 6H); ^{13}C NMR (125 MHz, CD_3OD): 175.0 (2), 170.2, 168.6, 139.0, 138.9, 136.1, 135.7, 135.6, 131.1, 126.2, 126.1, 125.1, 125.0, 124.9, 124.6, 121.0, 117.4, 117.3, 49.9, 48.3, 42.5, 16.6; HRMS (MALDI; dithranol): 623.0686 (100, $[M]^+$), calculated for $C_{29}H_{25}N_3O_5S_4$ 623.0672.

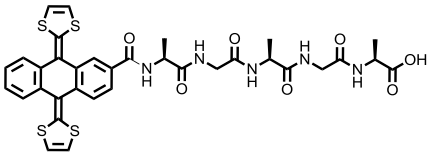

Compound 13. *N*-[9,10-Di(1,3-dithiol-2-ylidene)-9,10-dihydroanthracene-2-carbonyl]-L-alanylglycyl-L-alanyl-glycyl-L-alanine. To a solution of KOH 0.2M in ethanol/H_2O (9:1, 5 mL), compound **19** (35 mg, 46 mmol) was added. The mixture reaction was stirred for 120 min at room temperature. After addition of hydrochloric acid until aqueous solution became neutral, the product was extracted with CH_2Cl_2 (3 x 10 ml). The combined organic layers were dried over Na_2SO_4 before the solvent was removed in vacuum to yield final product **13** as an orange powder (33 mg, 95%). $[\alpha]_D$ = 99.2 (0.013M in methanol); ^{1}H NMR (500MHz, CD_3OD): 8.25 (s, 1H), 7.86–7.81 (m, 1H), 7.78–7.73 (m, 1H), 7.73–7.66 (m, 2H), 7.33–7.27 (m, 2H), 6.50 (s, 1H), 6.47 (s, 1H), 4.55–4.47 (m, 1H), 4.44–4.31 (m, 2H), 4.05–3.81 (m, 4H), 1.54 (d, ^3J = 7Hz, 3H), 1.52–1.45 (m, 3H), 1.38 (d, ^3J = 7Hz, 3H); ^{13}C NMR

(125 MHz, CD_3OD): 175.0, 174.5, 170.9, 170.2, 139.1, 136.1, 135.6, 135.5, 130.8, 126.1, 125.1, 125.0, 124.6, 120.9, 117.7, 117.3, 51.2, 50.0, 48.8, 42.9, 42.5, 16.8, 16.7, 16.4; HRMS (MALDI; dithranol): 751.1252 (100, $[M]^+$), calculated for $C_{34}H_{33}N_5O_7S_4$: 751.1257.

*1.5.1.3. Synthesis of cationic PBI derivatives **20** and **21***

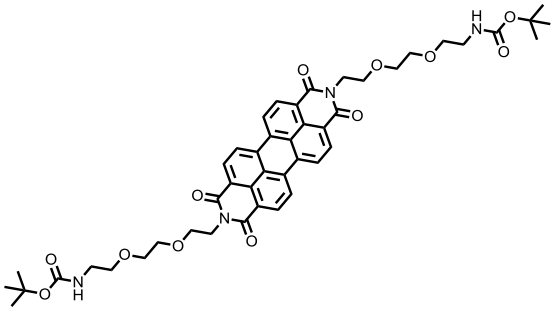

Compound 22. 2,9-Bis[2-(12, 12-dimethyl-10-oxo-3,6,11-trioxa-9-azatridec-1-yl)]-anthra[2,1,9-def:6,5,10-d'e'f']diisoquinoline- 1,3,8, 10(2H,9H)-tetrone. *tert-Butyl 2-[2-(2-aminoethoxy) ethoxy]ethylcarbamate* (1.3 g, 5.24 mmol), perylene-3,4,9,10-tetracarboxylic acid bisimide (690 mg, 1.75 mmol), zinc acetate (766 mg, 3.49 mmol) and imidazole (1 g) were stirred under argon atmosphere at 150 ºC for 3 hours. The reaction mixture was filtered through celite to remove the precipitate, and the filter was washed with CH_2Cl_2 (100 mL). After removing the solvent under reduced pressure, the crude product was purified by flash column chromatography (CH_2Cl_2/CH_3OH, 30:1), to give **22** as a red solid (1.2 g, 80%). *Rf* = 0.19 (CH_2Cl_2:CH_3OH 20:1); IR: 2957 (m), 2926 (s), 2855 (m), 1695 (s), 1656 (s), 1594 (m), 1365 (m); ^{1}H NMR (300 MHz, $CDCl_3$): 8.56 (d, 4H, ^3J = 8.0 Hz), 8.40 (d, 4H, ^3J = 8.0 Hz), 5.08 (br s, 2H), 4.51 (t, 4H, ^3J = 5.8 Hz), 3.93 (t, 4H, ^3J = 5.8 Hz), 3.81 - 3.74 (m, 4H), 3.69 - 3.62 (m, 4H), 3.55 (t, 4H, ^3J = 5.2 Hz), 3.34 - 3.25 (m, 4H), 1.46 (s, 18H); ^{13}C NMR (75 MHz, $CDCl_3$): 163.3, 156.0, 134.3, 131.2, 129.1, 126.1, 123.0, 123.1, 79.2, 77.3, 70.5, 70.3, 70.0, 68.0, 39.3, 28.5; MS (MALDI, dithranol): 875.36 (100, $[M+Na]^+$), calculated for $C_{46}H_{52}N_4O_{12}Na$: 875.35.

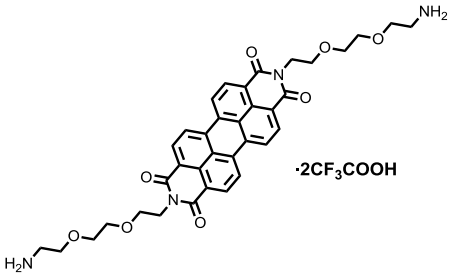

Compound 23. **2,9-Bis{2-[2-(2-aminoethoxy)ethoxy]ethyl]}-anthra[2,1,9-def:6,5,10-d'e'f'] diisoquinoline- 1,3,8,10(2H,9H)-tetrone ditrifluoroacetate salt.** A solution of **22** (1.0 g, 1.17 mmol) in $CHCl_3$ (6 mL) and TFA (4 mL) was stirred at room temperature for 1 h. The solvent was removed under reduced pressure. The solid residue was washed with $CHCl_3$ (25 mL) to remove any trace

of starting material and then dried under vacuum. The pure compound was obtained as a red solid without further purification (830 mg, 95%). IR: 2959 (w), 2927 (m), 1694 (s), 1655 (s), 1594 (m), 1204 (m), 1129 (m); ^{1}H NMR (300 MHz, CD_3OD): 8.02 (d, 4H, ^{3}J = 8.0 Hz), 7.91 (d, 4H, ^{3}J = 8.0 Hz), 4.33 (t, 4H, ^{3}J = 6.0 Hz), 3.86 (t, 4H, ^{3}J = 6.0 Hz), 3.83 - 3.78 (m, 4H), 3.78 - 3.70 (m, 8H), 3.16 (t, 4H, ^{3}J = 5.2 Hz); ^{13}C NMR (75 MHz, $CDCl_3$): 163.1, 133.4, 130.5, 128.0, 124.7, 123.5, 122.1, 70.4, 70.3, 67.9, 66.9, 39.7, 39.5; MS (MALDI, dithranol): 653.13 (100, $[M+H]^+$), calculated for $C_{36}H_{37}N_4O_8$: 653.26.

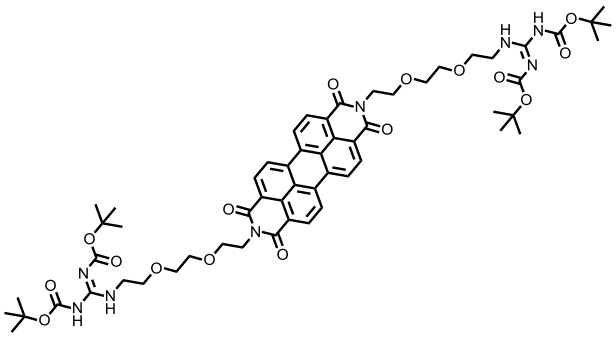

Compound 24. To a solution of diamine **23** (500 mg, 0.57 mmol) in dry DMF (10 mL) were added 1,3-bis(*tert*-butoxycarbonyl)-2-methyl-2-thiopseudourea (330 mg, 1.14 mmol) and TEA (0.475 mL, 3.41 mmol). The mixture was stirred at room temperature for 5 min. To the resulting solution, $HgCl_2$ (340 mg, 1.25 mmol) was added and the mixture was allowed to react at room temperature. After 30 min, it was diluted with CH_2Cl_2 (100 mL) and filtered through celite to remove the precipitate, and the filter was washed with CH_2Cl_2 (100 mL). The filtrate was washed with a saturated NH_4Cl aqueous solution (3 x 100 mL), water (2 x 100 mL) and brine (100 mL). The organic layer was dried over Na_2SO_4 and the solvent was removed under reduced pressure. The crude product was purified by flash column chromatography (CH_2Cl_2/CH_3OH, 30:1) affording **24** as a red solid (240 mg, 37%). *Rf* = 0.26 (CH_2Cl_2/CH_3OH, 20:1); IR: 3328 (br), 2956 (m), 2924 (s), 285 (m), 1698 (s), 1645 (s), 1367 (m), 1140 (s); ^{1}H NMR (300 MHz, $CDCl_3$): 11.42 (s, 2H), 8.79 (br s, 2H), 8.32 (d, 4H, ^{3}J = 8.0 Hz), 8.09 (d, 4H, ^{3}J = 8.0 Hz), 4.49 (t, 4H, ^{3}J = 5.2 Hz), 3.95 (t, 4H, ^{3}J = 5.2 Hz), 3.86 - 3.64 (m, 16H), 1.57 (s, 18H), 1.49 (s, 18H); ^{13}C NMR (75 MHz, $CDCl_3$): 163.3 156.7, 153.0, 136.9, 133.9, 131.2, 128.8, 123.1, 122.8, 83.8, 77.4, 70.4, 69.9, 69.6, 68.3, 41.1, 39.7, 28.4, 28.2; MS (MALDI, dithranol): 1159.50 (100, $[M+Na]^+$), calculated for $C_{58}H_{72}N_8O_{16}Na$: 1159.50.

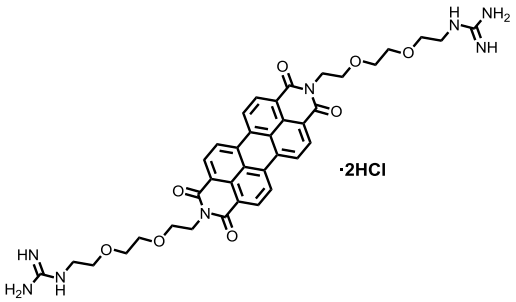

Compound 20. 2,9-Bis{2-[2-(2-guanidinoethoxy)ethoxy]ethyl}-anthra[2,1,9-def:6,5,10-d'e'f'] diisoquinoline- 1,3,8,10(2H,9H)-tetrone dihydrochloride. To a solution of **24** (150 mg, 0.13 mmol) in CH_3OH (5 mL), HCl (*aq*) (2 mL) was added and the mixture was stirred at room temperature. After 20 h, the solvent was removed under reduced pressure. The solid residue was precipitated and centrifuged in cold diethyl ether to remove any trace of impurities and then dried under vacuum. The pure compound was obtained as a purple solid without further purification (105 mg, 99%). IR: 3316 (br), 3173 (br), 1694 (m), 1654 (s), 1594 (m), 1344 (w); ^{1}H NMR (700 MHz, DMSO-d_6, 50 ºC): 8.54 (d, 4H, ^3J (H,H) = 6.5 Hz), 8.31 (d, 4H, ^3J = 6.5 Hz), 7.53 (t, 2H, ^3J = 4.7 Hz), 7.12 (br s, 8H), 4.26 (t, 4H, ^3J = 5.8 Hz), 3.73 (t, 4H, ^3J = 5.8 Hz), 3.65 (t, 4H, ^3J = 4.5 Hz), 3.59 (t, 4H, ^3J = 4.5 Hz), 3.51 (m, 4H, ^3J = 4.8 Hz), 3.29 – 3.26 (m, 4H); ^{13}C NMR (175 MHz, DMSO-d_6, 50 ºC): 163.0, 157.7, 134.1, 131.1, 128.6, 125.6, 124.4, 122.7, 70.2, 70.1, 69.1, 67.5, 41.4, 39.4; HRMS (MALDI, dithranol): 737.3042 (100, $[M+H]^+$), calculated for $C_{38}H_{41}N_8O_8$: 737.3047.

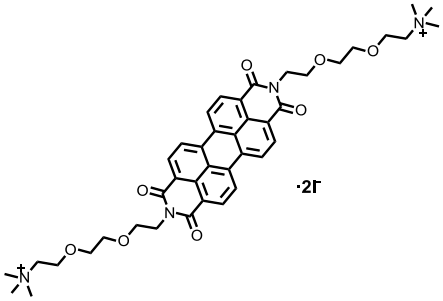

Compound 21. To a solution of **23** (60 mg, 0.068 mmol) and K_2CO_3 (190 mg, 1.37 mmol) in CH_2Cl_2:CH_3OH (3:1, 5 mL), was added iodomethane (36µL, 0.58 mmol) and the reaction mixture was allowed to react at room temperature for 24 hours. The solid residue was isolated by filtration through celite followed by rotary evaporation. The product was precipitated and centrifuged in cold diethyl ether to remove any trace of impurities and then dried under vacuum. The pure compound was obtained as a purple solid without further purification (42 mg, 62%). IR: 3348 (br), 1636 (s), 1451 (w), 1316 (m), 1084 (w); ^{1}H NMR (700 MHz, DMSO, 50 ºC): 8.84 (d, ^3J = 8.2 Hz, 4H), 8.51 (d, ^3J = 8.2 Hz, 4H), 4.29 (t, ^3J = 6.5 Hz, 4H), 3.88 – 3.84 (m, 4H), 3.75 (t, ^3J = 6.5 Hz, 4H), 3.65 (dd, ^3J = 5.6, 3.0 Hz, 4H), 3.62 (dd, ^3J = 5.6, 3.0 Hz, 4H), 3.60 – 3.56 (m, 4H), 3.15 (s, 18H); ^{13}C NMR (175 MHz, DMSO, 50 ºC): 163.2, 134.5, 131.5, 128.9, 126.0, 124.7, 123.0, 69.9, 69.9, 67.6, 65.0, 64.6, 53.7, 39.5; HRMS

(MALDI, dithranol): 738.3630 (100, $[M]^+$), calculated for $C_{42}H_{50}N_4O_8$: 738.3629.

2.5.2. Characterization of nanohybrids, hydrogels and solid materials

Absorbance measurements. Absorption spectra were recorded with a Varian Cary 50 UV-*vis* spectrophotometer and a UV-3600 Shimadzu ultraviolet–visible–NIR spectrophotometer. The absorbance spectra of **1**, **12**, **13**, **20** and **21** were acquired in a 1 cm path length quartz cuvette using a 4 nm slit-width. For the titration with SWCNTs in the case of **1**, **12** and **13**, a very concentrated dispersion of SWCNTs in THF was used. For the denaturalization experiments, absorption spectra of **12** and **13** in different percentage of methanol were recorded. The equilibrium denaturation studies were performed by preparing two stock solutions at the same concentration of **12** and **13** in water and in methanol, and mixing them at different ratios. The absorbance spectra of *n*/*p*-materials $\mathbf{13_220}$ and $\mathbf{13_221}$ were acquired after vigorously shaking the corresponding aqueous dispersions.

Raman measurements. **1**/SWCNTs were characterized by using a Renishaw inVia Raman microscope (laser power 0.05%, 785 nm, optical lens 1000x, on a glass microscope slide). In the case of **12**/SWCNTs and **13**/SWCNTs, Raman spectra were acquired by a Fourier transform–Raman spectrometer RFS100 from Bruker with an excitation wavelength of 1,064 nm and a liquid nitrogen-cooled germanium detector.

Fluorescence experiments and femtosecond transient absorption studies. Fluorescence spectra were recorded on a FluoroLog3 spectrometer (Horiba) with a IGA Symphony (512x1x1 μm^3) detector in the NIR detection range while femtosecond transient absorption studies were performed with 387 nm laser pulses (1 kHz, 150 fs pulse width, 200 nJ) from an amplified Ti/sapphire laser system (Model CPA 2101, Clark-MXR Inc., output 775 nm).

Scanning Electron Microscopy. In all the cases, SEM images were acquired on a JEOL JSM 6335F microscope working at 10 kV, by depositing the sample on graphite and metallizing with Au before observation. In the particular cases of **12**/SWCNTs, **13**/SWCNTs, $\mathbf{13_220}$ and $\mathbf{13_221}$ a previous treatment of the samples was necessary in order to remove the occluded water without perturbing the structure of the materials: concentrated samples were fixed by an aqueous solution of glutaraldehyde and paraformaldehyde (2.5% and 4%, respectively) for 2 h. After washing several times with deionized water, sample dehydration

was carried out by slow exchanging with a gradient of water–ethanol mixtures (30, 50, 70 up to 100% of ethanol) until the gel was in 100% ethanol. Samples were immersed in each solution for at least 10 min. The ethanol was removed by critical point drying.

Transmission Electron Microscopy. TEM images were performed in a JEOL JEM 1011 electron microscope operated at 100 kV. Images were directly recorded using a GATAN Erlangshen ES 1000W camera attached to the microscope. In the case of HRTEM, images were acquired in a JEOL JEM 3000F electron microscope operated at 300 kV. The samples were prepared by drop-casting the samples on Lacey carbon film on 200 mesh copper grids and drying by air for 24 hours. In the case of **$13_2$20** and **$13_2$21**, samples were negatively stained with 2% uranyl acetate on carbon coated grids for 1 minute as follows: A small drop of the sample is deposited on the carbon coated grid, allowed to settle/incubate for approximately one minute, blotted dry, washed with water for 5 minutes and then covered with a small drop of the stain (2% uranyl acetate). After 1 minute, this drop was also blotted dry and washed with water. TEM images were obtained after drying the sample by air for 24 hours.

Atomic Force Microscopy. AFM images of **1**/SWCNTs, **12**, **13**, **12**/SWCNTs and **13**/SWCNTs were acquired under ambient conditions using SPM Nanoscope IIIa multimode working on tapping mode with a RTESPA tip (Veeco) at a working frequency of B235 Khz. Height and phase images were simultaneously obtained. The samples were prepared by drop-casting on freshly cleaved mica or highly ordered pyrolytic graphite and were dried under ambient conditions for 24 h. AFM images of **20**, **21**, **$13_2$20** and **$13_2$21** were performed using a JPK NanoWizard II, coupled to a Nikon Eclipse Ti-U inverted fluorescence optical microscope. NT-MDT NSG01 silicon tips grown on silicon cantilevers having typical values of 5.1 N/m for the force constant, and 150 kHz for the resonant frequency, were employed in dynamic mode at standard ambient conditions.

Powder X-Ray Diffraction. XRD was performed in a Panalytical X'Pert PRO diffractometer with Cu tube (lambda Kα = 1.54187 Å) operated at 45 kV, 40 mA, Ni beta filter, programmable divergence and anti-scatter slits working in fixed mode, and fast linear detector (X'Celerator) working in scanning mode. Samples were deposited in a silicon zero background sampleholder and measured in reflection mode.

Small-Angle X-ray Scattering. All the measurements were performed on a modified Kratky camera, enhanced by Hecus-Braun. This device is installed on a PANalytical X-ray generator PW3830.

X-ray Photoelectron Spectroscopy. XPS analysis was obtained on a SPECS GmbH (PHOIBOS 150 9 MCD) spectrometer working in the constant analyzer energy mode and a non monochromatic aluminium X-ray source (1486.61 eV) powered at 200 W and a voltage of 12 eV. For recording both survey and high resolution spectra pass energies of 75 and 25 eV were applied. Survey data were acquired from kinetic energies of 1487 – 400 eV with 0.1 eV of energy step and 100 ms dwell time per point. The high resolution scans were registered around the significant emission lines with 0.1 eV steps and 100 ms dwell time per point. The spectrometer control and data handling were monitorized using SpecsLab Version 2.48 software. Binding energies were calibrated relatively to the C 1s peak at 284.6 eV and the atomic ratios were computed from experimental intensity rations.

FP-TRMC and TAS measurements. Charge carrier mobility was evaluated by flash-photolysis time-resolved microwave conductivity (FP-TRMC) and transient absorption spectroscopy (TAS) techniques at room temperature under air. Solid films of **13**, **20**, **21**, **13$_2$20** and **13$_2$21** were prepared by drop-casting of their Milli-Q water solution. Charge carriers were photochemically generated using a third harmonic generation (λ = 355 nm) of a Spectra Physics model INDI-HG Nd:YAG laser with a pulse duration of 5–8 ns and frequency of 10 Hz. The photon density of a 355 nm pulse was 9.1×10^{15} photons cm^{-2} $pulse^{-1}$. The microwave frequency and power were set at ~9.1 GHz and 3 mW, respectively. The TRMC signal, picked up by a diode (rise time < 1 ns), was monitored by a Tektronics model TDS3032B digital oscilloscope.

Chapter 2.

TPR proteins as a new tool for the organization of organic materials.

2.1. Background

2.1. Background.

2.1.1. DNA-based nanostructures.

Proteins are the material of choice for building the structural, catalytic and regulatory components of cells, but the folding of the peptide chain using a countless number of non-covalent interactions remains challenging to predict and design, despite decades of research and undeniable progress. By contrast, DNA, as the carrier of the genetic information in cells, has only four deoxynucleotide chemical building blocks, a high chemical stability and predictable folding and assembly properties that are readily amenable to the rational design and construction of 3D nanostructures by programmable self-assembly.[61]

The DNA double helix itself, molded by Watson-Crick base pairing between complementary nucleotides, is inherently a nanoscale object; its diameter is about 2 nm and the separation of the stacking bases is 3.4 Å; the helical periodicity is 10 – 10.5 nucleotide pairs per turn, or around 3.5 nm per turn. It seems natural that the structural and biochemical knowledge of DNA gained over the past decades should be used in the emerging nanotechnology field.

DNA nanotechnology refers to the construction of supra-objects with robust topological or geometrical features from DNA components. This idea was first introduced in the early 1980s by Prof. Seeman. The great potential of DNA architectonics is best exemplified by the quasi-digital approach of scaffolded DNA origami, developed by Prof. Rothemund,[62] which can generate with remarkable efficiency any arbitrary shape and pattern with sizes ranging from 20 nm to 200 nm. In this strategy, a long single-stranded DNA scaffold is folded with complementary oligonucleotides that act as staples. Once synthetized and mixed, the staples and scaffold strands self-assemble in one single step. The structure can be programmed into complex patterns, such as words and images, as depicted in Figure 65.

61 a) N. C. Seeman, *Biochemistry* **2003**, *42*, 7259-7269; b) L. Jaeger and A. Chworos, *Curr. Opin. Struct. Biol.* **2006**, *16*, 531-543.
62 P. W. K. Rothemund, *Nature* **2006**, *440*, 297-302.

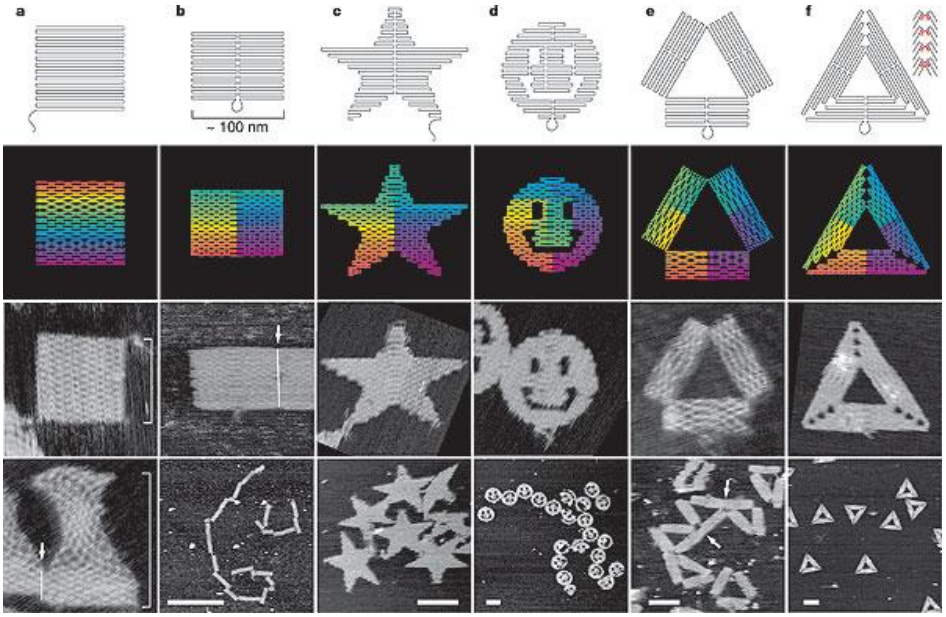

Figure 65. DNA origami shapes. (a) Square, (b) rectangle, (c) star, (d) disk with three holes, (e) triangle with rectangular domains, (f) sharp triangle with trapezoidal domains.

2.1.2. Protein-based nanostructures.

Peptides and proteins are linear polymers of α-amino acids, generally referred to as "polypeptides". The polymer chain itself is called the backbone and the chemical functionalities associated with each amino acid are known as the side chains. The conformation of polypeptide backbones are restricted by steric clashes between backbone and side-chain atoms.[63]

The two possibilities of secondary structures in proteins are the α-helix, where the conformation is obtained through internally hydrogen bonding along the polypeptide chain, and *β*-strands, where internal hydrogen bonding is not possible and, so, two or more *β*-strands pair form extended structures called *β*-sheets, already introduced in Chapter 1.

63 a) C. E. MacPhee and D. N. Woolfson, *Curr. Opin. Solid State Mater. Sci.* **2004**, *8*, 141-149; b) T. O. Yeates and J. E. Padilla, *Curr. Opin. Struct. Biol.* **2002**, *12*, 464-470; c) R. V. Ulijn and D. N. Woolfson, *Chem. Soc. Rev.* **2010**, *39*, 3349-3350.

With appropriate placement of hydrophobic and polar side chains along the polypeptide sequence, both secondary structures can be made amphipathic, that is, they can have distinct hydrophobic and polar faces, guiding their self-assembly and conforming their tertiary or even quaternary structure.

With this brief outline, the difficulty that exists nowadays to rational redesign or *de novo* design a protein with defined properties and features to form a functional material is highlighted. For this reason, the technology for the generation of protein-based materials is accomplished mostly by "trial and error" experimental approaches, having a very limited knowledge of their sequence-structure-function relationship.

Large progress has been recently developed to control assembly into tailored nanostructures, but bridging the nanoscale to the mesoscale architectures to create useful macroscopic materials remains a great challenge. Protein-based fibrillar materials created up to date can be classify into two main groups, that is, amyloid-like and α-helix-based assemblies, as detailed below:

2.1.2.1. Amyloid-like assemblies.

The design of amyloid-like fibrils relies on the general tendency of *β*-strands to aggregate. A very illustrative example where molecule-level interactions can be prolonged to a macroscopic material was described by Welland and col.[64] In this work, amyloidogenic protein molecules, intrinsically composed by *β*-sheet rich linear aggregates, assembled in a first-step into elongated fibrils where the formation of intermolecular interactions is favored over intramolecular ones. In a second-step, during the casting process, the fibrils align in the film plane with nematic order in the presence of a plasticizing additive (Figure 66). The application of this approach results in materials that have a hierarchy of length scales: nanometer ordering within the fibrils and micrometer-scale ordering in the stacking of the fibrils. Moreover, this protein-based nanostructured film possessed mechanical properties similar to that of the most rigid proteinaceous materials found in nature, such as keratin and collagen.

64 T. P. J. Knowles, T. W. Oppenheim, A. K. Buell, D. Y. Chirgadze and M. E. Welland, *Nat Nano* **2010**, *5*, 204-207.

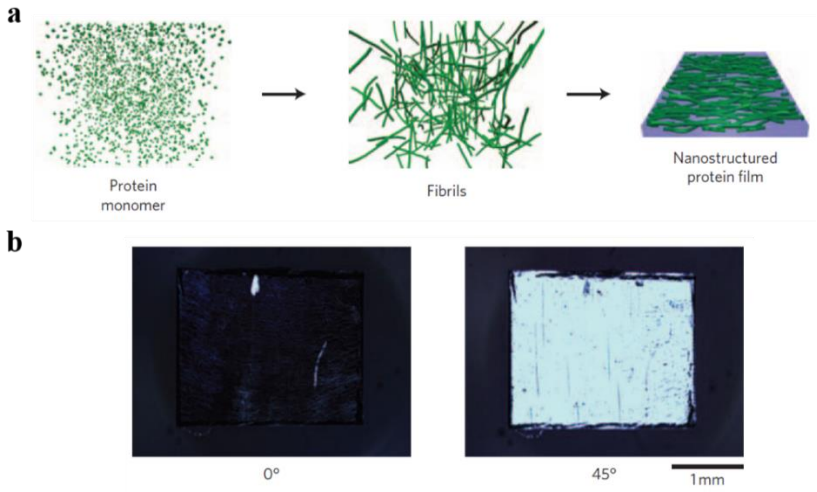

Figure 66. Example of amyloid-like assembly. (a) Multiscale hierarchical self-assembly of amyloid-like proteins into ordered films. (b) Optical images of plasticizer containing amyloid films under crossed polarizers show low transmission through the protein film when the objective polarizer is parallel to the fibril alignment in the film (left) and maximal transmission at an angle of 45º (right).

2.1.2.2. α-Helix-based assemblies.

α-Helical folding represents a more attractive perspective comparing to amyloid-like assembly since an α-helix is a "self-contained" and true element of secondary structure. Nonetheless, research activity in development of fibrous-protein materials based on the α-helix motif lags behind the corresponding in amyloid-like assemblies.

A well-studied and defined α-helical motif is the coiled-coil. In particular, considerable attention has been devoted to one type of coiled-coil architecture, namely the leucine-zipper motif, which is accepted as the archetypal two-stranded, parallel coiled-coil.[63a,63b,65] These structures can be engineered to form offset dimers with complementary sticky ends to promote

65 D. Papapostolou, A. M. Smith, E. D. T. Atkins, S. J. Oliver, M. G. Ryadnov, L. C. Serpell and D. N. Woolfson, *Proc. Natl. Acad. Sci. U.S.A.* **2007**, *104*, 10853-10858.

longitudinal assembly into fibers. Sequence-to-structure relationship tends to be better defined for these kinds of assemblies (Figure 67).

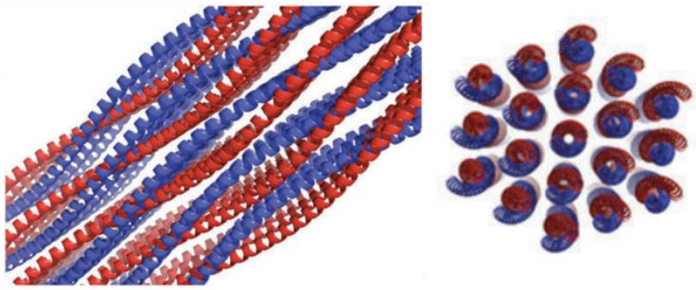

Figure 67. Filaments formed by self-assembled α-helical coiled-coils.

At this point, another particularly versatile α-helical structural motif is the tetratricopeptide repeat (TPR). Due to its high importance in this chapter, it will be tackled in a separate section.

2.1.2.3. TPR proteins: the versatile helix

The TPR is a structural motif presented in a wide range of proteins, consisting of 3 – 20 tandem-repeats of 34 amino acids residues.[66] The X-ray structure of a domain containing three TPRs from protein phosphatase 5 revealed that TPR adopts a helix-turn-helix arrangement, with adjacent TPR motifs packing in a parallel fashion, resulting in a spiral of repeating anti-parallel α-helices. The two helices are denoted helix A and helix B (Figure 68). The packing angle between helix A and helix B is around 24º within a single TPR and generates a right-handed superhelical shape in which eight repeats comprise one full turn of the superhelix. Helix A interacts with helix B and with helix A' of the next TPR.[67]

66 L. D. D'Andrea and L. Regan, *Trends Biochem. Sci.* **2003**, *28*, 655-662.
67 T. Kajander, A. L. Cortajarena, S. Mochrie and L. Regan, *Acta Crystallogr., Sect. D: Biol. Crystallogr.* **2007**, *63*, 800-811.

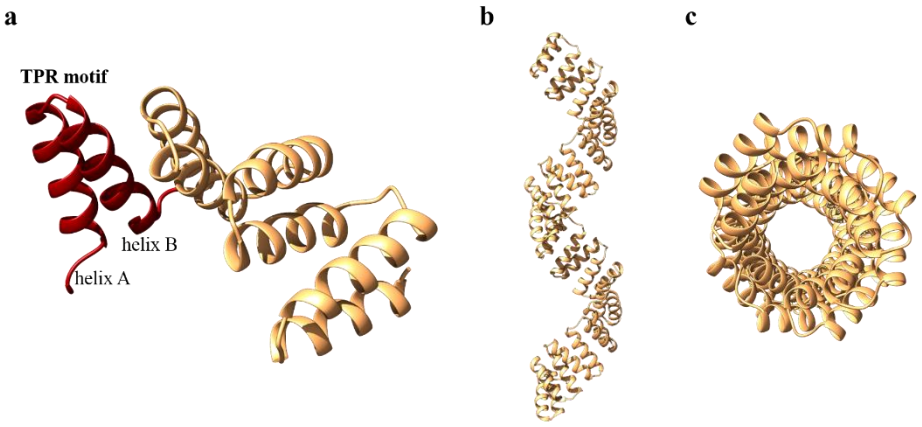

Figure 68. TPR protein. (a) Ribbon representation of 4-TPR modules. One TPR motif is coloured in red, shown the helix A-turn-helix B arrangement. (b) Perpendicular view to the superhelical axis of the crystal structure of CTPR16 in ribbon representation. (c) Same crystal structure than (b), viewed parallel to the superhelical axis.

The consensus sequence of a TPR is defined by a pattern of small and large hydrophobic amino acids. Residues are very conserved at only a few positions (e.g. Gly or Ala at position 8, and Ala at position 20 and 27); the other consensus positions have a stronger preference for a class of amino acids (small, large or aromatic) rather than for a specific residue. Furthermore, some positions are more tolerant of substitution.

A decade ago, a newly designed protein based on a statistical analysis of TPR sequences has been shown to fold into a particularly stable TPR motif. This work has made possible to consider this protein as a versatile and robust framework, where only preservation of specific positions of the sequence is sufficient to define the TPR fold.[68]

In line with the creation of protein-based nanostructured macroscopic materials, Cortajarena and col. demonstrated some years ago the ability of these CTPR proteins to retain their original structure and their functionality in the solid

68 a) E. R. G. Main, Y. Xiong, M. J. Cocco, L. D'Andrea and L. Regan, *Structure*, *11*, 497-508; b) A. L. Cortajarena, S. G. J. Mochrie and L. Regan, *Protein Sci.* **2011**, *20*, 1042-1047; c) T. Kajander, A. L. Cortajarena, E. R. G. Main, S. G. J. Mochrie and L. Regan, *J. Am. Chem. Soc.* **2005**, *127*, 10188-10190.

state.[69] In this work, the authors proved that, under certain conditions, macroscopic films were formed after solvent evaporation of a CTPR aqueous solution. In particular, the assembly of the superhelices of a CTPR18 was hypothesized to occur through head-to-tail and side-to-side interactions, similar to the ones presented in the crystalline form. Macroscopic ordering was confirmed by a wide range of techniques such as X-ray diffraction, atomic force microscopy (AFM) and fluorescence anisotropy experiments. Moreover, the α-helix folding is preserved along the solvent casting process as shown in the CD spectrum of the film, practically indistinguishable from the spectrum of the protein in solution (Figure 69).

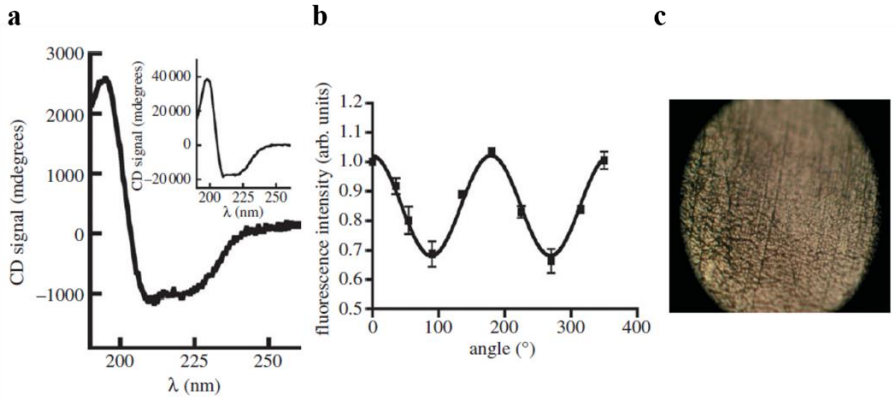

Figure 69. Structural and functional characterization of protein fims. (a) CD spectrum of a CTPR18 protein film. Inset: CD spectrum of the same protein in solution. (b) Change in fluorescence intensity of a peptide ligand bound to the film, demonstrating its anisotropy. (c) Birefringence of a CTPR protein solid film observed under a microscope with 90º crossed polarizers, showing the macroscopic alignment of the CTPR units.

2.1.3. DNA and protein as scaffolds for chromophore arrays

Nowadays, many bottom-up approaches have been undertaken to direct the self-assembly of dyes and extended π-conjugated molecules, with potential applications for light-harvesting and electronics, enabling the formation of 1D, 2D and even 3D self-assembled architectures. Nonetheless, the majority of these methodologies lacks the selective positioning of the different functional

69 T. Z. Grove, L. Regan and A. L. Cortajarena, *J. R. Soc. Interface* **2013**, *10*.

components, geometrical and relative orientational control and monodispersity. For instance, average size of the assemblies can be only partially controlled by concentration, temperature or nature of the solvent using the basic principles of supramolecular self-assembly, from an entirely chemical point of view. However, templating these components with biological or Nature's inspired scaffolds can provide the control in the location, monodispersity and chirality needed for technological purposes.

DNA is an especially appealing template because of its molecular recognition abilities enabling the formation of programmed nanostructures with geometrical, size and positional control.[70] Recently, Stulz and col. shown that a porphyrin substituted deoxy-uridine provided a versatile building block for the synthesis of porphyrin arrays on the nanometer scale (Figure 70).[71] Introducing site specifically these modified nucleobases into the DNA strands by reprogramming the input sequence in a DNA synthesizer, they are able to tune the electronic properties of the array, depending on the exact positions of the porphyrins. Moreover, it was found that the structure stabilization was independent of the number of porphyrins, thus, enlarging the attractiveness of the approach.

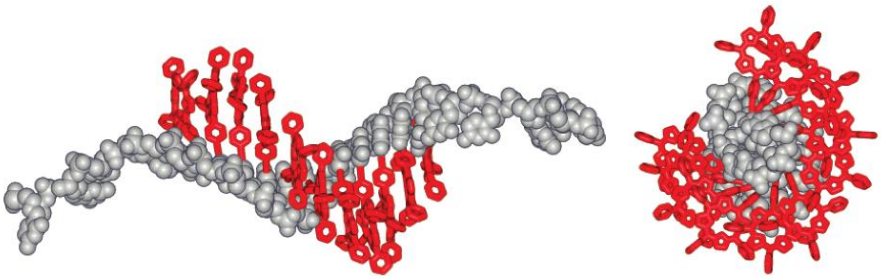

Figure 70. DNA-porphyrin conjugates. Side- and top-view of the force-field minimized structure of a single-strand DNA modified with porphyrin motifs.

70 a) Y. N. Teo and E. T. Kool, *Chem. Rev.* **2012**, *112*, 4221-4245; b) A. Ruiz-Carretero, P. G. A. Janssen, A. Kaeser and A. P. H. J. Schenning, *Chem. Commun.* **2011**, *47*, 4340-4347.

71 L.-A. Fendt, I. Bouamaied, S. Thöni, N. Amiot and E. Stulz, *J. Am. Chem. Soc.* **2007**, *129*, 15319-15329.

Peptides[72], peptoids[73] and virus capsids[74] have also been used for selectively controlling the position of a great variety of chromophores, including porphyrins. Seo and col. employed different peptoid helix scaffolds to design and synthetized porphyrin-peptoid conjugates, with precisely defined distance, orientation and number or porphyrins.[73] All conjugates were prepared by resin solid phase, by coupling of tetraphenylporphyrin (TPP) carboxylic acid to *N*-lysine primary amine of the resin bounded peptoid. A deep study about distance dependency was performed, by comparing conjugates having two porphyrins positioned one pitch or two pitches apart, on one face of the α-helix. Additionally, two porphyrins in a distorted orientation, three porphyrins on one face and an unstructured conjugate were also prepared (Figure 71). The degree of *J*-aggregation, color change, and excitonic coupling between porphyrins could be modulated, offering new insights into the design of artificial photosynthetic complexes.

72 a) A. D'Urso, M. E. Fragala and R. Purrello, *Chem. Commun.* **2012**, *48*, 8165-8176; b) J. R. Dunetz, C. Sandstrom, E. R. Young, P. Baker, S. A. Van Name, T. Cathopolous, R. Fairman, J. C. de Paula and K. S. Åkerfeldt, *Org. Lett.* **2005**, *7*, 2559-2561; c) Q. Zou, L. Zhang, X. Yan, A. Wang, G. Ma, J. Li, H. Möhwald and S. Mann, *Angew. Chem., Int. Ed.* **2014**, *53*, 2366-2370.

73 B. Kang, S. Chung, Y. D. Ahn, J. Lee and J. Seo, *Org. Lett.* **2013**, *15*, 1670-1673.

74 a) M. Endo, H. Wang, M. Fujitsuka and T. Majima, *Chem. Eur. J.* **2006**, *12*, 3735-3740; b) M. Endo, M. Fujitsuka and T. Majima, *Chem. Eur. J.* **2007**, *13*, 8660-8666.

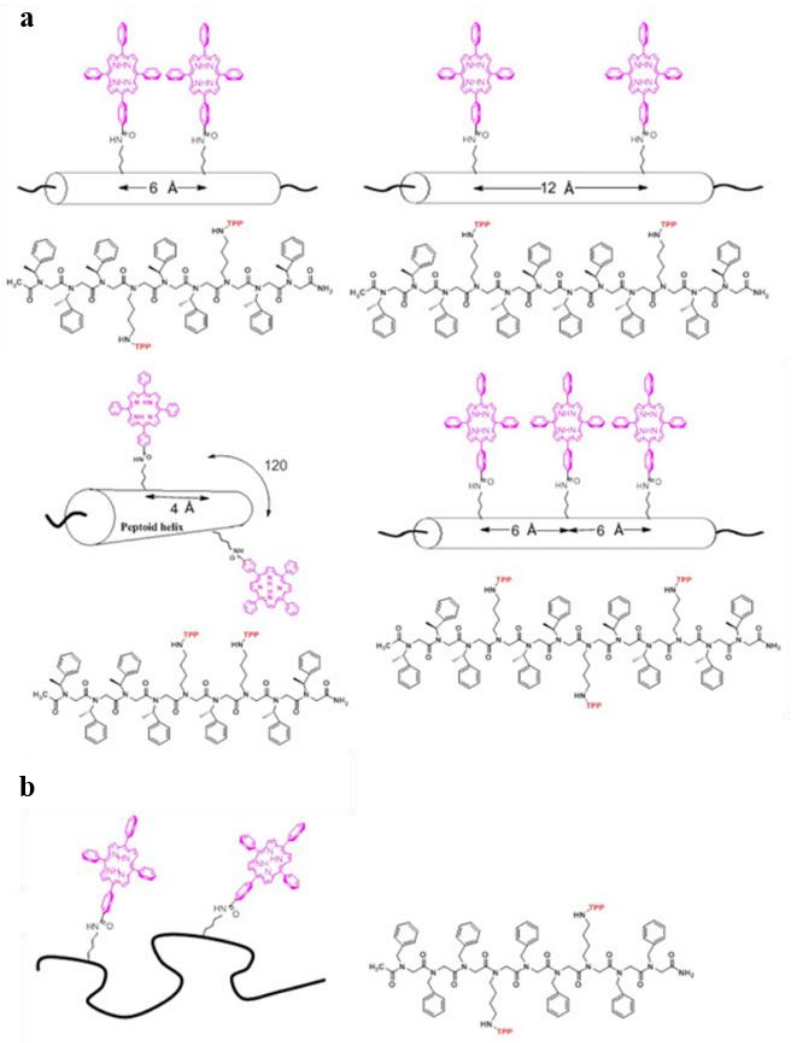

Figure 71. Distance, orientation and number-controlled porphyrin-peptoid conjugates. (a) Helical peptoid scaffolds with four different configurations. (b) Unstructured peptoid scaffold.

Meanwhile, Majima and col. demonstrated the construction of multiple porphyrin arrays in the tobacco mosaic virus (TMV) supramolecular structures (Figure 72).[74b] Firstly, a porphyrin derivative was incorporated at the 127 position of the TMV coat protein (TMVCP) monomer by a maleimido-thiol coupling reaction. Nanostructures of TMV are easily controlled by pH values of the solution, assembling the monomers into double-layered disk-like structures or even multiple-layered rod like structures by decreasing the pH value. In this sense, hierarchical structures of the porphyrin-TMVCP monomer were obtained using this protocol and examined by AFM. Moreover, photophysical studies of the aggregates were performed to prove the interactions of porphyrins in the assembly.

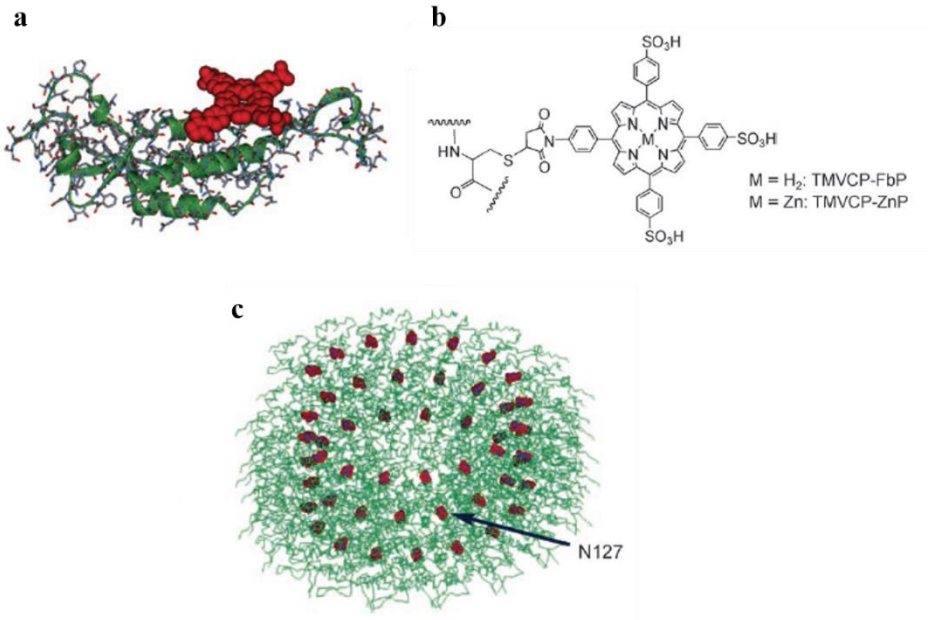

Figure 72. Structure of TMV and TMVCP conjugated with porphyrin derivatives. (a) Structure of TMVCP–porphyrin conjugated monomer; the porphyrin moiety was introduced at the 127 position. (b) Porphyrin derivatives introduced to the cysteine residue of a TMV monomer through maleimido–thiol coupling. (c) Crystal structure of the TMV assembly; amino acid N127 is shown in red.

2.1.4. Non-covalent interactions between proteins and CNTs

In the background section of Chapter 1, one representative example of assembly based on peptides and CNTs was introduced. Now, in this section, we go in depth on this topic giving some illustrative cases of non-covalent interactions between proteins and CNTs.

Although several examples can be found in the literature regarding DNA-based systems with CNTs to produce highly ordered materials,[44-45,75] to the best of our knowledge, this topic remains challenging in the field of protein scaffolds probably due to the limited understanding of their sequence-structure-function relationship to fabricate *de novo* designs.

Nonetheless, some evaluations of non-covalent interactions between complex proteins and these carbon nanostructures have been performed during the last years.[76] Two of these have been chosen as representative examples of the different nature of the supramolecular forces that enable these interactions:

In the first one, Fang and col. demonstrated by Molecular Dynamic (MD) simulations the introduction of SWCNTs of different diameters inside the hydrophobic pocket of a WW domain of a protein.[77] Trp and Tyr residues in this binding site of WW protein were found to stabilize this interaction through π-stacking between the aromatic side-chain of the amino acids and the surface of CNTs. Interestingly, this contact resulted in the alteration of the functionality of the protein, inhibiting the recognition of PRM ligand (Figure 73).

75 B. Gigliotti, B. Sakizzie, D. S. Bethune, R. M. Shelby and J. N. Cha, *Nano Lett.* **2006**, *6*, 159-164.
76 F. De Leo, A. Magistrato and D. Bonifazi, *Chem. Soc. Rev.* **2015**.
77 G. Zuo, Q. Huang, G. Wei, R. Zhou and H. Fang, *ACS Nano* **2010**, *4*, 7508-7514.

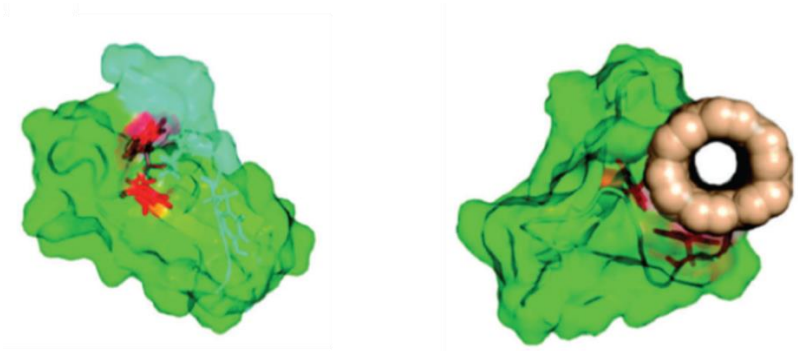

Figure 73. Binding of a SWCNT to WW domain. Representation of WW domain in complex with the PRM ligand (left) and with a SWCNT (right).

In the other example, reported by Bonifazi and col., the interactions between the monoclonal Ab Cetuximab (Ctx) and CNTs of different diameters were studied by experimental and theoretical approaches.[78] Investigations by MD simulations and Density Functional Theory (DFT) calculations revealed that the most interacting residues with CNTs were the charged (Arg, Lys and Glu) and the polar ones (His and Thr), as shown in Figure 74. These charged or polar moieties in the amino acids pointed towards the solvent, while the long alkyl chains would act as surfactants when contacting with the CNTs. Thus, the nature of this binding was, as the previous example, hydrophobic but involving other kind of aminoacids and not only aromatic ones.

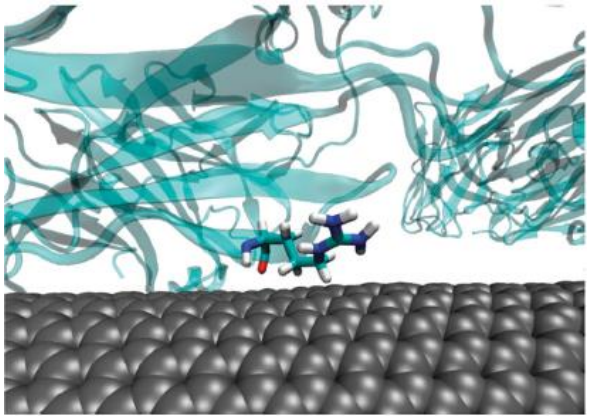

Figure 74. Orientation of Arginine residue in Ctx onto the surface of a CNT.

78 R. Marega, F. De Leo, F. Pineux, J. Sgrignani, A. Magistrato, A. D. Naik, Y. Garcia, L. Flamant, C. Michiels and D. Bonifazi, *Adv. Funct. Mater.* **2013**, *23*, 3173-3184.

2.2. Objectives

2.2. Objectives

In this chapter, we focus on the evaluation of CTPR proteins as robust frameworks for their use in nanotechnological applications.

As first objective, we will exploit the two unique features of the CTPR proteins, namely: i) the structural understanding of the CTPR module and the small number of conserved residues that define the CTPR fold to accurately modify selected positions of the amino acid sequence without perturbing its secondary structure and ii) the extraordinary capability of CTPR scaffolds to form nanostructured solid films, to ultimately employing them as a framework to fabricate well-ordered hybrid bio-organic materials. In particular, we will evaluate a mutated CTPR protein with four repeats, **CTPR4**, as scaffold of photoactive porphyrin arrays both in solution and in the solid state through the conjugation of mutated residues of the protein with maleimide functional group in the design porphyrins.

The second objective will be testing these proteins and their corresponding bio-organic porphyrin-protein conjugates as wrapping agents for SWCNTs, for obtaining stable nanohybrids. In this case, we will take advantage of the peculiar superhelical conformation of CTPR proteins with an optimal inner cavity for accommodating this carbon nanostructure. Specifically, three different lengths of CTPR proteins will be evaluated: **CTPR4**, **CTPR8** and **CTPR16**; together with their corresponding conjugates with a zinc metalloporphyrin derivative, in order to clarify the importance of the preorganization and steric hindrance of these systems for the achievement of our goal.

2.3. Results and Discussion

2.3. Results and Discussion

2.3.1. TPR protein scaffolds as templates for ordering porphyrin arrays in solution and solid state.

In this work, we use a designed CTPR protein as scaffold for assembling photoactive porphyrin rings in solution and solid state.

Thus, we describe in this section the design and synthesis of two porphyrin derivatives and the design of the mutated protein. Moreover, the characterization in solution of the bio-organic conjugates obtained is fully detailed. In the next stage, solid thin films of these conjugates are prepared and studied in terms of organization and orientation. Finally, the anisotropic photoconductive properties of these ordered solid materials are elucidated.

*2.3.2.1. Design and synthesis of porphyrin derivatives **25** and **26***

In the design of the porphyrin moiety two important requirements should be considered: (i) porphyrin molecules must exhibit high solubility in water avoiding charged functional groups, since undesired interactions with charged side-chains of the aminoacids inside the protein sequence should be eliminated and, (ii) an efficient cross-linker must be placed in the porphyrin structure in order to promote quantitative or quasi-quantitative conjugation with the cysteine residues of the designed protein. With this in mind, two porphyrin derivatives were synthesized, free-base and zinc-metalloporphyrin (**25** and **26**, respectively), decorated with twelve triethyleneglycol water-soluble tails and a maleimide reactive group as efficient cross-linker for the conjugation reaction with the cysteine residues in CTPR protein (Scheme 12).

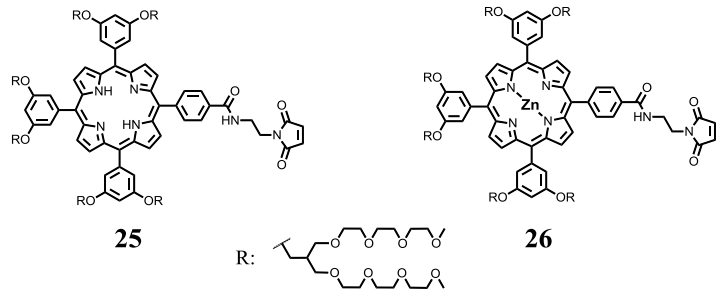

25 **26**

Scheme 12. Designed porphyrin derivatives 25 and 26.

Firstly, the synthesis of tosylate derivative **27** was carried out, according with Scheme 13. For this purpose, a previously described procedure was followed, involving *o*-alkylation of two triethyleneglycol monomethyl ethers with 3-chloro-2-(chloromethyl)-1-propene, hydroboration-oxidation of the corresponding alkene and tosylation of the primary alcohol, yielding **27** in multigram amount.[79]

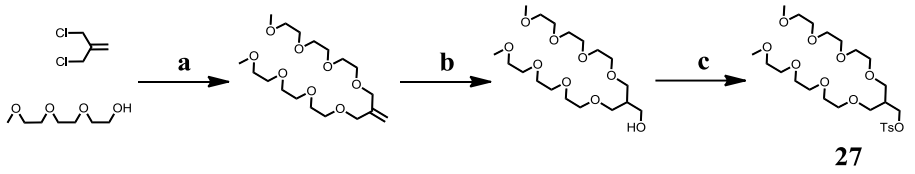

27

Scheme 13. Synthetic scheme for the synthesis of tosylate 27. (a) NaH, dry THF, rt to 65 ºC, 85%; (b) 1. BH_3, THF, 0 ºC; 2. NaOH; 3. H_2O_2, rt, 80%; (c) 4-toluenesulfonyl chloride, Et_3N, dry CH_2Cl_2, rt, 55%.

Meanwhile, the AB_3-type porphyrin **29** was synthesized by acid-catalyzed cross-condensation according to the Lindsey procedure,[80] using pyrrole, 3,5-dimethoxybenzaldehyde and methyl 4-formylbenzoate as starting materials. After dealkylation of methoxy groups in **28** with BBr_3 and subsequent etherification of **29** with tosylate **27**, intermediate **30** was obtained in good yield. Finally, target porphyrin **25** was obtained by basic hydrolysis of the ester **30** yielding **31** and amidation reaction of the corresponding carboxylic acid with 2-maleimidoethylamine (Scheme 14).

79 I.-S. Park, Y.-R. Yoon, M. Jung, K. Kim, S. Park, S. Shin, Y.-b. Lim and M. Lee, *Chem. Asian J.* **2011**, *6*, 452-458.

80 a) J. S. Lindsey, I. C. Schreiman, H. C. Hsu, P. C. Kearney and A. M. Marguerettaz, *J. Org. Chem.* **1987**, *52*, 827-836; b) D. Paul, H. Miyake, S. Shinoda and H. Tsukube, *Chem. Eur. J.* **2006**, *12*, 1328-1338.

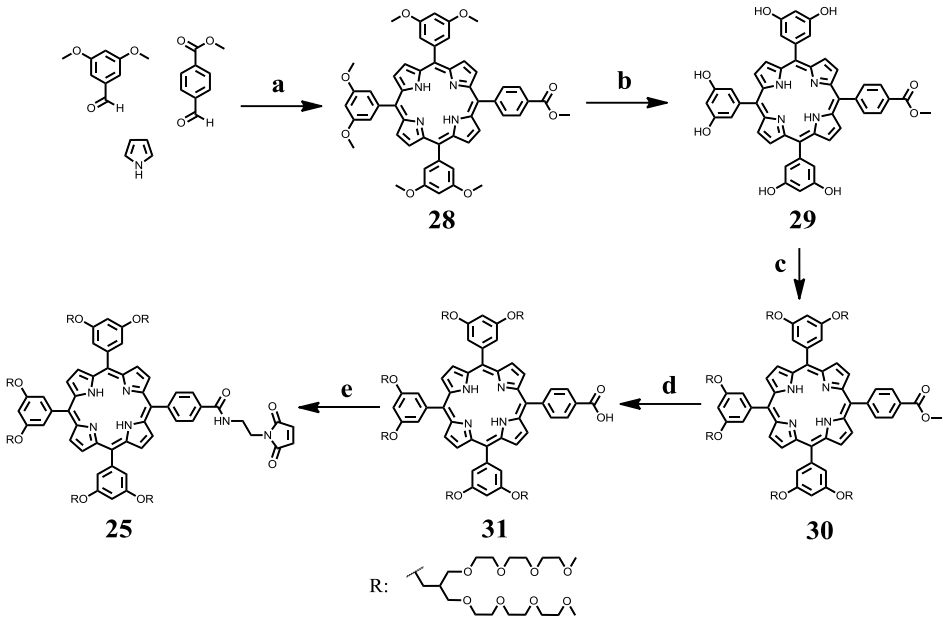

Scheme 14. Synthetic scheme for the synthesis of porphyrin 25. (a) 1. $BF_3 \cdot OEt_2$, dry $CHCl_3$, rt; 2. 2,3-dichloro-5,6-dicyano-1,4-benzoquinone, 15%; (b) BBr_3, dry CH_2Cl_2, 0 ºC to rt, 90%; (c) 3,6,9-trioxadecyl *p*-toluenesulfonate, K_2CO_3, 18-crown-6, DMF, 80 ºC, 64%; (d) KOH, THF:H_2O, reflux, 51%; (e) 2-maleimidoethylamine trifluoroacetate salt, HBTU, Et_3N, CH_2Cl_2, rt, 73%.

Zinc porphyrinate **26** was obtained from compound **25** by treatment with $Zn(OAc)_2$ in good yield, as shown in Scheme 15.

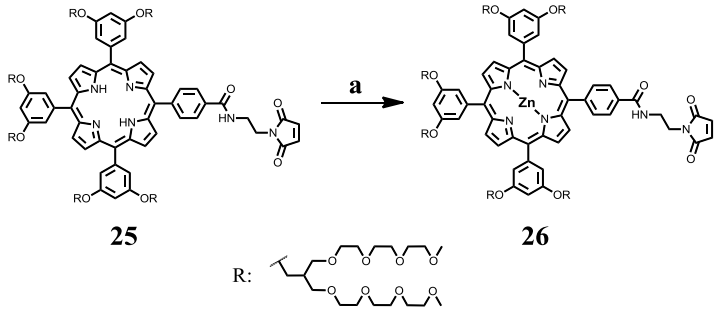

Scheme 15. Synthetic scheme for the synthesis of porphyrin 26. (a) $Zn(OAc)_2 \cdot 2H_2O$, CH_2Cl_2/CH_3OH, rt, 83%.

2.3.2.2. *Design and synthesis of* mutated *CTPR protein*

Without going into details about the synthesis of the protein, since this part of the project has been performed in the group of Dr. Cortajarena, it is important to emphasize the main features of the protein design to facilitate the understanding of the approach:

As there are only few conserved residues that define the CTPR fold,[68b] modifications can be introduced in the CTPR sequence in selected residues without significantly affecting the structure or the stability of the protein scaffold. In this sense, large quantities of homogeneous and monodisperse protein material were produced using bacterial recombinant expression systems. In a TPR protein containing four repeat units, that is, **CTPR4**, two cysteine residues were introduced in the loops of each repeated unit to provide unique reactivities for the immobilization of the porphyrins through a maleimide-thiol bond (Figure 75a). Thus, mutated **CTPR4** resulted in a protein with eight *quasi*-equally spaced cysteine residues in four loops of the protein (Figure 75b). The distance between the Cys side chains is about 7 - 8 Å, in the order of the distance required to establish π-π interactions between the porphyrin rings, in a *J*-type aggregate. A well-expressed, stable protein sample with the same helical structure as the parent protein was obtained, as demonstrated by CD studies (Figure 75c).

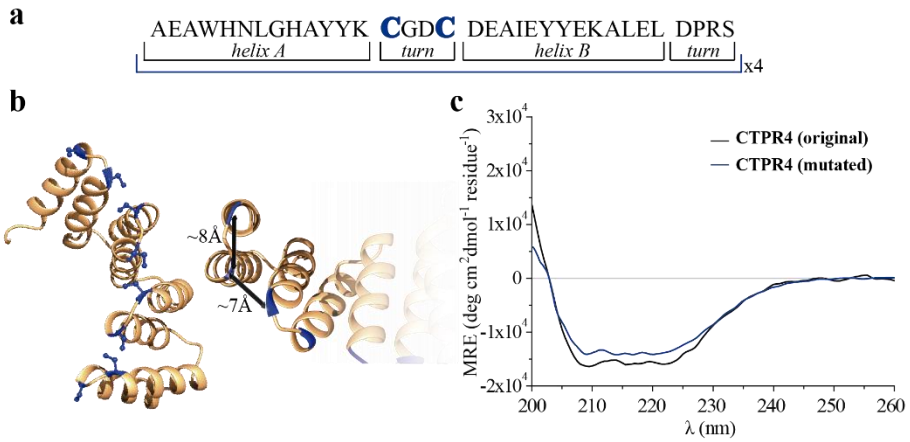

Figure 75. Mutated CTPR4 protein. (a) Sequence of amino acid of the repeat module, highlighting the positions 14 and 17 that have been mutated to Cysteine. (b) Ribbon representation of mutated **CTPR4** protein structural model based on the structure of **CTPR8** (PDB ID: 2HYZ[67]). The mutated cysteine residues for the porphyrin attachment are highlighted in blue. (c) CD spectra of mutated **CTPR4** comparing with the original **CTPR4**.

2.3.2.3. *Synthesis of **CTPR4-25** and **CTPR4-26** conjugates*

The designed protein (**CTPR4**) and porphyrin moieties (**25** or **26**) were conjugated using the maleimide-cysteine chemistry, as follows: 300µl of 50µM of freshly reduced protein was mixed with 40 equivalents of **25** or **26** giving a ratio of 1:5 cysteine:maleimide and shaken gently. After one hour, an extra of 20 equivalents of **25** or **26** were added to the mixture giving a final ratio 1:7.5 cysteine:maleimide. The conjugation reaction is displayed in Figure 76.

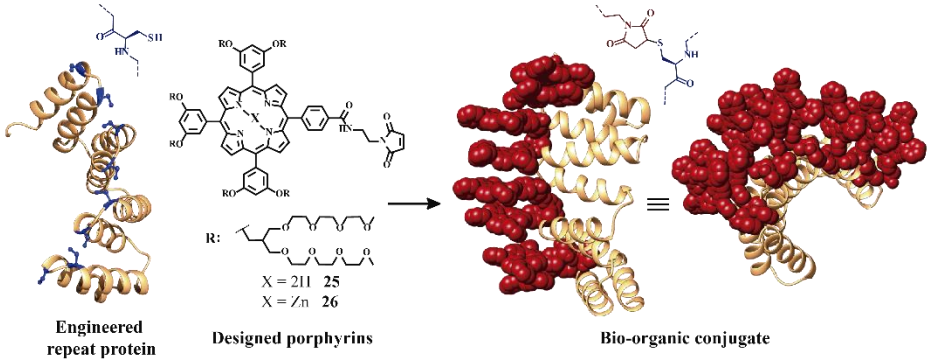

Figure 76. Conjugation reaction to obtain conjugates CTPR4-25 and CTPR4-26. Schematic representation of the maleimide-cysteine reaction between mutated **CTPR4** and porphyrin **25** or **26**. The conjugate is shown from different perspectives.

At different times during the conjugation reaction, the analysis of the samples by gel electrophoresis showed that a conjugate of higher molecular weight than **CTPR4** protein (MW = 19163 Da) and porphyrins (MW_1 = 3160 Da, MW_2 = 3223 Da) was obtained even at the shortest reaction time (Figure 77a). When the gel was imaged without staining, the fluorescence signal of the porphyrin could be detected showing a new band between 31 KDa and 45 KDa, corresponding to the molecular weight expected for **CTPR4-25** or **CTPR4-26** conjugates, containing from four to eight porphyrin moieties. Moreover, the staining of the protein with Coomassie Blue confirmed that the higher molecular weight band was composed of both protein and porphyrin.

To quantify the number of porphyrin molecules bound per protein in the conjugation reaction, mass spectrometry was used (Figure 77b). After three-hour reaction time, there was not signal corresponding to the **CTPR4** protein and the most abundant peak appeared at 41 KDa in the case of conjugated **CTPR4-25**, which corresponds to the **CTPR4** protein covalently linked to six to eight porphyrin units.

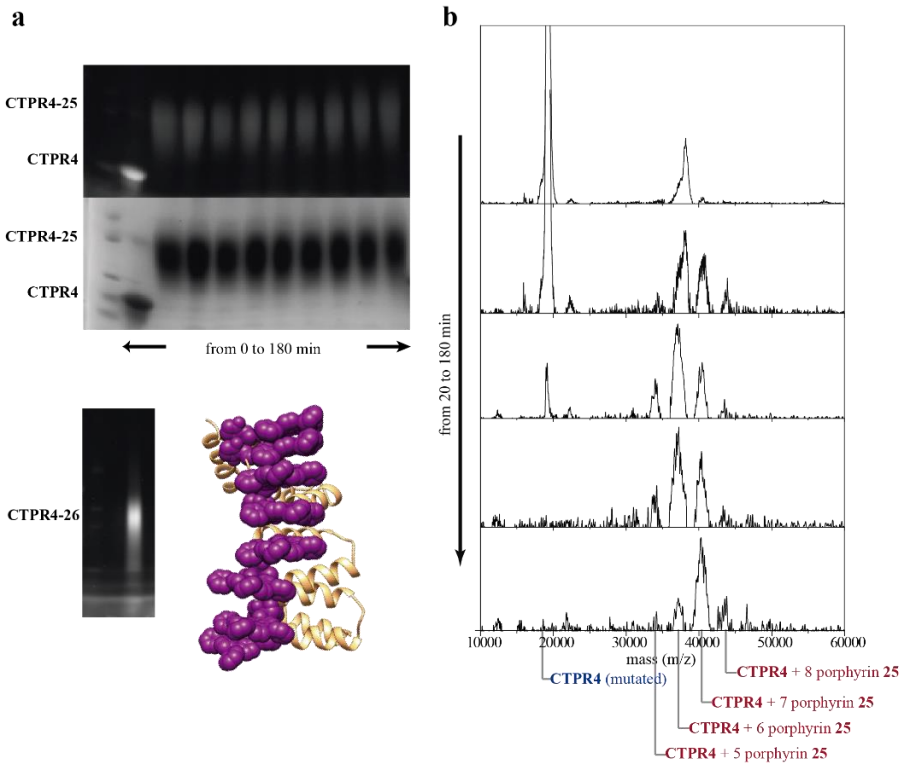

Figure 77. Monitoring experiments for the conjugation reaction. (a) Top: SDS-Page electrophoresis gel of the **CTPR4-25** conjugation at different reaction times (20, 40, 60, 80, 100, 120, 140, 160 and 180 minutes, lanes 3 to 11). Molecular weight marker (lane 1) and CTPR4 control protein with Amresco EZ-vision fluorescent loading buffer (lane 2). The gel is shown prior staining imaged using UV-light to monitor the fluorescence of the porphyrins (upper panel) and after Coomassie Blue staining (lower panel). Bottom: SDS-Page electrophoresis gel of the **CTPR4-26** conjugate. Molecular weight marker with Amresco EZ-vision fluorescent loading buffer (lane 1) and **CTPR4-26** conjugate (lane 2). (b) MALDI-TOF spectra of the conjugation reaction in **CTPR4-25** at different reaction times.

The purification of the protein-porphyrin conjugates from the excess of free porphyrin is an essential step for further use and characterize homogeneous hybrid structures. **CTPR4-25** and **CTPR4-26** purification was successfully carried out using size exclusion chromatography (Figure 78). All the characterization experiments were performed using the purified conjugates.

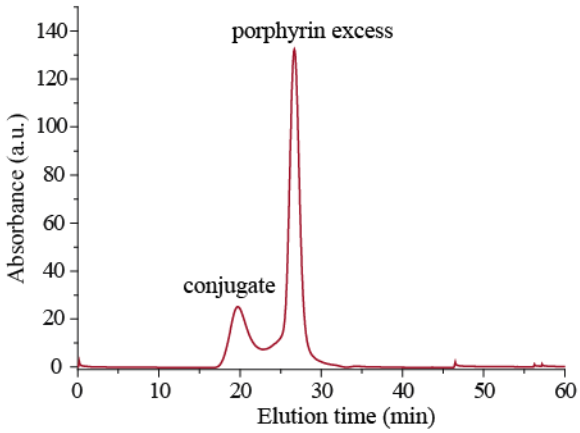

Figure 78. Size exclusion chromatogram of the purification process of the conjugate for removing the excess of porphyrin.

2.3.2.4. Characterization of conjugates in solution

As it has been previously mentioned, **CTPR4** protein was designed with an appropriate distance between the reactive moieties that, considering the rotational freedom of both the protein side chains and the linked porphyrins, will enable an efficient π-π intermolecular interaction between porphyrin rings. It is well established that porphyrins have the ability to self-aggregate noncovalently to form *H*-aggregates (face to face) or *J*-aggregates (side to side), depending on whether the Soret and Q bands are blue or red shifted, respectively, comparing with to the Soret and Q bands of the monomer.

Thus, the UV-*vis* spectrum of both porphyrins, **25** and **26**, as references and **CTPR4-25** and **CTPR4-26** conjugates were recorded in order to obtain more information about the conformation of the porphyrins in the conjugates. The absorption spectrum of porphyrin **25** in a PBS buffer solution presents an intense Soret band at 406 nm and four Q-bands in the region between 500-700 nm. Meanwhile, porphyrin **26** presents the Soret band at 425 nm and two feature Q-bands at 555 and 595 nm. However, the UV-*vis* spectra for **CTPR4-26** and **CTPR4-25** conjugates showed a red shift of 5 and 18 nm in the Soret band of the porphyrin, respectively (Figure 79a,c). Furthermore, this red shifting was also noticeable in the Q-bands, for the case of **CTPR4-26**. These shifts suggest the formation, in both conjugates, of *J*-type porphyrin arrays, certainly induced by the geometry of the protein and the exact locations of the cysteines in the structure. To further confirm the π-π interaction between porphyrin moieties

within the conjugates, UV-*vis* spectra were measured at different H_2O:CH_3OH ratio leading to an increased intensity and a blue-shift of the Soret band, and the Q-bands in **CTPR4-26**, while the percentage of methanol increased (Figure 79b,d). This fact is in agreement with the disruption of the π-π interaction when the protein scaffold is unstructured due to the denaturalization process with an organic solvent.

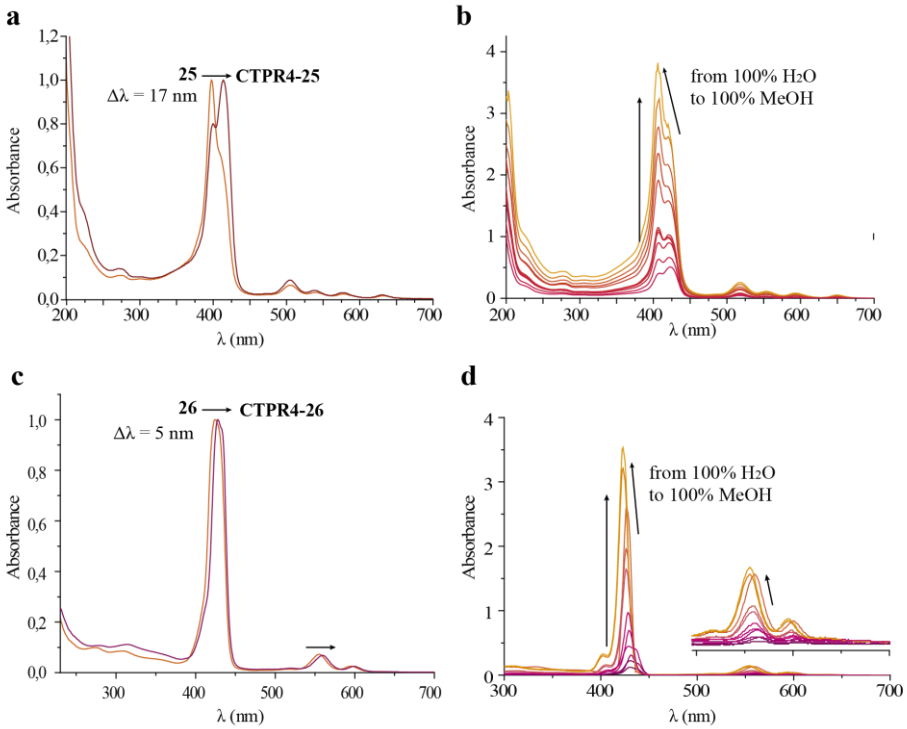

Figure 79. UV-*vis* spectra of conjugates. (a,c) Normalized UV-*vis* spectrum of **CTPR4-25** and **CTPR4-26** conjugates, respectively, compared to UV-*vis* spectra of **25** and **2**, respectively, in PBS buffer. (b,d) UV-*vis* spectra of **CTPR4-25** and **CTPR4-26**, respectively, at different methanol concentrations. Arrows show the increase of the methanol concentration from 0 to 100%.

CD studies in solution were performed on the **CTPR4-25** and **CTPR4-26** conjugates (Figure 80). In the first case, **CTPR4-25** conjugate showed a bisignate signal with a negative Cotton effect at 417 nm, a positive Cotton effect at 428 nm and a zero cross point at 423 nm. In the second case, a strong trisignate signal with a negative Cotton effect at 425 nm, positive Cotton effect at 434 nm and another negative Cotton effect at 446 nm with zero cross points at 429 nm and 442 nm was showed for the **CTPR4-26** conjugate. These dichroic signals in

the porphyrin absorption region further confirmed the selective positioning of the different porphyrin moieties and demonstrated the transfer of chirality from CTPR protein scaffold to the porphyrin molecules, since free porphyrins **25** and **26** lacked of optical activity in the CD spectrometer (Figure 80a). Furthermore, the feature CD signal for alpha-helical secondary structure of the **CTPR4** protein was retained in both **CTPR4-25** and **CTPR4-26** conjugates (Figure 80b). This result verified the successful ability of CTPR proteins to be used as scaffold for ordering organic chromophores, preserving its secondary and tertiary structure even when six to eight porphyrin molecules were incorporated. It is important to note that the final molecular weight of both conjugates represent more than twice the initial one corresponding to the protein alone; however, the structural integrity of the biological framework is fully conserved.

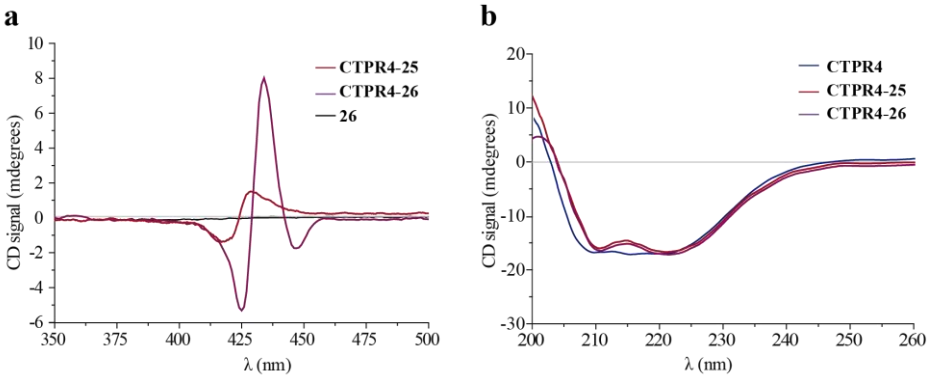

Figure 80. Circular dichroism spectra of conjugates. (a) Circular dichroism spectra of porphyrin **26** and **CTPR4-25** and **CTPR4-26** conjugates in PBS buffer in the spectral region of the porphyrin absorption. (b) Circular dichroism spectra of **CTPR4**, **CTPR4-25** and **CTPR4-26** conjugates in PBS buffer in the spectral region of the protein's secondary structure elements absorption.

2.3.2.5. *Characterization of conjugates in the solid state*

One valuable advantage that provides the use CTPR proteins to organize porphyrins is the capability to control the assembly into higher ordered thin films.[69] The formation of protein-based solid ordered materials has been achieved in very few protein systems. Furthermore, the combination with the building-block tunability is unique of the CTPR scaffold. Given the good results in terms of structural stability of **CTPR4-25** and **CTPR4-26** in solution, we expected that the **CTPR4** protein framework would impose a similar directional order at larger scales, that is, in the solid film scale into the porphyrin molecules.

In this sense, thin films with both conjugates were successfully generated under similar experimental conditions to those used for CTPR proteins alone (Figure 81a,b).[69] Initially, CD experiments of the **CTPR4-25** and **CTPR4-26** conjugate films were recorded to examine two important points: (i) if the protein structure is retained in the film and (ii) if the porphyrins are organized within the film. Figure 81c,d showed how the secondary structure of **CTPR4** protein and the chiral environment of the porphyrins were maintained.

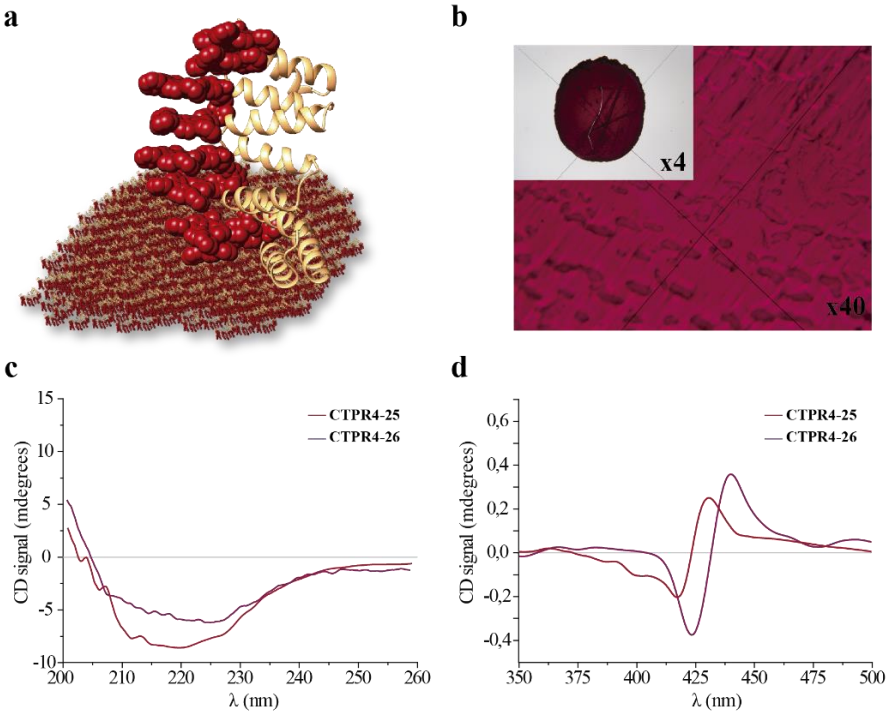

Figure 81. Characterization of CTPR4-25 and CTPR4-26 conjugates in the solid state. (a) Schematic representation of the oriented film obtained from the porphyrin-protein conjugate. (b) Photograph of a thin film obtained after evaporation of a 5% w/v **CTPR4-26** in 10 mM sodium chloride, 10 mM sodium phosphate buffer (pH = 7.0) on Teflon tape. (c) Circular dichroism of the **CTPR4-25** and **CTPR4-26** conjugates in solid thin films in the spectral region of the protein's secondary structure elements absorption. (d) Circular dichroism of the **CTPR4-25** and **CTPR4-26** conjugates in solid thin films in the spectral region of the porphyrin absorption.

Moreover, as it has been previously reported, CTPR proteins are macroscopically aligned in these films, thus it was expected that our conjugates would also be aligned. To shed light on this fact, fluorescence anisotropy and

XRD measurements were carried out. Figure 82a shows the change in the fluorescence intensity of the porphyrin moieties when the emission polarizer was rotated from 0º to 360º. The signal showed clear maximum and minimum values, which indicates the anisotropy of the sample. The data can be well fitted to a sine wave function with maximum to minimum peak distance of 107º, in agreement with the alignment phase determined for the CTPR films.[69] This result indicates that the macroscopic ordered pattern of the film is indeed imposed on the porphyrins that are, otherwise, isotropic.

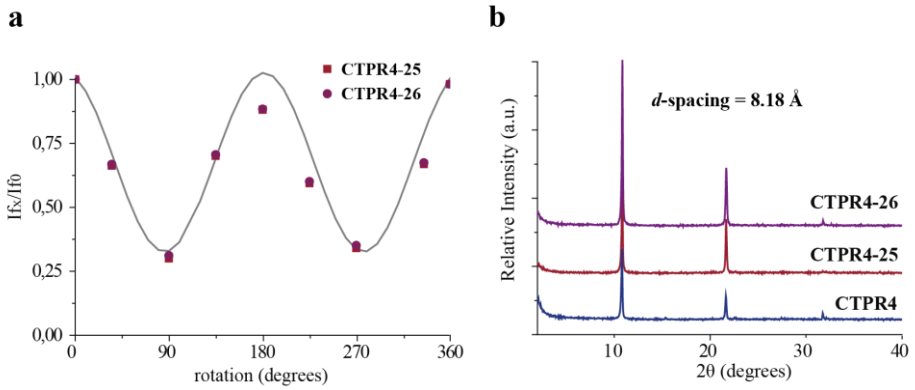

Figure 82. Characterization of CTPR4-25 and CTPR4-26 conjugates in the solid state. (a) Fluorescence anisotropy of the **CTPR4-25** and **CTPR4-26** films. The fluorescence intensity of the porphyrin is plotted as function of the angle of the emission polarizer when the excitation polarizer is fixed at 0º. The intensity data are shown as filled squares, the best fit of the data to a sine wave function (y = baseline + amplitude sin (frequency X + phaseshift)) is shown as a solid line. (b) X-ray powder diffractogram of **CTPR4**, **CTPR4-25** and **CTPR4-26** thin films.

A deep understanding on the organization of the films was reached by XRD experiments. The XRD pattern of a film obtained from **CTPR4** protein showed a set of three clear and intense sharp peaks at 2θ = 10.82º, 21.64º and 32.05º that could correspond to a lamellar packing with a periodical *d*-spacing of 8.18 Å (Figure 82b). These *d*-spacing is not easy to index attending to the crystal structure of the protein.[67] Nonetheless, these data demonstrate the remarkable orientation of the protein on a surface when is forming a film. Moreover, the most interesting finding came from the diffraction patterns observed for the films of both porphyrin conjugates (**CTPR4-25** and **CTPR4-26**), which presented exactly the same reflections peaks as **CTPR4** (Figure 82b). These experimental findings indicate that the long-range order of the protein is

preserved even with this number of porphyrins introduced in its structure, thus highlighting the robustness of this biological scaffold to be used as an efficient template for ordering organic chromophores not only in solution but in the technologically relevant solid state.

2.3.2.6. Characterization of the anisotropic photoconductivity of the thin films

Organized porphyrin arrays on the protein scaffold are interesting as charge carrier transporting and photoconductive motifs. The photoconductivity along the arrays in **CTPR4-25** and **CTPR4-26** conjugate films was examined by using FP-TRMC technique.[59-60] In this non-contact method, charge carriers are photo-generated upon exposure to 355 nm laser pulses to the films. Then, local-scale motions of the generated charge carriers can be probed by monitoring the reflected microwave (~9.1 GHz) power from the film sample set at the microwave cavity.

Upon laser flash, drop-cast film of **CTPR4-25** showed a conductivity transient with prompt rise and slow decay features (Figure 83a). The conductivity ($\phi\Sigma\mu$) indicates the product of charge carrier generation efficiency (ϕ) upon photoexcitation and sum of charge carrier mobilities ($\Sigma\mu$: $\mu_h + \mu_e$). At the same time, the same film yielded a clear transient absorption spectra (TAS), where photo-bleach of the neutral and generation of radical cations were observed at the Q-band region of free-base porphyrins (Figure 83b). In fact, the normalized profiles of FP-TRMC and TAS at 530 nm gave almost identical kinetic traces, indicating that hole transport is the dominant factor for the observed local-scale photoconductivity of **CTPR4-25** under air. By using a typical absorption coefficient of the radical cation of tetraphenyl free-base porphyrin,[81] ϕ was calculated to be 5.0×10^{-2}, followed by the evaluation of one-dimensional mobility (μ_h) of 1.5×10^{-3} $cm^2V^{-1}s^{-1}$. Then, through the same measurement processes, μ_h of **CTPR4-26** was determined as 1.3×10^{-3} $cm^2V^{-1}s^{-1}$ (Figure 84).

81 Z. Gasyna, W. R. Browett and M. J. Stillman, *Inorg. Chem.* **1985**, *24*, 2440-2447.

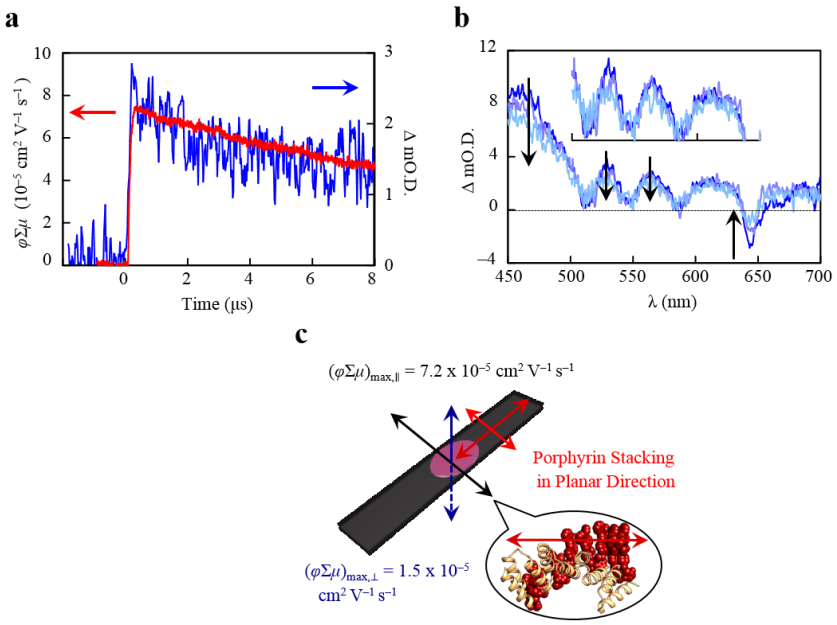

Figure 83. Photoconductivity of CTPR4-25 thin films. (a) Kinetic traces of FP-TRMC (red) and transient absorption spectra of a film of **CTPR4-25**. (b) Snapshot of transient absorption spectra of a film of **CTPR4-25** at ca. 0.2 (blue), 3 (light purple), and 8 (turquoise) μs after an excitation. (c) Schematic illustration of a **CTPR4-25** film on a quartz and stacking direction of porphyrin arrays together with observed values of conductivity maxima in perpendicular and planar direction to the substrate surface.

Of further interest, we revealed that structural alignment of the arrays in a macroscopic scale gave rise to anisotropic electrical conductivity. For example, by changing the direction of the **CTPR4-25** sample in the cavity,[82] $(\phi\Sigma\mu)_{max}$ along the perpendicular and parallel directions to the substrate surface were evaluated as 1.5 x 10^{-5} and 7.2 x 10^{-5} $cm^2V^{-1}s^{-1}$, respectively (Figure 83c). The degree of anisotropy of ca. 5 suggests the stacking direction of porphyrins should be parallel to the substrate surfaces, which agrees well with the above discussion on the porphyrin ordering and orientation in the solid state based on the fluorescence anisotropy and XRD analysis.

82 T. Osawa, T. Kajitani, D. Hashizume, H. Ohsumi, S. Sasaki, M. Takata, Y. Koizumi, A. Saeki, S. Seki, T. Fukushima and T. Aida, *Angew. Chem., Int. Ed.* **2012**, *51*, 7990-7993.

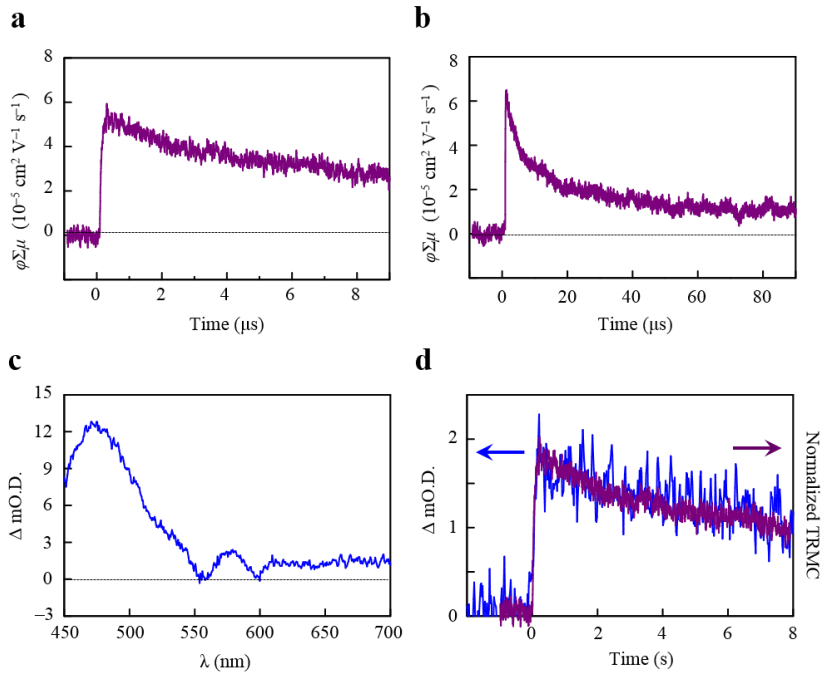

Figure 84. Photoconductivity of CTPR4-26 thin films. FP-TRMC kinetic traces of a film of **CTPR4-26** at (a) 0–8 μs and (b) 0–80 μs time ranges. (c) Snapshot of transient absorption spectra of a film of **CTPR4-26** at ca. 0.2 μs. (d) Kinetic traces of transient absorption spectra at 530 nm (blue) and normalized FP-TRMC profile (red) of a film of **CTPR4-26.**

2.3.2. Donor/acceptor nanohybrids based on superhelical protein-porphyrin conjugates and SWCNTs.

In this section, CTPR proteins with different lengths, **CTPR4**, **CTPR8** and **CTPR16**, and their corresponding zinc-metalloporphyrin conjugates have been used as wrapping agents for SWCNTs. Firstly, we expose the seemingly perfect accommodation of SWCNTs inside the cavity of a CTPR superhelix and the possible interacting amino acids. Secondly, we describe the synthesis and characterization of three different protein-porphyrin conjugates. And finally, a depth study of the supramolecular interaction between the proteins and conjugates with the SWCNTs is presented.

2.3.2.1. Compatibility of morphology and composition of CTPR proteins and SWCNTs.

As previously mentioned, CTPR repeats combined in tandem form a superhelical structure in which the long axis of the superhelix increases while the number of repeats unit augmented (Figure 85a). Observing this superhelix perpendicular to its long axis, a tubular proteinic cavity can be found which, a priori, could result an optimum pocket to accommodate one SWCNT, placed parallel to the long axis of the superhelix, thus, drastically reducing the contact of this carbon nanostructure with water.

Based on the knowledge that one superhelical turn in CTPR crystal packing is comprised of eight repeat units, the crystal structure of **CTPR8** seems to be the adequate CTPR model to study the shape affinity between the superhelix and one SWCNT. The structure of **CTPR8** was solved by Regan and col. in three different crystal forms (in space groups $P4_12_12$, $P3_121$ and $P2_12_12_1$, PDB files 2AVP, 2FO7 and 2HYZ, respectively), depending on the crystallization conditions.[67] The superhelical pitch varied from about 68 to 72 Å in the different crystal forms. Therefore, the diameter of the superhelix also varied from about 42 to 38 Å, respectively.

In this sense, we utilized the crystal form with the $P3_121$ structure, with a pitch of exactly 68.6 Å and the larger diameter, of 42.1 Å. With this diameter, and considering the molecular surface of the protein, the diameter of the cavity in the $P3_121$ structure was calculated around 7.5 Å. This value of the cavity diameter was insufficient for accommodating most of the sizes of commercially available SWCNTs (ranging from 7 to 15 Å) inside the superhelix of the protein.

Nonetheless, proteins present not only optimal structures, but also deformability properties which, in many cases, play an important role in the

protein functionalities.[83] In the particular case of CTPR proteins, Haran and col. have recently demonstrated by fluorescence correlation spectroscopy (FCS) and single-molecule Foerster Resonance Energy Transfer (smFRET) studies their remarkable native-state expansion through the reduction of the hydrophobic inter-repeat contacts.[84] Thus, these proteins can be classified as soft springs, with a spring constant of 2 - 20 pN nm^{-1}, featuring high flexibility.

At this point, we used a web-based tool for the analysis of **CTPR8** flexibility, FlexServ, developed by Orozco and col.[85] This platform offers the possibility to generate protein trajectories by different algorithms, using the PDB code of the crystal structure. One of the possible trajectories produced by FlexServ over **CTPR8** implied the expansion-contraction movements of the superhelix within its short axis (Figure 85b). From the most expanded dynamic mode, a PDB file was created. The new cavity diameter of this expanded protein was calculated considering the molecular-surface of the protein, providing a value of around 12 - 13 Å. With this information acquired by the analysis of the flexibility of CTPR proteins, (7,6)-SWCNTs, with a diameter of 8.9 Å, was chosen as the optimal chirality to fulfill the shape requirements of the CTPR superhelix cavity (Figure 85c).

83 K. A. Henzler-Wildman, M. Lei, V. Thai, S. J. Kerns, M. Karplus and D. Kern, *Nature* **2007**, *450*, 913-916.
84 S. S. Cohen, I. Riven, A. L. Cortajarena, L. De Rosa, L. D. D'Andrea, L. Regan and G. Haran, *J. Am. Chem. Soc.* **2015**.
85 J. Camps, O. Carrillo, A. Emperador, L. Orellana, A. Hospital, M. Rueda, D. Cicin-Sain, M. D'Abramo, J. L. Gelpí and M. Orozco, *Bioinformatics* **2009**, *25*, 1709-1710.

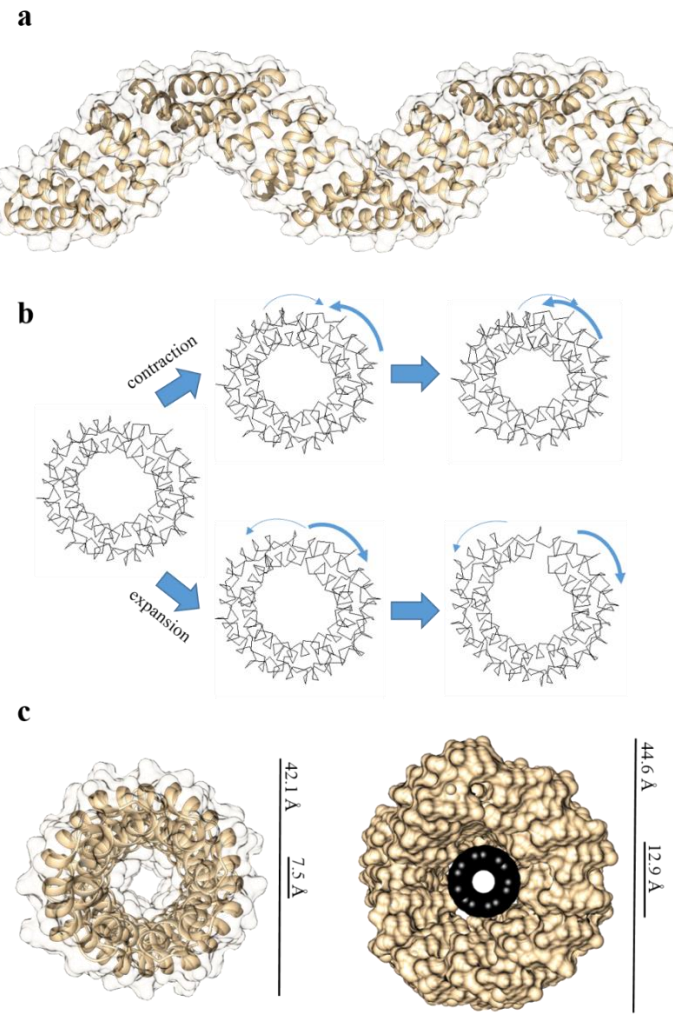

Figure 85. Morphological and shape compatibility between CTPR proteins and SWCNTs. (a) Ribbon and molecular-surface representation of the superhelical conformation of a CTPR16 protein. (b) Contraction-expansion trajectories of **CTPR8** acquired by FlexServ tool (only α-carbons are shown). (c) Molecular-surface representation of the short-axis of the CTPR8 protein before (left) and after (right) treatment with FlexServ. In the case of the most expanded dynamic mode, the shape compatibility with a (7,6)-SWCNT is depicted.

Moreover, not only shape compatibility but also favorable bindings between protein residues and CNT surface are important for an effective interaction. In this sense, a deep search in literature of the reported non-covalent

forces ruling the adsorption of peptides and proteins onto CNT surfaces was made. This examination was aimed to validate the composition of the protein and, if possible, modify those non-conserved positions of the repeat sequence by more interacting amino acids, without affecting the structure of the protein framework.

As described in recent theoretical and experimental works, the strongest interacting residues with CNTs are those bearing aromatic units in their side chains by stablishing π-π and XH···π (X = C, N) contacts.[76,86] In this sense, Trp, Tyr, Phe and His are good candidates to be situated in those positions forming part of the internal cavity in CTPR proteins. Among these, important experimental evidences demonstrated that peptide sequences rich in Trp, Tyr and His show strong adsorption to the CNT surface.[77,87]

With this knowledge and the perfect understanding of the consensus positions in TPR sequence, positions 5 and 9, both localized in the internal proteinic cavity, were modified by His residues to increase the interacting surface exposed to the CNT. Luckily, Tyr residues are found in the original sequence of TPR unit, two of them with the phenol group pointing through the internal cavity. Moreover, not only aromatic but charged amino acids, specially positively charged, exhibit a singularly propensity to adsorb onto the CNT surface due to their surfactant behavior, where the alkyl chain is contacting with the nanotube and the charged termini is pointing toward the solvent.[78,88] Again, a close inspection of the cavity composition revealed the presence of one Lys residue per repeat unit. Altogether, two His, two Tyr and one Lys in each repeat fragment could play a major role in the adsorption of the protein to the CNT.

86 S. Az'hari and Y. Ghayeb, *Mol. Simul.* **2013**, *40*, 392-398.
87 a) V. Z. Poenitzsch, D. C. Winters, H. Xie, G. R. Dieckmann, A. B. Dalton and I. H. Musselman, *J. Am. Chem. Soc.* **2007**, *129*, 14724-14732; b) S. Wang, E. S. Humphreys, S.-Y. Chung, D. F. Delduco, S. R. Lustig, H. Wang, K. N. Parker, N. W. Rizzo, S. Subramoney, Y.-M. Chiang and A. Jagota, *Nat. Mater.* **2003**, *2*, 196-200.
88 a) F. De Leo, J. Sgrignani, D. Bonifazi and A. Magistrato, *Chem. Eur. J.* **2013**, *19*, 12281-12293; b) A. de Leon, A. F. Jalbout and V. A. Basiuk, *Chem. Phys. Lett.* **2008**, *457*, 185-190.

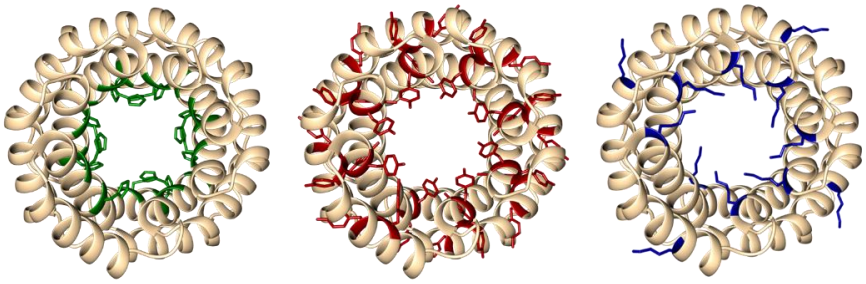

Figure 86. Interacting residues of CTPR8 protein with SWCNTs. From left to right: Two His residues per repeat unit, introduced by mutation of positions 5 and 9 in the parent sequence of a TPR unit; two Tyr residues per repeat unit and one Lys residue per repeat unit.

2.3.2.2. *Design, synthesis and characterization of CTPR proteins and conjugates*

For the study described herein, we employ three mutated TPR proteins with three different lengths (**CTPR4**, **CTPR8** and **CTPR16**) and their corresponding conjugates with zinc-metalloporphyrin **26** (**CTPR4-26**, **CTPR8-26** and **CTPR16-26**).

The previously described mutated-**CTPR4** was used as the smaller protein scaffold, with a dimension of approximately 40 x 40 Å and eight cysteine residues in the outer area of the superhelix, in particular, in the four loops of the protein, for the conjugation with the maleimide-type porphyrin. Meanwhile, two new mutated proteins were designed, that is, **CTPR8** and **CTPR16**. **CTPR8** consisted on eight repeat units comprising one superhelical turn with overall molecular dimensions of approximately 80 x 40 Å and 16 cysteine residues. Finally, **CTPR16**, with two superhelical turns, a dimension of 160 x 40 Å and 32 cysteine residues, was the larger biological framework. Moreover, two His residues per repeat unit were introduced in the sequence of the proteins. As expected, the two Cys and two His mutations in each repeat unit did not significantly affect the helical structure of the protein scaffold. Thus, well-expressed, stable protein samples with the same α-helical structure as the parent protein were obtained (Figure 87).

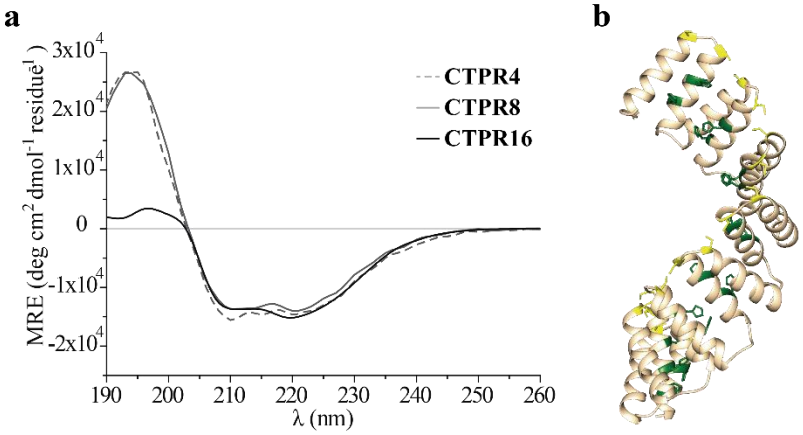

Figure 87. Mutated CTPR4, CTPR8 and CTPR16 proteins. (a) CD spectra of **CTPR4**, **CTPR8** and **CTPR16**. (b) Ribbon representation of the **CTPR8** highlighting Cys residues in yellow and His residues in green.

The designed proteins and porphyrin **26** were conjugated using the maleimide-cysteine chemistry, as follows: 300 µl of 50 µM, 25 µM or 12.5 µM of freshly reduced **CTPR4**, **CTPR8** or **CTPR16** protein, respectively, was mixed with 40 equivalents of **26** giving a ratio of 1:5 cysteine:maleimide and shaken gently. After one hour, an extra of 20 equivalents of **26** were added to the mixture giving a final ratio 1:7.5 cysteine:maleimide. The reactions were stirring at room temperature and covered from light overnight.

The analysis of the samples by gel electrophoresis showed that conjugates of higher molecular weight than their corresponding CTPR proteins were obtained (Figure 88a). When the gel was imaged without staining, the fluorescence signal could be detected, as expected, only in the lanes containing conjugates, holding the porphyrin moieties.

The purification of the protein-porphyrin conjugates from the excess of free porphyrin was successfully carried out using size exclusion chromatography (Figure 88b) using the same conditions previously optimized for the purification of **CTPR4-25** and **CTPR4-26**. As expected, the elution volume decreased while increasing the size of the conjugate.

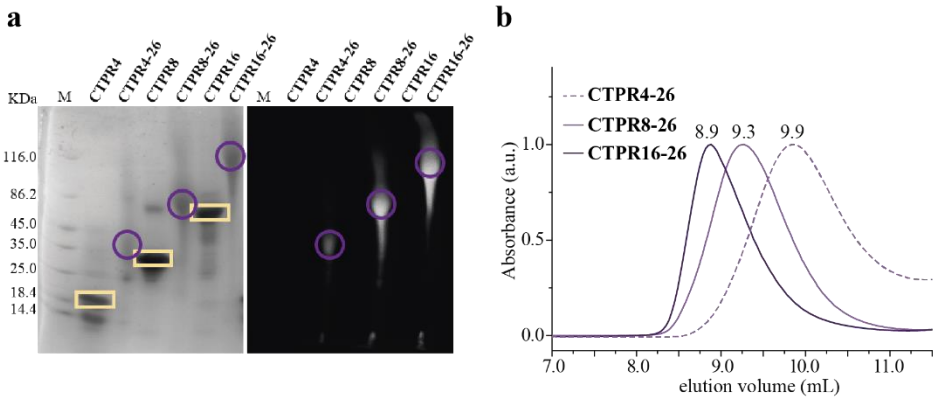

Figure 88. Analysis and purification of conjugates. (a) SDS-Page electrophoresis gel of the conjugation reactions: Molecular weight marker (lane 1), CTPR control proteins (lane 2, 4 and 6) and CTPR-porphyrin conjugates (lane 3, 5 and 7). The gel is shown prior staining imaged using UV-light to monitor the fluorescence of the porphyrins (right panel) and after Coomassie Blue staining (left panel). (b) Size exclusion chromatogram showing the different elution volumes of the three conjugates.

A precise quantification of the number of porphyrins attached to each protein was not possible to elucidate by mass spectrometry due to the high content in porphyrin molecules and the high molecular weight of these new conjugates (80-87 KDa for **CTPR8-26** with 14-16 porphyrins and 158-171 KDa for **CTPR16-26** with 28-32 porphyrins), which probably difficult the volatilization of the samples. The effectiveness of the conjugation reaction was qualitatively demonstrated using absorption spectroscopy by the relative intensity of the Soret absorption band of porphyrin **26**, at 430 nm, compared to the protein absorption band, at 280 nm. Figure 89a shows, on one hand, that the Soret and the Q-bands in the **CTPR8-26** and **CTPR16-26** conjugates were not displaced to neither higher or lower wavelengths comparing to **CTPR4-26**, thus, the location of the porphyrins and their electronic communication should be comparable, that is, establishing *J*-type aggregates. On the other hand, the ratio of the absorbance at $\lambda = 430$ nm respecting to $\lambda = 280$ nm in the three conjugates unambiguously proved that the relative amount of porphyrins is maintained while the dimension of the protein is enlarged. In the previous section, we demonstrated by mass spectrometry that 6 to 8 porphyrins were attached to the **CTPR4**. Therefore, we can conclude that the effectiveness of the conjugation reaction is maintained in all the cases and is unaffected by the size increment in **CTPR8** and **CTPR16** (Figure 89b).

Regarding secondary structure of the protein scaffold within the conjugate and the spatial organization of the porphyrin moieties, CD studies were carried out. In the absorption region of proteins, that is, from 190 to 300 nm, all conjugates revealed the feature CD signal for α-helical secondary structure presented in CTPR proteins (Figures 89c). Furthermore, optical activity is exhibited in the Soret absorption band of achiral porphyrins, indicating a chiral arrangement of these chromophores in the conjugates (Figure 89d). These results confirmed the successful ability of all the mutated CTPR proteins employed in this work to be used as a robust biological scaffold for ordering porphyrins.

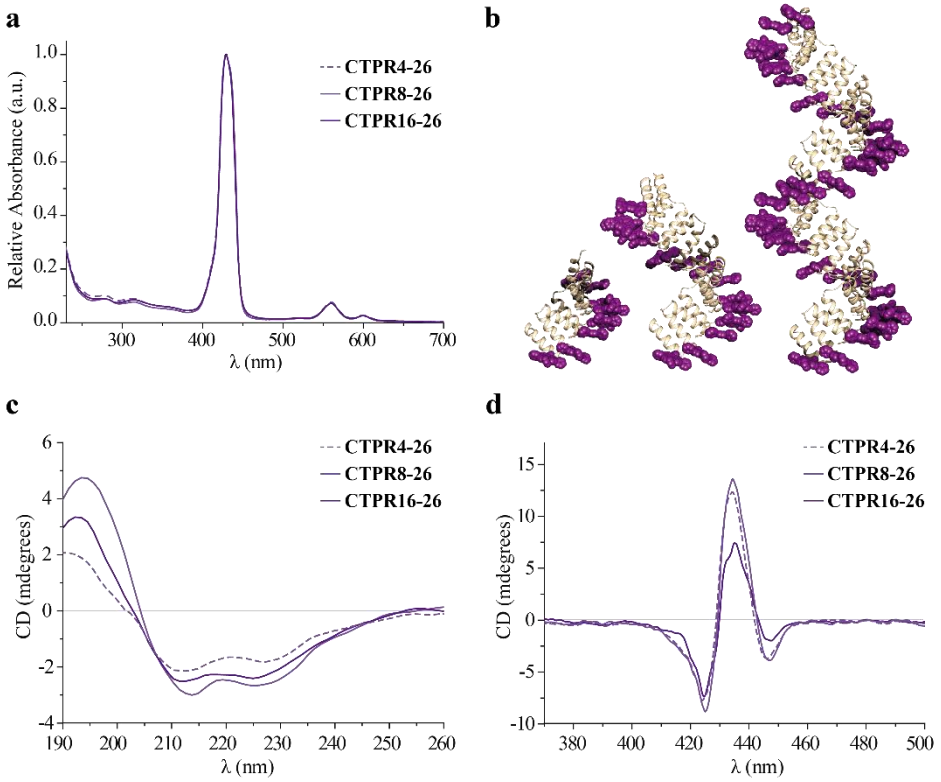

Figure 89. Spectroscopic characterization of bio-organic conjugates. (a) Normalized UV-*vis* spectra of conjugates. (b) Representation of the three conjugates. (c) CD spectra of the conjugates in the protein absorption region. (d) Same than (c) but in the Soret band absorption region of the zinc-metalloporphyrin.

2.3.2.3. *Wrapping SWCNTs by CTPR proteins and conjugates.*

After obtaining and characterizing the corresponding CTPR proteins and conjugates, they were evaluated as wrapping agents for SWCNTs by following this procedure:

Firstly, the absorbance at λ = 280 nm of the corresponding **CTPR4**, **CTPR8** and **CTPR16** mutated proteins was adjusted to 0.13, that is, a final concentration of 2.5 μM, 1.25 μM and 0.63 μM, respectively, in PBS buffer. These molar concentrations implied a weight/weight percent of 0.005% (w/w) for all the samples. Meanwhile, in the case of **CTPR4-26**, **CTPR8-26** and **CTPR16-26** conjugates, the same methodology was followed, adjusting the absorbance at λ = 280 nm to 0.13. Nevertheless, the exact concentration of these conjugates, although in the same order of magnitude that the proteins, was not possible to precisely calculate because at this wavelength not only the protein fragment of the conjugate absorbed, but also the porphyrin moieties.

Secondly, 2 mL of each sample were transferred to a glass vial and were sonicated in an ultrasound bath in the presence of around 1 mg of (7,6)-enriched SWCNTs. The temperature of the bath was maintained at around 10-15 ºC to avoid denaturalization of the proteins due to an increase of temperature of the solution. Every 15 min, each dispersion was transferred to a microcentrifuge tube and was centrifuged at 12000 r.p.m. for 3 min. The 75% of the supernatant was recovered from the centrifugation tubes, avoiding sediment at the bottom, and was transferred to an absorbance cuvette for monitoring the amount of wrapped SWCNTs. This process was repeated until no more changes in the UV-*vis* spectra were observed.

Finally, the supernatant obtained for all nanohybrids was centrifuged 30 min more at 5000 r.p.m. to perfectly remove the non-functionalized SWCNTs, obtaining clear solutions in all the cases, as shown in Figure 90. These solutions were kept in the fridge where they remained stable over months.

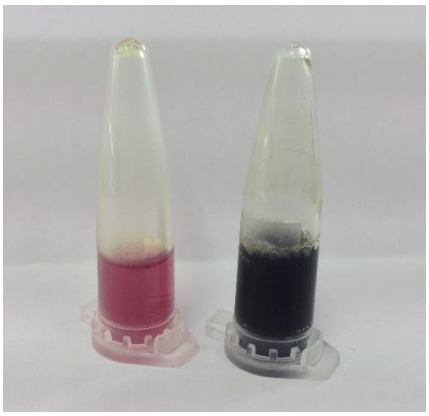

Figure 90. Solutions containing CTPR8-26 conjugate (left) and CTPR8-26/SWCNT nanohybrid (right), in PBS buffer.

Insights into protein-SWCNT and conjugate-SWCNT ground-state electronic interactions came from UV-*vis* spectroscopic experiments. The study performed on the protein-SWCNT nanohybrids is depicted in Figure 91. Although only three lengths of CTPR proteins have been used for this study, some trends can be pointed out:

On one hand, at the same amount of protein, that is 0.005% (w/w), the most preorganized systems were able to more effectively dissolve SWCNTs in aqueous media. In particular, **CTPR16**, with two completed superhelical turns, were the most efficient wrapping agents followed by **CTPR8**, with one superhelical turn. Meanwhile, **CTPR4**, being the less preorganized and the shorter biological scaffold, was also the less effective in this issue (Figure 91a).

On the other hand, Figure 91b shows the absorption intensity at five different wavelengths as function of the protein length in the nanohybrid. In all the cases, data could be more precisely plotted to a non-linear fitting rather than a linear one, attesting that the limit of the effectiveness of CTPR proteins as wrapping agents of SWCNTs was not going further than 16 to 20 repeat units. This experimental data could be explained by the increment of required expansion-contraction movements of the protein while the number of superhelical turns augmented, hindering the perfect accommodation of the SWCNT inside the cavity. It is important to mention that these findings together with the high stability of the nanohybrids, even centrifuging at high rate, suggested the introduction of the nanotube inside the cavity of the protein. In summary, **CTPR16** was, comparing the three systems, the most effective

wrapping framework so far. Possible models of the nanohybrids are illustrated in Figure 91c.

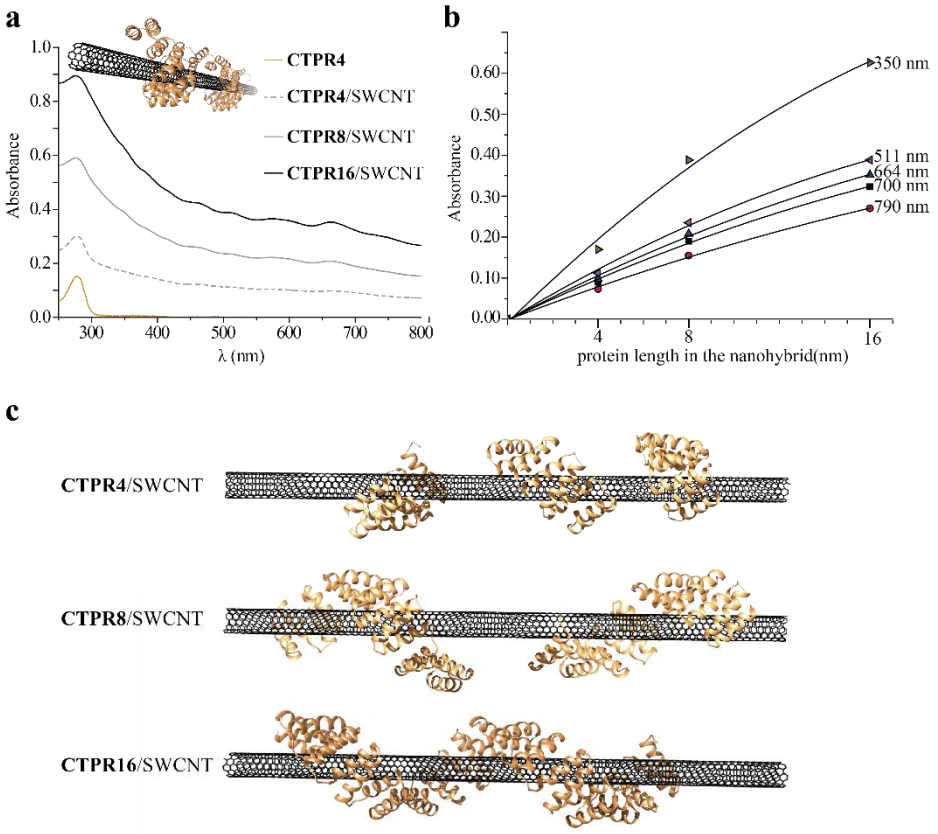

Figure 91. CTPR proteins as wrapping agents of SWCNTs. (a) UV-*vis* spectra of **CTPR4** (yellow line), **CTPR4**/SWCNT (grey dashed line), **CTPR8**/SWCNT (grey solid line) and **CTPR16**/SWCNT (black solid line). (b) Absorption intensities of protein-SWCNT nanohydrids as function of protein lengths, at five different wavelengths. (c) Possible models of the three nanohybrids.

Meanwhile, the same comparative study was performed over the three different conjugates. For initially stablishing the influence on the exfoliation and supramolecular functionalization of SWCNTs of the zinc metalloporphyrin fragment **26** in the conjugates, a control experiment was carried out. To a solution containing non-conjugated porphyrin **26** (6.1 μM in PBS buffer) around 1 mg of SWCNTs was added and the same procedure aforementioned for the

protein-SWCNT and conjugate-SWCNT nanohybrids was followed, that is, prolonged sonication and high-rating centrifugation. Figure 92a shows the result, remarking that the presence of SWCNTs in solution is negligible and more than 90% of porphyrin **26** has precipitated out, probably because of π-π interaction with the surface of nanotube, establishing porphyrin-SWCNT nanohybrids with no stability in water. Thus, it could be anticipated that the photoactive moieties in the conjugates should play a negligible role in the formation of highly water-stable structures.

UV-*vis* studies performed on the conjugates with SWCNTs are illustrated in Figure 92b,c with comparable results relating to their analogue non-conjugated proteins. The trend was similar to that in the proteins, that is, at the same amount of the conjugates, longer scaffolds were more effective wrapping agents for the carbon nanostructures. Nevertheless, the maximum efficiency of these bio-organic structures seemed to be attained with lengths near or even lower than 16 nm, in contrast to the corresponding proteins (Figure 92c). This fact could be explained by the steric hindrance increment and the protein flexibility reduction, both induced by the introduction of the bulky chromophores. A model of the **CTPR16-26**/SWCNT nanohybrids is shown in Figure 92d.

It is also visible that the Soret band of the zinc-metalloporphyrins decreased, in spite of the increasing intensities in the whole spectral region of protein-SWCNT. This behavior could be attributed to interactions between this chromophore and the nanotube surface of the same nanohybrid or others nanotubes in the solution.

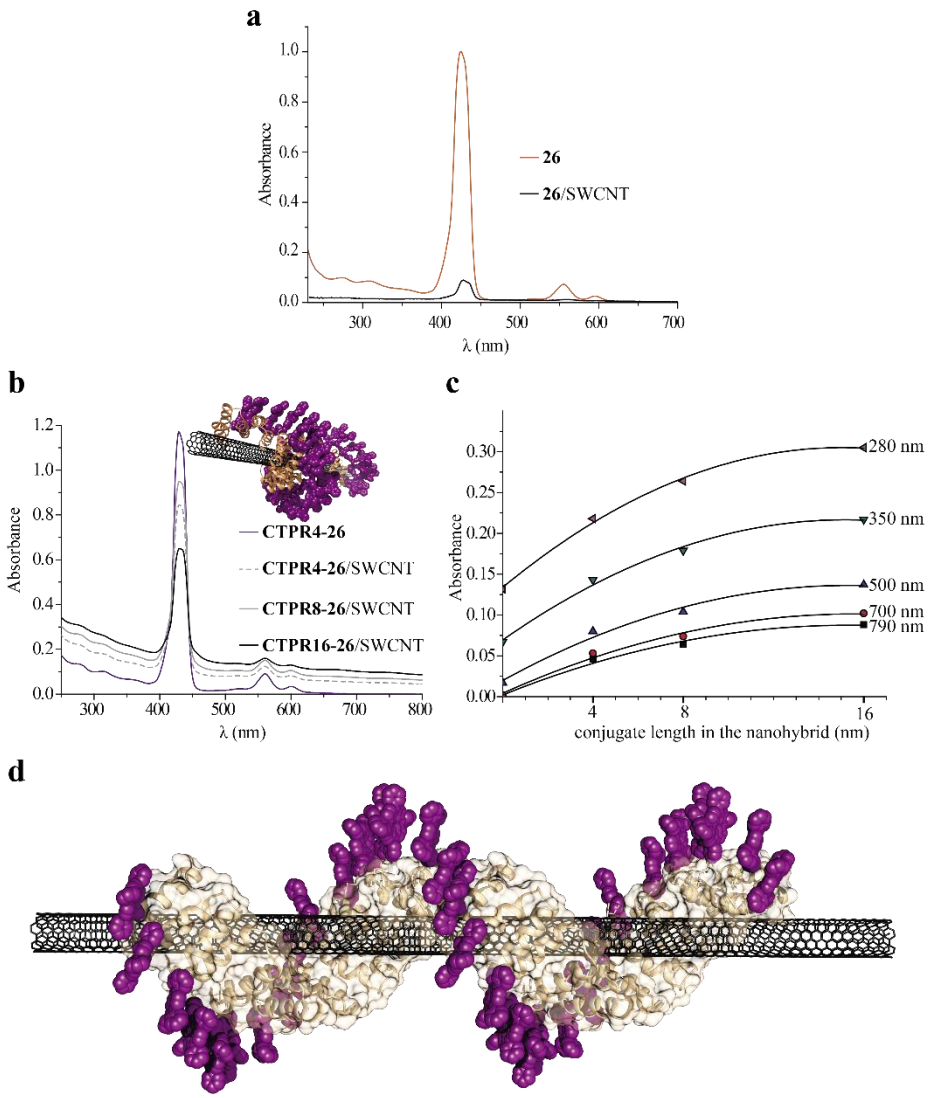

Figure 92. CTPR-porphyrin conjugates as wrapping agents of SWCNTs. (a) UV-*vis* spectra of **26** (orange line) and **26**/SWCNT (black line). (b) UV-*vis* spectra of **CTPR4-26** (purple line), **CTPR4-26**/SWCNT (grey dashed line), **CTPR8-26**/SWCNT (grey solid line) and **CTPR16-26**/SWCNT (black solid line). (c) Absorption intensities of conjugate-SWCNT nanohydrids as function of conjugate lengths, at five different wavelengths. (d) Possible model of the **CTPR16-26**/SWCNT nanohybrids.

Structural integrity of the proteins and conjugates, when they are constituting their corresponding nanohybrids with SWCNTs, was proven by CD assays. Figure 93 shows how the α-helix signature of CTPR framework is maintained in all the cases. The only difference to point out is the slight reduction in the dichroic signal comparing with the pristine samples without SWCNTs. This experimental finding could be attributed to a decrease of the protein/conjugate concentration during the centrifugation process. Those CNTs without a dense covering of proteinaceous material could precipitate out of the aqueous solution, carrying with them some wrapped macromolecules. Nevertheless, partial unfolding of the α-helices could be another explanation to consider.

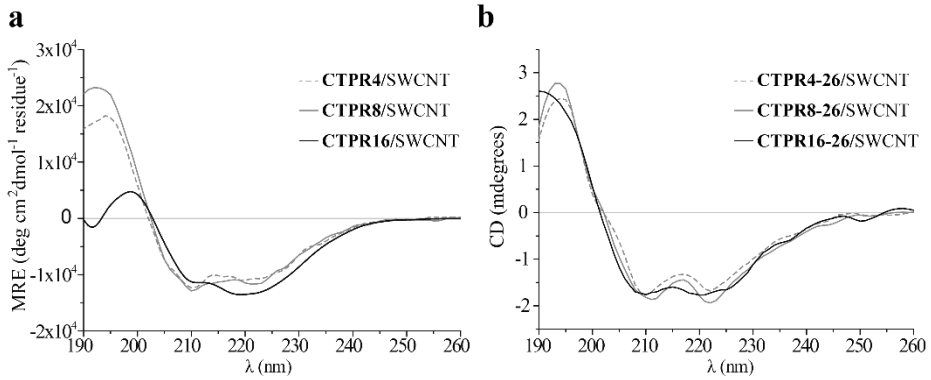

Figure 93. CD spectra of CTPR proteins (a) and their conjugates (b) in the presence of SWCNTs.

Complementary studies came from Raman experiments. The first evidence to highlight is that D band intensities, relating to G bands, reveal no difference comparing with pristine SWCNTs, as expected from a non-covalent interaction (Figure 95a). In contrast, Figure 95b shows the changes in RBM bands in intensity and frequency with an overall decrease (Figure 95b inset) and a 2 cm^{-1} and 6 cm^{-1} shift to lower frequencies in **CTPR16**/SWCNT and **CTPR16-26**/SWCNT, respectively, comparing to pristine SWCNTs. Modified RBMs are in agreement with data reported for wrapped SWCNTs with polymers and related macromolecules. More interestingly, **CTPR16-26** conjugate seemed to have a preferential affinity for (7,6)-chirality (at 260 - 270 cm^{-1}), avoiding larger diameter SWCNTs (lower wavenumbers), while **CTPR16** protein did not provided such selectivity. These experimental findings further demonstrated the assumption of protein flexibility reduction after introducing bulky porphyrin moieties. Finally, G-modes, shown in Figure 95c, downshifted from 1592 cm^{-1},

in pristine SWCNTs, to 1589 and 1585 cm^{-1}, in **CTPR16/**SWCNT and **CTPR16-26/**SWCNT, respectively. Previous studies have demonstrated that the G-band peak in CNTs shifts to lower frequencies when doping with electron donor agents and to higher frequencies with electron acceptor ones.[89] However, in the particular case of using peptides as wrapping agents of SWCNTs, even with modified Phe residues by Tyr residues (more electron donor moieties), the G-mode is upshifted comparing with uncoated SWCNTs.[87a] Only when comparing the Phe-rich peptide/SWCNT with the Tyr-rich peptide/SWCNT, a slight downshift of the G-mode was appreciate (0.6 cm^{-1}). In our case, a remarkable downshift of 3 cm^{-1} in **CTPR16/**SWCNT comparing with pristine SWCNT was found. This experimental finding attested the strong interactions of electron-donating residues in **CTPR16** with the surface of the nanotube. In particular, 32 His and 32 Tyr presented in the proteinic cavity of **CTPR16** could be the responsible of such substantial shift to lower frequencies in the G-band peak of SWCNTs. In the case of **CTPR16-26** conjugate, the effect was even more forceful, with a downshift of 7 cm^{-1}, supplying evidence of a possible charge transfer process between the porphyrins and the SWCNTs.

89 a) A. M. Rao, P. C. Eklund, S. Bandow, A. Thess and R. E. Smalley, *Nature* **1997**, *388*, 257-259; b) K. E. Wise, C. Park, E. J. Siochi and J. S. Harrison, *Chem. Phys. Lett.* **2004**, *391*, 207-211; c) R. Voggu, C. S. Rout, A. D. Franklin, T. S. Fisher and C. N. R. Rao, *J. Phys. Chem. C* **2008**, *112*, 13053-13056.

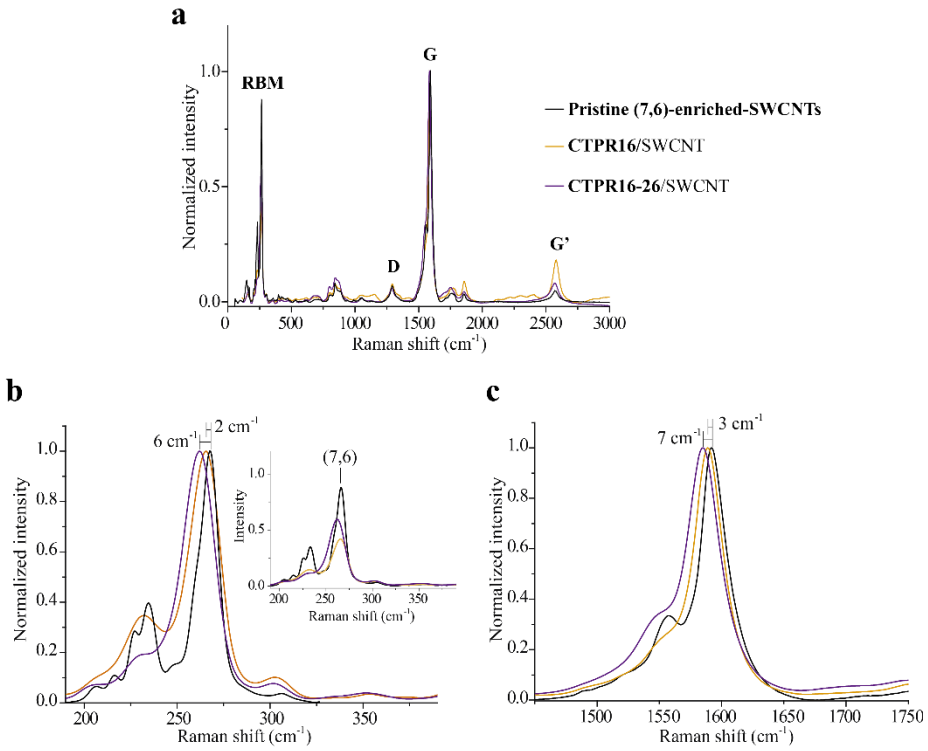

Figure 95. Raman spectra of solid samples of pristine SWCNTs (black line), CTPR16/SWCNT (yellow line) and CTPR16-26/SWCNT (purple line). (a) Normalized Raman spectra from 50 to 3000 cm^{-1}. (b) Raman spectra in the RBM region. (c) Raman spectra in the region of G-mode. All of them have been acquired at the excitation wavelength of 785 nm.

For envisioning the morphology of the protein/SWCNT and conjugate/SWCNT nanohybrids and to evaluate the homogeneity of the samples, microscopy studies were carried out. TEM images were acquired by drop-casting the corresponding aqueous solution onto a carbon grid. In all the cases, images could be best interpreted as dense layers of debundled nanotubes covered or surrounded by organic material (Figure 96a). As previously mentioned, CTPR proteins very easily assemble by head-to-tail and side-to-side interactions into films. Thus, obtaining single CNTs wrapped by the proteinaceous material was virtually inaccessible. However, after a thorough inspection of all the grid, it was possible to find a few small areas where the predicted helical wrapping structure of the nanohybrid was unmistakably perceived, as shown in Figure 96b.

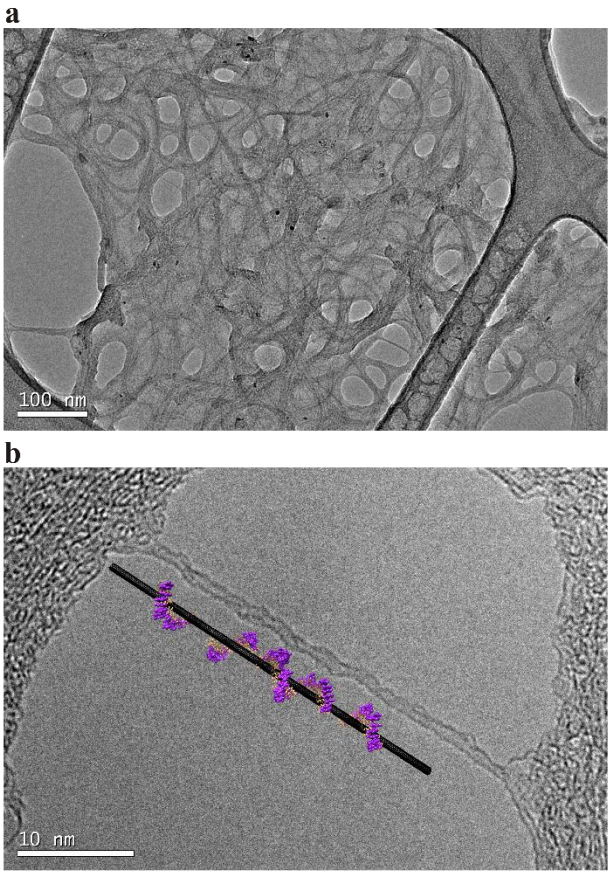

Figure 96. TEM images of CTPR8-26/SWCNT nanohybrids. Scale bars: 100 nm in (a) and 10 nm in (b). Please, note the drawing in (b).

In the previous section we have described that ordered thin films with porphyrin-protein conjugates were effectively generated, preserving their structural integrity and displaying directional order and interesting anisotropic photoconductivity. Now, we produced the aforementioned thin films with these new hybrid materials containing SWCNTs and we tested their features. This evaluation was performed only with the conjugates and nanohybrids derived from **CTPR16**, since is the most effective framework to capture carbon nanotubes inside its cavity, then, providing the highest content of SWCNTs in the solid films. XRD data of the conjugate **CTPR16-26** and **CTPR16**/SWCNT and **CTPR16-26**/SWCNT nanohybrids all revealed a most intense broad signal at 2θ around 19 to 21 º (Figure 97). This value with a *d*-spacing of around 0.43 nm has been previously associated to the α-helical pitch of tandem repeats

configuring the superhelix.[69,90] Therefore, **CTPR16** scaffold retained its superhelical conformation both with the enormous amount of porphyrins covalently attached to the structure and the SWCNT introduced in its proteinic cavity.

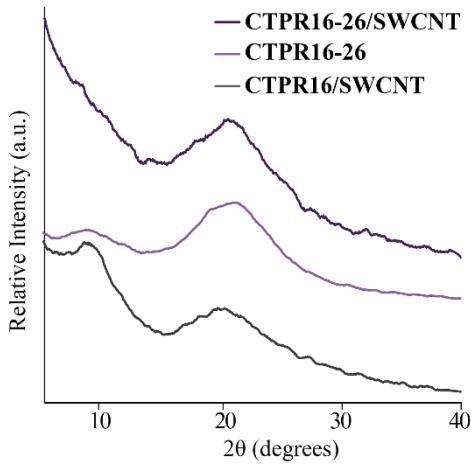

Figure 97. X-ray diffractograms of the films.

90 N. A. Carter and T. Z. Grove, *Biomacromolecules* **2015**, *16*, 706-714.

2.4. Conclusions

2.4. Conclusions Chapter 2

Part 1. *TPR protein scaffolds as templates for ordering porphyrin arrays in solution and solid state.*

This work has described an innovative approach in which a protein building block is designed to organize organic electroactive chromophores. We have evidenced this potential by precisely organizing porphyrin molecules, **25** and **26**, on the **CTPR4** scaffold at the distance required to achieve efficient π-π interactions between the rings.

In the final conjugates, the protein has retained its signature helical structure and has imposed order and chirality into the porphyrin molecules that show efficient stacking interactions. Another feature that has made the applied system superior to other protein templates is its assembly properties. In this work, as a proof of concept, we have shown the formation of ordered films using hybrid protein-porphyrin conjugates. The films obtained displayed nanostructured directional order both in the protein and in the photoactive components. Finally, the photoconductivity of the hybrid thin films showed anisotropy in agreement with the directional order of the photoactive molecules.

Part 2. *Donor/Acceptor assemblies based on superhelical protein-porphyrin conjugates and SWCNTs.*

This work has presented a designed protein serving as wrapping agent of SWCNTs. The optimal superhelical conformation of CTPR proteins for this purpose and the possibility to mutate some residues with more interacting amino acids have made possible such ambitious goal. We have highlighted the effectiveness of our approach by a wide range of techniques, corroborating the introduction of the SWCNT inside the cavity of the superhelix and the stability of the folding state of the protein even with the carbon nanostructure inside. Additionally, we have performed a comparative study regarding the length of the protein, using **CTPR4**, **CTPR8** and **CTPR16**, concluding that preorganization of the superhelical conformation is highly beneficial for improving their wrapping capability.

Moreover, we have expanded this approach to the conjugates with metalloporphyrin **26**, overlooking the great impact that these newly nanohydrids containing donor and acceptor entities could have in materials science. The

ability of the conjugates for coating SWCNTs has been demonstrated to be virtually identical than their corresponding non-conjugated proteins. Only some differences derived from their higher steric hindrance and lower flexibility have been found.

2.5. Experimental Section

2.5. Experimental Section Chapter 2

2.5.1. Synthesis

*2.5.1.1. Synthesis of porphyrin derivatives **25** and **26***

Reagents for synthesis were mostly purchased from Sigma-Aldrich and Acros. Column chromatography was carried out on silica gel 60 (Fluka, 40-63 µm) and FPLC on silica gel GF (Analtech, 1 mm). IR spectra were recorded on a Bruker Tensor 27 spectrometer equipped with ATR and reported as wavenumbers in cm^{-1} with band intensities indicated as s (strong), m (medium), w (weak), br (broad). ^{1}H and ^{13}C NMR spectra were recorded either on a Bruker DPV 300MHz, a Bruker AV 500MHz or a Bruker AVIII 700MHz and reported as chemical shifts (δ) in ppm relative to tetramethylsilane (δ = 0) at room temperature. Spin multiplicities are reported as a singlet (s), broad singlet (br s), doublet (d), triplet (t) and quartet (q) with proton-proton coupling constants (*J*) given in Hz, or multiplet (m). Matrix-assisted laser desorption ionization (MALDI) mass spectrometry (MS) was performed on a Bruker Ultraflex spectrometer using dithranol or DCTB as matrix.

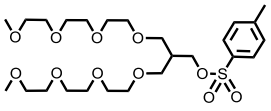

Compound 27. **13-(2,5,8,11-Tetraoxadodecyl)-2,5,8,11-tetraoxatetradecan-14-yl 4-methylbenzenesulfonate.** This product was synthesized according to reported procedures.[79]

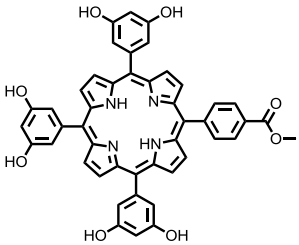

Compound 29. **Methyl 4-[10,15,20-tris(3,5-dihydroxyphenyl)-21H,23H-porphin-5-yl]-benzoate.** This product was synthesized according to reported procedures.[80b]

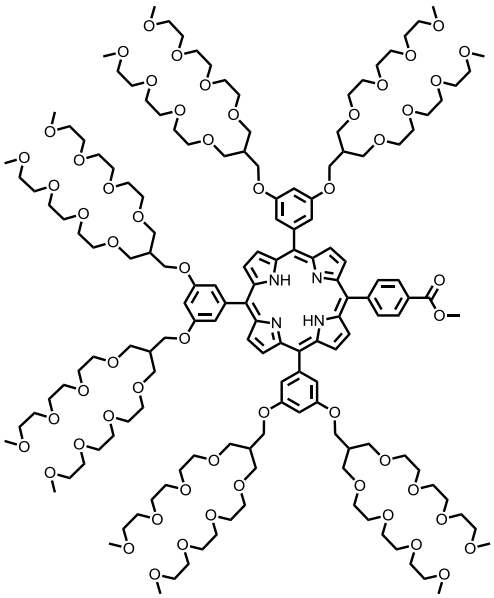

Compound 30. Methyl 4-{10,15, 20-tris[3,5 -bis((13-(2,5,8,11-tetraoxadodecyl)-2,5,8,11-tetraoxatetradecan-14-yl)oxy) phenyl]-21H,23H-porphin-5-yl}-benzoate. To a solution of **29** (40 mg, 0.052 mmol) in DMF (5 mL), 18-crown-6 (14 mg, 0.052 mmol) and K_2CO_3 (72 mg, 0.52 mmol) were added and the mixture was stirred under Argon and reflux for one hour. To the resulting dispersion, **27** (200 mg, 0.37 mmol) was added and the reaction mixture was allowed to react at 80ºC. After 20 hours, the reaction was cooled down, diluted with CH_2Cl_2 (25 mL) and filtered through celite. The solvent was removed under reduced pressure and the crude product was purified by flash column chromatography (CH_2Cl_2/CH_3OH 30:1), affording **30** as a reddish sticky oil (102 mg, 64%). IR (ATR): 3318 (w), 2869 (s), 1721 (m), 1589 (m), 1454 (m), 1434 (m), 1352 (m), 1279 (m), 1102 (s), 851 (m), 804 (m); ^{1}H NMR (500 MHz, $CDCl_3$): 8.95 (br s, 6H), 8.78 (d, ^3J = 4.6 Hz, 2H), 8.44 (d, ^3J = 8.0 Hz, 2H), 8.32 (d, ^3J = 8.0 Hz, 2H), 7.37 (d, ^4J = 2.1 Hz, 6H), 6.91 (d, ^4J = 2.1 Hz, 3H), 4.25 – 4.15 (m, 12H), 4.14 (s, 3H), 3.70 – 3.64 (m, 24H), 3.63 – 3.55 (m, 72H), 3.55 – 3.45 (m, 48H), 3.43 – 3.38 (m, 24H), 3.33 – 3.23 (m, 36H), 2.55 – 2.47 (m, 6H), -2.84 (br s, 2H); ^{13}C NMR (125 MHz, $CDCl_3$): 167.7, 158.7, 144.0, 134.9, 131.4, 129.8, 128.3, 120.4, 118.8, 114.9, 101.4, 72.2, 71.0, 70.9, 70.8, 70.7, 69.8, 67.0, 59.3, 52.8, 40.5; HRMS (MALDI, dithranol): 3050.6696 (100, $[M+H]^+$), calculated for $C_{154}H_{249}N_4O_{56}$: 3050.6760.

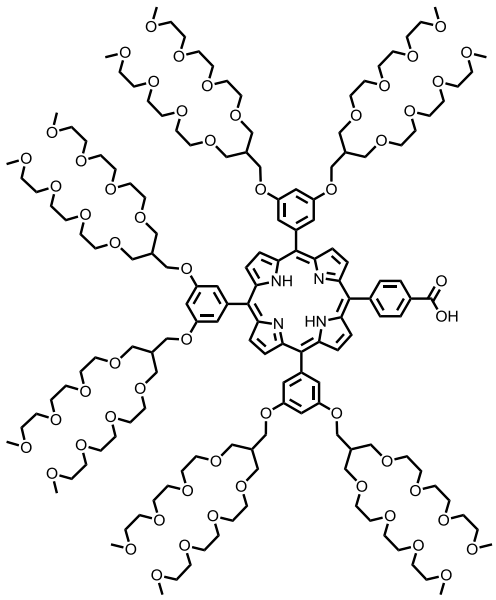

Compound 31. 4-{10,15,20-tris[3,5-bis((13-(2,5,8,11-tetraoxadodecyl)-2,5,8,11-tetraoxatetradecan-14-yl)oxy) phenyl]-21H,23H-porphin-5-yl}-benzoic acid. Compound **30** (90 mg, 0.029 mmol) was dissolved in a 0.15 M solution of KOH (50 eq) in THF/H_2O (9:1, 10 mL) and the reaction mixture was heated to reflux and allowed to react overnight. The next day, THF was removed under reduced pressure and around 20 mL of CH_2Cl_2 was added and the solution was transfered to an extraction funnel. A 0.1 M aqueous solution of HCl was added up to neutral pH. The product was extracted in CH_2Cl_2 (3 x 20 mL), dried over Na_2SO_4 and the solvent was removed under reduced pressure, affording **31** as a reddish sticky oil (45 mg, 51%). IR (ATR): 2871 (s), 1720 (w), 1590 (m), 1455 (m), 1435 (m), 1352 (m), 1106 (s), 851 (m), 804 (m); ^{1}H NMR (700 MHz, $CDCl_3$): 8.95 (br s, 6H), 8.78 (d, ^3J = 4.8 Hz, 2H), 8.54 (d, ^3J = 8.2 Hz, 2H), 8.37 (d, ^3J = 8.2 Hz, 2H), 7.42 – 7.35 (m, 6H), 6.93 – 6.90 (d, ^4J = 2.1 Hz, 3H), 4.26 – 4.16 (m, 12H), 3.72 – 3.64 (m, 24H), 3.64 – 3.57 (m, 72H), 3.56 – 3.47 (m, 48H), 3.45 – 3.39 (m, 24H), 3.33 – 3.23 (m, 36H), 2.54 – 2.49 (m, 6H), -2.85 (br s, 2H); ^{13}C NMR (175 MHz, $CDCl_3$): 169.4, 158.3, 147.7, 143.7, 134.6, 128.5, 120.2, 118.5, 114.5, 101.0, 71.8, 70.6, 70.53, 70.4, 69.5, 69.4, 69.4, 59.0, 40.0; HRMS (MALDI, dithranol): 3036.6469 (100, $[M+H]^+$); calculated for $C_{153}H_{247}N_4O_{56}$: 3036.6603.

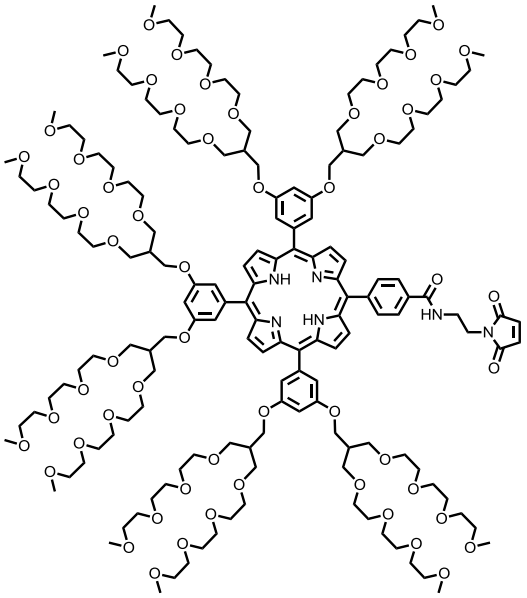

Compound 25. 4-{10,15,20-tris[3,5-bis((13-(2,5,8,11-tetraoxadodecyl)-2,5,8,11-tetraoxatetradecan-14-yl)oxy) phenyl]-21H,23H-porphin-5-yl}-*N*-[2-(2,5-dioxo-2,5-dihydro-1H-pyrrol-1-yl) ethyl]benzamide. To a solution of **31** (45 mg, 0.0148 mmol), 2-maleimidoethylamine trifluoroacetate salt (5.6 mg, 0.0222 mmol) and HBTU (6.2 mg, 0.0163 mmol) in dry CH_2Cl_2 (1 mL), Et_3N (4.1 µL, 0.030 mmol) was added. The reaction mixture was allowed to react at room temperature. After 15 min, CH_2Cl_2 (10 mL) was added and the product was cleaned with a saturated solution of $NaHCO_3$ (3 x 5 mL). The organic layer was dried over Na_2SO_4 and the solvent was removed under reduced pressure. The crude product was purified by PTLC (CH_2Cl_2/CH_3OH 25:1), affording **25** as a reddish sticky oil (34 mg, 73%). IR (ATR): 3320 (w), 2922 (s), 2856 (s), 1712 (m), 1660 (m), 1456 (m), 1352 (m), 1105 (s), 843 (s); ^{1}H NMR (500 MHz, $CDCl_3$): 9.01 – 8.90 (m, 6H), 8.78 (d, ^3J = 4.6 Hz, 2H), 8.29 (d, ^3J = 8.0 Hz, 2H), 8.18 (d, ^3J = 8.0 Hz, 2H), 7.37 (d, ^4J = 1.8 Hz, 6H), 7.24 – 7.17 (m, 1H), 6.91 (d, ^4J = 1.8 Hz, 3H), 6.86 (s, 2H), 4.27 – 4.12 (m, 12H), 4.03 – 3.97 (m, 2H), 3.89 – 3.85 (m, 2H), 3.70 – 3.64 (m, 24H), 3.63 – 3.55 (m, 72H), 3.55 – 3.45 (m, 48H), 3.44 – 3.37 (m, 24H), 3.33 – 3.21 (m, 36H), 2.49 (m, 6H), -2.85 (br s, 2H); ^{13}C NMR (1255 MHz, $CDCl_3$): 171.6, 168.3, 158.7, 146.0, 144.1, 135.0, 134.9, 134.0, 125.8, 120.5, 119.0, 114.9, 101.5, 72.3, 72.2, 71.3, 71.0, 70.9, 70.8, 70.3, 69.9, 67.0, 63.8, 59.3, 40.4, 38.1; HRMS (MALDI, DCTB): 3180.6871 (100, $[M+Na]^+$), calculated for $C_{159}H_{252}N_6O_{57}Na$: 3180.6897.

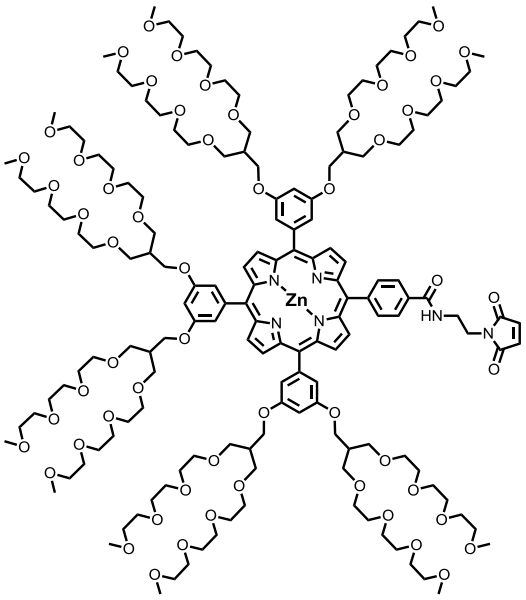

Compound 26. 4-{10,15,20-tris[3,5 –bis[((13-(2,5,8,11-tetraoxadodecyl)-2,5,8,11-tetraoxatetradecan-14-yl)oxy) phenyl]-porphin-5-yl(2-)-κN^{21}, κN^{22}, κN^{23}, κN^{24}]zinc(II)}- *N*-[2-(2,5-dioxo-2,5-dihydro-1H-pyrrol-1-yl) ethyl]benzamide. To a solution of **25** (25mg, 7.9 µmol) in CH_2Cl_2 (2 mL), $Zn(OAc)_2{\cdot}2H_2O$ (3.5 mg, 15.8 µmol) in CH_3OH (2 mL) was added. The mixture was allowed to react and, after 2 hours, the crude compound was concentrated under reduced pressure and purified by flash column chromatography (CH_2Cl_2/CH_3OH, 25:1). The pure compound was obtained as a purple sticky oil without further purification (21 mg, 83%). IR (ATR): 3488 (br), 2872 (s), 1712 (m), 1664 (m). 1454 (m), 1434 (m), 1350 (m), 1106 (s), 942 (m); ^{1}H NMR (500 MHz, $CDCl_3$): 9.04 – 8.94 (m, 6H), 8.84 (m, 2H), 8.28 (d, ^3J = 8.0 Hz, 2H), 8.16 (d, ^3J = 8.0 Hz, 2H), 7.38 (d, ^4J = 1.8 Hz, 6H), 7.18 – 7.09 (m, 1H), 6.90 (d, ^4J = 1.8 Hz, 3H), 6.86 (s, 1H), 4.26 – 4.15 (m, 12H), 4.03 – 3.97 (m, 2H), 3.91 – 3.85 (m, 2H), 3.70 – 3.50 (m, 96H), 3.47 – 3.38 (m, 24H), 3.33 – 3.24 (m, 24H), 3.21 – 3.11 (m, 24H), 3.06 – 2.99 (m, 18H), 2.54 – 2.46 (m, 6H); ^{13}C NMR (1255 MHz, $CDCl_3$): 171.6, 168.4, 158.5, 150.3, 150.2, 150.2, 150.1, 149.9, 145.3, 135.0, 134.9, 133.5, 132.4, 132.3, 131.7, 125.5, 121.2, 119.7, 114.8, 101.4, 72.3, 71.9, 71.9, 71.8, 71.0, 70.9, 70.8, 70.5, 70.4, 69.9, 67.0, 59.2, 59.1, 59.0, 40.4, 38.1; HRMS (MALDI, DCTB): 3242.5995 (100, $[M+Na]^+$), calculated for $C_{159}H_{250}N_6O_{57}ZnNa$: 3242.6032.

2.5.1.2. Synthesis of conjugates

Conjugation reaction. Prior to any conjugation, purified **CTPR4** at a protein concentration of about 100µM was freshly reduced with 1 mM 1,4-dithio-DL-treitol (DTT) during 20 minutes to ensure full reduction of the cysteine residues. DTT was removed by buffer exchange over a NAP-5 column (GE Healthcare Life Science) in PBS buffer. Protein fractions without DTT are collected at 4 ºC and 1mM tris(2-carboxyethyl)phosphine (TCEP) was added to

avoid the formation of disulfide bonds between cysteines during the conjugation reaction. The protein concentration was measured by UV-absorbance. 300µl of 50µM of freshly reduced protein was mixed with 40 equivalents of **25** or **26** (around 1.9 mg) giving a ratio of 1:5 cysteine:maleimide and mixed gently. After one hour, an extra of 20 equivalents of **25** or **26** was added to the mixture (around 1 mg) giving a final ratio 1:7.5 cysteine:maleimide. The reaction mixture was incubated during 3 hours shaking and protected from light. 15% SDS-PAGE electrophoresis gels were used to monitor the conjugation process. Samples of the **CTPR4** protein control and marker were prepared using Amresco EZ-vision loading buffer and the conjugates were mixed with SDS loading buffer. The gel prior staining was imaged using UV-light to monitor the fluorescence of the porphyrins. Then, the gels were stained with Coomassie Blue.

MALDI-TOF Mass spectrometry. The samples were analyzed using ABi 4800 MALDI TOF/TOF mass spectrometer. 4-Hydroxy-3-5-dimethoxycinnamic acid was used as matrix at 10mg/ml dissolved in a 70% acetonitrile and 0,1% TFA solution. The samples were prepared at a sample to matrix solution ratio of 1:4 (v/v) and 1µl of the mixture deposited on the sample plate. When the sample dried, 1µl extra of matrix was deposited over the sample.

Gel filtration chromatography. To purify the conjugate from the free porphyrins gel filtration chromatography was performed using an AKTA prime plus Fast Protein Liquid Chromatography (FPLC) equipment (GE Healthcare). The conjugation reaction was injected into a Superdex 75 HR 10/30 size exclusion chromatography column (GE Healthcare) and run at 0.5 mL/min in PBS buffer with 2mM β-mercaptoethanol. The purified samples were collected in 0.5 mL fractions and stored protected from light.

2.5.2. Characterization of conjugates

Absorbance measurements. Absorbance spectra were recorded using a VARIAN-80 UV-*vis* spectrophotometer. The absorbance spectra of the protein, porphyrin, and protein-porphyrin conjugates from 230 nm to 1000 nm were acquired in a 1 cm path length quartz cuvette using a 4 nm slit-width. For the denaturalization experiments, absorption spectra of the conjugates in different percentage of methanol were recorded. The equilibrium denaturation studies were performed by preparing two stock solutions at the same concentration (around 5µM) of **CTPR4-25** and **CTPR4-26** in a PBS buffer and in methanol. The two solutions were mixed at different ratios to obtain solutions

of conjugates at the same concentration but at different percentage of methanol (from 0 to 100%).

Circular dichroism (CD) measurements. CD spectra were measured using a Jasco J-815 CD Spectrometer. CD spectra of proteins and conjugates in PBS buffer were acquired in a 0.1 cm path length quartz cuvette or a 1 cm path length quartz cuvette. CD spectra of **25** and **26** were acquired under the same conditions using 15 μM of porphyrin concentration. All the CD spectra were recorded with a band-width of 1 nm at 1 nm increments and 10 second average time. CD spectra of CTPR protein films were acquired in 0.01 cm path length quartz cuvette. 10 μl of the conjugate at 1% (w/v) protein concentration in 10 mM sodium chloride, 10mM sodium phosphate buffer (pH = 7.0) were deposited on the quartz cuvette, and the solvent was left to evaporate. The CD spectra were recorded at 1 nm increments and 10 second average time. 10 scans were accumulated.

Film formation. Solid CTPR protein ordered films were generated as previously described.[69] **CTPR4** protein alone and porphyrin conjugates **CTPR4-25** and **CTPR4-26** were diluted to 3% (w/v) protein concentration in 10 mM NaCl, 10 mM Na phosphate pH 7.0 buffer. The solutions were deposited on different surfaces, depending on the experiments to be performed. Quartz cuvette was used for CD analysis and fluorescence spectra, quartz plate for conductivity measurements, and silicon wafer for XRD analysis. The drop volumes also vary between 10 to 30 μl. The solvent evaporated at room temperature during 12 hours, resulting in solid thin films.

Fluorescence anisotropy measurements. Fluorescence anisotropy experiments were recorded in a Fluorolog–TCSPC spectrofluorometer (Horiba) with excitation and emission polarizers. Protein films were placed on a quartz sandwich cuvette and the fluorescence intensity signal of the film of the **CTPR4-25** and **CTPR4-26** conjugates was monitored. The samples were excited at 420 nm with a 4 nm slit-width and the fluorescence emission of the porphyrins was recorded at 650 nm with slit width of 4 nm. The fluorescence intensity was recorded with a fixed polarizer at 0 degrees in the excitation path and varying the angle of the polarizer placed in the emission path. The change of the intensity of the porphyrin in solution was recorded to account the difference in transmission efficiencies when the emission polarizer is placed at different angles. The intensity signal of the film was corrected for this change and then calculated the intensity change with respect to the fluorescence intensity (FI) when both polarizer are placed at 0 degrees (FI/FI_0).

X-ray Diffraction (XRD). X-ray diffraction was performed in a Panalytical X'Pert PRO diffractometer with Cu tube (lambda Kα=1.54187 Å) operated at 45 kV, 40 mA, Ni beta filter, programmable divergence and anti-scatter slits working in fixed mode, and fast linear detector (X'Celerator) working in scanning mode.

FP-TRMC and TAS measurements. Charge carrier mobility was evaluated by flash-photolysis time-resolved microwave conductivity (FP-TRMC) and transient absorption spectroscopy (TAS) techniques at room temperature under air. Solid **CTPR4-25** and **CTPR4-26** films were prepared by drop-casting of their Milli-Q water solution. Charge carriers were photochemically generated using a third harmonic generation (λ = 355 nm) of a Spectra Physics model INDI-HG Nd:YAG laser with a pulse duration of 5–8 ns and frequency of 10 Hz. The photon density of a 355 nm pulse was 9.1×10^{15} photons cm^{-2} $pulse^{-1}$. The microwave frequency and power were set at ~9.1 GHz and 3 mW, respectively. The TRMC signal, picked up by a diode (rise time < 1 ns), was monitored by a Tektronics model TDS3032B digital oscilloscope. The observed conductivities were normalized, given by a photocarrier generation yield (ϕ) multiplied by sum of the charge carrier mobilities ($\Sigma\mu$), according to the equation, $\phi\Sigma\mu = (1/eAI_0F_{light})(\Delta P_r/P_r)$, where, e, A, I_0, F_{light}, P_r, and ΔP_r are unit charge of a single electron, sensitivity factor (S^{-1} cm), incident photon density of the excitation laser (photon cm^{-2}), correction (or filling) factor (cm^{-1}), and reflected microwave power and its change, respectively. TAS measurements were carried out at room temperature under air. The identical drop-cast films used for FP-TRMC measurements were used for TAS measurements. The film was photoexcited using a third harmonic generation (λ = 355 nm) of a Spectra Physics model INDI-HG Nd:YAG laser with a pulse duration of 5–8 ns and frequency of 10 Hz, where the photon density of a 355 nm pulse was 9.1×10^{15} photons cm^{-2} $pulse^{-1}$. A white light continuum from a Xe lamp was used as a probe light source for transient absorption spectroscopy. The monochromated probe light was guided into a Hamamatsu model C7700 wide-dynamic-range streak camera system, which collected a two-dimensional image of the spectral and temporal profiles of light intensity.

Chapter 3.

Evaluation of a collection of fullerenes in triple-channel photosystems.

3.1. Background

3.1. Background

3.1.1. Self-Organizing Surface-Initiated Polymerization

Building complex architectures with high precision at the molecular level, mimicking the nature and biological systems, is one of the biggest challenges for organic synthetic chemists in current science.

In this line, self-organizing surface-initiated polymerization (SOSIP) has been recently reported by Matile and col. as a versatile methodology for constructing complex organic architectures on conducting solid substrates, in particular, on indium tin oxide (ITO) surfaces.[91] This user-friendly approach combines the advantages of supramolecular chemistry to organize small building blocks through hydrogen bonds and π-stacking forces together with the benefits of surface-initiated polymerization[92] to produce oriented nanostructures with high grafting densities, starting from small building blocks acting as monomers.

The first description of ordered chromophores using the so-called SOSIP approach was realized using initiator **I** and propagator **P** (Figure 98). Both molecules have in common a naphtalenediimide (NDI) central aromatic unit, providing the electron/hole transporting channel, and two lysine-type side chains for producing the hydrogen-bonded network in the architecture. Moreover, initiator **P** further contains two bisphosphonic acids "feet" as anchoring groups to the ITO surface, and two *tert*-buthyl (^{t}Bu) disulfide groups. Phosphonic acids have been widely used for the attachment of electroactive organic molecules and biological photosystems on oxide surfaces, providing a dense coverage of the monolayer on the substrate.[93] Meanwhile, in propagator **P** the *t*-Bu disulfide group is replaced by an asparagusic acid. SOSIP occurs as follows: Once the

91 a) N. Sakai, M. Lista, O. Kel, S.-i. Sakurai, D. Emery, J. Mareda, E. Vauthey and S. Matile, *J. Am. Chem. Soc.* **2011**, *133*, 15224-15227; b) M. Lista, E. Orentas, J. Areephong, P. Charbonnaz, A. Wilson, Y. Zhao, A. Bolag, G. Sforazzini, R. Turdean, H. Hayashi, Y. Domoto, A. Sobczuk, N. Sakai and S. Matile, *Org. Biomol. Chem.* **2013**, *11*, 1754-1765.

92 a) P. Murugan, M. Krishnamurthy, S. N. Jaisankar, D. Samanta and A. B. Mandal, *Chem. Soc. Rev.* **2015**; b) G. L. Whiting, H. J. Snaith, S. Khodabakhsh, J. W. Andreasen, D. W. Breiby, M. M. Nielsen, N. C. Greenham, R. H. Friend and W. T. S. Huck, *Nano Lett.* **2006**, *6*, 573-578.

93 a) J. A. Bardecker, H. Ma, T. Kim, F. Huang, M. S. Liu, Y.-J. Cheng, G. Ting and A. K. Y. Jen, *Adv. Funct. Mater.* **2008**, *18*, 3964-3971; b) N. Doubina, J. L. Jenkins, S. A. Paniagua, K. A. Mazzio, G. A. MacDonald, A. K. Y. Jen, N. R. Armstrong, S. R. Marder and C. K. Luscombe, *Langmuir* **2012**, *28*, 1900-1908.

initiator has been immobilized to the surface, producing **S-1**, the *t*-Bu disulfide groups are reduced to thiols with DTT as reducing agent. Then, the surface is incubated in a solution of propagator **P** in the presence of a basic catalyst. Recognition of **P** on the surface of **S-1** is expected to position the terminal disulfides of **P** on top of two thiolates, facilitating the ring-opening disulfide exchange and generating the covalent structure. The new active thiolates formed after the capture will follow reacting with the next propagator **P**, resulting in the desire ordered and oriented polymeric architecture **S-2**.

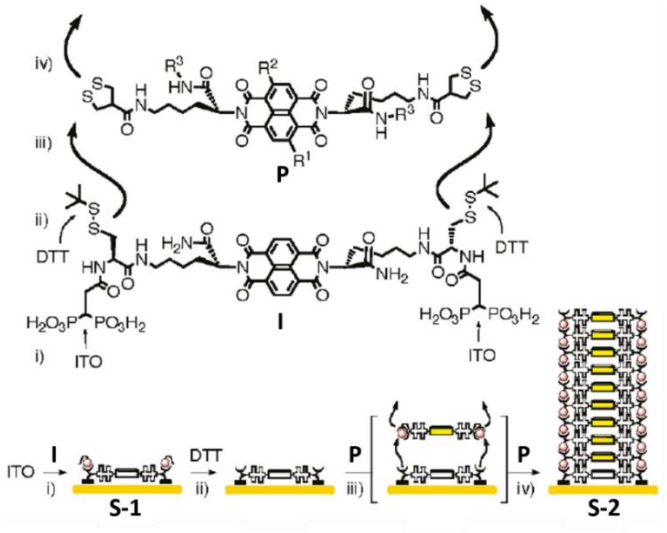

Figure 98. Design and synthesis of SOSIP architectures S-2 with initiator I and propagator P. (i) Deposition of initiator **I** on ITO; (ii) activation with DTT; (iii) self-organizing recognition of propagator **P** and ring-opening disulfide exchange; (iv) continuing SOSIP.

Authors confirmed that the propagator concentration strongly affects the efficiency of the polymerization process. The correct concentration was identified in $c_{SOSIP} \approx 12$ mM. At lower concentrations, SOSIP did not occur but at $c > 15$ mM the polymerization was not selectively initiated from the surface and occur in solution as well. Other factors such as solvent, temperature and the nature of the propagator also could affect the construction of an optimal architecture.

Photocurrent generation of this novel system was determined with a wet setup analogue to dye-sensitized solar cells, using the corresponding SOSIP photosystem as working electrode, a Pt wire as counter electrode, a Ag/AgCl as reference electrode and triethanolamine (TEOA) as mobile electron carrier.

Photosystem **S-2**, compared to a disorganized analogue, produced up to 5 times more photocurrent and a much faster photocurrent generation due to a lower resistivity with increasing organization of the molecular dyes.

Based on this approach, Matile and col. have also built panchromatic SOSIP photosystem **S-3** with oriented four-component redox gradients by increasing gradually the electron density of the propagators in terms of core-structure chemical modification. In particular, *O*,*O*-NDI (yellow), *O*,*N*-NDI (red) and *N*,*N*-NDI (blue) (Figure 99) were used as propagators with a very straightforward methodology, that is, incubating each propagator 1 h in the order of their LUMO energy level.

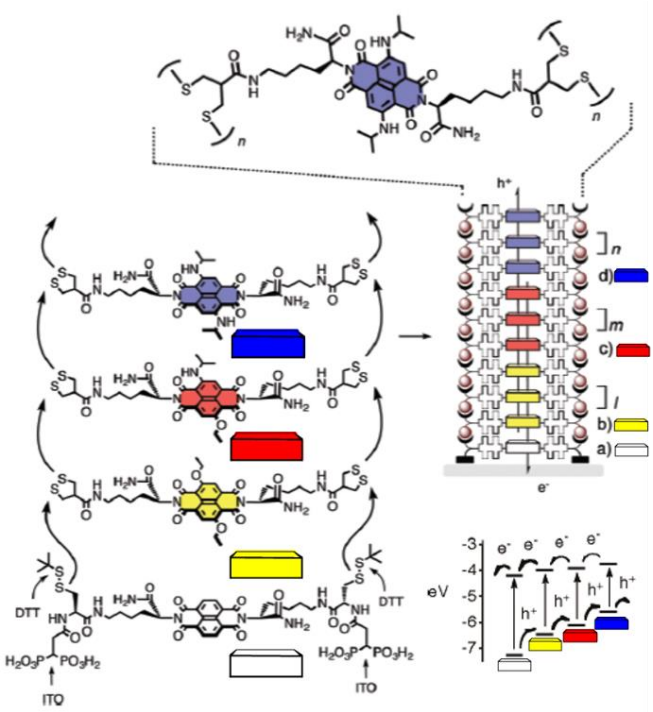

Figure 99. Panchromatic architecture S-3. This photoactive structure was built from initiator *H*,*H*-NDI (white), propagators *O*,*O*-NDI (yellow), *O*,*N*-NDI (red) and *N*,*N*-NDI (blue). Their HOMO and LUMO levels are depicted, as well.

3.1.2. Self-Organizing Surface-Initiated Polymerization Templated Stack Exchange

Searching for more complex photosystems, a new generation of SOSIP-building approach, that is post-SOSIP-Templated Stack Exchange (TSE), was presented by Matile and col., by the coaxial alignment of two molecular-sized columns able to transport holes and electrons in opposite directions after their separation with light.[94]

In this new approach, dynamic covalent bonds together with the chemo-orthogonality of disulfide chemistry and hydrazone exchange were introduced.[95] Now, propagators are laterally functionalized with two benzylhydrazones, serving as inert chemical groups and for reserving space along the growing stacks for the lateral columns of photoactive derivatives. After polymerization (Figure 100a), these templates were removed using excess hydroxylamine (Figure 100b) and then replaced under slightly acidic conditions by the corresponding "exchanger" bearing an aldehyde group (Figure 100c).

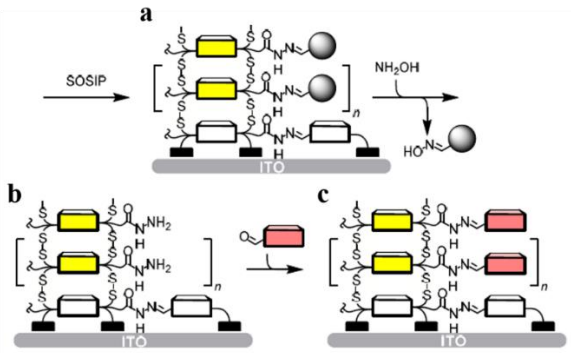

Figure 100. Post-SOSIP stack Exchange. Hydrazone exchange chemistry is used to replace the inactive benzylhydrazone template (gray circles in a), leaving hydrazine rich pores through the architecture (b), with active π-stacks bearing an aldehyde functional group (c).

The relevance of this approach for constructing double-channel supramolecular *n*/*p*-heterojunction (SHJ) was evaluated. Simple double-channel SHJ without redox gradient and [1+2] and [2+2] type SHJ with a redox gradient

94 N. Sakai and S. Matile, *J. Am. Chem. Soc.* **2011**, *133*, 18542-18545.
95 a) P. T. Corbett, J. Leclaire, L. Vial, K. R. West, J.-L. Wietor, J. K. M. Sanders and S. Otto, *Chem. Rev.* **2006**, *106*, 3652-3711; b) M. von Delius, E. M. Geertsema and D. A. Leigh, *Nat. Chem.* **2010**, *2*, 96-101.

were obtained and tested in terms of photocurrent generation, with the best result achieved in the case of antiparallel [2+2], where the charge recombination efficiency was minimal (22 ± 3%) comparing with the other cases (from 50 ± 3% to 76 ± 8%, depending on the system), due to the directional and opposite flow of electrons and holes in that photosystem (Figure 101). With these results, Matile and col. demonstrated that multicomponent systems with antiparallel gradients can be readily accessible without overly demanding synthetic efforts.

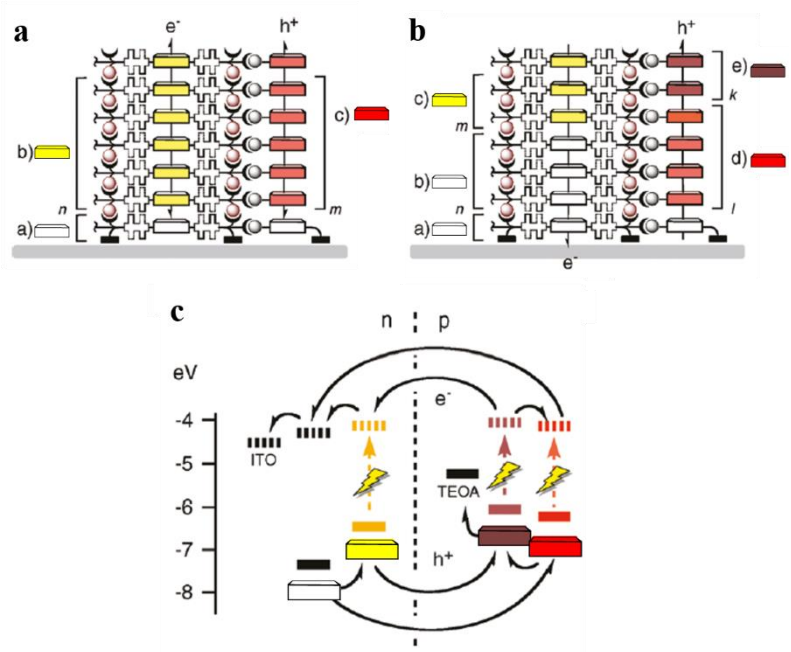

Figure 101. Multicomponent photosystems obtained by SOSIP-TSE. (a) [1+1] SHJ with central electron-transporting NDIs and lateral hole-transporting NDIs. (b) [2+2] SHJ with directional and opposite flow of electrons and holes in the photosystem. (c) HOMO (solid) and LUMO (dashed) energy diagram of NDIs in Figure 101a,b together with work function of ITO and HOMO of TEOA.

3.1.3. Non-NDI-based photosystems obtained from SOSIP-TSE strategy. Access to non-planar systems: fullerenes.

Further studies were made with new initiators and propagators, concerning the replacement of central NDIs by perilenebisimides (PBIs) and

oligothiophenes.[96] These aromatic moieties were particularly attractive since are among the most common components in electronic, photonic and optoelectronic materials. In both cases, the compatibility with SOSIP strategy was demonstrated. Moreover, TSE strategy was also expanded with other electroactive stacks such as triphenylamines, porphyrins and phthalocyanines as the second channel.[91b]

Special attention in this chapter deserves the two-component system formed by oligothiophene stacks as hole-transporting system and [60]fullerene as electron-transporting column. Accommodate the spherical C_{60} molecules into uniform stacks of planar aromatics is not a trivial issue, and enormous efforts have been made around this challenge in material science.[16a,16d-f] In particular, alignment of fullerenes along oligothiophene stacks has received particular attention because of the importance of this architecture in organic solar cells.[16g]

In a recent work, Matile and col. introduced this partner following the SOSIP-TSE strategy.[97] Oligothiophene stacks were used as "first-column", correctly decorated with two benzyl hydrazones for the subsequent TSE after the SOSIP (Figure 102). Meanwhile, two tri(ethylene glycol) (TEG) solubilizers were introduced in the structure of the fullerene derivative by a double Bingel cyclopropanation reaction on C_{60}, being sufficient to reach the correct concentration in the polar aprotic solvent needed for the TSE. Moreover, an aldehyde functional group was also introduced in this structure to form the hydrazone bond with the oligothiophene-based photosystem. Photocurrent generation was examined, obtaining, as expected, 7-times higher photocurrent than the photosystem with only oligothiophenes.

96 a) J. Areephong, E. Orentas, N. Sakai and S. Matile, *Chem. Commun.* **2012**, *48*, 10618-10620; b) P. Charbonnaz, N. Sakai and S. Matile, *Chem. Sci.* **2012**, *3*, 1492-1496.
97 A. Bolag, H. Hayashi, P. Charbonnaz, N. Sakai and S. Matile, *ChemistryOpen* **2013**, *2*, 55-57.

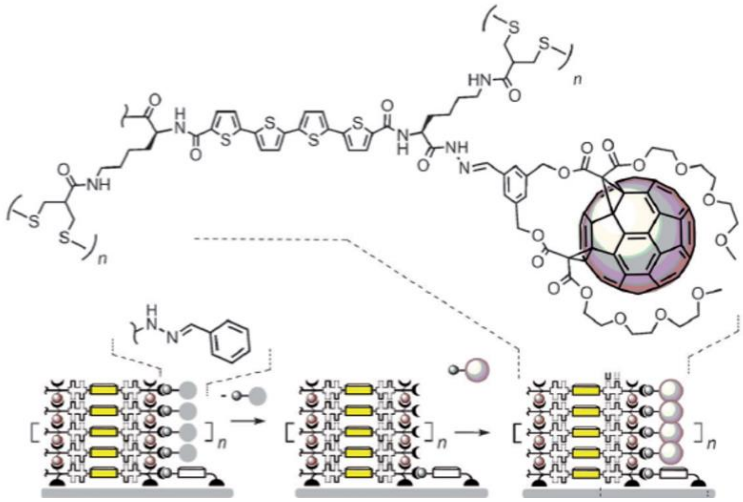

Figure 102. Schematic structure of oligothiophene-fullerene-based photosystem.

3.1.4. Triple-channel Oriented Photosystem

The next step toward higher sophisticated photosystems was the introduction of a third component. These "triple-channel" photosystems containing three coaxial charge-transporting pathways offer a better coverage of the solar spectrum as well as long-lived charge separation state, comparing with single or double-channel architectures. Moreover, they offer advantages on the orientation, organization and solid-supporting to the classical triads previously described in solution.

In this line, Matile and col. described triple-channel architectures bearing a set of optoelectronic building blocks, that is NDIs, PBIs, oligothiophenes, fullerenes, squaraines, pthalocyanines, porphyrins and triphenylamines.[98]

All these systems have in common the use of NDI stacks as first channel supported on the ITO, since this system was the best understood, acting additionally as electron-transporting column. Meanwhile, second channel was attached, as described previously, using the hydrazone chemistry developed for TSE in the double-channel photosystems. For the insertion of the third channel,

98 G. Sforazzini, E. Orentas, A. Bolag, N. Sakai and S. Matile, *J. Am. Chem. Soc.* **2013**, *135*, 12082-12090.

the second channel was endowed with an alkyloxime group on the opposite side to the orthogonally protected aldehyde for the TSE. Alloc and acetal protection were selected, respectively, for this propose. In this way, it is possible, firsly, the in-solution formation of the dyad corresponding to second and third channel through an oxime bridge, after Pd-mediated Alloc removal, giving adequate stability to endure the reaction conditions used for the acetal removal and subsequent TSE with the single-channel photosystem. The whole procedure can be certainly visualized in Figure 103.

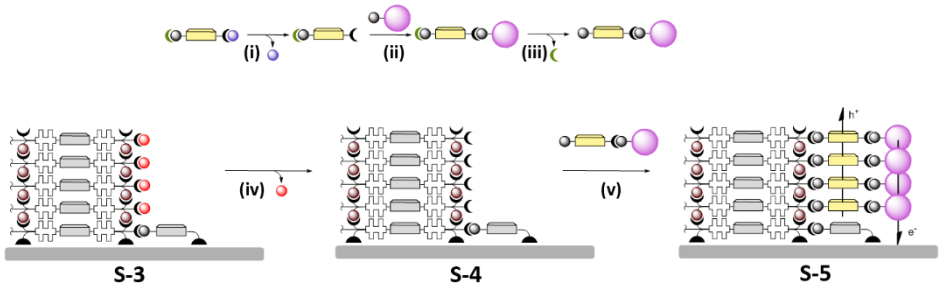

Figure 103. SOSIP-TSE methodology apply to triple-channel surface architecture, representing the chemo-orthogonal approach. Firstly, in solution, Alloc group attached to the second-channel is selectively removed (i) and the dyad involving second and third channel is formed through an oxime bridge (ii). Secondly, architecture **S-3** carrying the first-channel is deprotected obtaining **S-4** (iv) and, after acetal-removal of the dyad (iii), triple-channel photosystem **S-5** is achieved using the TSE methodology developed for double-channel photosystems (v).

About the nature of these second and third channels, either electron-rich or electron-deficient chromophores were used in both cases. However, very different results were obtained in terms of photocurrent generation when using a planar or non-planar moiety as third chromophore. A remarkable result was obtained with triad containing NDI-squaraine-fullerene, where the photocurrent generation was 9.9 μAcm^{-2}, more than the sum of dyad controls (less than 1.0 μAcm^{-2} in both NDI-squarine and NDI-fullerene). The same conclusions were obtained when combining NDI-PBI-triphenylamine. In sharp contrast, when all-planar triple-channel systems were built, photocurrent was extremely poor, inhibiting rather than enabling the corresponding photocurrent generated by double-channel analogs. The authors explained these experimental findings considering processes of folding and interdigitations as shown in Figure 104, which resulted completely unfavorable for a correct hole and electron coaxial transporting.

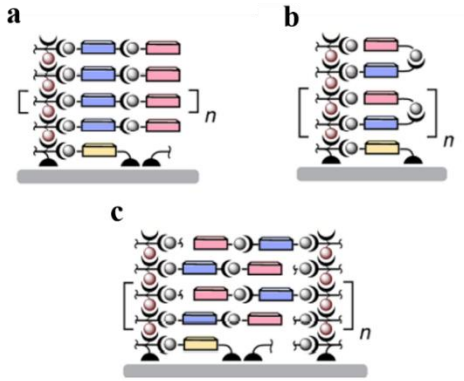

Figure 104. Possible models to explain the inactivity of photosystems obtained by SOSIP-TSE. (a) Optimal triple-channel architectures. (b) Folded donor-acceptor systems with completely planar dyads. (c) Interdigitated donor-acceptor systems with completely planar dyads.

3.1.5. Tuning the LUMO levels of fullerene derivatives by chemical modifications

To improve the efficiency of heterojunction photovoltaic cells, not only the composite morphology play a role. Open circuit voltage (V_{OC}) is a critical parameter.[99] Besides the mechanistic steps (Figure 105),[100] V_{OC} has a close relationship with the donor-HOMO and the acceptor-LUMO energy difference (ΔE_a). Empirically, it appears that a minimum energy difference of 0.3 V is required for a forward electron transfer from the donor to the acceptor. In this sense, much efforts have been done for optimizing the electronic match between these two components.

Hence, in the field of fullerenes, one of the main challenges has been to drastically alter their electronic properties by means of modification of the nature and especially position of their substituents.

99 B. C. Thompson and J. M. J. Fréchet, *Angew. Chem., Int. Ed.* **2008**, *47*, 58-77.
100 a) C. J. Brabec, N. S. Sariciftci and J. C. Hummelen, *Adv. Funct. Mater.* **2001**, *11*, 15-26; b) K. A. Mazzio and C. K. Luscombe, *Chem. Soc. Rev.* **2015**, *44*, 78-90.

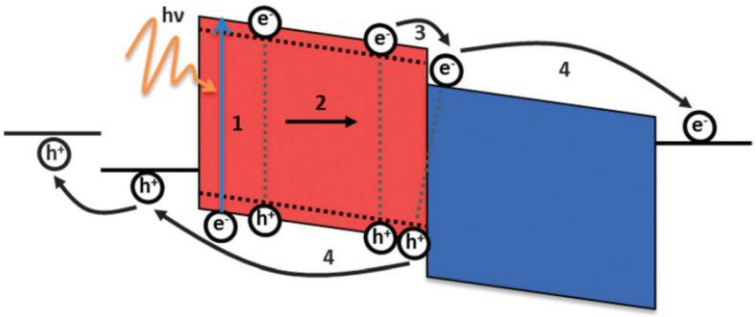

Figure 105. Scheme of the operating principles of photovoltaic cells highlighting the desired transport of charge pairs through the donor (red) and acceptor (blue) materials. Upon photoabsorption, (step 1), an electron can be excited from the donor HOMO to its LUMO, forming an exciton. This exciton must then diffuse to a donor/acceptor interface via a chemical potential gradient (step 2) where the electron can transfer to the LUMO of the acceptor material, forming a charge transfer (CT) complex that can become a charge separated (CS) state (step 3), which will be favorable to occur when the energy difference between the donor LUMO and the acceptor LUMO (ΔEA) is greater than the binding energy of the exciton. Any dissociated charges can then be transported through *p*-type or *n*-type domains to the electrodes, with holes being collected at the anode and electrons being collected at the cathode (step 4), where they can be used to do work in an external circuit.

Modification of pristine C_{60}, phenyl-C61-butyric acid methyl ester (PCBM) and diphenylmethano[60]fullerene (DPM), two of the most extended fullerene derivatives so far, have been widely investigated for fine-tuning their electronic properties.

In the case of C_{60}, an increasing number of addends can reduce the conjugation of the carbon cage, generally raising the LUMO level.[101] The most stable and smallest 1,2-disubstituted fullerene derivative available is the 1,2-dihydromethano-[60]fullerene, with one cyclopropane appended to the spherical structure of the carbon cage (Figure 106). This 58-π-electron methanofullerene provides a cathodic shift of 0.11 V in the first reduction potential comparing to C_{60}. This compound has been firsly synthetized in 1993, through 1,3-dipolar

101 J. L. Delgado, P.-A. Bouit, S. Filippone, M. A. Herranz and N. Martin, *Chem. Commun.* **2010**, *46*, 4853-4865.

cycloaddition reaction of diazomethane[102] or diiodomethane[103] as the one carbon source, with very low reaction yields. In 2011, Nakamura and col. introduced a new efficient and scalable methodology to obtain this derivative by a new type of oxidative C-C bond formation on the surface of the fullerene core, providing a novel tool to the organoelectronic community.[104]

Figure 106. Molecular structure of 1,2-dihydromethano-[60]fullerene.

Wudl and col. have found that *para* substituents on the phenyl groups of DPM have negligible effect on its reduction potential both with electron-donating or electron-withdrawing groups (Figure 107a). In contrast, the same author claimed that in spiromethanofullerenes an intramolecular electronic interaction through "periconjugation" between the aromatic substituent and the fullerene cage, results in more extended conjugated molecules with tunable electronic properties (107b).[105] As a combination of these two approaches, Hummelen and col. hypothesized that an electron-donating methoxy substituent on the *ortho* position of the phenyl ring in PCBM could have a direct through space effect on the electronic properties of the carbon cage.[106] However, the authors did not observe a clear difference in the first reduction potential of a series of ortho substituted derivatives when comparing with the *para* substituted analogues (107c). Therefore, the expected overlap between the oxygen lone pair and the fullerene π-system did *not* occur. Furthermore, a pentafluoro[60]PCBM derivative was synthetized, with a slight electron-withdrawing effect of the

102 a) A. B. Smith, R. M. Strongin, L. Brard, G. T. Furst, W. J. Romanow, K. G. Owens and R. C. King, *J. Am. Chem. Soc.* **1993**, *115*, 5829-5830; b) A. B. Smith, R. M. Strongin, L. Brard, G. T. Furst, W. J. Romanow, K. G. Owens, R. J. Goldschmidt and R. C. King, *J. Am. Chem. Soc.* **1995**, *117*, 5492-5502.

103 a) M. W. J. Beulen and L. Echegoyen, *Chem. Commun.* **2000**, 1065-1066; b) Z. Yinghuai, S. Bahnmueller, C. Chibun, K. Carpenter, N. S. Hosmane and J. A. Maguire, *Tetrahedron Lett.* **2003**, *44*, 5473-5476.

104 Y. Zhang, Y. Matsuo, C.-Z. Li, H. Tanaka and E. Nakamura, *J. Am. Chem. Soc.* **2011**, *133*, 8086-8089.

105 M. Eiermann, R. C. Haddon, B. Knight, Q. C. Li, M. Maggini, N. Martín, T. Ohno, M. Prato, T. Suzuki and F. Wudl, *Angew. Chem., Int. Ed.* **1995**, *34*, 1591-1594.

106 F. B. Kooistra, J. Knol, F. Kastenberg, L. M. Popescu, W. J. H. Verhees, J. M. Kroon and J. C. Hummelen, *Org. Lett.* **2007**, *9*, 551-554.

fluorine atoms to more positive potential comparing with the first reduction potential of PCBM (Figure 107).

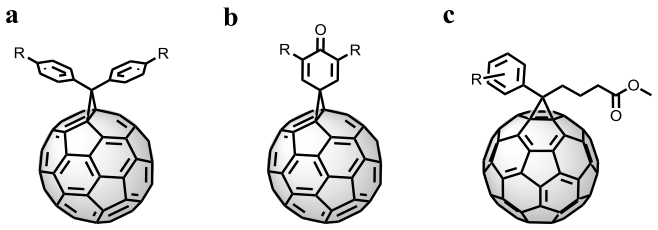

Figure 107. Molecular structure of different methanofullerene derivatives. (a) DPM derivative. (b) PCBM derivative. R represents substituents with electron-donating or electron-withdrawing nature. (c) Quinone-type spiromethane derivative.

In 2011, Wuld and col. reported a new series of fullerene derivatives functionalized through the "1,4" position, in clear contrast to the most common "1,2" addends (Figure 108).[107] The main properties of this new class of fullerene derivatives were: 1) straightforward synthesis starting from the same material: fullerenol (Figure 108a); 2) tunable LUMO energy level by appending electron-donating or electron-withdrawing substituents on the phenyl group. Compared with the previously cited PCBM analogues described by Hummelet and col., the nature of the substituent on the 1,4-fullerene addends appeared to affect their redox potential to a greater degree. Particularly, one pentafluorophenyl group on PCBM raised the redox potential 0.038 V more positive, whereas the corresponding 1,4-analogue (Figure 108b) shifted 0.110 V.

Interestingly, Wuld and col. obtained a great redox gradient of 240 mV with the series of 1,4-fullerene derivatives. The higher LUMO energy level, 100 mV higher than that of PCBM, was achieved appending three strong electron-donating hexyloxy substituents to one of the phenyl groups (Figure 108e). In an effort to create a higher-LUMO derivative, fullerenol starting material was reacted with aniline, but under these synthetic conditions a C-N bond is directly created on the fullerene (Figure 108c), lowering the LUMO level due to the electronegativity of the nitrogen. Meanwhile, a 1,4-fullerene derivative with a LUMO level similar to PCBM was obtained attaching a mono-substituted alkyloxy benzene (Figure 108d).

107 A. Varotto, N. D. Treat, J. Jo, C. G. Shuttle, N. A. Batara, F. G. Brunetti, J. H. Seo, M. L. Chabinyc, C. J. Hawker, A. J. Heeger and F. Wudl, *Angew. Chem., Int. Ed.* **2011**, *50*, 5166-5169.

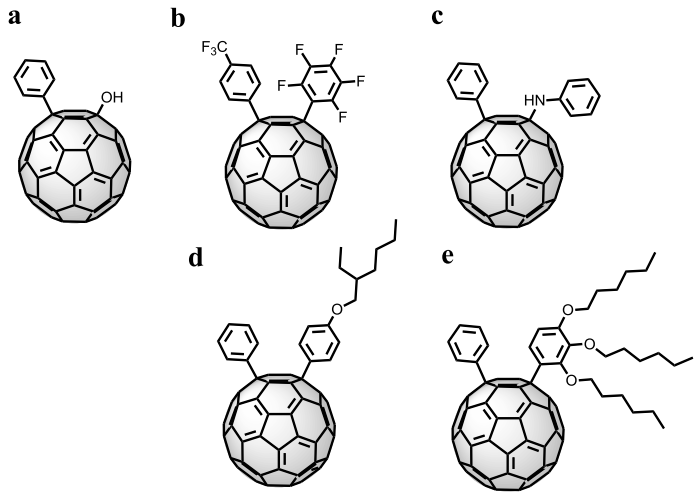

Figure 108. Molecular structure of 1,4-fullerene addends. (a) Fullerenol. (b-e) 1,4-Addends bearing both electron-withdrawing and electron-donating groups.

As previously described, saturation of a double bond of C_{60} in methanofullerenes causes, in general, a negative shift of about 100-150 mV for the first three reduction waves. Quinone-type methanofullerene derivatives (Figure 107c), with the quinone moiety and the sp^3 carbon atoms of C_{60} separated by a spiro carbon atom, results in more extended conjugated molecules, thus being stronger acceptors than C_{60}. This periconjugative interaction transmits the inductive effect of the addends of the quinone moiety and produce a small stabilization of the orbitals of C_{60}, giving rise to a stabilization of the LUMO energy level.[108]

Moreover, 1,2-dicyano-1,2-dihydrofullerene[109] and dicyano-1,2-dihydromethanofullerene[110] were reported, separately, by Wudl and col. as new examples of low-LUMO fullerene derivatives (Figure 109).

---

108 a) T. Ohno, N. Martín, B. Knight, F. Wudl, T. Suzuki and H. Yu, *J. Org. Chem.* **1996**, *61*, 1306-1309; b) B. Knight, N. Martín, T. Ohno, E. Ortí, C. Rovira, J. Veciana, J. Vidal-Gancedo, P. Viruela, R. Viruela and F. Wudl, *J. Am. Chem. Soc.* **1997**, *119*, 9871-9882; c) N. Martín, L. Sánchez, B. Illescas and I. Pérez, *Chem. Rev.* **1998**, *98*, 2527-2548.

109 M. Keshavarz-K, B. Knight, G. Srdanov and F. Wudl, *J. Am. Chem. Soc.* **1995**, *117*, 11371-11372.

110 M. Keshavarz-K, B. Knight, R. C. Haddon and F. Wudl, *Tetrahedron* **1996**, *52*, 5149-5159.

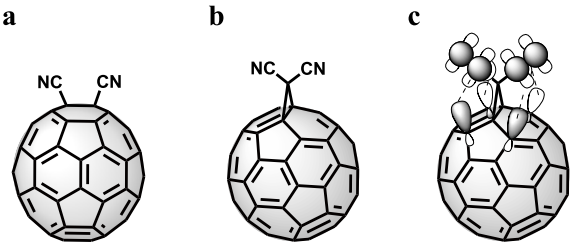

Figure 109. Cyano-containing fullerene derivatives and periconjugation-type effect in the dicyanomethanofullerene.

In the first case, the authors compensate the negative shift caused by the saturation of one double bond of C_{60} directly introducing two electron-withdrawing groups onto the buckmisterfullerene cage (Figure 109a). Firstly, the addition of cyanide anion to the fullerene produced the intermediate $C_{60}(CN)^-$ anion, which could be subsequently quenched with different electrophiles. Using *p*-toluenesulfonyl cyanide, the 1,2-dicyano C_{60} was formed, as a single isomer, in high yield. The main achievement of this methodology is the great shift in the first reduction wave to an exceptional 120 mV more positive than pristine C_{60}.

Meanwhile, the effect of cyano substitution in the 61-position of methanofullerene (Figure 109b) has another explanation. In this case, substituents are not conjugated with the fullerene and only inductive effect and not through resonance should be expected. Wuld and col. prepared for this study a series of different methanofullerene derivatives bearing electron-withdrawing groups. They observed that the presence of two moderately strong electron-withdrawing ester groups or one single very strong electron-withdrawing nitro group was not sufficient to compensate for the saturation of one C_{60} double bond. However, the existence of two cyano groups appended to the cyclopropane functionality caused a shift in the first peak reduction potential of 156 mV more positive than pristine C_{60}. This fact was explained by the authors by a periconjugative-type orbital interaction as shown in Figure 109c, which only could be possible with this substitution.

3.2. Objectives

3.2. Objectives

The objective of this chapter is to evaluate different fullerene derivatives as electron pathways in triple-channel oriented photosystems supported onto ITO. For this goal, the first points to consider are, on one hand, the correct functionalization of the fullerene derivatives with an aldehyde group for the chemo-orthogonal oxime formation with the oligothiophene derivative and, on the other hand, the solubility of the design molecules in polar aprotic solvents for the TSE step.

Given these requirements, in the first part of the chapter, we aim to compare different functionalization of fullerenes exploiting their established reactivity. In particular, we will use 1,4-addition and cyclopropanation reactions to create a series of fullerene derivatives with different energy levels. Once synthetized, these molecules will be attached to the oligothiophene hole channel through an oxime bridge to be lately implemented in the triple-channel photosystem by hydrazone exchange with a free hydrazine presented in the NDI-functionalized ITO surface. Finally, we will compare all the photosystems to extract some trends in relations to chemical functionalization and energy levels of the fullerenes.

The second part of the chapter will be focused in the preparation of fullerene derivatives with increasing π-acidity or, in other words, with lower LUMO energy levels again to be evaluated in triple-channel photosystems as partners of NDIs and oligothiophenes. To fulfill this goal, we will functionalized pristine fullerene with cyano groups, both directly attaching this electron withdrawing group to the fullerene core and through a cyclopropane ring. As a final point, we will implement the obtained fullerenes to the triple-channel photosystems and evaluate their potential.

3.3. Results and Discussion

3.3. Results and Discussion

3.3.1. 1,4-Diaryl[60]fullerene and 1,2-dihydromethano[60]fullerene derivatives for synthetic access towards oriented charge-transfer cascades in triple-channel photosystems.[111]

A new collection of fullerene derivatives is introduced, that is compatible with the construction of triple-channel architectures next to stacks of oligothiophenes and naphtalenediimides. For this purpose, two different chemical reactions on fullerenes have been applied, namely cyclopropanation and 1,4-addition. These modified fullerenes, in the next stage, are attached to the second-channel oligothiophene through an oxime bridge, creating the collection **T4-32** to **T4-37** (Scheme 16), which are finally implemented in the triple-channel photosystem by dynamic covalent hydrazone chemistry.

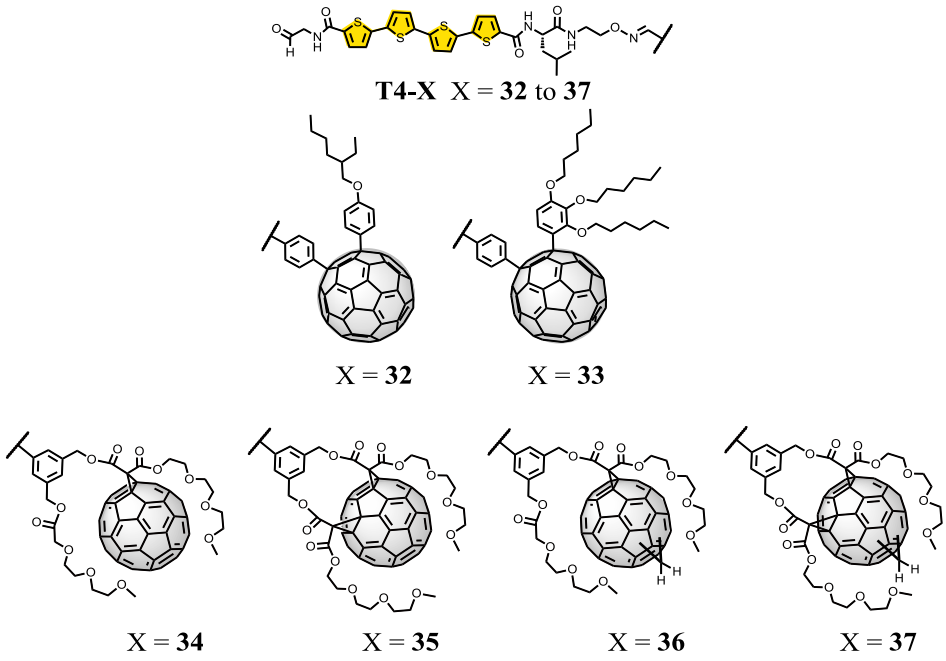

Scheme 16. Chemical structure of the dyads T4-1 to T4-6.

111 A. Bolag, J. López-Andarias, S. Lascano, S. Soleimanpour, C. Atienza, N. Sakai, N. Martín and S. Matile, *Angew. Chem., Int. Ed.* **2014**, *53*, 4890-4895.

3.3.1.1. Synthesis of fullerenes **32-37** and dyads **T4-32** and **T4-33**

Firstly, the synthesis of 1,4-diarylfullerene derivatives was carried out. Compound **1** was synthesized as follows in Scheme 17:

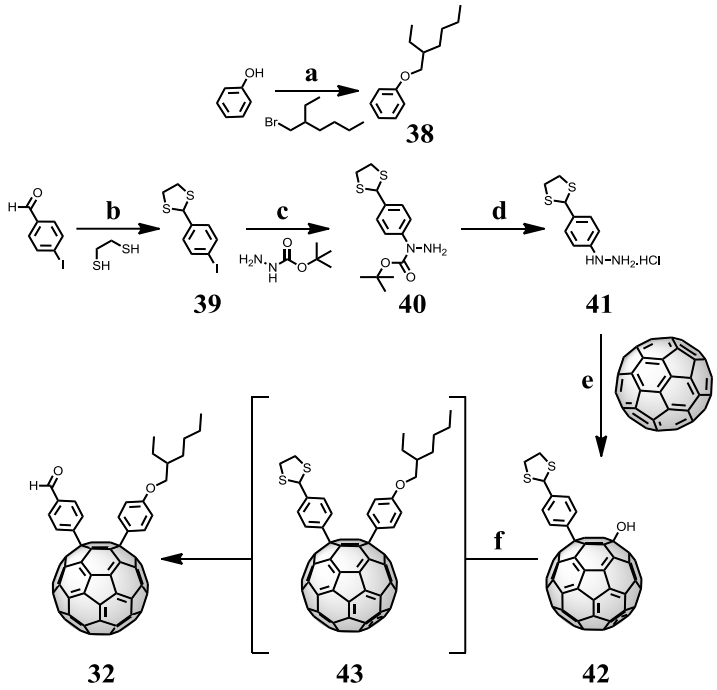

Scheme 17. Synthesis of formyl-fullerene 32. (a) ^{t}BuOK, DMF, 80 ºC, 98%; (b) $BF_3{\cdot}Et_2O$, CH_2Cl_2, rt, 96%; (c) CuI, 1,10-phenanthroline, Cs_2CO_3, DMF, 80 ºC, 67%; (d) HCl_{aq}, CH_3OH, 50 ºC, quantitative; (e) $NaNO_2$, HCl, O_2, sonication, toluene, 50 ºC, 15%; (f) 1. **38**, *p*-TsOH, 80 ºC; 2. HgO, $BF_3{\cdot}Et_2O$, THF/H_2O (9:1, v:v), rt, 10% (2 steps).

The synthesis of the 1,4-diarylfullerene addends was first reported by Wang and col. and expanded by Wuld and col.[112,107] In this case, the introduction of a dithiane-protected benzaldehyde into the fullerenol was selected as the best method to retain the aldehyde group protected along the synthetic route. The hydrazine **41** was readily accessible from *p*-iodobenzaldehyde in a three-step synthetic procedure, involving aldehyde-protection, Cu-catalyzed C-N coupling with *tert*-butylcarbazate and Boc-deprotection under acidic conditions. The alkoxybenzene **38** was prepared by simple alkylation of the corresponding

112 G.-W. Wang, Y.-M. Lu and Z.-X. Chen, *Org. Lett.* **2009**, *11*, 1507-1510.

phenol under basic conditions, with quantitative yield. The Wang radical reaction with the phenyl hydrazine **41** in the presence of $NaNO_2$ gave the desired product **42** in, at least in this context, reasonable 15% yield. 1,4-addition was completed with the alkoxybenzene **38** in the presence of *p*-toluenesulfonic acid (*p*-TsOH), and HgO-mediated hydrolysis of the non-isolable intermediate **43** afforded the desired product **32**.

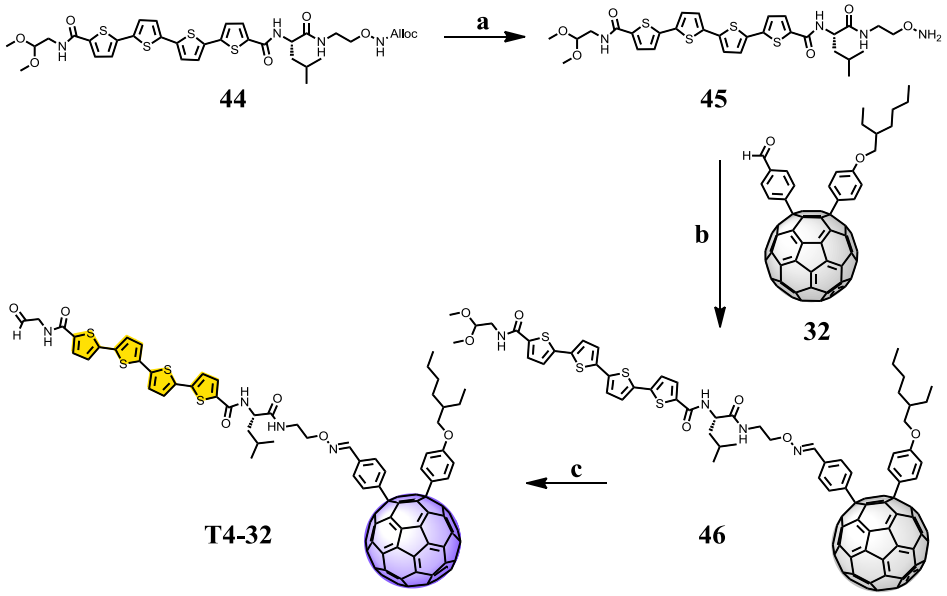

Scheme 18. Synthesis of dyad T4-32. (a) $[Pd(PPh_3)_2Cl_2]$, Bu_3SnH, AcOH, CH_2Cl_2, rt; (b) **32**, rt, 47% (2 steps); (c) TFA/CH_2Cl_2 (1:2, v:v), rt, 72%.

Scheme 18 shows the synthesis of dyad **T4-32**: Chemoselective palladium-catalyzed reductive deprotection of Alloc group in quaterthiophene derivative **44** liberated the reactive alkoxyamine in **45**. Spontaneous oxime formation between **45** and **32** then gave the dyad **46** essentially in situ. Aldehyde deprotection afforded the desired dyad **T4-32** under mild reaction conditions, and made ready for TSE. **T4-33**, the electron-rich homologue of **T4-32**, was prepared analogously from **33** using the alkylated pyrogallol **47** instead of **38** (Scheme 19).

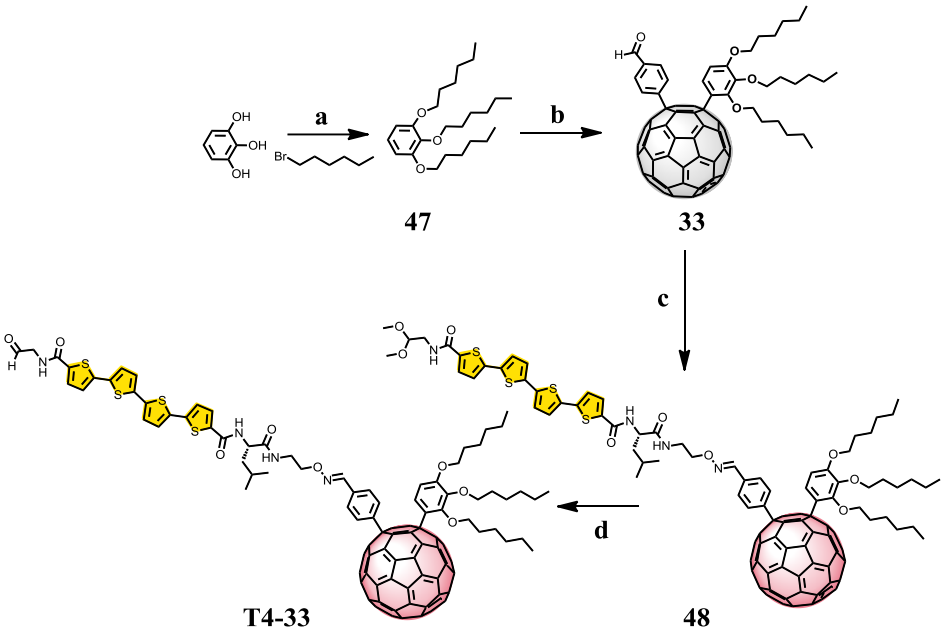

Scheme 19. Synthesis of dyad T4-33. (a) K_2CO_3, DMF, 80 ºC, 76%; (b) 1. *p*-TsOH, C_{60}, **42**, 80 ºC; 2. HgO, $BF_3 \cdot Et_2O$, THF/H_2O (9:1, v:v), rt, 28% (2 steps); (c) 1. **45**, $[Pd(PPh_3)_2Cl_2]$, Bu_3SnH, AcOH, CH_2Cl_2, rt; 2. **33**, rt, 52% (2 steps); (d) TFA/CH_2Cl_2 (1:2, v:v), rt, 93%.

In the case of the methanofullerene-based dyads, three novel fullerene derivatives were synthesized (Scheme 20), with a similar structure to that of fullerene **35** previously described by Matile and col.[97] The diol **49**, previously synthetized and described in the literature,[113] was converted into the malonate **53** by consecutive esterification reactions with the TEG-glycolate **50** and TEG-malonate **52**[97]. Cyclopropanation of pristine C_{60} with **53** gave the Bingel-type fullerene **54**.

113 M. Morisue, N. Haruta, D. Kalita and Y. Kobuke, *Chem. Eur. J.* **2006**, *12*, 8123-8135.

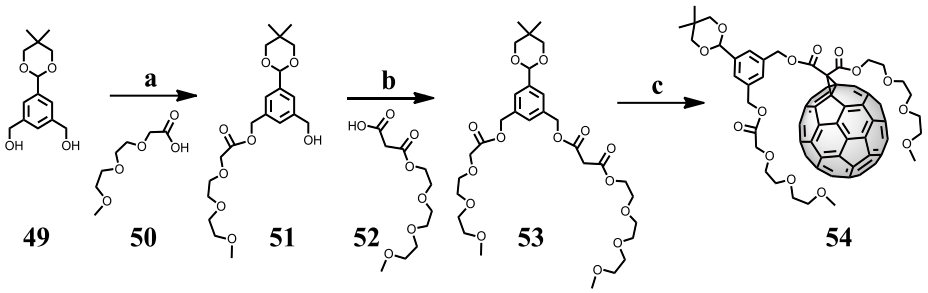

Scheme 20. Synthesis of Bingel-fullerene 54. (a) EDC, DMAP, CH_2Cl_2, rt, 67%; b) EDC, DMAP, CH_2Cl_2, rt, 66%; c) C_{60}, I_2, DBU, toluene, -15 ºC to rt, 64%.

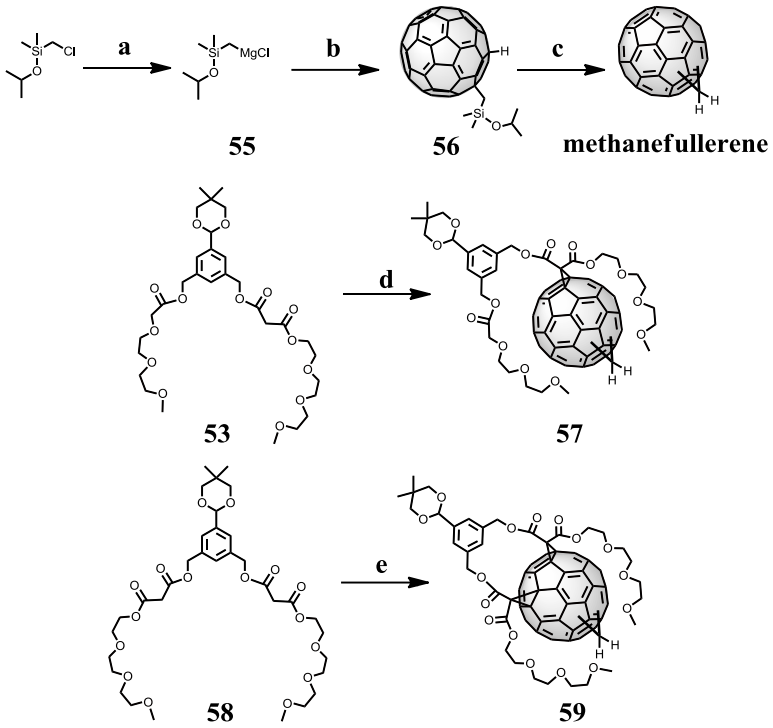

Scheme 21. Synthesis of Bingel-fullerenes 57 and 59. (a) Mg, 1,2-dibromoethane, THF, reflux; (b) C_{60}, DMF, *o*-DCB, rt, 89% (2 steps); (c) 1. ^{t}BuOK; 2. $CuCl_2$, *o*-DCB, 100 ºC, 79% (one pot); (d) 1,2-dihydromethanofullerene, I_2, DBU, toluene, -15 ºC to rt, 38%; (e) 1,2-dihydromethanofullerene, I_2, DBU, toluene, -15 ºC to rt, 40%.

1,2-Dihydromethanofullerene, having a cyclopropane group, was synthesized using the original procedure.[104] Namely, addition of the Grignard reagent **55** and subsequent deprotonation of the obtained silylfullerene and oxidative cyclopropane formation in the presence of $CuCl_2$ at 100 ºC. 1,2-Dihydromethanofullerene was converted into **57** and **59** by using the procedure described above for **54**, using malonate **53** or double-malonate **58**, respectively (Scheme 21).

T4-34, **T4-35**, **T4-36** and **T4-37** were prepared following the exceptionally mild procedure described above for **T4-32**, after deprotection of all the corresponding aldehyde functionalities of Bingel-fullerene compounds.

Moreover, compounds **32** and **33** were converted into their respective methyloximes **o-32** and **o-33** (Scheme 22) in order to study the influence of the substituent on the phenyl group of a 1,4-addend on their reduction potentials. In this way, the value of the first reduction wave of these two derivatives can be reliably comparable with those belonged to the dyads **T4-32** and **T4-33**.

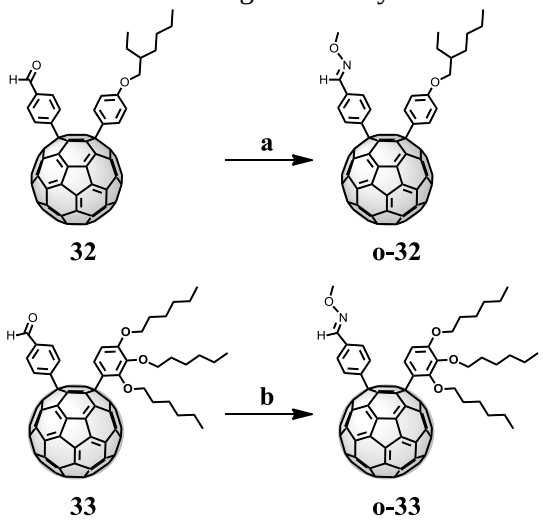

Scheme 22. Synthesis of oximes o-32 and o-33. AcOH, $CH_3ONH_2 \cdot HCl$, CH_2Cl_2, 60 ºC, 40% (a), 85% (b).

3.3.1.2. Electrochemical characterization of fullerene derivatives

The reduction potentials of **o-32**, **o-33** and **34**-**37** were determined using differential pulse voltammograms (DPV, scan rate 100 mV/s) vs Fc/Fc^+ in DCM (100 mM Bu_4NPF_6 as supporting electrolyte, Pt as working electrode, Pt wire as

counter electrode and SCE as reference electrode). LUMO energies *vs* vacuum were estimated from first reduction peak in DPV assuming 5.1 eV for Fc^+/Fc using the equation E1.[98] The optical band gap (E_g^{opt}) was calculated from the onset of the lowest energy band using the equation E2. HOMO energy levels were estimated from difference between E_{LUMO} and E_g^{opt} (E3).

$$E_{LUMO} = -5.1 \text{ eV} - E_{DPV} \textit{ vs } (Fc/Fc^+) \qquad \text{(E1)}$$

$$E_g^{opt} = 1240 / \lambda_{max}^{onset} \text{ (nm)} \qquad \text{(E2)}$$

$$E_{HOMO} = E_{LUMO} - E_g^{opt} \qquad \text{(E3)}$$

For DPV measurements, **32** and **33** were converted into their respective methyloximes. Consistent with the presence of fewer alkoxy donors, the LUMO level of **o-32** was 60 meV below that of **o-33** (Figure 110a). For the Bingel quartet **37**, **36**, **35**, and **33**, a marvelous stepwise decrease of the LUMO energies by 60 meV each could be detected unambiguously by DPV against Fc^+/Fc as the internal standard (Figure 110b).

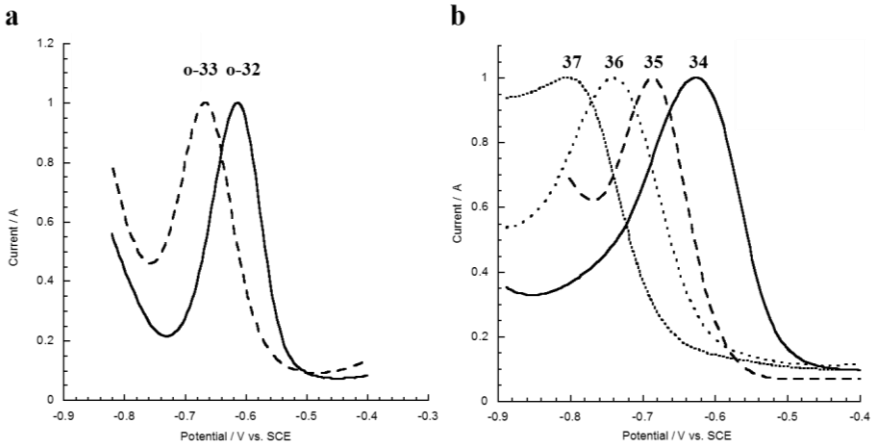

Figure 110. Normalized DPVs. (a) oximes **o-32** and **o-33**; (b) **34-37**, measured in CH_2Cl_2 against internal Fc^+/Fc standards at 0 mV.

An accurate estimation from the HOMO/LUMO gap in the absorption spectra is difficult because of the weak and gradually decreasing tail of fullerene derivatives reaching up to about 650 nm. A constant HOMO/LUMO gap of 2.3 eV for Bingel fullerenes was assumed based on the literature.[114] For **o-32** and **o-33**, the HOMO/LUMO gap was arbitrarily reduced to 2.2 eV considering the

114 Y. Yang, F. Arias, L. Echegoyen, L. P. F. Chibante, S. Flanagan, A. Robertson and L. J. Wilson, *J. Am. Chem. Soc.* **1995**, *117*, 7801-7804.

previously reported red shift caused by their lowered symmetry.[107] The direct determination of the LUMO energy levels of the fullerenes, of central importance for this study, is most accurate, while the intrinsic uncertainty of the absolute values of the HOMO energy levels is inconsequential (Figure 111).

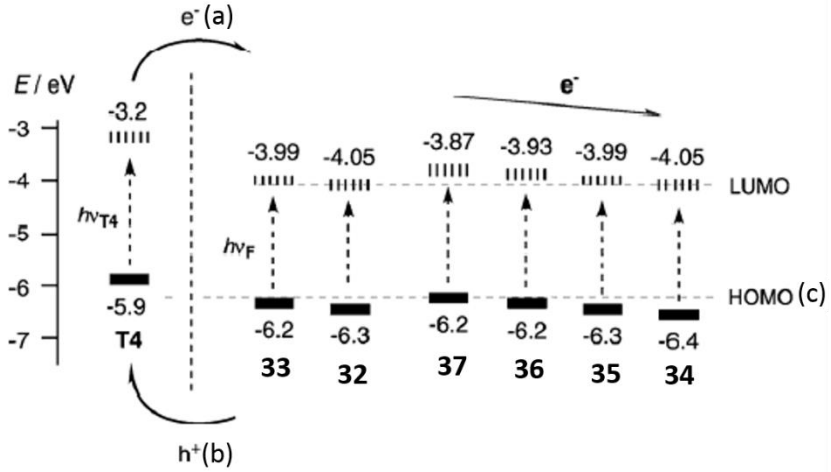

Figure 111. Energy levels of HOMO (bold) and LUMO (dashed) of all fullerene derivatives and T4[97] (in eV against vacuum, assuming -5.1 eV for Fc^+/Fc). (a) Electron transfer after excitation of **T4** ($h\upsilon_{T4}$) and (b) proton transfer after excitation of fullerenes ($h\upsilon_F$). (c) HOMO levels of fullerenes, estimated by reducing 2.3 V to the LUMO level of Bingel fullerenes **34** to **37** and 2.2 eV to the corresponding of 1,4-fullerenes **o-32** and **o-33**.

*3.3.1.3. Stack Exchange of dyads **T4-32** to **T4-37***

To explore the compatibility of this new set of fullerene derivatives in triple-channel photosystems, an initial channel of NDI stacks was grown onto ITO by the establish SOSIP strategy.[94] These NDI templates where decorated with benzaldehyde hydrazone (**B**) along the column, for the subsequent TSE with the oligothiophene-fullerene dyads synthetized. The absorption of the so-obtained ITO-**NDI-B** was adjusted at A_{380} = 0.17 to maximize comparability between photosystems. This absorbance corresponds to around 142 stacked NDIs, with a thickness nearby 47 nm. In a common experiment, the obtained electrode was treated with aqueous NH_2OH (1 M) for 24 h at 40 ºC, removing the benzaldehyde protecting group and leading to the photosystem ITO-**NDI**. This prepared electrode was dipped in a solution of the corresponding dyads in DMSO and acetic acid (9:1, 8-12 mM) and shaken for 24 h at 40 ºC (Figure 112a).

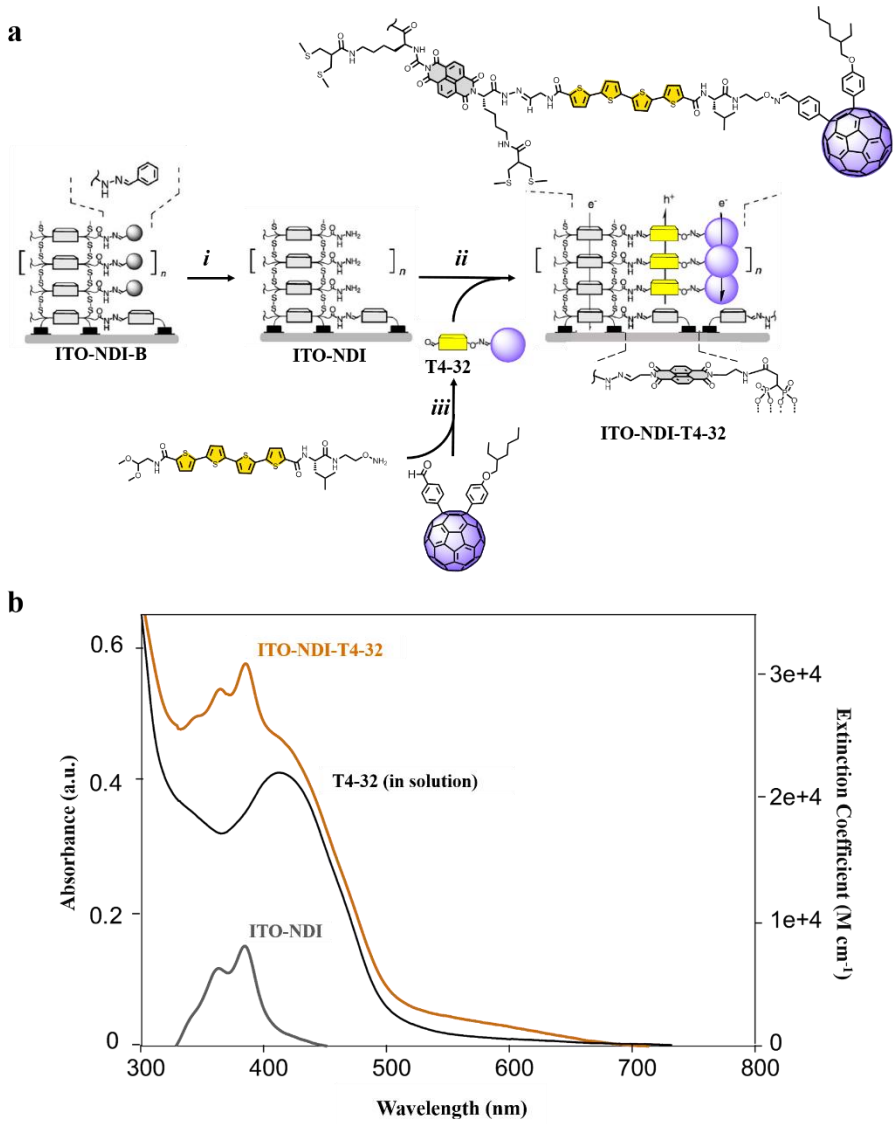

Figure 112. Stack-Exchange of dyad T4-32. (a) SOSIP-TSE approach to triple-channel surface architecture exemplified for dyad **T4-32**: After formation of ITO-**NDI-B** by disulfide-exchange, hydrazine groups are deprotected with excess NH_4OH (i), and subsequent TSE with chemo-orthogonal hydrazone exchange with aldehyde **T4-32** yield ITO-**NDI-T4-32** (ii). Previously to TSE, dyad **T4-32** is created through an oxime bridge between oligothiophene and fullerene derivatives followed by acetal removal (iii). (b) Extinction coefficient of **T4-32** (black) and changes in the absorption spectra of the surface architecture before (grey) and after (orange) TSE, after incubation for 24 hours.

The desired **ITO-NDI-T4-32** photosystem was obtained when no more changes in UV-*vis* absorption spectra were observed. The yield of stack exchange was roughly estimated from the molar ratio R obtained from the absorbances of the film after stack exchange at 390 nm and 450 nm by using the following equations:

$$A'_{\text{at 390 nm}} = \varepsilon'_{\text{NDI}}[\text{NDI}] + \varepsilon'_{\text{dyad}}[\text{dyad}]$$

$$A''_{\text{at 450 nm}} = \varepsilon''_{\text{NDI}}[\text{NDI}] + \varepsilon''_{\text{dyad}}[\text{dyad}]$$

$$R = [\text{dyad}] / [\text{NDI}] \qquad [\%] = (R / 2) \times 100$$

where A' and A'' are the absorbances at 390 nm and 450 nm, $\varepsilon'_{\text{NDI}}$ and $\varepsilon''_{\text{NDI}}$ are the molar absorption coefficients of NDI at 390 nm and 450 nm, and $\varepsilon'_{\text{dyad}}$ and $\varepsilon''_{\text{dyad}}$ are the molar absorption coefficients of the corresponding dyad at 390 nm and 450 nm, respectively. Quantitative yield was assumed for a 2:1 ratio (R = 2.0).

Figure 112b shows the absorption spectrum of ITO-**NDI-T4-32**, where the presence of all components is clearly observable. From the absorption spectra, a TSE yield of 82% was estimated. The formation of the other triple-channel architectures (ITO-**NDI-T4-33** to ITO-**NDI-T4-37**) occurred with similar satisfactory yield (Table 1).

	Photosystem	TSE [%]
1	ITO-**NDI-T4-32**	82
2	ITO-**NDI-T4-33**	70
3	ITO-**NDI-T4-34**	67
4	ITO-**NDI-T4-35**	89
5	ITO-**NDI-T4-36**	78
6	ITO-**NDI-T4-37**	62

Table 1. Yield for TSE, estimated from absorption spectra of each photosystem.

*3.3.1.4. Functional characterization of dyads **T4-32** to **T4-37***

Photocurrent measurement of the final triple-channel photosystems were measured under routine conditions, using each architecture as a working electrode, a Pt wire as a counter electrode and Ag/AgCl as a reference electrode. To close this circuit, a 50 mM aqueous solution of the sacrificial mobile hole

transporter TEOA in 0.1 M Na_2SO_4 was used. Electrodes were irradiated with a solar simulator and their changes in current upon on-off switching of irradiations were measured at 0 V *vs* Ag/AgCl. The highest currents were observed for ITO-**NDI-T4-34**. This is the most active triple-channel photosystem prepared so far,[98] with a photocurrent generation of J_{SC} = 12.0 µA cm^{-2}. To probe the role of electron-accepting fullerene in the photocurrent produced by this architecture, a fullerene-free double-channel control (ITO-**NDI-T4**) was prepared. Although an extraordinary high TSE yield (90%) was achieved, the value of its photocurrent generation was J_{SC} = 2.4 µAcm^{-2}, supporting the significance of operational triple-channel architectures. The presence of an electron-transporting channel next to the hole-transporting **T4** channel in **ITO-NDI-T4-34** thus caused a greater than fivefold increase in activity, although the TSE yield and thus the relative **T4** content was with 67% clearly lower than in the fullerene-free control ITO-**NDI-T4**. High photocurrents were also found for ITO-**NDI-T4-35** with defined positions of the two cyclopropanes, whereas the 1,4-diarylfullerenes containing ITO-**NDI-T4-32** and ITO-**NDI-T4-33** were less active, and ITO-**NDI-T4-36** and ITO-**NDI-T4-37** with methanofullerenes were worst (Figure 113).

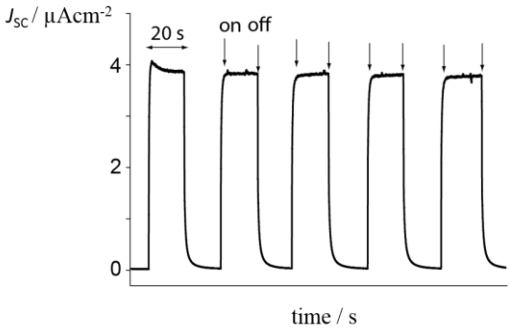

	Photosystem	J_{SC} [µAcm^{-2}]
1	ITO-**NDI-T4-32**	3.9
2	ITO-**NDI-T4-33**	2.8
3	ITO-**NDI-T4-34**	12.0
4	ITO-**NDI-T4-35**	8.8
5	ITO-**NDI-T4-36**	2.1
6	ITO-**NDI-T4-37**	2.2

Figure 113. Photocurrent generated by ITO-**NDI-T4-32** (top) and Table representing the values obtained for all surface photosystems (down).

For a better understanding of these tendencies, action spectra of all photosystems in the presence of TEOA as sacrificial electron donor were measured. Furthermore, bimolecular recombination efficiencies η_{BR} were calculated from the dependence of photocurrent densities (J_{SC}) to the irradiation power (I). Action spectra of ITO-**NDI-T4-34** demonstrated the significant contribution of oligothiophene above λ = 400 nm and fullerene and NDI below this wavelength. However, in the case of ITO-**NDI-T4-36**, weak photocurrent generation by the oligothiophenes in the action spectrum is observed, probably due to poor electron transfer from excited oligothiophene to fullerenes with high LUMO energy value (Figure 114a). Moreover, recombination efficiency in this system was very high with η_{BR} = 92% especially comparing with η_{BR} = 58% calculated for ITO-**NDI-T4-34** (Figure 114b). The weaker activities of ITO-**NDI-T4-32** and ITO-**NDI-T4-33** comparing with the best system ITO-**NDI-T4-34** could become from reduced hole transfer of excited fullerenes with high HOMO to oligothiophenes. The importance of hole transfer from excited fullerenes has been suggested before for other systems.[115]

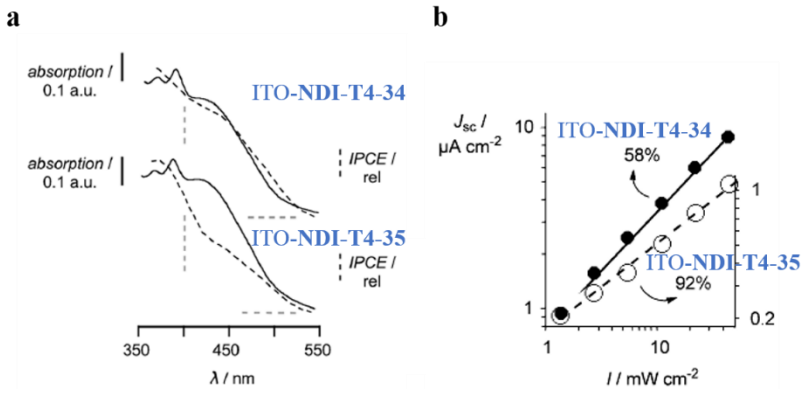

Figure 114. Electrode characterization. (a) Absorption spectra (solid lines) and action spectra (dashed lines). (b) Dependence of the short-circuit current density J_{SC} on the light intensity; for ITO-**NDI-T4-34** and ITO-**NDI-T4-35**.

115 T. E. Kang, H.-H. Cho, C.-H. Cho, K.-H. Kim, H. Kang, M. Lee, S. Lee, B. Kim, C. Im and B. J. Kim, *ACS Appl. Mater. Interfaces* **2013**, *5*, 861-868.

However, probably one of the most important aspects to explain these trends could be the organization of strings of fullerenes in the triple-channel photosystem, where the most structurally defined fullerene **34** is the most homogeneous system, comparing with regioisomeric mixtures in **36** and **37** but, otherwise, more flexible to fit in the free spaces of the architecture, comparing with the stiffer aryl addends in **32** and **33**. Fullerene **35** is a particular example of bisadduct since the position of both cyclopropanes is defined by the number of carbons between the malonates in building block **58**, thus obtaining a monodisperse regioisomeric fullerene derivative.

3.3.2. Electron-deficient fullerenes in triple-channel photosystems.[116]

In this section, fullerenes with decreasing LUMO energy level are designed, synthetized and attached to oligothiophene derivative **T4** to build dyads **T4-60** to **T4-64** (Scheme 23). These dyads are finally evaluated in multicomponent surface architectures.

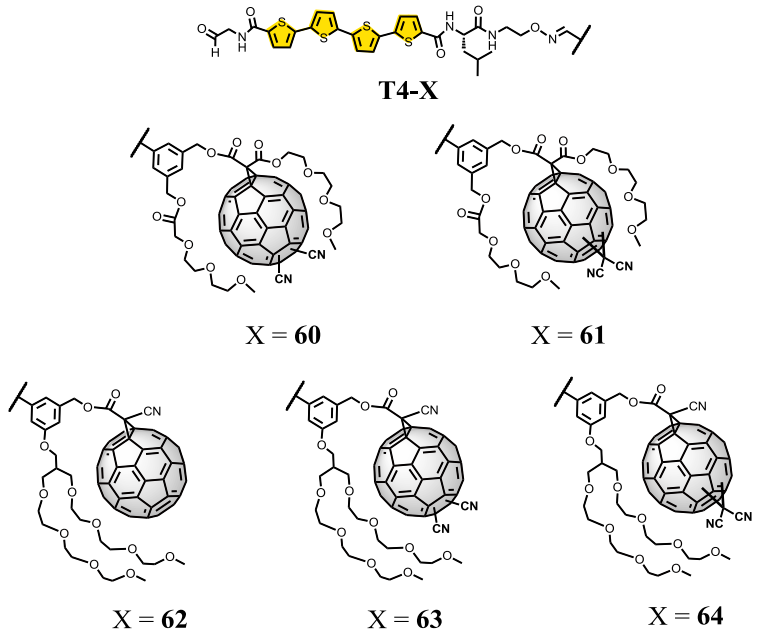

Scheme 23. Chemical structure of the dyads T4-60 to T4-64.

*3.3.2.1. Synthesis of fullerenes **60-64***

In order to systematically reduce the LUMO energy level of the fullerene sphere, one, two or three electron-withdrawing cyano groups were introduced in its structure, either directly or as substituent in a cyclopropane functionality. For this purpose, two new fullerene building blocks were synthetized, namely 1,2-dicyanofullerene[109] and 1,2-dicyanomethanofullerene[110].

116 J. Lopez-Andarias, A. Bolag, C. Nancoz, E. Vauthey, C. Atienza, N. Sakai, N. Martin and S. Matile, *Chem. Commun.* **2015**, *51*, 7543-7545.

As depicted in Scheme 24, 1,2-dicyanofullerene was obtained by addition of cyanide anion to the fullerene cage, producing the intermediate $C_{60}(CN)^-$, which was subsequently quenched with *p*-toluenesulfonyl cyanide electrophile. Meanwhile, the extremely mild conditions described by Wang and col.[117] were chosen for the synthesis of 1,2-dicyanomethanofullerene, using malononitrile in the presence of $Mn(OAc)_3 \cdot 2H_2O$ instead of the previously reported method using the hazardous diazomalononitrile.[110]

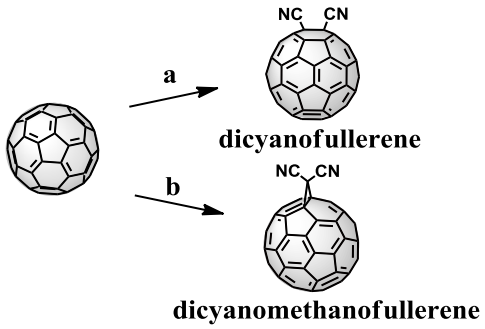

Scheme 24. Synthesis of dicyano[60]fullerene and dicyanomethano[60]fullerene. (a) 1. NaCN, DMF, toluene, rt; 2. *p*-TsCN, 61% (2 steps); (b) malononitrile, $Mn(OAc)_3 \cdot 2H_2O$, chlorobencene, reflux, 18%.

Dicyanofullerene and dicyanomethanofullerene were converted into bisadducts **60** and **61**, respectively, by classical Bingel cyclopropanation reaction with malonate **53** followed by deprotection reaction of the corresponding benzaldehyde group (Scheme 25). Both bisadducts **60** and **61** were obtained as a regioisomeric mixture.

117 T.-H. Zhang, P. Lu, F. Wang and G.-W. Wang, *Org. Biomol. Chem.* **2003**, *1*, 4403-4407.

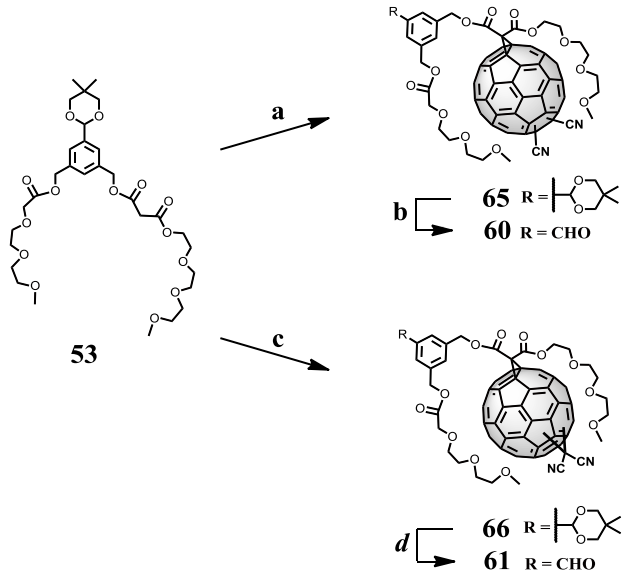

Scheme 25. **Synthesis of formyl-fullerenes 60 and 61**. (a) Dicyanofullerene, I_2, DBU, toluene, -15 ºC to rt, 60%; (b) TFA/H_2O, CH_2Cl_2, rt, 58%; (c) dicyanomethanofullerene, I_2, DBU, -15 ºC to rt, 56%; (d) TFA/H_2O, CH_2Cl_2, rt, 56%.

Meanwhile, in **62**, with one cyano group, and **63** and **64**, with three, the Bingel reaction was performed with cyanoacetate **71** instead of malonate **53** (Scheme 26). In this sense, to maintain the good solubility in aprotic polar solvents achieved with the two TEG tails in malonate **53**, cyanoacetate **71** was designed preserving both solubilizers and constructed in a six-step synthetic procedure: Firstly, alcohol **67** was obtained by *O*-alkylation of two triethyleneglycol monomethyl ethers with 3-chloro-2-(chloromethyl)-1-propene and hydroboration-oxidation of the alkene.[118] Secondly, Mitsunobu reaction between alcohol **67** and dimethyl 5-hydroxyisophthalate was carried out to obtain diester **68** which was reduced to dialcohol **69** in good yield. Finally, after mono-esterification of **70** with cyanoacetic acid and oxidation of the remaining benzyl alcohol with Dess-Martin periodinane, cyanoacetate **71** was obtained in an overall moderate yield. Again, bisadducts **63** and **64** were obtained as a regioisomeric mixture.

118 S. Zhu, J. Zhang, G. Vegesna, F.-T. Luo, S. A. Green and H. Liu, *Org. Lett.* **2011**, *13*, 438-441.

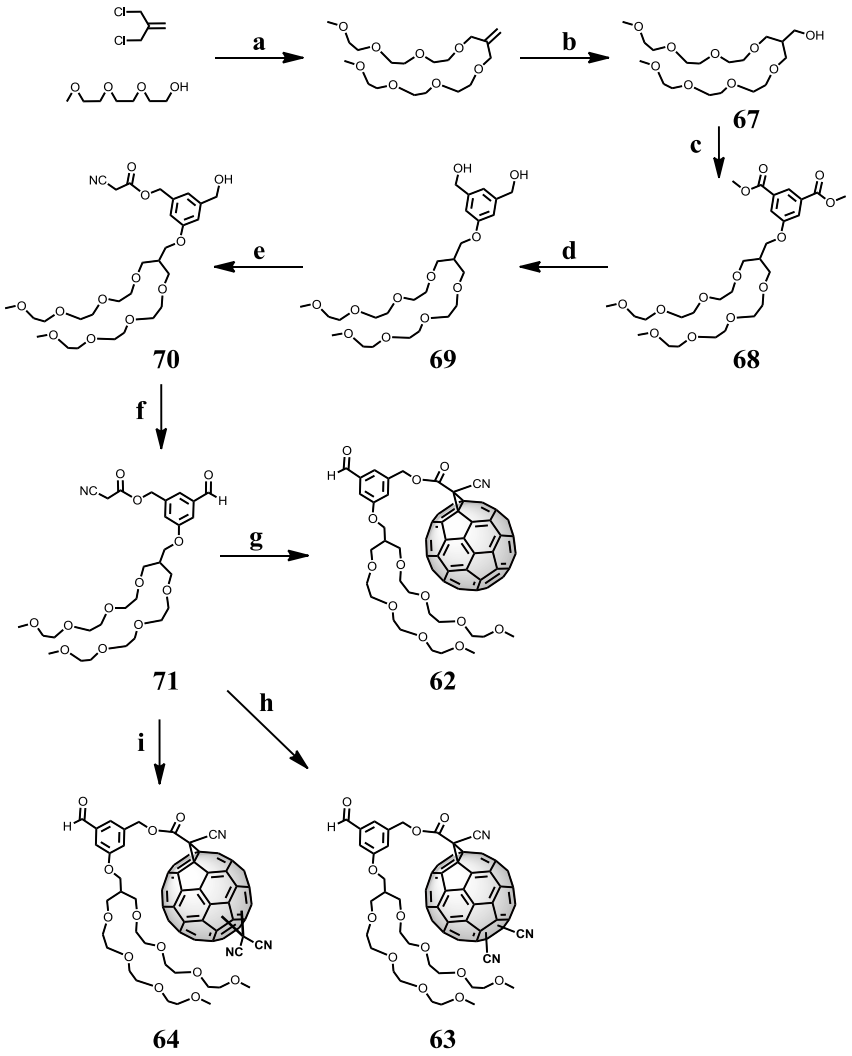

Scheme 26. Synthesis of formyl-fullerenes 62, 63 and 64. (a) NaH, dry THF, rt to 65 ºC, 85%; (b) 1. BH_3, THF, 0 ºC; 2. NaOH; 3. H_2O_2, rt, 80%; (c) DIAD, PPh_3, CH_2Cl_2, 0 ºC to rt, 50%; (d) $LiAlH_4$, THF, 0 ºC to rt, 87%; (e) 2-cyanoacetic acid, EDC, DMAP, CH_2Cl_2, 0 ºC to rt, 55%; (f) Dess-Martin periodinane, CH_2Cl_2, rt, 85%; (g) C_{60}, DBU, I_2, toluene, –15 ºC, 15%; (h) dicyanofullerene, DBU, I_2, toluene, -15 ºC, 16%; dicyanomethanofullerene, DBU, I_2, toluene, -15 ºC, 9%.

*3.3.2.2. Electrochemical characterization of fullerene derivatives **60** to **64***

To estimate the LUMO energy levels of the new electron-deficient fullerenes **60**-**64**, differential pulse voltammetry (DPV) against the Fc^+/Fc couple as an internal standard were accomplished (Figure 115). LUMO energies *vs* vacuum were estimated from first reduction peak in DPV assuming 5.1 eV for Fc^+/Fc using the equation E1.[98] As predicted, highest LUMO energy level was found at -4.10 eV for **62** with only one cyano acceptor group. In the case of bisadducts **60** and **61** with two electron-withdrawing cyano groups, the cyclopropane modality seemed to have a more pronounced effect on the π-acidity of fullerene core, decreasing the LUMO level 50 meV to -4.15 eV in **61**, while bisadduct **60** with two cyano acceptors attached directly to the fullerene core caused a decrease of 30 meV to -4.13 eV. Fullerenes **63** and **64** with three cyano acceptors were the most π-acidic, with nearly no difference in their first reduction potential (around 10 meV) that is, a LUMO energy level at -4.22 meV and -4.21 meV, for **64** and **63**, respectively. Together with the previously reported fullerenes **32**–**37**, these results yield an electron transfer cascade of eleven fullerene derivatives (nine of them of high structural similarity, that is, Bingel-type fullerenes), covering 350 meV down to -4.22 eV.

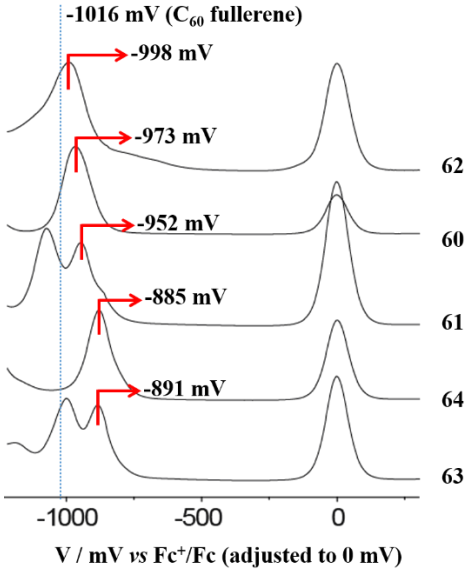

Figure 115. Normalized differential pulse voltammograms (DPV) of fullerene derivatives 60 to 64.

As envisioned in Figure 115, fullerenes **62** and **64** endowed with a dicyanomethane group, presented two reduction peaks very near one to the other. A possible explanation for this behavior is the irreversibility of the first reduction wave in dicyanomethanofullerene derivatives, as described in the literature,[110] suggesting that a thermally activated process, possibly a cyclopropane ring-opening occurs upon reduction. On the other hand, it has also been reported in related cyclopropanes linked to strong electron-acceptor units that they undergo the reduction process via an open-cyclopropane structure, obtained after the attachment of the second electron, which produces the heterolytic opening of the cyclopropane ring.[108b]

*3.3.2.3. Stack Exchange of dyads **T4-60** to **T4-64***

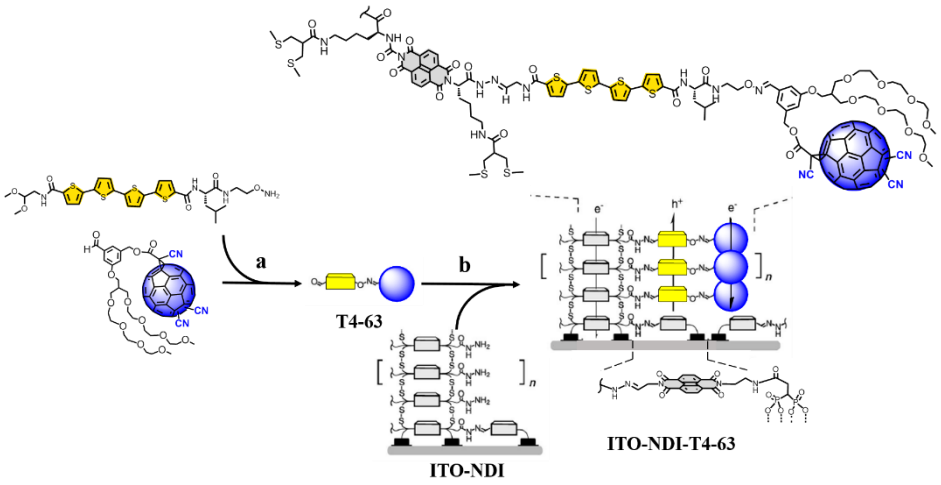

Figure 116. SOSIP-TSE approach to triple-channel surface architecture illustrated for dyad T4-63. (a) Dyad **T4-63** is created through an oxime bridge between oligothiophene **T4** and fullerene **63** followed by acetal removal. (b) TSE with chemo-orthogonal hydrazone exchange with aldehyde **T4-63** and ITO-**NDI** yield ITO-**NDI-T4-63.**

The new electron-deficient fullerenes were engineered into multicomponent surface architectures under the conditions developed for the electron-rich fullerene series described before. As exemplified for the most π-acidic **63** (Figure 116), oxime formation with the reported quaterthiophene gave rise to dyad **T4-63** after hydrolysis of the acetal under acidic conditions. The free aldehyde was used for templated stack exchange (TSE) with **ITO-NDI** using

dynamic covalent hydrazone chemistry. The obtained triple-channel architecture **ITO-NDI-T4-63** is expected to contain hole-transporting oligothiophene stacks between electron-transporting channels composed of co-axial columns of fullerenes and NDIs.

Triple-channel architectures with all other new fullerenes were prepared analogously. As expected for the bulky dyads, TSE yields were between 51 and 74% (Table 2).

	Photosystem	TSE [%]
1	ITO-**NDI-T4-60**	74
2	ITO-**NDI-T4-61**	72
3	ITO-**NDI-T4-62**	52
4	ITO-**NDI-T4-63**	58
5	ITO-**NDI-T4-64**	51

Table 2. Yield for TSE, estimated from absorption spectra of each photosystem.

*3.3.2.4. Functional characterization of dyads **T4-60** to **T4-64***

Photocurrent generation by the new photosystems was measured under the conditions used before to assure the comparability of the results. The highest short-circuit photocurrent densities J_{SC} = 8.1 µA cm^{-2} were obtained with the photosystem containing only one cyano group attached to the fullerene, that is, **ITO-NDI-T4-60**. All other photosystems with more electron-deficient fullerenes **61-64** had a similar activity around J_{SC} = 5.5 ± 0.5 µA cm^{-2}. These results suggested that the activity in triple-channel photosystems does not directly increase with increasing π-acidity of the fullerene, although hole transfer to the oligothiophene after excitation of the fullerene should improve.[115] Further analysis did not reveal distinct differences with regard to charge recombination efficiencies (35–64%), open-circuit voltages (270–320 mV) or activation energies (Table 3).

	Photosystem	J_{SC} [µA cm^{-2}]	η_{BR} [%]	V_{OC} [V]	E_a [meV]
1	ITO-**NDI-T4-60**	8.1	64	0.32	258
2	ITO-**NDI-T4-61**	5.2	51	0.30	243
3	ITO-**NDI-T4-62**	5.3	43	0.31	196
4	ITO-**NDI-T4-63**	5	35	0.26	-
5	ITO-**NDI-T4-64**	6	46	0.27	-

Table 3. Photocurrent generation densities, bimolecular recombination efficiencies, open-circuit voltages and activation energies of photosystems ITO-NDI-T4-60 to ITO-NDI-T4-64.

3.4. Conclusions

3.4. Conclusions

A new collection of fullerenes, from **32-37** to **60-64**, has been synthesized in order to build triple-channel photosystems having oriented strings of NDIs, oligothiophenes and fullerenes for directional electron transfer. The redox potentials of the fullerenes could be adjusted without losses in reactivity and solubility with gradients of LUMO levels over 350 meV, from -3.87 eV down to -4.22 eV.

Confirmed compatibility with SOSIP-TSE methodology provided exceptionally mild, fast and easy conditions for the directional positioning of the new fullerenes in triple-channel architectures with molecular-level precision.

Best activities were found for fullerenes with the best preserved π-system and with the least rigid substituents, i.e., fullerenes **34** (J_{SC} = 12.0 μA cm^{-2}) and **60** (J_{SC} = 8.1 μA cm^{-2}) with just one cyclopropane addend. Photosystems with fullerene **35**, characterized by a defined positioning of the two cyclopropanes, generated significant photocurrent as well (J_{SC} = 7.8 μA cm^{-2}). All mixtures of regioisomers gave clearly weaker activity; notwithstanding, those regioisomers with lower LUMO levels (**63** and **64**) present better photocurrent values than that with higher LUMO level (**36** and **37**). These observations suggested that the preserved integrity and structural homogeneity of the fullerenes are most important for their activity in the described triple-channel photosystems, whereas decreasing LUMO energies are clearly beneficial but overall less important. Possible explanations of these trends include poorer organization of the strings of fullerenes with regioisomers and weakened electron affinity with decreasing tension in the π-system.

3.5. Experimental Section

3.5. Experimental Section

3.5.1. Synthesis

Reagents for synthesis were mostly purchased from Fluka, Sigma-Aldrich, and Across. Fullerene C_{60} was purchased from IoLiTec Ionic Liquids Technologies GmbH (Heilbronn, Germany). Column chromatography was carried out on silica gel 60 (Fluka, 40-63 μm). Analytical (TLC) and preparative thin layer chromatography (PTLC) was performed on silica gel 60 (Fluka, 0.2 mm) and silica gel GF (Analtech, 1 mm), respectively. IR spectra were recorded on a Perkin Elmer Spectrum One FT-IR spectrometer (ATR, Golden Gate) and are reported as wavenumbers ν in cm^{-1} with band intensities indicated as s (strong), m (medium), w (weak), br (broad). ^{1}H and ^{13}C NMR spectra were recorded either on a Bruker 300 MHz, 400 MHz, 500 MHz or 700 MHz spectrometer and are reported as chemical shifts (δ) in ppm relative to tetramethylsilane (δ = 0) at room temperature. Spin multiplicities are reported as a singlet (s), broad singlet (br s), doublet (d), triplet (t) and quartet (q) with proton-proton coupling constants (*J*) given in Hz, or multiplet (m). ESI-MS for the characterization of new compounds was performed on an ESI API 150EX and is reported as mass-per-charge ratio m/z (intensity in %, [assignment]). ESI-HRMS for the characterization of new compounds were performed on a QSTAR Pulsar (AB/MDS Sciex) and are reported as mass-per-charge ratio m/z calculated and observed. MALDI-TOF was performed on a Bruker Autoflex using dithranol or DCTB as matrix.

*3.5.1.1. Synthesis of 1,4-fullerene addends **32** and **33** and their oligothiophene-based dyads **T4-32** and **T4-33***

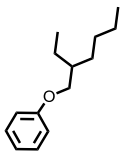

Compound 38. [(2-Ethylhexyl)oxy]benzene. This product was synthesized according to reported procedures.[119]

119 S. W. Kim, S. C. Shim, B.-J. Jung and H.-K. Shim, *Polymer* **2002**, *43*, 4297-4305.

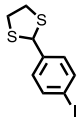

Compound 39. 2-(4-iodophenyl)-1,3-dithiolane. To a solution containing 4-iodobenzaldehyde (4.64 g, 20 mmol) and boron trifluoride diethyl etherate (1.7 ml, 20 mmol) in dried CH_2Cl_2 (60 mL), 1,2-ethanedithiol (2.5 mL, 20 mmol) was slowly added. The mixture was stirred at room temperature for 15 min, and 20 ml of an aqueous solution of NaOH (5%) was added and stirred during 10 min more. The organic layer was washed with NaOH (5%, 2 x 20 ml) and water (1 x 20 ml), dried over $MgSO_4$, and the solvent was removed under vacuum, to afford the desired compound **39** as a white solid (5.92 g, 96 %). R_f: 0.70 (CH_2Cl_2/hexane 1:1); M.p. = 74-75 ºC; IR (neat): 3050 (w), 2911 (m), 1702 (m), 1582 (m), 1420 (m), 1268 (m), 854 (C), 829 (C), 740 (C); ^{1}H NMR (300 MHz, $CDCl_3$): 7.73-7.61 (m, 2H), 7.36-7.23 (m, 2H), 5.59 (s, 1H), 3.59-3.46 (m, 2H), 3.45-3.33 (m, 2H); ^{13}C NMR (75 MHz, $CDCl_3$): 140.4 (C), 137.6 (CH), 129.9 (CH), 93.5 (C), 55.6 (CH), 40.4 (CH_2); MS (EI, CH_2Cl_2): 306.8 (100, $[M-H]^+$), 307.8 (56, $[M]^+$), 308.8 (18, $[M+H]^+$).

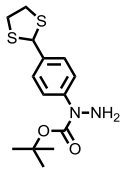

Compound 40. *tert*-Butyl 1-[4-(1,3-dithiolan-2-yl)phenyl]hydrazinecarboxylate. To a solution of CuI (150 mg, 0.78 mmol, 10 mol%), 1,10-phenanthroline (280 mg, 1.56 mmol, 20 mol%) and Cs_2CO_3 (3.30 g, 10.13 mmol), in anhydrous DMF (15 mL), under Argon atmosphere, *tert*-butylcarbazate (1.24 mg, 9.34 mmol) and **39** (2.40 g, 7.79 mmol) were added. The reaction mixture was stirred at 80 °C for 6 h. The resulting suspension was cooled down to room temeprature and filtered through celite eluting with EtOAc. The filtrate was concentrated. The crude was purified by flash chromatography on silica gel (CH_2Cl_2/AcOEt 3:1) provided compound **40** as a pale yellow oil (1.63 g, 67%). R_f: 0.20 (CH_2Cl_2); IR (neat): 3335 (w), 2975 (m), 2926 (m), 1688 (C), 1505 (m), 1363 (m), 1363 (m), 1144 (C), 1049 (m), 844 (m), 758 (m), 733 (m). ^{1}H NMR (300 MHz, $CDCl_3$): 7.53-7.41 (m, 4H), 5.66 (s, 1H), 4.44 (bs, 2H), 3.61-3.46 (m, 2H), 3.46-3.30 (m, 2H), 1.54 (s, 9H); ^{13}C NMR (75 MHz, $CDCl_3$): 155.1 (C), 142.9 (C), 136.1 (C), 127.9 (CH), 123.2 (CH), 82.2 (C), 56.1 (CH), 40.3 (CH_2), 28.5 (CH_3); MS (ESI, +ve): 335 (100, $[M+Na]^+$), 351 (33, $[M+K]^+$).

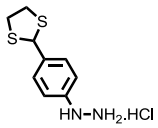

Compound 41. [4-(1,3-Dithiolan-2-yl)phenyl]hydrazine hydrochloride. To a solution of **40** (1.60 g, 5.12 mmol) in CH_3OH (10 mL) concentrated aqueous HCl (2 mL) was added and the mixture was stirred at 50 ºC for 2 h. The resulting red

solution was added over cold diethyl ether (100 mL). The precipitate was filtered and washed with cold diethyl ether (50 ml), obtaining compound **41** as a purple powder in quantitative yield. Mp: 150 ºC; IR (neat): 3203 (w), 2912 (m), 2844 (m), 2674 (m), 1566 (m), 1511 (C), 1418 (w), 86 (m), 835 (C), 752 (m), 653 (m). ^{1}H NMR (300 MHz, CD_3OD): 7.55-7.46 (m, 2H), 6.94-6.86 (m, 2H), 5.66 (s, 1H), 3.56-3.44 (m, 2H), 3.41-3.32 (m, 2H); ^{13}C NMR (75 MHz, CD_3OD): 146.0 (C), 136.3 (C), 130.3 (CH), 115.6 (CH), 56.7 (CH), 41.1 (CH_2); MS (ESI, +ve): 213 (100, $[M+H]^+$), 235 (22, $[M+Na]^+$).

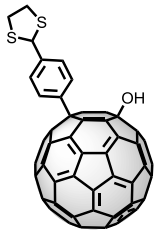

Compound 42. 1-[4-(1,3-Dithiolan-2-yl)phenyl]-4-hydroxyl-1,4-dihydro[60]fullerene. Fullerene C_{60} (400 mg, 0.56 mmol), **41** (276 mg, 1.11 mmol) and $NaNO_2$ (76 mg, 1.11 mmol) were sonicated in toluene (300 mL) for 30 min at 50 ºC. Concentrated HCl (0.1 ml) and water (12 ml) were added and the mixture was stirred at 50 ºC for another 2 h. The solvent was removed under reduced pressure and the crude mixture was purified by flash chromatography on silica gel. Unreacted C_{60} was recovered using CS_2 and **42** was eluted using PhMe. The product was obtained as a brown solid (93 mg, 18%). R_f: 0.45 (PhMe); ^{1}H NMR (700 MHz, THF-d_8): 8.36 (d, ^{3}J = 8.1 Hz, 2H), 7.83 (d, ^{3}J = 8.1 Hz, 2H), 7.68 (br s, 1H), 5.81 (s, 1H), 3.61-3.56 (m, 2H), 3.43-3.38 (m, 2H); ^{13}C NMR (175 MHz, THF-d_8): 154.9 (C), 154.7 (C), 153.8 (C), 152.0 (C), 150.5 (C), 149.7 (C), 149.3 (C), 148.5 (C), 148.4 (C), 148.1 (C), 147.8 (C), 147.7 (C), 147.5 (C), 147.4 (C), 147.1 (C), 146.5 (C), 146.3 (C), 146.2 (C), 145.9 (C), 145.8 (C), 145.4 (C), 145.3 (C), 145.2 (C), 145.0 (C), 144.9 (C), 144.8 (C), 144.7 (C), 144.6 (C), 144.2 (C), 144.0 (C), 143.9 (C), 143.8 (C), 143.7 (C), 143.3 (C), 143.1 (C), 143.0 (C), 142.4 (C), 142.0 (C), 141.6 (C), 140.8 (C), 140.4 (C), 139.6 (C), 139.4 (C), 138.7 (C), 130.1 (CH), 128.8 (CH), 76.5 (C), 62.4 (C), 56.6 (CH), 41.1 (CH_2); MS (MALDI, dithranol): 917.9 (100, $[M]^+$).

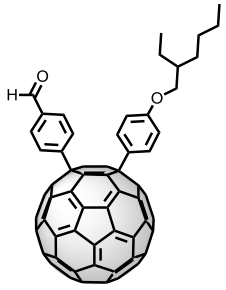

Compound 32. 1-[4-(2-ethyl-hexyloxy)phenyl]-4-(4-formylphenyl)-1,4-dihydro[60]fullerene. To a solution of fullerenol **42** (90 mg, 0.098 mmol) in 5 ml of compound **38**, *p*-toluenesulfonic acid monohydrate (75 mg, 0.392 mmol) was added. The reaction mixture was stirred at 80 ºC overnight, in the dark and under Argon atmosphere. After this time, the mixture was cooled down to rt and poured in a centrifuge tube, precipitating the fullerene derivatives

with CH_3OH (2 x 20 ml). After removing the supernatant, the precipitate, containing **43**, was used without further purification for the deprotection reaction of the aldehyde group, due to the high instability of this intermediate. For this purpose, to a solution of the precipitate in THF/H_2O (9:1, 15 mL), HgO (26 mg, 0.12 mmol) and 3 drops of boron trifluoride diethyl etherate were added. The reaction mixture was stirred for 3 h at 70 ºC. After this time, the crude mixture was diluted with $CHCl_3$ (30 mL) and dried over Na_2SO_4. The solvent was removed under reduce pressure and the crude product was purified by flash chromatography on silica gel using a mixture of CS_2/toluene (2:1) as eluent. Compound **32** was obtained as brown sticky oil after washing with CH_3OH (12 mg, 10%). R_f: 0.66 (PhMe); ^{1}H NMR (700 MHz, $CDCl_3$): 10.15 (s, 1H), 8.34 (d, ^3J = 8.3 Hz, 2H), 8.07 (d, ^3J = 8.3 Hz, 2H), 8.01 (d, ^3J = 8.7 Hz, 2H), 7.06 (d, ^3J = 8.7 Hz, 2H), 3.96-3.91 (m, 2H), 1.82-1.77 (m, 1H), 1.60-1.54 (m, 2H), 1.53-1.47 (m, 4H), 1.47-1.41 (m, 2H), 0.98 (t, ^3J = 7.0 Hz, 3H), 0.94 (t, ^3J = 7.0 Hz, 3H); ^{13}C NMR (175 MHz, $CDCl_3$): 191.9 (CH), 159.7 (C), 157.1 (C), 155.7 (C), 151.5 (C), 150.2 (C), 149.0 (C), 148.9 (C), 148.6 (C), 147.4 (C), 147.3 (C), 147.2 (C), 147.1 (C), 147.0 (C), 146.3 (C), 145.9 (C), 145.4 (C), 145.2 (C), 145.0 (C), 144.9 (C), 144.7 (C), 144.6 (C), 144.5 (C), 144.4 (C), 144.3 (C), 144.2 (C), 143.9 (C), 143.5 (C), 143.4 (C), 143.0 (C), 142.9 (C), 142.8 (C), 142.7 (C), 142.5 (C), 142.4 (C), 142.3 (C), 141.4 (C), 139.4 (C), 138.8 (C), 138.0 (C), 137.4 (C), 136.2 (C), 132.3 (C), 131.0 (CH), 129.2 (C), 128.6 (CH), 128.5 (CH), 128.4 (C), 125.6 (C), 115.6 (CH), 70.9 (CH_2), 61.6 (C), 61.4 (C), 39.6 (CH), 30.7 (CH_2), 29.3 (CH_2), 24.0 (CH_2), 23.2 (CH_2), 14.3 (CH_3), 11.3 (CH_3); MS (MALDI, dithranol): 1031.2 (100, $[M]^+$).

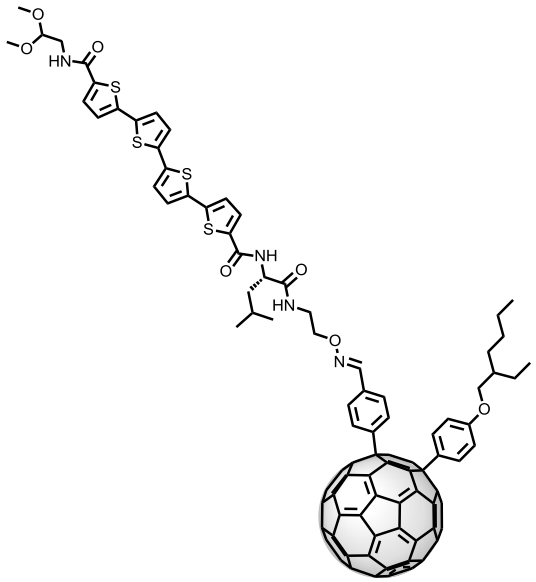

Compound 46. To a solution of **44** (13.2 mg, 17.4 μmol) in CH_2Cl_2 (1.5 ml) and AcOH (80 μl) *n*-Bu_3SnH (62 μl, 232 μmol) and $Pd(PPh_3)_2Cl_2$ (6.1 mg, 8.7 μmol) were added. The mixture was stirred for 15 min at room temperature and more *n*-Bu_3SnH (20 μl, 75 μmol) was added. After stirring 30 min more, **32** (15 mg, 14.5 μmol) was added to the mixture. The reaction mixture was stirred for 2 h, then diluted with CH_2Cl_2, washed with sat. aq. $NaHCO_3$, dried over Na_2SO_4 and concentrated *in vacuo*. The residue was purified by flash chromatography on silica gel (CH_2Cl_2/CH_3OH, 10:1) and then by PTLC (CH_2Cl_2/CH_3OH 40:1) to give **46** (12 mg, 47%) as a yellow brown solid. R_f: 0.55 (CH_2Cl_2/CH_3OH 10:1); ^{1}H NMR (400 MHz, $CDCl_3$/CD_3OD, 95:5): 8.13 (s, 1H), 8.09 (d, ^3J = 8.0 Hz, 2H), 7.98 (d, ^3J = 8.6 Hz, 2H), 7.68 (d, ^3J = 8.0 Hz, 2H), 7.47-7.43 (m, 1H), 7.38 (d, ^3J = 3.9 Hz, 1H), 7.11-6.95 (m, 8H), 4.68 (br t, 1H), 4.49 (t, ^3J = 5.2 Hz, 1H), 4.37-4.23 (m, 2H), 3.91 (br d, ^3J = 5.5 Hz, 2H), 3.70-3.60 (m, 2H), 3.56 (d, ^3J = 5.1 Hz, 2H), 3.44 (s, 6H), 1.78-1.67 (m, 3H), 1.57-1.42 (m, 3H), 1.38-1.21 (m, 6H), 0.98-0.84 (m, 12H); ^{13}C NMR (100 MHz, $CDCl_3$/CD_3OD, 95:5): 161.9 (C), 159.6 (C), 157.1 (C), 156.3 (C), 151.5 (C), 150.6 (C), 149.1 (C), 148.9 (CH), 148.6 (C), 147.3 (C), 147.2 (C), 147.0 (C), 145.9 (C), 145.8 (C), 145.2 (C), 144.9 (C), 144.6 (C), 144.5 (C), 144.4 (C), 144.2 (C), 144.1 (C), 143.9 (C), 143.4 (C), 143.3 (C), 142.9 (C), 142.8 (C), 142.7 (C), 142.4 (C), 142.2 (C), 142.1 (C), 141.6 (C), 141.2 (C), 139.2 (C), 138.9 (C), 137.6 (C), 137.4 (C), 137.0 (C), 136.9 (C), 136.7 (C), 135.7 (C), 135.6 (C), 134.9 (C), 134.8 (C), 134.7 (C), 132.6 (C), 132.5 (C), 132.0 (C), 129.4 (CH), 129.1 (CH), 128.6 (CH), 128.2 (CH), 128.0 (CH), 125.9 (CH), 125.6 (CH), 125.0 (CH), 124.1 (CH), 124.0 (CH), 115.5 (CH), 102.8 (CH), 77.4 (CH), 72.4 (CH_2), 70.9 (CH_2), 61.6 (C), 61.4 (C), 52.1 (CH_3), 50.7 (CH), 41.6 (CH_2), 41.0 (CH_2), 39.6 (CH), 39.4 (CH_2), 34.3 (CH_2), 34.2 (CH_2), 30.7 (CH_2), 30.4 (CH_2), 29.2 (CH_2), 25.0 (CH_2), 24.0 (CH), 23.2 (CH_2), 23.0 (CH_2), 22.4 (CH_3), 14.2 (CH_3), 11.3 (CH_3); MS (MALDI, DCTB): 1692 (100, $[M-2H+3D]^+$), 1689 (33, $[M+H]^+$).

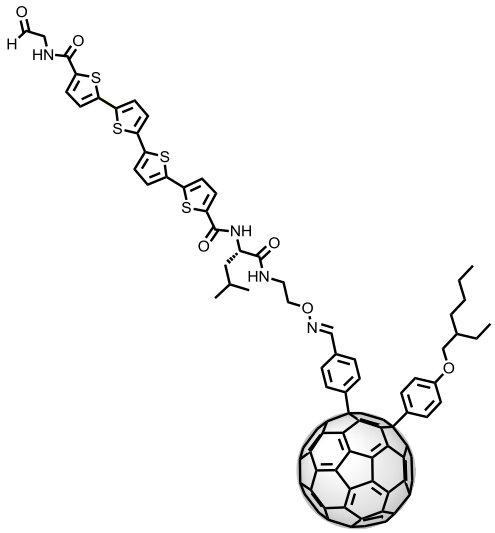

Compound T4-32. To a solution of **46** (10.0 mg, 61 µmol) in CH_2Cl_2 (1.0 ml) TFA (0.5 ml) was added. Then immediately the mixture was concentrated *in vacuo*. The crude was redissolved in THF (3 x 5 ml) and the decomposed precipitate was removed by centrifugation. The supernatant was concentrated *in vacuo* and used for stack exchange without further purification (7 mg, 72%). ^{1}H NMR (400 MHz, THF-d_8/DMSO-d_6 3:1): 9.56 (s, 1H), 8.90 (t, ^3J = 5.5 Hz, 1H), 8.48 (d, ^3J = 8.6 Hz, 1H), 8.29 (s, 1H), 8.18 (d, ^3J = 7.9 Hz, 2H), 8.05 (d, ^3J = 7.9 Hz, 2H), 7.98 (t, ^3J = 5.2 Hz, 1H), 7.89 (d, ^3J = 4.0 Hz, 1H), 7.82 (d, ^3J = 8.2 Hz, 1H), 7.79 (d, ^3J = 4.0 Hz, 1H), 7.37-7.25 (m, 6H), 7.14 (d, ^3J = 8.8 Hz, 2H), 4.61-4.54 (m, 1H), 4.23 (t, ^3J = 5.9 Hz, 2H), 4.05 (d, ^3J = 5.2 Hz, 2H), 3.97 (d, ^3J = 5.6 Hz, 2H), 3.52-3.44 (m, 2H), 1.69-1.59 (m, 3H), 1.53-1.44 (m, 3H), 1.34-1.22 (m, 6H), 0.97-0.87 (m, 12H); MS (MALDI, DCTB): 1643.4 (100, $[M]^+$).

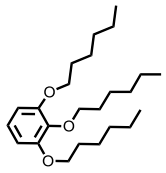

Compound 47. 1,2,3-Tris(hexyloxy)benzene. This product was synthesized according to the reported procedure.[120]

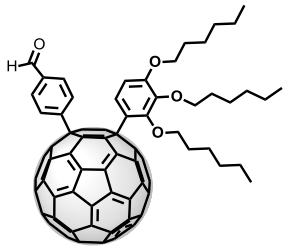

Compound 33. 1-(4-formylphenyl)-4-[2,3,4-(trihexyloxy)phenyl]-1,4-dihydro[60]fullerene. To a solution of fullerenol **42** (70 mg, 76 µmol) in trihexyloxybenzene **47** (5 mL), *p*-toluenesulfonic acid monohydrate (58 mg, 0.30 mmol) was added. The reaction mixture was stirred at 80 ºC overnight, in the dark and under Argon atmosphere. After this time, the mixture was cooled down to room temperature and poured in a centrifuge tube, precipitating the fullerene derivatives with CH_3OH (2 x 20 ml). After removing the supernatant, the precipitate was used without further purification for the

120 C. V. Yelamaggad, A. S. Achalkumar, D. S. S. Rao and S. K. Prasad, *J. Org. Chem.* **2007**, *72*, 8308-8318.

deprotection reaction of the aldehyde group, due to the high instability of this intermediate. For this purpose, to a solution of the precipitate in THF/H_2O (9:1, 15 mL) HgO (20 mg, 0.092 mmol) and 3 drops of boron trifluoride diethyl etherate were added. The reaction mixture was stirred for 3 h at 70 ºC. After this time, the crude reaction was diluted with $CHCl_3$ (30 mL) and dried over Na_2SO_4. The solvent was removed under reduce pressure and the crude product was purified by flash chromatography on silica gel using a mixture of CS_2/PhMe (1:2) as eluent. Compound **33** was obtained as a brown sticky oil after washing with CH_3OH (25.5 mg, 28%). R_f: 0.52 (toluene/CS_2, 1:1); ^{1}H NMR (500 MHz, $CDCl_3$): 10.11 (s, 1H), 8.28 (d, ^3J = 8.2 Hz, 2H), 8.00 (d, ^3J = 8.2 Hz, 2H), 7.78 (d, ^3J = 8.8 Hz, 1H), 6.78 (d, ^3J = 8.8 Hz, 1H), 4.31-4.21 (m, 2H), 4.12-4.03 (m, 4H), 1.94-1.87 (m, 2H), 1.87-1.80 (m, 2H), 1.75-1.67 (m, 2H), 1.60-1.49 (m, 4H), 1.44-1.34 (m, 8H), 1.34-1.27 (m, 2H), 1.27-1.18 (m, 4H), 0.95 (t, ^3J = 7.0 Hz, 3H), 0.92 (t, ^3J = 7.0 Hz, 3H), 0.82 (t, ^3J = 7.0 Hz, 3H); ^{13}C NMR (125 MHz, $CDCl_3$): 191.8 (CH), 156.9 (C), 155.3 (C), 154.2 (C), 152.6 (C), 151.7 (C), 149.9 (C), 149.0 (C), 148.9 (C), 148.1 (C), 147.6 (C), 147.5 (C), 147.4 (C), 147.3 (C), 147.1 (C), 146.6 (C), 145.8 (C), 145.6 (C), 145.5 (C), 145.2 (C), 145.1 (C), 145.0 (C), 144.7 (C), 144.6 (C), 144.3 (C), 144.2 (C), 144.0 (C), 143.8 (C), 143.6 (C), 143.5 (C), 143.4 (C), 143.3 (C), 143.1 (C), 142.9 (C), 142.8 (C), 142.6 (C), 142.5 (C), 142.4 (C), 142.0 (C), 141.2 (C), 139.3 (C), 138.7 (C), 138.3 (C), 138.1 (C), 136.1 (C), 130.8 (CH), 128.5 (CH), 126.4 (C), 124.1 (CH), 108.3 (CH), 74.5 (CH_2), 74.0 (CH_2), 69.0 (CH_2), 61.5 (C), 59.8 (C), 32.0 (CH_2), 31.8 (CH_2), 30.6 (CH_2), 30.0 (CH_2), 29.5 (CH_2), 26.0 (CH_2), 25.7 (CH_2), 22.9 (CH_2), 22.8 (CH_2), 22.7 (CH_2), 14.2 (CH_3); MS (MALDI, Dithranol): 1202.2 (100, $[M]^+$).

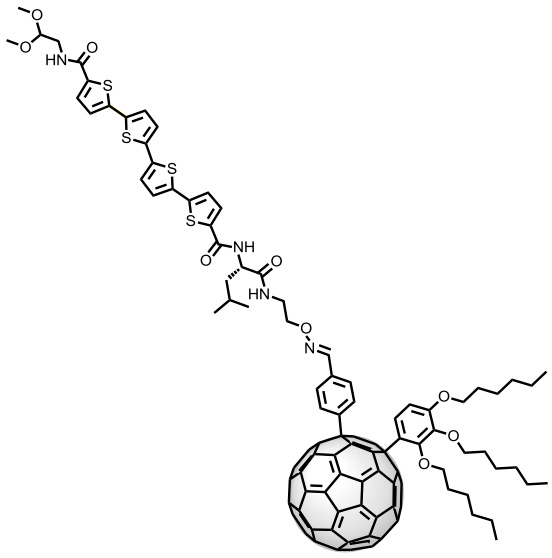

Compound 48. To a solution of **44** (11.5 mg, 15 μmol) in DCM (1.5 ml) and AcOH (80 μl) *n*-Bu_3SnH (54 μl, 200 μmol) and $Pd(PPh_3)_2Cl_2$ (5.6 mg, 8 μmol) were added. The mixture was stirred for 30 min at rt. Then, **33** (15 mg, 12.5 μmol) was added to the mixture. The reaction was stirred for 2 h, then diluted with CH_2Cl_2, washed with sat. aq. $NaHCO_3$, dried over Na_2SO_4 and concentrated *in vacuo*. The residue was purified by flash chromatography on silica gel (CH_2Cl_2/CH_3OH, 50:1) and then by PTLC (CH_2Cl_2/CH_3OH, 50:1) to give compound **48** as a yellow brown solid (12 mg, 52%). R_f: 0.70 (CH_2Cl_2/CH_3OH, 40:1); ^{1}H NMR (500 MHz, $CDCl_3$/CD_3OD 95:5): 8.07 (s, 1H), 8.01 (d, ^3J = 8.0 Hz, 2H), 7.72 (d, ^3J = 8.5 Hz, 1H), 7.59 (d, ^3J = 8.0 Hz, 2H), 7.48-7.44 (m, 1H), 7.40 (d, ^3J = 8.3 Hz, 1H), 7.11-6.99 (m, 6H), 6.73 (d, ^3J = 8.5 Hz, 1H), 4.59 (t, ^3J = 6.0 Hz, 1H), 4.46 (t, ^3J = 6.2 Hz, 1H), 4.29-4.17 (m, 4H), 4.07-3.94 (m, 4H), 3.70 (t, ^3J = 6.2 Hz, 1H), 3.57 (t, ^3J = 4.7 Hz, 2H), 3.50 (d, ^3J = 5.1 Hz, 2H), 3.41 (s, 6H), 3.39-3.37 (m, 1H), 3.36-3.33 (m, 1H), 1.88-1.80 (m, 2H), 1.80-1.74 (m, 2H), 1.71-1.70 (m, 5H), 1.54-1.42 (m, 4H), 1.40-1.13 (m, 14H), 0.93-0.89 (m, 6H), 0.89 (t, ^3J = 6.8 Hz, 3H), 0.86 (t, ^3J = 6.8 Hz, 3H), 0.77 (t, ^3J = 6.8 Hz, 3H); ^{13}C NMR (125 MHz, $CDCl_3$/CD_3OD 95:5): 172.9 (C), 162.1 (C), 162.0 (C), 156.9 (C), 155.9 (C), 154.0 (C), 152.6 (C), 151.6 (C), 150.3 (C), 149.0 (C), 148.9 (C), 148.8 (CH), 148.1 (C), 147.6 (C), 147.3 (C), 147.2 (C), 147.0 (C), 146.9 (C), 146.1 (C), 145.7 (C), 145.6 (C), 145.3 (C), 145.1 (C), 145.0 (C), 144.9 (C), 144.7 (C), 144.6 (C), 144.5 (C), 144.4 (C), 144.2 (C), 144.1 (C), 143.9 (C), 143.8 (C), 143.7 (C), 143.5 (C), 143.3 (C), 143.2 (C), 143.1 (C), 142.9 (C), 142.8 (C), 142.7 (C), 142.5 (C), 142.3 (C), 142.2 (C), 142.1 (C), 141.8 (C), 141.7 (C), 140.9 (C), 139.1 (C), 138.7 (C), 138.0 (C), 137.9 (C), 137.0 (C), 136.9 (C), 136.8 (C), 136.6 (C), 135.7 (C), 135.6 (C), 131.7 (C), 129.5 (CH), 129.4 (CH), 129.2 (CH), 128.0 (CH), 126.5 (C), 125.9 (CH), 125.0 (CH), 124.1 (CH), 124.0 (CH), 108.3 (CH), 102.9 (CH), 102.8 (CH), 74.4 (CH_2), 73.9 (CH_2), 72.3 (CH_2), 68.9 (CH_2), 68.0 (CH_2), 61.4 (C), 59.7 (C), 54.9 (CH_3), 51.9 (CH), 41.5 (CH_2), 40.9 (CH_2), 39.2 (CH_2), 31.9 (CH_2), 31.7 (CH_2), 31.6 (CH_2), 30.4 (CH_2), 29.9 (CH_2), 29.7 (CH_2), 29.4 (CH_2), 29.1 (CH_2), 26.9 (C), 25.9 (CH_2), 25.6 (CH_2), 25.3 (CH_2),

24.9 (CH), 22.7 (CH_2), 22.6 (CH_2), 22.2 (CH_3), 14.1 (CH_3), 14.0 (CH_3); MS (MALDI, DCTB): 1861.7 (100, $[M]^+$).

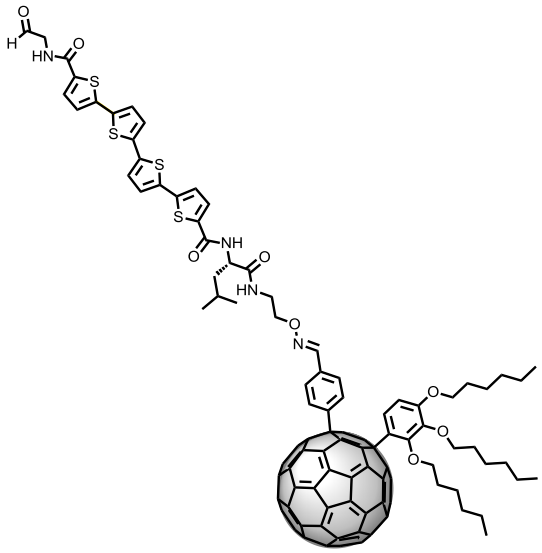

Compound T4-33. To a solution of **48** (12.0 mg, 6.4 μmol) in CH_2Cl_2 (1.0 mL) TFA (0.5 mL) was added. Then immediately the mixture was concentrated *in vacuo*. The product was used for the stack exchange without further purification (11 mg, 93%). R_f: 0.35 (CH_2Cl_2/CH_3OH, 40:1); ^1H NMR (400 MHz, DMSO-d_6/$CDCl_3$ 1:5): 9.55 (s, 1H), 8.77 (t, ^3J = 5.3 Hz, 1H), 8.37-8.29 (m, 1H), 8.05 (s, 1H), 7.99 (d, ^3J = 8.4 Hz, 2H), 7.77-7.62 (m, 3H), 7.58 (d, ^3J = 8.4 Hz, 2H), 7.20-7.03 (m, 6H), 7.01 (br d, ^3J = 3.8 Hz, 1H), 6.78 (d, ^3J = 8.4 Hz, 1H), 4.57-4.48 (m, 1H), 4.21-4.11 (m, 4H), 4.06-3.94 (m, 6H), 3.50-3.43 (m, 2H), 1.83-1.57 (m, 9H), 1.51-1.38 (m, 4H), 1.34-1.25 (m, 10H), 1.17-1.11 (m, 4H), 0.92-0.81 (m, 12H), 0.75 (t, ^3J = 6.8 Hz, 3H); MS (MALDI, DCTB): 1815.6 (100, $[M]^+$).

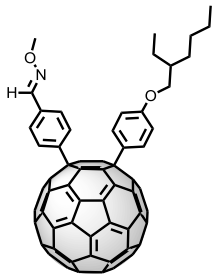

Compound o-32. 1-[4-(2-ethyl-hexyloxy)phenyl]-4-{4-[(methoxyimino)methyl]phenyl}-1,4-dihydro[60]fullerene. To a solution of **32** (8.5 mg, 8.2 μmol) in CH_2Cl_2 (1.5 ml) and AcOH (80 μl) methoxyamine hydrochloride (7 mg, 84 μmol) was added. The mixture was stirred for 3 h at 60 ºC. Then, the reaction was filtered for removing the excess of methoxyamine hydrochloride and concentrated *in vacuo*. The residue was purified by flash chromatography on silica gel (CS_2/toluene, 4:1) to give **o-32** as brown sticky oil after washing with CH_3OH and hexane (3.5 mg, 40%). R_f: 0.45 (toluene/CS_2, 1:4); ^1H NMR (700 MHz, $CDCl_3$): 8.17 (s, 1H), 8.15 (d, ^3J = 8.2 Hz, 2H), 8.02 (d, ^3J = 8.5 Hz, 2H), 7.76 (d, ^3J = 8.2 Hz, 2H), 7.06 (d, ^3J = 8.5 Hz, 2H), 4.04 (s,

3H), 3.97-3.92 (m, 2H), 1.82-1.77 (m, 1H), 1.70-1.56 (m, 2H), 1.53-1.47 (m, 2H), 1.40-1.34 (m, 4H), 0.98 (t, ^{3}J = 7.0 Hz, 3H), 0.94 (t, ^{3}J = 7.0 Hz, 3H); ^{13}C NMR (175 MHz, $CDCl_3$): 159.6 (C), 157.2 (C), 156.4 (C), 151.6 (C), 150.8 (C), 149.0 (C), 148.9 (CH), 148.7 (C), 148.2 (C), 147.4 (C), 147.3 (C), 147.2 (C), 147.1 (C), 146.0 (C), 145.8 (C), 145.3 (C), 145.2 (C), 145.0 (C), 144.8 (C), 144.7 (C), 144.6 (C), 144.5 (C), 144.4 (C), 144.3 (C), 144.2 (C), 144.1 (C), 144.0 (C), 143.4 (C), 143.0 (C), 142.9 (C), 142.8 (C), 142.5 (C), 142.4 (C), 142.3 (C), 141.2 (C), 139.2 (C), 139.0 (C), 138.0 (C), 137.8 (C), 137.4 (C), 132.6 (C), 132.3 (C), 129.2 (C), 128.7 (CH), 128.4 (C), 128.2 (CH), 128.1 (CH), 125.4 (C), 115.5 (CH), 70.9 (CH_2), 62.3 (CH_3), 61.7 (C), 61.4 (C), 39.6 (CH), 30.7 (CH_2), 29.3 (CH_2), 24.0 (CH_2), 23.2 (CH_2), 14.3 (CH_3), 11.3 (CH_3); MS (MALDI, dithranol): 1060.2 (100, $[M]^+$).

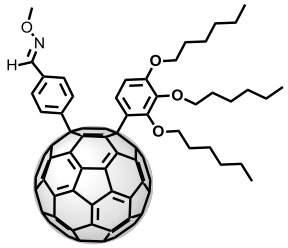

Compound o-33. 1-{4-[(methoxyimino) methyl]phenyl}-4-[2,3,4-(trihexyloxy)phenyl]-1,4-dihydro[60]fullerene. To a solution of **33** (7.5 mg, 6.2 μmol) in CH_2Cl_2 (1.5 ml) and AcOH (80 μl) methoxyamine hydrochloride (6 mg, 73 μmol) was added. The mixture was stirred for 3 h at 60 ºC. Then, the reaction was filtered for removing the excess of methoxyamine hydrochloride and concentrated *in vacuo*. The residue was purified by flash chromatography on silica gel using CS_2 as solvent to give **o-33** as a brown sticky oil after washing with CH_3OH (6.5 mg, 85%). R_f: 0.60 (CS_2); ^{1}H NMR (700 MHz, $CDCl_3$): 8.13 (s, 1H), 8.08 (d, ^{3}J = 8.2 Hz, 2H), 7.79 (d, ^{3}J = 8.7 Hz, 1H), 7.68 (d, ^{3}J = 8.2 Hz, 2H), 6.78 (d, ^{3}J = 8.7 Hz, 1H), 4.29-4.21 (m, 2H), 4.13-4.04 (m, 4H), 4.02 (s, 3H), 1.93-1.88 (m, 2H), 1.87-1.81 (m, 2H), 1.74-1.67 (m, 2H), 1.59-1.50 (m, 4H), 1.43-1.34 (m, 8H), 1.33-1.27 (m, 2H), 1.24-1.19 (m, 4H), 0.95 (t, ^{3}J = 7.0 Hz, 3H), 0.93 (t, ^{3}J = 7.0 Hz, 3H), 0.83 (t, ^{3}J = 7.0 Hz, 3H); ^{13}C NMR (175 MHz, $CDCl_3$): 157.0 (C), 155.9 (C), 154.1 (C), 152.6 (C), 151.7 (C), 150.5 (C), 149.0 (C), 148.9 (C), 148.2 (C), 148.1 (C), 147.7 (C), 147.5 (C), 147.3 (C), 147.2 (C), 147.1 (C), 147.0 (C), 146.2 (C), 145.7 (C), 145.4 (C), 145.2 (C), 145.1 (C), 145.0 (C), 144.8 (C), 144.6 (C), 144.5 (C), 144.3 (C), 144.2 (C), 144.0 (C), 143.9 (C), 143.8 (C), 143.5 (C), 143.4 (C), 143.3 (C), 143.2 (C), 143.0 (C), 142.9 (C), 142.8 (C), 142.6 (C), 142.4 (C), 142.3 (C), 142.0 (C), 141.0 (C), 139.1 (C), 138.8 (C), 138.1 (C), 132.1 (C), 128.2 (CH), 128.0 (CH), 126.5 (C), 124.2 (CH), 108.3 (CH), 74.5 (CH_2), 73.9 (CH_2), 68.9 (CH_2), 62.3 (CH_3), 61.5 (C), 59.7 (C), 32.1 (CH_2), 32.0 (CH_2), 31.8 (CH_2), 30.6 (CH_2), 30.0 (CH_2), 29.8 (CH_2), 29.5 (CH_2), 26.0 (CH_2), 25.7 (CH_2), 22.8 (CH_2), 22.7 (CH_2), 14.3 (CH_3), 14.2 (CH_3); MS (MALDI, dithranol): 1232.3 (100, $[M]^+$).

*3.5.1.2. Synthesis of Bingel fullerenes **54**, **57** and **59***

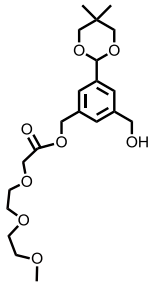

Compound 51. 3-(5,5-Dimethyl-1,3-dioxan-2-yl)-5-(hydroxymethyl)benzyl 2-(2-(2-methoxyethoxy)ethoxy) acetate. To a solution of **49**[113] (480 mg, 1.9 mmol), **50** (0.17 ml, 1.1 mmol) and DMAP (24 mg, 0.2 mmol) in dry CH_2Cl_2 (15 ml) under an Ar atmosphere at 0 ºC, a solution of EDC (230 mg, 1.2 mmol) in dry CH_2Cl_2 (5 ml) was added. The mixture was allowed to reach room temperature and it was stirred for 18 h. The solvent was evaporated to dryness and the crude was purified by silica gel column chromatography (CH_2Cl_2/EtOAc/CH_3OH, 40:10:1) to give **51** as a colorless oil (255 mg, 57%). R_f: 0.22 (CH_2Cl_2/EtOAc/CH_3OH, 30:10:1); IR (neat): 2910 (m), 2869 (m), 1753 (C), 1456 (m), 1391 (m), 1361 (m), 1197 (C), 1106 (C), 1027 (C), 986 (C), 864 (m), 706 (w), 559 (w); ^{1}H NMR (300 MHz, $CDCl_3$): 7.49 (s, 1H), 7.42 (s, 1H), 7.38 (s, 1H), 5.40 (s, 1H), 5.30 (s, 2H), 4.71 (d, ^3J = 6 Hz, 2H), 4.20 (s, 2H), 3.79-3.64 (m, 10H), 3.54-3.52 (m, 2H), 3.37 (s, 3H), 1.82 (t, ^3J = 6.4 Hz, 1H), 1.29 (s, 3H), 0.81 (s, 3H); ^{13}C NMR (100 MHz, $CDCl_3$): 170.3 (C), 141.7 (C), 139.3 (C), 135.9 (C), 127.3 (CH), 125.5 (CH), 124.66 (C), 101.2 (CH), 77.7 (CH_2), 71.9 (CH_2), 70.7 (CH_2), 70.5 (C), 68.7 (CH_2), 66.2 (CH_2), 64.9 (CH_2), 59.0 (CH_3), 41.3 (CH_2), 30.3 (C), 23.1 (CH_3), 21.9 (CH_3); MS (ESI, +ve): 413 (9, $[M+H]^+$), 430 (100, $[M+NH_4]^+$)

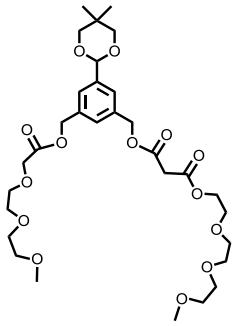

Compound 53. 3-(5,5-Dimethyl-1,3-dioxan-2-yl)-5-(3-oxo-2,5,8,11-tetraoxadodecyl)benzyl {2-[2-(2-methoxyethoxy)ethoxy]ethyl] malonate. To a solution of **51** (250 mg, 0.61 mmol), **52**[97] (0.2 ml, 0.79 mmol) and DMAP (38 mg, 0.31 mmol) in dry CH_2Cl_2 (10 ml) under an Ar atmosphere at 0 ºC, a solution of EDC (234 mg, 1.2 mmol) in dry CH_2Cl_2 (5 ml) was added. The mixture was allowed to reach rt and it was stirred for 18 h. The mixture was evaporated to dryness and after purification of the residue by silica gel column chromatography (CH_2Cl_2/EtOAc/CH_3OH, 40:10:1) **53** was obtained as a colorless oil (254 mg, 66%). R_f: 0.21 (CH_2Cl_2/EtOAc/CH_3OH, 30:10:1); IR (neat): 2948 (m), 2876 (m), 1752 (C), 1738 (C), 1613 (w), 1458 (m), 1330 (m), 1269 (m), 1194 (C), 1137 (C), 1099 (C), 1030 (C), 984 (C), 858 (m), 767 (w), 706 (w); ^{1}H NMR (300 MHz, $CDCl_3$): 7.49 (s, 2H), 7.36 (s, 1H), 5.41 (s, 1H), 5.21 (s, 4H), 4.33 (t, ^3J = 4.5 Hz), 2H), 4.23 (s, 2H), 3.81-3.45 (m, 24H), 3.39 (s, 6H), 1.30 (s, 3H), 0.83 (s, 3H); ^{13}C NMR (100 MHz, $CDCl_3$): 170.3 (C), 166.2 (C), 139.5 (C), 135.8 (C), 128.7

(CH), 126.2 (CH), 100.9 (CH), 77.7 (CH_2), 71.9 (CH_2), 71.0 (CH_2), 68.8 (CH_2), 68.6 (CH_2), 66.7 (CH_2), 66.0 (CH_2), 64.6 (CH_2), 59.1 (CH_3), 41.3 (CH_2), 30.3 (C), 23.1 (CH_3), 21.9 (CH_3); MS (ESI, $CH_3OH/CHCl_3$, 1:1): 667 (100, $[M+Na]^+$).

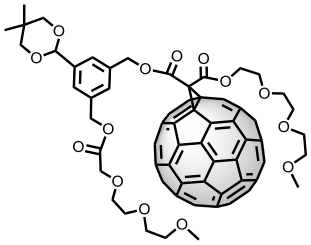

Compound 54. To a solution of C_{60} (200 mg, 0.28 mmol), **53** (100 mg, 0.16 mmol) and I_2 (71 mg, 0.28 mmol) in toluene (120 ml) under Ar atmosphere, DBU (0.07 ml, 0.47 mmol) was added at 0 ºC slowly and then removed the ice bath. The resulting mixture was stirred for 30 min, then filtered through short pad of SiO_2 and washed with toluene and CH_2Cl_2. The crude was purified by silica gel column chromatography (CH_2Cl_2/ CH_3OH, 100:5) followed by PTLC purification (toluene/acetone/CH_3OH, 20:1:1) to give compound **54** as dark-red solid (135 mg, 64%). R_f: 0.31 (toluene/acetone/CH_3OH, 20:1:1); Mp: 74-75 °C; IR: 2919 (C), 2863 (C), 1746 (m), 1458 (m), 1366 (w), 1231 (m), 1105 (m), 1028 (w), 863 (w), 706 (w); ^{1}H NMR (400 MHz, $CDCl_3$): 7.61 (s, 1H), 7.50 (s, 1H), 7.44 (s, 1H), 5.53 (s, 2H), 5.38 (s, 1H), 5.19 (s, 2H), 4.62 (t, ^3J = 4.4 Hz, 2H), 4.20 (s, 2H), 3.83-3.53 (m, 24H), 3.37 (s, 6H), 1.27 (s, 3H), 0.86 (s, 3H); ^{13}C NMR (100 MHz, $CDCl_3$): 170.2 (C), 163.4 (C), 163.3 (C), 145.3 (C), 145.2 (C), 145.1 (C), 144.9 (C), 144.7 (C), 144.6 (C), 144.5 (C), 143.8 (C), 143.1 (C), 143.0 (C), 142.9 (C), 142.2 (C), 141.9 (C), 140.9 (C), 139.7 (C), 139.2 (C), 138.8 (C), 136.1 (C), 135.1 (C), 129.0 (CH), 126.7 (CH), 100.8 (CH), 77.6 (CH_2), 71.9 (CH_2), 71.0 (CH_2), 70.6(CH_2), 68.6 (CH_2), 66.2 (CH_2), 59.1 (CH_3), 51.9 (C), 30.3 (C), 23.2 (CH_3), 21.9 (CH_3); MS (MALDI, DCTB): 1362.65 (100, $[M]^+$).

1,2-dihydromethano[60]fullerene. This product was synthesized according to reported procedures.[104]

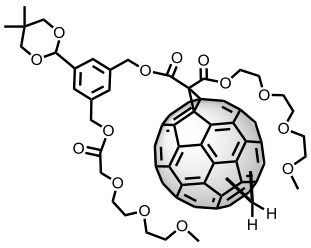

Compound 57. To a solution of 1,2-dihydromethano[60]fullerene (184 mg, 0.27 mmol), **53** (90 mg, 0.14 mmol) and I_2 (64 mg, 0.25 mmol) in toluene (150 ml) under Ar atmosphere, DBU (63 μl, 0.42 mmol) was added at 0 ºC slowly and then removed the ice bath. The resulting mixture was stirred for 10 min, then filtered through short plug of SiO_2 and washed with toluene and CH_2Cl_2. The crude was purified by silica gel column chromatography (CH_2Cl_2/CH_3OH, 100:5) followed by PTLC purification (toluene/acetone/CH_3OH, 20:1:1) to give compound **57** as dark-red solid (73 mg, 40%). R_f: 0.26 (toluene/acetone/CH_3OH, 20:1:1); Mp: 74-75 °C; IR: 2921 (C), 2864 (C), 1752 (m), 1458 (m), 1370 (w), 1235 (m), 1102 (m), 1031 (w), 860 (w), 707 (w); ^{1}H NMR (400 MHz, $CDCl_3$): 7.75-7.41 (m, 3H), 5.68-5.17 (m, 5H), 4.77-4.53 (m, 2H), 4.24-4.09 (m, 2H), 3.77-3.51 (m, 24H), 3.39-3.37 (m, 6H), 1.30-1.27 (m, 3H), 0.82-0.81 (m, 3H), ^{13}C NMR (100 MHz, $CDCl_3$): 170.2 (C), 163.7 (C), 163.4 (C), 163.3 (C), 163.2 (C), 152.7 (C), 152.4 (C), 150.6 (C), 150.1 (C), 147.6 (C), 146.8 (C), 145.9 (C), 145.5 (C), 145.4 (C), 145.2 (C), 144.7 (C), 144.5 (C), 144.3 (C), 143.8 (C), 143.6 (C), 143.3 (C), 142.4 (C), 141.8 (C), 141.7 (C), 139.9 (C), 139.6 (C), 138.4 (C), 136.6 (C), 136.0 (C), 135.3 (C), 135.2 (C), 128.9 (CH), 126.7 (CH), 126.5 (CH), 100.8 (CH), 77.6 (CH_2), 71.9 (CH_2), 71.0 (CH_2), 70.6 (CH_2), 68.6 (CH_2), 68.3 (CH_2), 66.0 (CH_2), 59.1 (CH_3), 51.2 (C), 30.3 (C), 29.7 (C), 27.1 (C), 25.7 (C), 23.2 (CH_3), 21.9 (CH_3) (Comment: Because of the presence of regioisomers, too many ^{13}C peaks were observed. Here only selected ^{13}C peaks were listed); MS (MALDI, DCTB): 1377.13 (100, $[M]^+$).

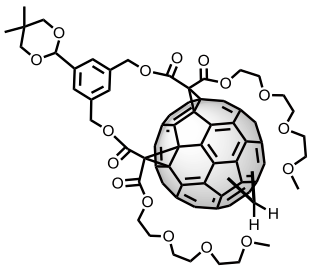

Compound 59. To a solution of 1,2-dihydromethano[60]fullerene (200 mg, 0.27 mmol), **58** (108 mg, 0.15 mmol) and I_2 (140 mg, 0.55 mmol) in toluene (300 ml) under Ar atmosphere, DBU (0.14 ml, 0.91 mmol) was added at 0 ºC slowly. The resulting mixture was allowed to reach to room temperature, stirred for 10 min, then filtered through short pad of SiO_2 and washed with toluene and CH_2Cl_2. The crude was purified by silica gel column chromatography (CH_2Cl_2/CH_3OH, 100:5) followed by PTLC purification (toluene/acetone/CH_3OH, 20:1:1) to give compound **59** as dark-red solid (87 mg, 40%). R_f: 0.21 (toluene/acetone/CH_3OH, 20:1:1); Mp: 93-94 °C; IR(neat): 2871 (m), 1748 (C), 1455 (w), 1392 (w), 1234 (C), 1209 (m), 1106 (C), 1025 (w), 752

(w), 705 (w); ^{1}H NMR (400 MHz, $CDCl_3$): 7.75-7.41 (m, 3H), 6.04-5.80 (m, 2H), 5.50-4.45 (m, 1H), 5.31-5.11 (m, 2H), 4.69-4.42 (m, 4H), 3.91-3.51 (m, 26H), 3.40-3.38 (m, 6H), 1.34-1.31 (m, 3H), 0.86-0.84 (m, 3H); ^{13}C NMR (100 MHz, $CDCl_3$): 162.9 (C), 150.6 (C), 149.7 (C), 149.4 (C), 148.9 (C), 148.5 (C), 148.1 (C), 147.5 (C), 147.2 (C), 146.9 (C), 146.7 (C), 146.5 (C), 146.2 (C), 146.0 (C), 145.7 (C), 145.2 (C), 145.1 (C), 144.6 (C), 144.4 (C), 144.1 (C), 143.9 (C), 143.5 (C), 143.1 (C), 142.7 (C), 141.5 (C), 140.8 (C), 140.4 (C), 139.9 (C), 139.2 (C), 138.6 (C), 137.4 (C), 136.9 (C), 136.8 (C), 124.0 (CH), 100.8 (CH), 77.7 (CH_2), 71.9 (CH_2), 70.6 (CH_2), 68.7 (CH_2), 66.1 (CH_2), 66.0 (CH_2), 59.1 (CH_3), 53.5 (C), 48.8 (C), 46.8 (C), 31.7 (C), 30.3 (C), 29.7 (C), 23.1 (CH_3), 21.9 (CH_3), 19.2 (CH_3), 13.9 (C) (Comment: Because of the presence of regioisomers, too many ^{13}C peaks were observed. Here only selected ^{13}C peaks were listed); MS (MALDI, HABA): 1470.38 (100, $[M+Na]^+$).

*3.5.1.3. Synthesis of electron-deficient fullerenes **60** to **64***

1,2-Dicyano[60]fullerene. This product was synthesized according to the reported procedure.[109]

Dicyanomethano[60]fullerene. This product was synthesized according to the reported procedure.[117]

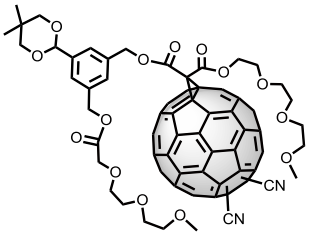

Compound 65. To a solution of **53** (115 mg, 0.18 mmol), 1,2-dicyano[60]fullerene (250 mg, 0.32 mmol) and I_2 (82 mg, 0.32 mmol) in dry toluene (120 mL) under Ar atmosphere, DBU (80 μL, 0.54 mmol) was slowly added at –15 ºC. The resulting mixture was allowed to react for 15 min and then, the solvent was removed under reduced pressure. The crude mixture was purified by flash chromatography on silica gel (unreacted 1,2-dicyano[60]fullerene was recovered using toluene and **65** was eluted using CH_2Cl_2/CH_3OH, 30:1) followed by PTLC purification (CH_2Cl_2/CH_3OH, 30:1; R_f = 0.33, CH_2Cl_2/CH_3OH, 30:1). The product **65** (151 mg, 60%) was obtained as

a brown powder. M.p.: 91-92 ºC; IR (neat): 2940 (m), 2900 (m), 2242 (w), 1748 (C), 1464 (w), 1269 (m), 1141 (m), 1106 (C), 1031 (w); ^{1}H NMR (500 MHz, $CDCl_3$): 7.78-7.31 (m, 3H), 5.72-5.29 (m, 3H), 5.29-4.99 (m, 2H), 4.82-4.36 (m, 2H), 4.35-4.13 (m, 2H), 4.02-3.50 (m, 22H), 3.44-3.22 (m, 3H), 1.30-1.20 (m, 3H), 0.87-0.76 (m, 3H); ^{13}C NMR (125 MHz, $CDCl_3$): 170.3 (C), 162.7 (C), 162.5 (C), 149.6 (C), 149.5 (C), 149.5 (C), 149.4 (C), 148.7 (C), 148.2 (C), 147.4 (C), 146.8 (C), 146.8 (C), 146.6 (C), 146.5 (C), 146.0 (C), 145.8 (C), 145.6 (C), 145.5 (C), 145.2 (C), 145.2 (C), 144.8 (C), 144.8 (C), 144.7 (C), 144.6 (C), 144.5 (C), 144.2 (C), 144.1 (C), 143.3 (C), 143.1 (C), 143.0 (C), 142.9 (C), 142.5 (C), 141.7 (C), 141.6, (C) 141.5 (C), 141.2 (C), 139.8 (C), 139.2 (C), 139.1 (C), 137.8 (C), 137.7 (C), 136.2 (C), 135.0 (C), 129.2 (CH), 126.8 (CH), 126.8 (CH), 116.7 (C), 116.7 (C), 100.8 (CH), 77.8 (CH_2), 77.7 (CH_2), 72.0 (CH_2), 71.1 (CH_2), 70.7 (CH_2), 70.5 (C), 68.7 (CH_2), 68.6 (CH_2), 66.4 (CH_2), 66.0 (CH_2), 65.9 (CH_2), 59.2 (CH_3), 57.3 (C), 50.9 (C), 30.4 (C), 23.2 (CH_3), 21.9 (CH_3) (Comment: Because of the presence of regioisomers, too many ^{13}C peaks were observed. Here only selected ^{13}C peaks were listed); MS (MALDI, DCTB): 1438 (100, $[M+Na]^+$).

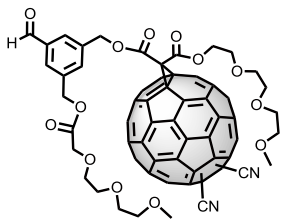

Compound 60. A mixture of **65** (46 mg, 31 μmol), CH_2Cl_2 (2 mL), TFA (1 mL) and H_2O (1 mL) was stirred at rt for 2 h. The organic layer was then washed with H_2O, dried over Na_2SO_4 and the solvent was evaporated. PTLC purification (CH_2Cl_2/CH_3OH, 25:1; R_f = 0.57 CH_2Cl_2/CH_3OH, 19:1) followed by washing firstly with CH_3OH and then with hexane gave compound **60** as a brown powder (25 mg, 58%). M.p.: 84-85 ºC; IR (neat): 2923 (m), 2873 (m), 2241 (w), 1747 (C), 1699 (m), 1457 (w), 1244 (m), 1144 (m), 1106 (m); ^{1}H NMR (500 MHz, $CDCl_3$): 10.16-9.97 (m, 1H), 8.22-7.81 (m, 2H), 7.81-7.55 (m, 1H), 5.82-5.38 (m, 2H), 5.37-5.15 (m, 2H), 4.85-4.38 (m, 2H), 4.37-4.15 (m, 2H), 3.88-3.50 (m, 18H), 3.43-3.23 (m, 3H); ^{13}C NMR (125 MHz, $CDCl_3$): 191.3 (CH), 170.3 (C), 162.7 (C), 162.5 (C), 149.5 (C), 149.4 (C), 149.3 (C), 148.7 (C), 148.2 (C), 147.5 (C), 146.9 (C), 146.6 (C), 146.5 (C), 146.0 (C), 145.8 (C), 145.7 (C), 145.5 (C), 145.3 (C), 145.3 (C), 145.2 (C), 144.9 (C), 144.8 (C), 144.7 (C), 144.6 (C), 144.2 (C), 143.3 (C), 143.2 (C), 143.0 (C), 142.5 (C), 142.4 (C), 141.8 (C), 141.7 (C), 141.6 (C), 141.2 (C), 141.1 (C), 139.1 (C), 137.8 (C), 137.7 (C), 137.6 (C), 137.3 (C), 136.4 (C), 135.0 (C), 134.0 (CH), 129.8 (CH), 129.4 (CH), 116.6 (C), 77.4 (CH), 77.2 (CH_2), 72.0 (CH_2), 71.2 (CH_2), 71.0 (CH_2), 70.8 (CH_2), 70.7 (CH_2), 70.4 (CH_2), 68.7 (CH_2), 67.9 (CH_2), 66.5 (CH_2), 65.4 (CH_2), 65.3 (CH_2), 59.2 (CH_3), 57.3 (C), 50.7 (C) (Comment:

Because of the presence of regioisomers, too many ^{13}C peaks were observed. Here only selected ^{13}C peaks were listed); MS (MALDI, DCTB): 1352 (100, $[M+Na]^+$).

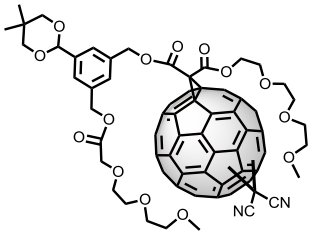

Compound 65. To a solution of **53** (89 mg, 0.14 mmol), dicyanomethano[60]fullerene (195 mg, 0.25 mmol) and I_2 (63 mg, 0.25 mmol) in dry toluene (100 mL) under Ar atmosphere, DBU (62 μL, 0.41 mmol) was slowly added at –15 ºC. The resulting mixture was allowed to react for 15 min and then, the solvent was removed under reduced pressure. The crude mixture was purified by flash chromatography on silica gel (unreacted dicyanomethano[60]fullerene was recovered using toluene and **65** was eluted using CH_2Cl_2/CH_3OH, 30:1) followed by PTLC purification (CH_2Cl_2/CH_3OH, 30:1; R_f = 0.18 with CH_2Cl_2/CH_3OH, 40:1). The product **65** was obtained as a dark-brown powder (110 mg, 56%). M.p.: 123-124 ºC; IR (neat): 2923 (C), 2854 (C), 2247 (w), 1746 (C), 1461 (m), 1232 (C), 1106 (C), 749 (m); ^1H NMR (500 MHz, $CDCl_3$): 7.73-7.32 (m, 3H), 5.72-5.33 (m, 3H), 5.29-5.08 (m, 2H), 4.78-4.42 (m, 2H), 4.28-4.15 (m, 2H), 4.08-3.47 (m, 22H), 3.45-3.21 (m, 3H), 1.33-1.24 (m, 3H), 0.88-0.75 (m, 3H); ^{13}C NMR (125 MHz, $CDCl_3$): 170.4 (C), 163.0 (C), 162.9 (C), 148.2 (C), 147.9 (C), 147.6 (C), 146.7 (C), 146.3 (C), 146.2 (C), 146.1 (C), 145.9 (C), 145.4 (C), 145.3 (C), 145.1 (C), 144.8 (C), 144.7 (C), 144.4 (C), 144.2 (C), 144.1 (C), 143.8 (C), 143.7 (C), 143.6 (C), 143.3 (C), 143.2 (C), 142.7 (C), 142.6 (C), 141.9 (C), 141.6 (C), 141.6 (C), 141.6 (C), 140.6 (C), 140.2 (C), 139.9 (C), 139.8 (C), 139.4 (C), 139.3 (C), 136.3 (C), 135.1 (C), 129.2 (CH), 126.9 (CH), 126.8 (CH), 109.9 (C), 109.8 (C), 100.9 (CH), 77.8 (CH_2), 77.2 (CH_2), 72.1 (CH_2), 71.1 (CH_2), 70.8 (CH_2), 70.7 (CH_2), 68.7 (CH_2), 67.8 (CH_2), 66.4 (CH_2), 66.0 (CH_2), 59.2 (CH_3), 51.2 (C), 30.4 (C), 23.3 (CH_3), 22.0 (CH_3) (Comment: Because of the presence of regioisomers, too many ^{13}C peaks were observed. Here only selected ^{13}C peaks were listed); MS (MALDI, DCTB): 1450 (100, $[M+Na]^+$).

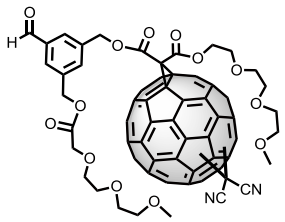

Compound 61. A mixture of **65** (52 mg, 36 μmol), CH_2Cl_2 (2 mL), TFA (1 mL) and H_2O (1 mL) was stirred at rt for 2 h. The organic layer was washed with H_2O, dried over Na_2SO_4 and the solvent was evaporated. PTLC purification (CH_2Cl_2/CH_3OH, 25:1; R_f = 0.55 CH_2Cl_2/CH_3OH, 19:1) followed by washing firstly with CH_3OH and then with hexane gave **61** as a reddish brown powder (28 mg, 56%). M.p.: 117-118 ºC; IR (neat): 2924 (C), 2855 (m), 2248 (w), 1747 (C), 1699 (m), 1460 (m), 1233 (C), 1143 (m), 1110 (m); ^{1}H NMR (500 MHz, $CDCl_3$): 10.28-9.89 (m, 1H), 8.19-7.62 (m, 3H), 5.78-5.41 (m, 2H), 5.34-5.18 (m, 2H), 4.81-4.41 (m, 2H), 4.31-4.17 (m, 2H), 3.38-3.49 (m, 18H), 3.41-3.28 (m, 3H); ^{13}C NMR (125 MHz, $CDCl_3$): 191.3 (CH), 170.3 (C), 161.0 (C), 162.8 (C), 148.1 (C), 147.9 (C), 147.8 (C), 147.6 (C), 146.7 (C), 146.6 (C), 146.3 (C), 146.2 (C), 146.1 (C), 146.1 (C), 145.9 (C), 145.8 (C), 145.6 (C), 145.4 (C), 145.1 (C), 145.0 (C), 144.8 (C), 144.7 (C), 144.5 (C), 144.4 (C), 144.3 (C), 144.2 (C), 144.1 (C), 144.0 (C), 143.7 (C), 143.6 (C), 143.5 (C), 143.4 (C), 143.3 (C), 142.7 (C), 142.3 (C), 142.0 (C), 141.6 (C), 141.5 (C), 141.4 (C), 140.6 (C), 140.4 (C), 140.3 (C), 139.9 (C), 139.5 (C), 139.4 (C), 139.3 (C), 139.2 (C), 137.6 (C), 137.3 (C), 136.5 (C), 134.1 (CH), 134.0 (CH), 129.7 (CH), 129.6 (CH), 109.9 (C), 109.8 (C), 77.4 (CH), 77.2 (CH_2), 72.0 (CH_2), 71.2 (CH_2), 71.1 (CH_2), 70.8 (CH_2), 70.7 (CH_2), 70.2 (CH_2), 68.7 (CH_2), 67.9 (CH_2), 66.5 (CH_2), 65.3 (CH_2), 59.2 (CH_3), 51.0 (C) (Comment: Because of the presence of regioisomers, too many ^{13}C peaks were observed. Here only selected ^{13}C peaks were listed); MS (MALDI, DCTB): 1364 (100, $[M+Na]^+$), 1300 (38, $[M-C(CN)_2+Na]^+$).

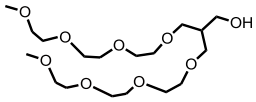

Compound 67. 13-(2,5,8,11-Tetraoxadodecyl)-2,5,8,11-tetraoxatetradecan-14-ol. This product was synthesized according to the reported procedure.[118]

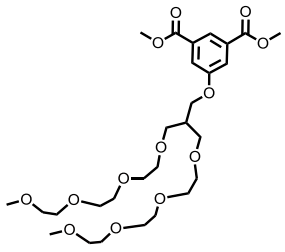

Compound 68. Dimethyl 5-{[13-(2,5,8,11-tetraoxadodecyl)-2,5,8,11-tetraoxatetradecan-14-yl]oxy}isophthalate. To a solution of dimethyl 5-hydroxyisophthalate (550 mg, 2.61 mmol), **67** (1.04 g, 2.61 mmol) and triphenylphosphine (753 mg, 2.87 mmol) in dry CH_2Cl_2 (25 mL) at 0 ºC and under Ar atmosphere, DIAD (0.57 mL, 2.87 mmol) was added

dropwise. The resulting mixture was stirred at rt overnight. After solvent evaporation under reduced pressure, the crude mixture was purified by flash chromatography on silica gel (CH_2Cl_2/CH_3OH/acetone, 40:1:2; R_f = 0.39 CH_2Cl_2/CH_3OH, 19:1). The product **68** was obtained as a colorless oil (750 mg, 50%). IR (neat): 2871 (br), 1724 (C), 1595 (w), 1435 (m), 1339 (m), 1240 (C), 1100 (C) 1046 (m), 759 (m); ^{1}H NMR (300 MHz, $CDCl_3$): 8.24 (t, ^4J = 1.3 Hz, 1H), 7.73 (d, ^4J = 1.3 Hz, 2H), 4.10 (d, ^3J = 5.6 Hz, 2H), 3.92 (s, 6H), 3.66-3.55 (m, 24H), 3.55-3.47 (m, 4H), 3.35 (s, 6H), 2.47-2.36 (m, 1H); ^{13}C NMR (75 MHz, $CDCl_3$): 166.3 (C), 159.3 (C), 131.8 (C), 123.0 (CH), 119.9 (CH), 72.0 (CH_2), 70.8 (CH_2), 70.7 (CH_2), 70.6 (CH_2), 69.3 (CH_2), 66.7 (CH_2), 59.1 (CH_3), 52.5 (CH_3), 40.0 (CH); HRMS (ESI, +ve): 613.2834 (100, $[M+Na]^+$), calculated for $C_{28}H_{46}O_{13}Na$: 613.2830.

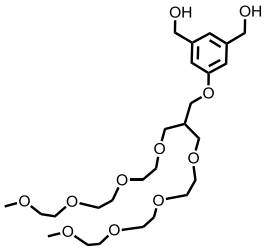

Compound 69. {5-[(13-(2,5,8,11-Tetraoxadodecyl)-2,5,8,11-tetraoxatetradecan-14-yl)oxy]-1,3-phenylene}dimethanol. To a solution of **68** (657 mg, 1.11 mmol) in dry THF (5 mL) at 0 ºC under Ar atmosphere, $LiAlH_4$ (170 mg, 4.48 mmol) was added portionwise. After 5 h stirring at room temperature, some drops of methanol and then water were added carefully at 0 ºC. The mixture was filtered through a pad of celite using ethyl acetate as eluent. After removing the solvent, the crude mixture was purified by flash chromatography on silica gel (CH_2Cl_2/CH_3OH, 15:1; R_f = 0.19 CH_2Cl_2/CH_3OH, 19:1), obtaining the pure compound **69** as a colorless oil (516 mg, 87%). IR (neat): 3444 (br), 2869 (m), 1738 (w), 1597 (m), 1453 (m), 1293 (m), 1096 (C), 1030 (m), 847 (m); ^{1}H NMR (300 MHz, $CDCl_3$): 6.88 (s, 1H), 6.87 (s, 2H), 4.63 (s, 4H), 4.08 (d, ^3J = 5.6 Hz, 2H), 3.67-3.55 (m, 24H), 3.52 (m, 4H), 3.36 (s, 6H), 2.45-2.33 (m, 1H); ^{13}C NMR (75 MHz, $CDCl_3$): 159.7 (C), 143.1 (C), 117.5 (CH), 112.2 (CH), 72.0 (CH_2), 70.8 (CH_2), 70.7 (CH_2), 70.6 (CH_2), 69.4 (CH_2), 66.1 (CH_2), 65.1 (CH_2), 59.1 (CH_3), 40.0 (CH); HRMS (ESI, +ve): 557.2929 (100, $[M+Na]^+$), calculated for $C_{26}H_{46}O_{11}Na$: 557.2932.

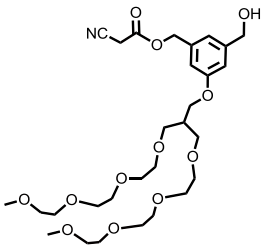

Compound 70. 3-{[13-(2,5,8,11-Tetraoxadodecyl)-2,5,8,11-tetraoxatetradecan-14-yl]oxy}-5-(hydroxymethyl)benzyl 2-cyanoacetate. To a solution of **69** (129 mg, 0.24 mmol), 2-cyanoacetic acid (16 mg, 0.19 mmol) and 4-dimethylaminopyridine (5 mg, 40 μmol) in dry CH_2Cl_2 (5 mL) at 0 ºC under Ar atmosphere, EDC hydrochloride (40 mg, 0.21 mmol) was added portionwise. The resulting mixture was allowed to warm to room temperature and it was stirred at rt overnight under Ar atmosphere. After solvent removal, the crude mixture was separated by flash chromatography on silica gel (CH_2Cl_2/CH_3OH 30:1; R_f = 0.25 with CH_2Cl_2/CH_3OH, 19:1), to give the pure compound **70** as a colorless oil (79 mg, 55%). IR (neat): 3448 (br), 2814 (m), 1748 (m), 1599 (m), 1455 (m), 1296 (m), 1094 (C), 1029 (m), 848 (m); ^{1}H NMR (300 MHz, $CDCl_3$): 6.97 (s, 1H), 6.90 (s, 1H), 6.81 (s, 1H), 5.17 (s, 2H), 4.64 (s, 2H), 4.07 (d, ^3J = 5.6 Hz, 2H), 3.67-3.55 (m, 24H), 3.55-3.48 (m, 6H), 3.35 (s, 6H), 2.50 (br s, 1H), 2.46-2.34 (m, 1H); ^{13}C NMR (75 MHz, $CDCl_3$): 163.0 (C), 159.7 (C), 143.6 (C), 135.9 (C), 119.0 (CH), 114.2 (CH), 113.1 (CH), 113.0 (C), 72.0 (CH_2), 70.8 (CH_2), 70.7 (CH_2), 70.6 (CH_2), 69.4 (CH_2), 68.4 (CH_2), 66.2 (CH_2), 64.8 (CH_2), 59.1 (CH_3), 40.0 (CH), 24.9 (CH_2); HRMS (ESI, +ve): 624.2967 (100, $[M+Na]^+$), calculated for $C_{29}H_{47}NO_{12}Na$: 624.2990.

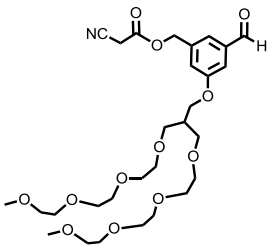

Compound 71. 3-{[13-(2,5,8,11-Tetraoxadodecyl)-2,5,8,11-tetraoxatetradecan-14-yl]oxy}-5-formylbenzyl 2-cyanoacetate. To a solution of **70** (79 mg, 131 μmol) in dry CH_2Cl_2 (5 mL) under Ar atmosphere, Dess-Martin periodinane (84 mg, 197 μmol) was added portionwise. The mixture was stirred at rt overnight, filtered through a small pad of silica gel (CH_2Cl_2/CH_3OH, 10:1) and the solvent was removed under reduced pressure. The crude mixture was purified by flash chromatography on silica gel (CH_2Cl_2/CH_3OH, 20:1; R_f = 0.32 with CH_2Cl_2/CH_3OH, 19:1), obtaining the pure compound **71** as a colorless oil (67 mg, 85%). IR (neat): 2872 (br), 1750 (m), 1697 (m), 1597 (C), 1455 (C), 1297 (m), 1092 (w), 853 (m); ^{1}H NMR (300 MHz, $CDCl_3$): 9.96 (s, 1H), 7.45-7.42 (m, 1H), 7.40 (dd, ^4J (H,H) = 2.4, 1.3 Hz, 1H), 7.20-7.16 (m, 1H), 5.25 (s, 2H), 4.11 (d, ^3J (H,H) = 5.6 Hz, 2H), 3.67-3.56 (m, 24H), 3.57-3.49 (m, 6H), 3.36 (s, 6H), 2.47-2.36 (m, 1H); ^{13}C NMR (75 MHz, $CDCl_3$): 191.7 (CH), 162.9 (C), 160.1 (C), 138.3 (C), 136.9 (C), 122.5 (CH), 121.4 (CH), 114.2 (CH), 112.8 (C), 72.0 (CH_2), 70.8 (CH_2), 70.7 (CH_2),

70.6 (CH_2), 69.3 (CH_2), 67.6 (CH_2), 66.7 (CH_2), 59.1 (CH_3), 40.0 (CH), 24.9 (CH_2); HRMS (ESI, +ve): 622.2827 (100, $[M+Na]^+$), calculated for $C_{29}H_{45}NO_{12}Na$: 622.2833.

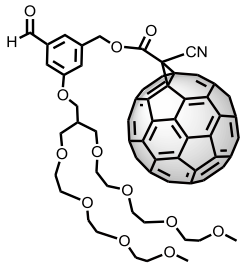

Compound 62. To a solution of **71** (65 mg, 0.11 mmol), C_{60} fullerene (140 mg, 0.19 mmol) and I_2 (49 mg, 0.19 mmol) in dry toluene (70 mL) under Ar atmosphere, DBU (48 μL, 0.32 mmol) was added dropwise at –15 ºC. Resulting mixture was allowed to react for 15 min and then solvent was removed under reduced pressure. The crude mixture was purified by flash chromatography on silica gel (unreacted fullerene was recovered using carbon disulfide and **62** was eluted using CH_2Cl_2/CH_3OH (15:1) followed by PTLC purification (CH_2Cl_2/CH_3OH, 20:1; R_f = 0.39 in CH_2Cl_2/CH_3OH, 19:1). Compound **62** was obtained as a brown powder (21 mg, 15%). M.p.: 92-93 ºC; IR (neat): 2956 (m), 2924 (C), 2856 (m), 2249 (w), 1754 (w), 1698 (w), 1459 (w), 1237 (m), 1136 (m), 1107 (m); ^{1}H NMR (500 MHz, $CDCl_3$): 10.03 (s, 1H), 7.66 (s, 1H), 7.48 (s, 1H), 7.41 (s, 1H), 5.62 (s, 2H), 4.17 (d, ^3J (H, H) = 5.5 Hz, 2H), 3.71-3.59 (m, 24H), 3.57-3.52 (m, 4H), 3.38 (s, 6H), 2.46 (m, 1H); ^{13}C NMR (125 MHz, $CDCl_3$): 191.7 (CH), 161.5 (C), 160.3 (C), 145.8 (C), 145.7 (C), 145.6 (C), 145.5 (C), 145.4 (C), 145.3 (C), 145.0 (C), 144.9 (C), 144.7 (C), 144.6 (C), 144.5 (C), 144.2 (C), 144.1 (C), 143.6 (C), 143.4 (C), 143.4 (C), 143.3 (C), 143.2 (C), 143.1 (C), 142.4 (C), 142.3 (C), 141.8 (C), 141.7 (C), 141.5 (C), 141.3 (C), 139.1 (C), 138.5 (C), 136.6 (C), 123.0 (CH), 121.8 (CH), 114.2 (CH), 113.0 (C), 77.2 (CH_2), 72.1 (CH_2), 70.8 (CH_2), 70.8 (CH_2), 70.7 (CH_2), 70.6 (CH_2), 69.6 (C), 69.4 (CH_2), 68.9 (CH_2), 66.9 (CH_2), 59.2 (CH_3), 40.0 (CH); MS (MALDI, DCTB): 1341 (100, $[M+Na]^+$).

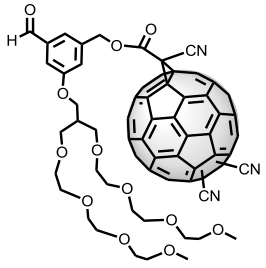

Compound 63. To a solution of **71** (110 mg, 0.18 mmol), 1,2-dicyano[60]fullerene (255 mg, 0.33 mmol) and I_2 (83 mg, 0.33 mmol) in dry toluene (100 mL) under Ar atmosphere, a solution of DBU (82 μL, 0.55 mmol) in 10 mL of dry toluene was added dropwise at –15 ºC. The resulting mixture was allowed to react for 15 min and then solvent was removed under reduced pressure. The crude mixture was purified by flash chromatography on silica gel (unreacted 1,2-dicyano[60]fullerene was recovered

using toluene and **63** was eluted using CH_2Cl_2/CH_3OH (20:1) followed by PTLC purification (CH_2Cl_2/CH_3OH, 20:1; R_f = 0.36 in CH_2Cl_2/CH_3OH, 19:1). Compound **63** was obtained as a brown powder after washing with diethyl ether (40 mg, 16%). M.p.: 101-102 ºC; IR (neat): 2924 (m), 2860 (m), 2245 (w), 1751 (w), 1698 (w), 1276 (m), 1260 (m), 1108 (m), 764 (C), 750 (C); ^{1}H NMR (700 MHz, $CDCl_3$): 10.12-9.95 (m, 1H), 7.73-7.30 (m, 3H), 5.67-5.36 (m, 2H), 4.27-4.10 (m, 2H), 3.99-3.51 (m, 28H), 3.50 -3.26 (m, 6H), 2.53-2.42 (m, 1H); ^{13}C NMR (175 MHz, $CDCl_3$): 191.5 (CH), 160.7 (C), 160.1 (C), 149.5 (C), 149.2 (C), 148.9 (C), 148.7 (C), 148.2 (C), 148.1 (C), 147.7 (C), 147.7 (C), 147.6 (C), 146.91 (C), 146.8 (C), 146.5 (C), 146.0 (C), 145.9 (C), 145.6 (C), 145.5 (C), 145.3 (C), 145.2 (C), 145.1 (C), 145.0 (C), 144.6 (C), 144.3 (C), 144.1 (C), 143.5 (C), 143.4 (C), 143.3 (C), 143.1 (C), 143.0 (C), 142.5 (C), 142.3 (C), 142.2 (C), 142.1 (C), 142.0 (C), 141.5 (C), 141.3 (C), 139.6 (C), 139.1 (C), 138.6 (C), 138.5 (C), 138.4 (C), 138.3 (C), 138.2 (C), 137.5 (C), 136.1 (C), 135.0 (C), 122.6 (CH), 122.4 (CH), 121.7 (CH), 121.1 (CH), 116.3 (C), 116.2 (C), 114.3 (CH), 113.1 (CH), 111.8 (C), 71.9 (CH_2), 70.7 (CH_2), 70.6 (CH_2), 70.5 (CH_2), 69.2 (CH_2), 69.0 (CH_2), 68.8 (CH_2), 68.1 (CH_2), 66.7 (CH_2), 66.5 (CH_2), 65.3 (CH_2), 59.1 (CH_3), 57.2 (C), 57.1 (C), 39.9 (CH) (Comment: Because of the presence of regioisomers, too many ^{13}C peaks were observed. Here only selected ^{13}C peaks were listed); MS (MALDI, DCTB): 1393 (100, $[M+Na]^+$).

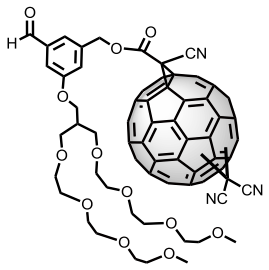

Compound 64. To a solution of **71** (74 mg, 0.12 mmol), dicyanomethano[60]fullerene (155 mg, 0.20 mmol) and I_2 (56 mg, 0.22 mmol) in dry toluene (80 mL) under Ar atmosphere, a solution of DBU (55 μL, 0.37 mmol) in dry toluene (10 mL) was added dropwise at –15 ºC. The resulting mixture was allowed to react for 15 min and then solvent was removed under reduced pressure. The crude mixture was purified by flash chromatography on silica gel (unreacted dicyanomethano[60]fullerene was recovered using toluene and **64** was eluted using CH_2Cl_2/CH_3OH, 20:1) followed by PTLC purification (CH_2Cl_2/CH_3OH, 20:1; R_f = 0.36 in CH_2Cl_2/CH_3OH, 19:1). Compound **64** was obtained as a brown powder after washing with diethyl ether (14.5 mg, 9%). M.p.: 128-129 ºC; IR (neat): 2924 (C), 2856 (m), 2248 (w), 1753 (w), 1699 (w), 1460 (w), 1254 (m), 1137 (m), 1107 (m), 747 (w); ^{1}H NMR (700 MHz, $CDCl_3$): 10.15-9.93 (m, 1H), 7.80-7.30 (m, 3H), 5.80-5.45 (m, 2H), 4.32-4.08 (m, 2H), 3.97-3.47 (m, 28H), 3.39 (s, 6H), 2.59-2.37 (m, 1H); ^{13}C NMR (175 MHz, $CDCl_3$): 191.9 (CH), 161.3 (C), 160.5 (C), 148.4 (C), 148.2 (C), 148.0 (C), 147.9

(C), 147.1 (C), 146.8 (C), 146.7 (C), 146.5 (C), 145.8 (C), 145.6 (C), 145.5 (C), 145.3 (C), 144.8 (C), 144.5 (C), 144.3 (C), 143.6 (C), 143.4 (C), 143.3 (C), 142.2 (C), 141.6 (C), 141.0 (C), 140.8 (C), 140.3 (C), 140.1 (C), 139.4 (C), 138.7 (C), 136.6 (C), 123.2 (CH), 123.1 (CH), 122.1 (CH), 122.0 (CH), 114.6 (CH), 114.5 (CH), 112.6 (C), 109.9 (C), 72.4 (CH_2), 71.1 (CH_2), 71.0 (CH_2), 70.9 (CH_2), 69.6 (CH_2), 69.3 (CH_2), 68.6 (CH_2), 68.0 (CH_2), 67.1 (CH_2), 59.5 (CH_3), 40.3 (CH) (Comment: Because of the presence of regioisomers, too many ^{13}C peaks were observed. Here only selected ^{13}C peaks were listed); MS (MALDI, DCTB): 1405 (100, $[M+Na]^+$), 1341 (23, $[M-C(CN)_2+Na]^+$).

3.5.2. Template Stack-Exchange and Electrode Characterization

Indium tin-oxide (ITO) coated glass substrates were obtained from Präzisions Glas & Optik GmbH (Iserlohn, Germany). During hydrazone-oxime experiment and subsequent covalent capture of aldehydes, vials were shaken in an Incubating Mini Shaker (VWR).

Absorbance measurements. UV-*vis* spectra were recorded on a JASCO V-650 spectrophotometer.

Electrochemical measurements. Electrochemical measurements were done on an Electrochemical Analyzer with Picoamp booster and Faraday cage (CH Instruments 660C). Photocurrents were measured using a 150 W solar simulator (Newport) and an Electrochemical Analyzer (CH Instruments 660C). The irradiation power was measured using a radiant power energy meter (Newport model 70260). Action spectra were measured upon excitation by monochromatic light (150 W Xe lamp with Oriel 1/8 m monochromator)

References

1. G. M. Whitesides, *Small* **2005**, *1*, 172-179.
2. H. W. Kroto, J. R. Heath, S. C. O'Brien, R. F. Curl, R. E. Smalley, *Nature* **1985**, *318*, 162-163.
3. a) D. S. Goodsell, *Bionanotechnology: Lessons from Nature*, Wiley, **2004**; b) J. Deisenhofer, H. Michel, *Science* **1989**, *245*, 1463-1473.
4. L. Tskhovrebova, J. Trinick, *Nat. Rev. Mol. Cell Biol.* **2003**, *4*, 679-689.
5. S. Iijima, *Nature* **1991**, *354*, 56-58.
6. K. S. Novoselov, A. K. Geim, S. V. Morozov, D. Jiang, Y. Zhang, S. V. Dubonos, I. V. Grigorieva, A. A. Firsov, *Science* **2004**, *306*, 666-669.
7. D. M. Guldi, B. M. Illescas, C. M. Atienza, M. Wielopolski, N. Martín, *Chem. Soc. Rev.* **2009**, *38*, 1587-1597.
8. a) T. F. A. De Greef, M. M. J. Smulders, M. Wolffs, A. P. H. J. Schenning, R. P. Sijbesma, E. W. Meijer, *Chem. Rev.* **2009**, *109*, 5687-5754; b) T. Aida, E. W. Meijer, S. I. Stupp, *Science* **2012**, *335*, 813-817; c) J. D. Tovar, *Acc. Chem. Res.* **2013**, *46*, 1527-1537; d) M. R. Wasielewski, *Acc. Chem. Res.* **2009**, *42*, 1910-1921; e) S. I. Stupp, L. C. Palmer, *Chem. Mater.* **2014**, *26*, 507-518.
9. J.-M. Lehn, *Angew. Chem., Int. Ed.* **1990**, *29*, 1304-1319.
10. a) P.-N. Cheng, J. D. Pham, J. S. Nowick, *J. Am. Chem. Soc.* **2013**, *135*, 5477-5492; b) J. D. Pham, R. K. Spencer, K. H. Chen, J. S. Nowick, *J. Am. Chem. Soc.* **2014**, *136*, 12682-12690.
11. A. Greenberg, C. M. Breneman, J. F. Liebman, *The Amide Linkage: Structural Significance in Chemistry, Biochemistry, and Materials Science*, Wiley, **2002**.
12. a) G. S. Vadehra, B. D. Wall, S. R. Diegelmann, J. D. Tovar, *Chem. Commun.* **2010**, *46*, 3947-3949; b) H. A. M. Ardona, K. Besar, M. Togninalli, H. E. Katz, J. D. Tovar, *J. Phys. Chem. C.* **2015**; c) S. R. Diegelmann, N. Hartman, N. Markovic, J. D. Tovar, *J. Am. Chem. Soc.* **2012**, *134*, 2028-2031; d) H. A. M. Ardona, J. D. Tovar, *Chem. Sci.* **2015**, *6*, 1474-1484; e) S. R. Diegelmann, J. M. Gorham, J. D. Tovar, *J. Am. Chem. Soc.* **2008**, *130*, 13840-13841.
13. H. C. Fry, J. M. Garcia, M. J. Medina, U. M. Ricoy, D. J. Gosztola, M. P. Nikiforov, L. C. Palmer, S. I. Stupp, *J. Am. Chem. Soc.* **2012**, *134*, 14646-14649.
14. a) S. S. Babu, S. Prasanthkumar, A. Ajayaghosh, *Angew. Chem., Int. Ed.* **2012**, *51*, 1766-1776; b) A. Das, S. Ghosh, *Angew. Chem., Int. Ed.* **2014**, *53*, 2038-2054.
15. a) S. Prasanthkumar, S. Ghosh, V. C. Nair, A. Saeki, S. Seki, A. Ajayaghosh, *Angew. Chem., Int. Ed.* **2015**, *54*, 946-950; b) S. K. M. Nalluri, N. Shivarova, A. L. Kanibolotsky, M. Zelzer, S. Gupta, P. W. J. M. Frederix, P. J. Skabara,

H. Gleskova, R. V. Ulijn, *Langmuir* **2014**, *30*, 12429-12437; c) S. K. M. Nalluri, R. V. Ulijn, *Chem. Sci.* **2013**, *4*, 3699-3705.
16. a) R. Charvet, S. Acharya, J. P. Hill, M. Akada, M. Liao, S. Seki, Y. Honsho, A. Saeki, K. Ariga, *J. Am. Chem. Soc.* **2009**, *131*, 18030-18031; b) R. Charvet, Y. Yamamoto, T. Sasaki, J. Kim, K. Kato, M. Takata, A. Saeki, S. Seki, T. Aida, *J. Am. Chem. Soc.* **2012**, *134*, 2524-2527; c) Y. Che, H. Huang, M. Xu, C. Zhang, B. R. Bunes, X. Yang, L. Zang, *J. Am. Chem. Soc.* **2011**, *133*, 1087-1091; d) H. Hayashi, W. Nihashi, T. Umeyama, Y. Matano, S. Seki, Y. Shimizu, H. Imahori, *J. Am. Chem. Soc.* **2011**, *133*, 10736-10739; e) Y. Hizume, K. Tashiro, R. Charvet, Y. Yamamoto, A. Saeki, S. Seki, T. Aida, *J. Am. Chem. Soc.* **2010**, *132*, 6628-6629; f) A. Kira, T. Umeyama, Y. Matano, K. Yoshida, S. Isoda, J. K. Park, D. Kim, H. Imahori, *J. Am. Chem. Soc.* **2009**, *131*, 3198-3200; g) W.-S. Li, Y. Yamamoto, T. Fukushima, A. Saeki, S. Seki, S. Tagawa, H. Masunaga, S. Sasaki, M. Takata, T. Aida, *J. Am. Chem. Soc.* **2008**, *130*, 8886-8887; h) Y. Yamamoto, T. Fukushima, Y. Suna, N. Ishii, A. Saeki, S. Seki, S. Tagawa, M. Taniguchi, T. Kawai, T. Aida, *Science* **2006**, *314*, 1761-1764; i) Y. Yamamoto, G. Zhang, W. Jin, T. Fukushima, N. Ishii, A. Saeki, S. Seki, S. Tagawa, T. Minari, K. Tsukagoshi, T. Aida, *Proc. Natl. Acad. Sci. U.S.A.* **2009**, *106*, 21051-21056.
17. B. Vigolo, A. Pénicaud, C. Coulon, C. Sauder, R. Pailler, C. Journet, P. Bernier, P. Poulin, *Science* **2000**, *290*, 1331-1334.
18. R. M. Capito, H. S. Azevedo, Y. S. Velichko, A. Mata, S. I. Stupp, *Science* **2008**, *319*, 1812-1816.
19. S. Zhang, M. A. Greenfield, A. Mata, L. C. Palmer, R. Bitton, J. R. Mantei, C. Aparicio, M. O. de la Cruz, S. I. Stupp, *Nat. Mater.* **2010**, *9*, 594-601.
20. B. D. Wall, S. R. Diegelmann, S. Zhang, T. J. Dawidczyk, W. L. Wilson, H. E. Katz, H.-Q. Mao, J. D. Tovar, *Adv. Mater.* **2011**, *23*, 5009-5014.
21. S. Dresselhaus, G. Dresselhaus, P. Avouris, *Carbon Nanotubes: Synthesis, Structure, Properties, and Applications*, Springer, **2001**.
22. R. Saito, G. Dresselhaus, S. Dresselhaus, *Physical Properties of Carbon Nanotubes*, Imperial College Press, **1998**.
23. C. Romero-Nieto, R. García, M. Á. Herranz, C. Ehli, M. Ruppert, A. Hirsch, D. M. Guldi, N. Martín, *J. Am. Chem. Soc.* **2012**, *134*, 9183-9192.
24. a) Y. K. Kang, O.-S. Lee, P. Deria, S. H. Kim, T.-H. Park, D. A. Bonnell, J. G. Saven, M. J. Therien, *Nano Lett.* **2009**, *9*, 1414-1418; b) J.-H. Olivier, P. Deria, J. Park, A. Kumbhar, M. Andrian-Albescu, M. J. Therien, *Angew. Chem., Int. Ed.* **2013**, *52*, 13080-13085.
25. G. R. Dieckmann, A. B. Dalton, P. A. Johnson, J. Razal, J. Chen, G. M. Giordano, E. Muñoz, I. H. Musselman, R. H. Baughman, R. K. Draper, *J. Am. Chem. Soc.* **2003**, *125*, 1770-1777.
26. C. Doe, H.-S. Jang, T.-H. Kim, S. R. Kline, S.-M. Choi, *J. Am. Chem. Soc.* **2009**, *131*, 16568-16572.

27. T. H. Kim, C. Doe, S. R. Kline, S. M. Choi, *Adv. Mater.* **2007**, *19*, 929-933.
28. G. Wanka, H. Hoffmann, W. Ulbricht, *Macromolecules* **1994**, *27*, 4145-4159.
29. a) D. O. Cowan, C. LeVanda, J. Park, F. Kaufman, *Acc. Chem. Res.* **1973**, *6*, 1-7; b) J. Ferraris, D. O. Cowan, V. Walatka, J. H. Perlstein, *J. Am. Chem. Soc.* **1973**, *95*, 948-949; c) M. Bendikov, F. Wudl, D. F. Perepichka, *Chem. Rev.* **2004**, *104*, 4891-4946.
30. a) F. G. Brunetti, J. L. Lopez, C. Atienza, N. Martín, *J. Mater. Chem.* **2012**, *22*, 4188-4205; b) J. Yamada, T. Sugimoto, *TTF Chemistry: Fundamentals and Applications of Tetrathiafulvalene ; with 47 Tables*, Kodansha, **2004**.
31. D. M. Guldi, L. Sánchez, N. Martín, *J. Phys. Chem. B* **2001**, *105*, 7139-7144.
32. R. Otero, D. Écija, G. Fernández, J. M. Gallego, L. Sánchez, N. Martín, R. Miranda, *Nano Lett.* **2007**, *7*, 2602-2607.
33. J. L. López, C. Atienza, W. Seitz, D. M. Guldi, N. Martín, *Angew. Chem., Int. Ed.* **2010**, *49*, 9876-9880.
34. J. L. López, C. Atienza, A. Insuasty, J. López-Andarias, C. Romero-Nieto, D. M. Guldi, N. Martín, *Angew. Chem., Int. Ed.* **2012**, *51*, 3857-3861.
35. a) W. Herbst, K. Hunger, *Industrial organic pigments: production, properties, applications*, VCH, **1993**; b) C. W. Struijk, A. B. Sieval, J. E. J. Dakhorst, M. van Dijk, P. Kimkes, R. B. M. Koehorst, H. Donker, T. J. Schaafsma, S. J. Picken, A. M. van de Craats, J. M. Warman, H. Zuilhof, E. J. R. Sudhölter, *J. Am. Chem. Soc.* **2000**, *122*, 11057-11066; c) C. D. Dimitrakopoulos, P. R. L. Malenfant, *Adv. Mater.* **2002**, *14*, 99-117.
36. P. E. Hartnett, A. Timalsina, H. S. S. R. Matte, N. Zhou, X. Guo, W. Zhao, A. Facchetti, R. P. H. Chang, M. C. Hersam, M. R. Wasielewski, T. J. Marks, *J. Am. Chem. Soc.* **2014**, *136*, 16345-16356.
37. S. K. Lee, Y. Zu, A. Herrmann, Y. Geerts, K. Müllen, A. J. Bard, *J. Am. Chem. Soc.* **1999**, *121*, 3513-3520.
38. P. M. Kazmaier, R. Hoffmann, *J. Am. Chem. Soc.* **1994**, *116*, 9684-9691.
39. a) Z. Chen, B. Fimmel, F. Wurthner, *Org. Biomol. Chem.* **2012**, *10*, 5845-5855; b) D. Görl, X. Zhang, F. Würthner, *Angew. Chem., Int. Ed.* **2012**, *51*, 6328-6348; c) S. Rehm, V. Stepanenko, X. Zhang, T. H. Rehm, F. Würthner, *Chem. Eur. J.* **2010**, *16*, 3372-3382; d) F. Wurthner, *Chem. Commun.* **2004**, 1564-1579; e) S. Yagai, T. Seki, T. Karatsu, A. Kitamura, F. Würthner, *Angew. Chem., Int. Ed.* **2008**, *47*, 3367-3371; f) X. Zhang, Z. Chen, F. Würthner, *J. Am. Chem. Soc.* **2007**, *129*, 4886-4887.
40. F. G. Brunetti, C. Romero-Nieto, J. López-Andarias, C. Atienza, J. L. López, D. M. Guldi, N. Martín, *Angew. Chem., Int. Ed.* **2013**, *52*, 2180-2184.
41. A. J. Moore, M. R. Bryce, *J. Chem. Soc., Perkin Trans. 1* **1991**, 157-168.
42. S. Zhang, H.-J. Sun, A. D. Hughes, B. Draghici, J. Lejnieks, P. Leowanawat, A. Bertin, L. Otero De Leon, O. V. Kulikov, Y. Chen, D. J. Pochan, P. A. Heiney, V. Percec, *ACS Nano* **2014**, *8*, 1554-1565.

43. C. Backes, C. D. Schmidt, F. Hauke, C. Böttcher, A. Hirsch, *J. Am. Chem. Soc.* **2009**, *131*, 2172-2184.
44. M. Zheng, A. Jagota, M. S. Strano, A. P. Santos, P. Barone, S. G. Chou, B. A. Diner, M. S. Dresselhaus, R. S. Mclean, G. B. Onoa, G. G. Samsonidze, E. D. Semke, M. Usrey, D. J. Walls, *Science* **2003**, *302*, 1545-1548.
45. H. Cathcart, V. Nicolosi, J. M. Hughes, W. J. Blau, J. M. Kelly, S. J. Quinn, J. N. Coleman, *J. Am. Chem. Soc.* **2008**, *130*, 12734-12744.
46. M. Á. Herranz, C. Ehli, S. Campidelli, M. Gutiérrez, G. L. Hug, K. Ohkubo, S. Fukuzumi, M. Prato, N. Martín, D. M. Guldi, *J. Am. Chem. Soc.* **2008**, *130*, 66-73.
47. J. L. Bahr, E. T. Mickelson, M. J. Bronikowski, R. E. Smalley, J. M. Tour, *Chem. Commun.* **2001**, 193-194.
48. a) S. Yagai, S. Kubota, H. Saito, K. Unoike, T. Karatsu, A. Kitamura, A. Ajayaghosh, M. Kanesato, Y. Kikkawa, *J. Am. Chem. Soc.* **2009**, *131*, 5408-5410; b) B. Ohler, I. Revenko, C. Husted, *J. Struct. Biol.* **2001**, *133*, 1-9.
49. J. López-Andarias, J. L. López, C. Atienza, F. G. Brunetti, C. Romero-Nieto, D. M. Guldi, N. Martín, *Nat. Commun.* **2014**, *5*, 3763.
50. a) A. Jatsch, E. K. Schillinger, S. Schmid, P. Bauerle, *J. Mater. Chem.* **2010**, *20*, 3563-3578; b) Q. Wang, Y. Chen, P. Ma, J. Lu, X. Zhang, J. Jiang, *J. Mater. Chem.* **2011**, *21*, 8057-8065; c) G. W. M. Vandermeulen, K. T. Kim, Z. Wang, I. Manners, *Biomacromolecules* **2006**, *7*, 1005-1010.
51. J. Howl, *Peptide Synthesis and Applications*, Humana Press, **2005**.
52. C. Schaefer, I. K. Voets, A. R. A. Palmans, E. W. Meijer, P. van der Schoot, P. Besenius, *ACS Macro Letters* **2012**, *1*, 830-833.
53. P. A. Korevaar, S. J. George, A. J. Markvoort, M. M. J. Smulders, P. A. J. Hilbers, A. P. H. J. Schenning, T. F. A. De Greef, E. W. Meijer, *Nature* **2012**, *481*, 492-496.
54. F. Freire, J. M. Seco, E. Quiñoá, R. Riguera, *Angew. Chem., Int. Ed.* **2011**, *50*, 11692-11696.
55. A. E. Jones, C. A. Christensen, D. F. Perepichka, A. S. Batsanov, A. Beeby, P. J. Low, M. R. Bryce, A. W. Parker, *Chem. Eur. J.* **2001**, *7*, 973-978.
56. J. López-Andarias, M. J. Rodriguez, C. Atienza, J. L. López, T. Mikie, S. Casado, S. Seki, J. L. Carrascosa, N. Martín, *J. Am. Chem. Soc.* **2015**, *137*, 893-897.
57. K. Sakakibara, P. Chithra, B. Das, T. Mori, M. Akada, J. Labuta, T. Tsuruoka, S. Maji, S. Furumi, L. K. Shrestha, J. P. Hill, S. Acharya, K. Ariga, A. Ajayaghosh, *J. Am. Chem. Soc.* **2014**, *136*, 8548-8551.
58. a) V. Percec, H.-J. Sun, P. Leowanawat, M. Peterca, R. Graf, H. W. Spiess, X. Zeng, G. Ungar, P. A. Heiney, *J. Am. Chem. Soc.* **2013**, *135*, 4129-4148; b) Z. Chen, U. Baumeister, C. Tschierske, F. Würthner, *Chem. Eur. J.* **2007**, *13*, 450-465.

59. A. Saeki, S. Seki, Y. Koizumi, S. Tagawa, *J. Photochem. Photobiol. A* **2007**, *186*, 158-165.
60. S. Seki, A. Saeki, T. Sakurai, D. Sakamaki, *Phys. Chem. Chem. Phys.* **2014**, *16*, 11093-11113.
61. a) N. C. Seeman, *Biochemistry* **2003**, *42*, 7259-7269; b) L. Jaeger, A. Chworos, *Curr. Opin. Struct. Biol.* **2006**, *16*, 531-543.
62. P. W. K. Rothemund, *Nature* **2006**, *440*, 297-302.
63. a) C. E. MacPhee, D. N. Woolfson, *Curr. Opin. Solid State Mater. Sci.* **2004**, *8*, 141-149; b) T. O. Yeates, J. E. Padilla, *Curr. Opin. Struct. Biol.* **2002**, *12*, 464-470; c) R. V. Ulijn, D. N. Woolfson, *Chem. Soc. Rev.* **2010**, *39*, 3349-3350.
64. T. P. J. Knowles, T. W. Oppenheim, A. K. Buell, D. Y. Chirgadze, M. E. Welland, *Nat Nano* **2010**, *5*, 204-207.
65. D. Papapostolou, A. M. Smith, E. D. T. Atkins, S. J. Oliver, M. G. Ryadnov, L. C. Serpell, D. N. Woolfson, *Proc. Natl. Acad. Sci. U.S.A.* **2007**, *104*, 10853-10858.
66. L. D. D'Andrea, L. Regan, *Trends Biochem. Sci.* **2003**, *28*, 655-662.
67. T. Kajander, A. L. Cortajarena, S. Mochrie, L. Regan, *Acta Crystallogr., Sect. D: Biol. Crystallogr.* **2007**, *63*, 800-811.
68. a) E. R. G. Main, Y. Xiong, M. J. Cocco, L. D'Andrea, L. Regan, *Structure*, *11*, 497-508; b) A. L. Cortajarena, S. G. J. Mochrie, L. Regan, *Protein Sci.* **2011**, *20*, 1042-1047; c) T. Kajander, A. L. Cortajarena, E. R. G. Main, S. G. J. Mochrie, L. Regan, *J. Am. Chem. Soc.* **2005**, *127*, 10188-10190.
69. T. Z. Grove, L. Regan, A. L. Cortajarena, *J. R. Soc. Interface* **2013**, *10*.
70. a) Y. N. Teo, E. T. Kool, *Chem. Rev.* **2012**, *112*, 4221-4245; b) A. Ruiz-Carretero, P. G. A. Janssen, A. Kaeser, A. P. H. J. Schenning, *Chem. Commun.* **2011**, *47*, 4340-4347.
71. L.-A. Fendt, I. Bouamaied, S. Thöni, N. Amiot, E. Stulz, *J. Am. Chem. Soc.* **2007**, *129*, 15319-15329.
72. a) A. D'Urso, M. E. Fragala, R. Purrello, *Chem. Commun.* **2012**, *48*, 8165-8176; b) J. R. Dunetz, C. Sandstrom, E. R. Young, P. Baker, S. A. Van Name, T. Cathopolous, R. Fairman, J. C. de Paula, K. S. Åkerfeldt, *Org. Lett.* **2005**, *7*, 2559-2561; c) Q. Zou, L. Zhang, X. Yan, A. Wang, G. Ma, J. Li, H. Möhwald, S. Mann, *Angew. Chem., Int. Ed.* **2014**, *53*, 2366-2370.
73. B. Kang, S. Chung, Y. D. Ahn, J. Lee, J. Seo, *Org. Lett.* **2013**, *15*, 1670-1673.
74. a) M. Endo, H. Wang, M. Fujitsuka, T. Majima, *Chem. Eur. J.* **2006**, *12*, 3735-3740; b) M. Endo, M. Fujitsuka, T. Majima, *Chem. Eur. J.* **2007**, *13*, 8660-8666.
75. B. Gigliotti, B. Sakizzie, D. S. Bethune, R. M. Shelby, J. N. Cha, *Nano Lett.* **2006**, *6*, 159-164.
76. F. De Leo, A. Magistrato, D. Bonifazi, *Chem. Soc. Rev.* **2015**.
77. G. Zuo, Q. Huang, G. Wei, R. Zhou, H. Fang, *ACS Nano* **2010**, *4*, 7508-7514.

78. R. Marega, F. De Leo, F. Pineux, J. Sgrignani, A. Magistrato, A. D. Naik, Y. Garcia, L. Flamant, C. Michiels, D. Bonifazi, *Adv. Funct. Mater.* **2013**, *23*, 3173-3184.
79. I.-S. Park, Y.-R. Yoon, M. Jung, K. Kim, S. Park, S. Shin, Y.-b. Lim, M. Lee, *Chem. Asian J.* **2011**, *6*, 452-458.
80. a) J. S. Lindsey, I. C. Schreiman, H. C. Hsu, P. C. Kearney, A. M. Marguerettaz, *J. Org. Chem.* **1987**, *52*, 827-836; b) D. Paul, H. Miyake, S. Shinoda, H. Tsukube, *Chem. Eur. J.* **2006**, *12*, 1328-1338.
81. Z. Gasyna, W. R. Browett, M. J. Stillman, *Inorg. Chem.* **1985**, *24*, 2440-2447.
82. T. Osawa, T. Kajitani, D. Hashizume, H. Ohsumi, S. Sasaki, M. Takata, Y. Koizumi, A. Saeki, S. Seki, T. Fukushima, T. Aida, *Angew. Chem., Int. Ed.* **2012**, *51*, 7990-7993.
83. K. A. Henzler-Wildman, M. Lei, V. Thai, S. J. Kerns, M. Karplus, D. Kern, *Nature* **2007**, *450*, 913-916.
84. S. S. Cohen, I. Riven, A. L. Cortajarena, L. De Rosa, L. D. D'Andrea, L. Regan, G. Haran, *J. Am. Chem. Soc.* **2015**.
85. J. Camps, O. Carrillo, A. Emperador, L. Orellana, A. Hospital, M. Rueda, D. Cicin-Sain, M. D'Abramo, J. L. Gelpí, M. Orozco, *Bioinformatics* **2009**, *25*, 1709-1710.
86. S. Az'hari, Y. Ghayeb, *Mol. Simul.* **2013**, *40*, 392-398.
87. a) V. Z. Poenitzsch, D. C. Winters, H. Xie, G. R. Dieckmann, A. B. Dalton, I. H. Musselman, *J. Am. Chem. Soc.* **2007**, *129*, 14724-14732; b) S. Wang, E. S. Humphreys, S.-Y. Chung, D. F. Delduco, S. R. Lustig, H. Wang, K. N. Parker, N. W. Rizzo, S. Subramoney, Y.-M. Chiang, A. Jagota, *Nat. Mater.* **2003**, *2*, 196-200.
88. a) F. De Leo, J. Sgrignani, D. Bonifazi, A. Magistrato, *Chem. Eur. J.* **2013**, *19*, 12281-12293; b) A. de Leon, A. F. Jalbout, V. A. Basiuk, *Chem. Phys. Lett.* **2008**, *457*, 185-190.
89. a) A. M. Rao, P. C. Eklund, S. Bandow, A. Thess, R. E. Smalley, *Nature* **1997**, *388*, 257-259; b) K. E. Wise, C. Park, E. J. Siochi, J. S. Harrison, *Chem. Phys. Lett.* **2004**, *391*, 207-211; c) R. Voggu, C. S. Rout, A. D. Franklin, T. S. Fisher, C. N. R. Rao, *J. Phys. Chem. C* **2008**, *112*, 13053-13056.
90. N. A. Carter, T. Z. Grove, *Biomacromolecules* **2015**, *16*, 706-714.
91. a) N. Sakai, M. Lista, O. Kel, S.-i. Sakurai, D. Emery, J. Mareda, E. Vauthey, S. Matile, *J. Am. Chem. Soc.* **2011**, *133*, 15224-15227; b) M. Lista, E. Orentas, J. Areephong, P. Charbonnaz, A. Wilson, Y. Zhao, A. Bolag, G. Sforazzini, R. Turdean, H. Hayashi, Y. Domoto, A. Sobczuk, N. Sakai, S. Matile, *Org. Biomol. Chem.* **2013**, *11*, 1754-1765.
92. a) P. Murugan, M. Krishnamurthy, S. N. Jaisankar, D. Samanta, A. B. Mandal, *Chem. Soc. Rev.* **2015**; b) G. L. Whiting, H. J. Snaith, S.

Khodabakhsh, J. W. Andreasen, D. W. Breiby, M. M. Nielsen, N. C. Greenham, R. H. Friend, W. T. S. Huck, *Nano Lett.* **2006**, *6*, 573-578.
93. a) J. A. Bardecker, H. Ma, T. Kim, F. Huang, M. S. Liu, Y.-J. Cheng, G. Ting, A. K. Y. Jen, *Adv. Funct. Mater.* **2008**, *18*, 3964-3971; b) N. Doubina, J. L. Jenkins, S. A. Paniagua, K. A. Mazzio, G. A. MacDonald, A. K. Y. Jen, N. R. Armstrong, S. R. Marder, C. K. Luscombe, *Langmuir* **2012**, *28*, 1900-1908.
94. N. Sakai, S. Matile, *J. Am. Chem. Soc.* **2011**, *133*, 18542-18545.
95. a) P. T. Corbett, J. Leclaire, L. Vial, K. R. West, J.-L. Wietor, J. K. M. Sanders, S. Otto, *Chem. Rev.* **2006**, *106*, 3652-3711; b) M. von Delius, E. M. Geertsema, D. A. Leigh, *Nat. Chem.* **2010**, *2*, 96-101.
96. a) J. Areephong, E. Orentas, N. Sakai, S. Matile, *Chem. Commun.* **2012**, *48*, 10618-10620; b) P. Charbonnaz, N. Sakai, S. Matile, *Chem. Sci.* **2012**, *3*, 1492-1496.
97. A. Bolag, H. Hayashi, P. Charbonnaz, N. Sakai, S. Matile, *ChemistryOpen* **2013**, *2*, 55-57.
98. G. Sforazzini, E. Orentas, A. Bolag, N. Sakai, S. Matile, *J. Am. Chem. Soc.* **2013**, *135*, 12082-12090.
99. B. C. Thompson, J. M. J. Fréchet, *Angew. Chem., Int. Ed.* **2008**, *47*, 58-77.
100. a) C. J. Brabec, N. S. Sariciftci, J. C. Hummelen, *Adv. Funct. Mater.* **2001**, *11*, 15-26; b) K. A. Mazzio, C. K. Luscombe, *Chem. Soc. Rev.* **2015**, *44*, 78-90.
101. J. L. Delgado, P.-A. Bouit, S. Filippone, M. A. Herranz, N. Martin, *Chem. Commun.* **2010**, *46*, 4853-4865.
102. a) A. B. Smith, R. M. Strongin, L. Brard, G. T. Furst, W. J. Romanow, K. G. Owens, R. C. King, *J. Am. Chem. Soc.* **1993**, *115*, 5829-5830; b) A. B. Smith, R. M. Strongin, L. Brard, G. T. Furst, W. J. Romanow, K. G. Owens, R. J. Goldschmidt, R. C. King, *J. Am. Chem. Soc.* **1995**, *117*, 5492-5502.
103. a) M. W. J. Beulen, L. Echegoyen, *Chem. Commun.* **2000**, 1065-1066; b) Z. Yinghuai, S. Bahnmueller, C. Chibun, K. Carpenter, N. S. Hosmane, J. A. Maguire, *Tetrahedron Lett.* **2003**, *44*, 5473-5476.
104. Y. Zhang, Y. Matsuo, C.-Z. Li, H. Tanaka, E. Nakamura, *J. Am. Chem. Soc.* **2011**, *133*, 8086-8089.
105. M. Eiermann, R. C. Haddon, B. Knight, Q. C. Li, M. Maggini, N. Martín, T. Ohno, M. Prato, T. Suzuki, F. Wudl, *Angew. Chem., Int. Ed.* **1995**, *34*, 1591-1594.
106. F. B. Kooistra, J. Knol, F. Kastenberg, L. M. Popescu, W. J. H. Verhees, J. M. Kroon, J. C. Hummelen, *Org. Lett.* **2007**, *9*, 551-554.
107. A. Varotto, N. D. Treat, J. Jo, C. G. Shuttle, N. A. Batara, F. G. Brunetti, J. H. Seo, M. L. Chabinyc, C. J. Hawker, A. J. Heeger, F. Wudl, *Angew. Chem., Int. Ed.* **2011**, *50*, 5166-5169.
108. a) T. Ohno, N. Martín, B. Knight, F. Wudl, T. Suzuki, H. Yu, *J. Org. Chem.* **1996**, *61*, 1306-1309; b) B. Knight, N. Martín, T. Ohno, E. Ortí, C. Rovira,

J. Veciana, J. Vidal-Gancedo, P. Viruela, R. Viruela, F. Wudl, *J. Am. Chem. Soc.* **1997**, *119*, 9871-9882; c) N. Martín, L. Sánchez, B. Illescas, I. Pérez, *Chem. Rev.* **1998**, *98*, 2527-2548.
109. M. Keshavarz-K, B. Knight, G. Srdanov, F. Wudl, *J. Am. Chem. Soc.* **1995**, *117*, 11371-11372.
110. M. Keshavarz-K, B. Knight, R. C. Haddon, F. Wudl, *Tetrahedron* **1996**, *52*, 5149-5159.
111. A. Bolag, J. López-Andarias, S. Lascano, S. Soleimanpour, C. Atienza, N. Sakai, N. Martín, S. Matile, *Angew. Chem., Int. Ed.* **2014**, *53*, 4890-4895.
112. G.-W. Wang, Y.-M. Lu, Z.-X. Chen, *Org. Lett.* **2009**, *11*, 1507-1510.
113. M. Morisue, N. Haruta, D. Kalita, Y. Kobuke, *Chem. Eur. J.* **2006**, *12*, 8123-8135.
114. Y. Yang, F. Arias, L. Echegoyen, L. P. F. Chibante, S. Flanagan, A. Robertson, L. J. Wilson, *J. Am. Chem. Soc.* **1995**, *117*, 7801-7804.
115. T. E. Kang, H.-H. Cho, C.-H. Cho, K.-H. Kim, H. Kang, M. Lee, S. Lee, B. Kim, C. Im, B. J. Kim, *ACS Appl. Mater. Interfaces* **2013**, *5*, 861-868.
116. J. Lopez-Andarias, A. Bolag, C. Nancoz, E. Vauthey, C. Atienza, N. Sakai, N. Martin, S. Matile, *Chem. Commun.* **2015**, *51*, 7543-7545.
117. T.-H. Zhang, P. Lu, F. Wang, G.-W. Wang, *Org. Biomol. Chem.* **2003**, *1*, 4403-4407.
118. S. Zhu, J. Zhang, G. Vegesna, F.-T. Luo, S. A. Green, H. Liu, *Org. Lett.* **2011**, *13*, 438-441.
119. S. W. Kim, S. C. Shim, B.-J. Jung, H.-K. Shim, *Polymer* **2002**, *43*, 4297-4305.
120. C. V. Yelamaggad, A. S. Achalkumar, D. S. S. Rao, S. K. Prasad, *J. Org. Chem.* **2007**, *72*, 8308-8318.